Measurements of L-Subshell Ionization Cross Sections by Energetic α Particles for Ho, Er, and Tm.

by

Bassam Abdulrahman Mahmoud Shehadeh

A Thesis Presented to the

FACULTY OF THE COLLEGE OF GRADUATE STUDIES

KING FAHD UNIVERSITY OF PETROLEUM & MINERALS

DHAHRAN, SAUDI ARABIA

In Partial Fulfillment of the
Requirements for the Degree of

MASTER OF SCIENCE

In

PHYSICS

June, 1994

Measurements of L-Subshell Ionization Cross Sections by Energetic α Particles for Ho, Er, and Tm.

BY

Bassam Abdulrahman Mahmoud Shehadeh

A Thesis Presented to the

FACULTY OF THE COLLEGE OF GRADUATE STUDIES

KING FAHD UNIVERSITY OF PETROLEUM & MINERALS

DHAHRAN, SAUDI ARABIA

In Partial Fulfillment of the
Requirements for the Degree of

MASTER OF SCIENCE

In

PHYSICS

June 1994

King Fahd University of Petroleum and Minerals

Dhahran 31261, Saudi Arabia

College of Graduate Studies

This thesis, written by **Bassam Abdulrahman M. Shehadeh** under the direction of his Thesis Advisor and approved by his Thesis Committee, has been presented to and accepted by the Dean of the College of Graduate Studies, in partial fulfillment of the requirements for the degree of MASTER OF SCIENCE.

Thesis Committee

Thesis Advisor (Dr. A. B. Hallak)

Thesis Co-Advisor (Dr. M. Garwan)

Member (Prof. O. B. Dabbousi)

Member (Dr. J. Nickel)

Department Chairman

Dean, College of Graduate Studies

Date

123-6

بسم الله الرحمن الرحيم

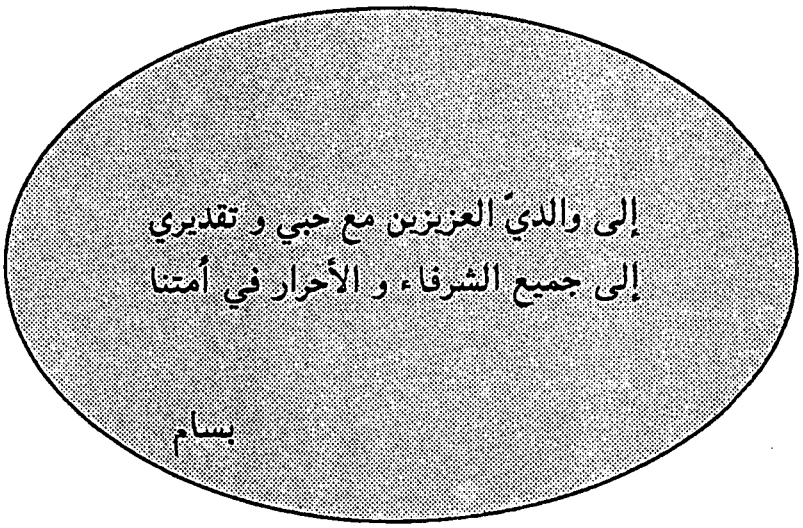
إلى والديّ العزيزين مع حبي و تقديري
إلى جميع الشرفاء و الأحرار في أمتنا
بسام

Acknowledgment

I would like to acknowledge KING FAHAD UNIVERSITY OF PETROLEUM AND MINERALS for its support of this work. Special thank is due to the Physics department represented by the chairman Dr. Abdulaziz Al-Harthi and the ex-chairman Dr. Abdulaziz Al-Haidari for offering me this priceless opportunity to accomplish this work and for their kind support and encouragement. Thank is due to Energy Research Laboratory represented by Dr. Hashim Yamani for making all facilities there available to me.

I would like to express my appreciation to Dr. Awni B. Hallak who served as my thesis advisor for his helpful comments, valuable suggestions, and appreciable support. I also would like to express my gratefulness to all members of my thesis committee: co-advisor Dr. Mohammad Garwan, Prof. Dr. Osama Dabbousi, and Dr. Joachim Nickel for their kind support and precious remarks. In particular, special thanks go to my academic advisor Prof. Dr. Osama Dabbousi for his kind supervision and valuable advises.

Also, I like extend my appreciation to Mr. Mohammad Daous and Mr. S. Madhusoodanan Pillai for teaching and helping me on the operation of the accelerator and to Dr. Ibraheem Nasser and Dr. N. Zettili for their valuable discussions. Recognition is due to my roommates and friends during my academic career Mr. Yaqoub Shehahdeh, Mr. Omar Al-Kaabi, Mr. Ihab Zharnah, and Mr. Hazzem Homaidi for their encouragements, advises, and assistance in editing this thesis.

Finally, I would like to sincerely thank my parents for their valuable supports and constant encouragement, in particular, to my father. I will never forget the risk he took during crises times to make it possible for me to pursue my higher education.

خلاصة الرسالة

الاسم الكامل : بسام عبد الرحمن محمود شحاده .

عنوان الدراسة : قياس المقطع العرضي التأيني للقشور الفرعية L بواسطة جسيمات ألفا المسرعة للهوليوم، الإيربيوم، و الثوليوم .

التخصص : الفيزياء .

تاريخ الشهادة : حزيران-يونيو ١٩٩٤م .

تم في هذه الرسالة قياس مقطع التأين العرضي للقشور الذرية الفرعية L لثلاثة عناصر من مجموعة الأرض النادرة وهي الهوليوم، الإيربيوم، و الثوليوم، بواسطة جسيمات ألفا المسرعة إلى طاقات تتراوح من 1-6 ميجا إلكترون فولت .

قورنت هذه القيم المخبرية مع التنبئات المستنتجة من نظرية *ECPSSR* (المنبثقة من تقريب بورن للموجات السطحية و المعدلة للأثر النسبي، الكولومي، و الإ ستقطاب الإديابتيكي للسحابة الإلكترونية مع الأخذ بالحسبان قيم الطاقة المفقودة) . وجد أن القيم المخبرية تتناقض نظامياً مع التنبئات النظرية عند الطاقات المنخفضة خاصة للقشرة الفرعية L_2 . وعند تعديل نظرية *ECPSSR* لتأخذ بالحسبان الإضطراب المسبب للإنتقالات الداخلية بين القشور الفرعية *(IS)* ، فإن التناقض النظامي إنخفض خاصة للقشرة الفرعية L_2 . لكن التناقض إمتد ليشمل جميع النقاط على مدى جميع الطاقات . وبتعديل طاقة الترابط الإلكترونية في القشور الفرعية عند طاقات الذرة الموحدة للحصول على النظرية المعدلة *ECPSSR-IS-UA* ، وجد أن القيم المخبرية للقشور الفرعية L_2 و L_3 تتفق تماماً مع إستنتاجات *ECPSSR-IS-UA* على مدى جميع الطاقات بإستثناء القشرة الفرعية L_1 .

أسباب التناقض أُرجعت إلى أن الشحنة المؤثرة لجسيمات ألفا يجب أن تخفض إلى أقل من 2 للأخذ بالحسبان أثر الحجب الناتج عن القشور الإلكترونية الخارجية. كذلك يعود التناقض إلى أن الدالة الموجية المستعملة في حساب نظرية *ECPSSR-IS-UA* للقشرة الفرعية L_1 يجب أن تتضمن الدالة الموجية النسبية المحسوبة بطريقة ديراك-هارتري-سلاتر بدلاً عن الدالة الهيدروجينية المحجوبة .

درجة الماجستير في العلوم

جامعة الملك فهد للبترول والمعادن

الظهران، المملكة العربية السعودية

حزيران-يونيو ١٩٩٤م

Measurements of L-Subshell Ionization Cross Sections by Energetic α Particles for Ho, Er, and Tm.

by

Bassam Abdulrahman M. SHEHADEH

Submitted to the College of Graduate Studies
on June, 1994, in partial fulfillment of the
requirements for the degree of
Master of Science

Abstract

The L-subshell ionization cross sections induced by 1 to 6 MeV α particles were measured for three elements of the rare earth group: holmium, erbium, and thulium. The measurements were performed by taking advantage of simultaneous *PIXE* and *RBS* detection. The measured data were compared with the theoretical calculations of the *ECPSSR* theory. The comparison shows that there are systematic discrepancies at low energies especially for L_2 subshell whereas better agreement is observed at high bombardment energies. When the effect of intra-shell transitions induced by the Coulomb field of the projectile (*IS*) was included in the *ECPSSR* formalism, the systematic discrepancies between the theoretical and the experimental values at low energies were reduced. However, the *ECPSSR-IS* predictions overestimates the experimental values over all the energy range 1-6 MeV for the three subshells. Using the *ECPSSR-IS* theory at binding energies corresponding to united atom (*UA*), the predictions of the modified model, *ECPSSR-IS-UA*, agrees exactly with the experimental values for L_2 and L_3 subshells over all energy range. Nevertheless, for L_1 subshell the discrepancies remain. The *ECPSSR-IS-UA* theory underestimates the experimental values of L_1 subshell at low energies and overestimates the experimental values at high energies. It is shown that at high energies the discrepancies for L_1 subshell are due to the screening effect of the electronic cloud, which reduces the effective charge of the projectile to values less than 2, but higher than 1. Possible reason of low energy discrepancies for L_1 subshell is referred to the necessity of using relativistic Dirac-Hartree-Slater wave function in the basic calculations of the *ECPSSR* instead of the adopted screened hydrogen-like wave function.

Contents

List of Figures

List of Tables

Chapter 1

Introduction

The first study of the effect of bombarding the atomic elements by light ions have been first made and reported by Rutherford, Chadwick and others. Since that time, the subject has been re-examined at intervals. During 1928-1941, a series of measurements were reported in which various elements were irradiated with α particles from radioactive nuclei[1]. The rapid development and increasing availability of particle accelerators, as well as the development of quantum mechanics, have induced the scientists to pay more attention to ion-atom collision in both experimental and theoretical points of view. Nowadays, most of the studies are directed towards explaining and predicting the experimental results of ion-atom collision. One of the important consequences of ion-atom collision is the ionization of inner-shell electrons, that produces characteristic X rays. This effect is mainly utilized in wide applications, specifically, basic research of quantum collision theories, X-ray production, and material science. Since we have mainly collision phenomena, the important physical quantity, through which the nature of collision can be understood, is the cross section. More recently, many attempts have been made to measure the ionization cross sections by light ion impacts experimentally and compare them with the available theoretical predictions.

In this study the L subshells ionization cross sections by α-particle bombardments are measured for three elements of rare earth group, namely, holmium (Ho), erbium

(Er), and thulium (Tm). The study is an advanced attempt after appreciable studies for the K-shell and L-subshell ionization cross sections by proton bombardments. The study of L-subshell ionization by α particles is selected because most of the theoretical and experimental studies have dealt with the K shell. This lack of attention paid to L shell is due to its greater complexity from both experimental and theoretical points of view. since the L shell consists of three degenerate or nearly degenerate subshells, L_1, L_2, and L_3 subshells with particular atomic parameters for each. Furthermore, studying L subshells by α particles offers a data base to test the validity of first order theories to draw a clear conclusion and obtain evident understanding for ion-atom collision since up to now, the experimental data for such study are far from sufficient[2].

For the sake of clarity, a brief view of the adaptation of singly ionized atom is presented, as well as the principles of the two analytical techniques, *PIXE* and *RBS*, through which the ionization cross sections are usually measured. Then, a phenomenological study of the ionization process by light ion impact, involves the main theories and up-to-date studies, is offered in chapter 2 prior to the experimental measurements and data analysis which are offered in chapter 3 and 4.

1.1 Atomic Inner-Shell Spectra

Shortly after the discovery of X-rays, efforts were made to investigate the spectral characteristics of the radiation in order to figure out the fine structure of the atomic inner shells. It was found that the radiation consists of continuous spectrum (as a consequence of charge deceleration radiation, *bermsstrahlung*) and line spectrum (due to the transitions among the energy levels of atomic inner shells). The characteristic radiation can be understood in considerable details from Bohr theory. The development of wave mechanics offered a detailed interpretation of the fine structure of the atomic spectra.

1.1.1 Energy Levels and X-Ray Spectra from Singly-Ionized Atoms

According to quantum mechanics, the electronic states are classified into energy levels (shells), *K, L, M* shell etc., of progressively decreasing binding energy. Except the *K* shell, each shell consists of several sub-shells with different energy for each. Each electron in a certain shell and sub-shell is specified by a set of quantum numbers, namely, principal quantum number $n = 1, 2, 3, ...$ corresponding to *K, L, M,* etc., orbital angular quantum number $l = 0, 1, 2, ...$ corresponding to *s, p, d,* etc., and total angular momentum quantum number j, where j is the angular momentum coupling between the orbital angular momentum l and the spin angular quantum number $s = \frac{1}{2}$ for electron. Where

$$\left|l - \frac{1}{2}\right| \leq j \leq \left|l + \frac{1}{2}\right| \tag{1.1}$$

This is arisen from the fact that the total angular momentum operator **J** is just the vectorial addition of orbital angular momentum operator **L** and spin operator **S**, i.e.

$$\mathbf{J} = \mathbf{L} + \mathbf{S} \tag{1.2}$$

By means of non-relativistic hydrogen-like wave function derived from Schrödinger equation, the energy of the nth level is given by[3]

$$E_n = -\frac{\mu}{2\hbar^2}\left(\frac{Z_s e^2}{4\pi\epsilon_o}\right)^2 \frac{1}{n^2} \tag{1.3}$$

Where μ denotes the reduced mass of the orbital electron and Z_s represents the effective atomic number, i.e. the atomic number Z modified to account the screening effect of the orbital electrons given as

$$Z_s = \begin{cases} Z & \text{for } Z = 1 \\ Z - \sigma_s & \text{for } Z > 1 \end{cases} \tag{1.4}$$

Where σ_s is the screening parameter given for $n = 1$ and 2 (K and L shells)

$$\sigma_s = \begin{cases} 0.30 & \text{for } K \text{ shell} \\ 4.15 & \text{for } L \text{ shell} \end{cases} \tag{1.5}$$

The screening effect of orbital electrons imposes much greater departure from the simple formula. Thus for high-Z elements it is possible to take $\mu \cong m$, where m is the mass of the electron. Hence equation (1.3) reduces to

$$E_n = -\frac{R_\infty hc}{n^2} Z_s^2 \tag{1.6}$$

Here R_∞ denotes Rydberg constant, given by

$$R_\infty = \left(\frac{1}{4\pi\epsilon_o}\right)^2 \frac{me^4}{4\pi\hbar^3 c}$$

Equation (1.3) or equation (1.6) is just a first order approximation because hydrogenic wave functions are l-degenerate. But in higher order approximations one must take into account the fact that for eccentric orbits of low angular momenta the electron spends appreciable time travelling very near to the nucleus at high velocity. This effect is accounted by using Bohr-Sommerfeld theory and enters as a relativistic correction, given by[1]

$$\Delta E_1 = -E_n \frac{(\alpha Z_s)^2}{n^2} \left(\frac{3}{4} - \frac{n}{l+\frac{1}{2}}\right) \tag{1.7}$$

Where α is fine structure constant, defined as

$$\alpha = \left(\frac{1}{4\pi\epsilon_o}\right) \frac{e^2}{\hbar c}$$

The effect of electron spin-orbit coupling must be accounted for. It may be written as

$$\Delta E_2 = -E_n(\alpha Z_s)^2 \frac{\hbar^2}{2nl(l+\frac{1}{2})(l+1)} \times \begin{cases} l & \text{for } j = l + \frac{1}{2} \\ -(l+1) & \text{for } j = l - \frac{1}{2} \end{cases} \tag{1.8}$$

Equation (1.6), equation (1.7), and equation (1.8) may be combined to give

$$E_{n,l,j} = E_n + \Delta E_1 + \Delta E_2 = E_n \left\{ 1 - \frac{(\alpha Z_s)^2}{n^2} \left(\frac{3}{4} - \frac{n}{j+\frac{1}{2}} \right) \right\} \tag{1.9}$$

For every $j = l \pm \frac{1}{2}$.

For the special case of $l = 0$, the spin orbit interaction vanishes and $\Delta E_2 = 0$. Nevertheless, a third term ΔE_3 called Darwin term is given by[1]

$$\Delta E_3 = -E_n \frac{(\alpha Z_s)^2}{n} \tag{1.10}$$

This term is active when $l = 0$ (for spherical symmetry). Make use of equation (1.10) into equation (1.9), a general formula can be obtained given by

$$E_{n,l,j} = -R_\infty hc \left\{ \frac{Z_s^2}{n^2} + \frac{\alpha^2 Z_s^4}{n^4} \left(\frac{n}{j+\frac{1}{2}} - \frac{3}{4} \right) \right\} \tag{1.11}$$

However equation (1.11) can be obtained directly by using relativistic wave function for state characterized by n, l, and j through solving Dirac equation[4]. Table (1.1) construct the electronic orbits with quantum numbers for *K, L, M,* and *N* shells.

Each subshell characterized by quantum number j can accommodate electrons up to $2j+1$ and each line in X-ray spectrum corresponds to a transition between two states subjected to selection rules which govern allowed transitions among states, given for dipole radiation (most probable transition)

$$\Delta l = \pm 1; \Delta s = 0; \Delta j = 0, \pm 1; \text{ and } \Delta n \neq 0 \tag{1.12}$$

Transitions for $\Delta l = 0, \pm 2; \Delta j = 0, \pm 1, \pm 2$, are infrequently observed despite their reduced intensity. These are known as electric quadruple transitions.

One can draw all possible transitions and hence the characteristics X-ray lines for singly ionized atom. This is shown in figure (1-1) where the more strongly bound

Table 1.1: Electronic orbits, with quantum numbers.

Principal quantum number	angular momentum		Spectral notation	Shell
n	l	j	nL_j	
1	0	$\frac{1}{2}$	$1s$	K
2	0	$\frac{1}{2}$	$2s_{\frac{1}{2}}$	L_1
2	1	$\frac{1}{2}$	$2p_{\frac{1}{2}}$	L_2
2	1	$\frac{3}{2}$	$2p_{\frac{3}{2}}$	L_3
3	0	$\frac{1}{2}$	$3s_{\frac{1}{2}}$	M_1
3	1	$\frac{1}{2}$	$3p_{\frac{1}{2}}$	M_2
3	1	$\frac{3}{2}$	$3p_{\frac{3}{2}}$	M_3
3	2	$\frac{3}{2}$	$3d_{\frac{3}{2}}$	M_4
3	2	$\frac{5}{2}$	$3d_{\frac{5}{2}}$	M_5
4	0	$\frac{1}{2}$	$4s_{\frac{1}{2}}$	N_1
4	1	$\frac{1}{2}, \frac{3}{2}$	$4p_{\frac{1}{2},\frac{3}{2}}$	$N_{2,3}$
4	2	$\frac{3}{2}, \frac{5}{2}$	$4d_{\frac{3}{2},\frac{5}{2}}$	$N_{4,5}$
4	3	$\frac{5}{2}, \frac{7}{2}$	$4f_{\frac{5}{2},\frac{7}{2}}$	$N_{6,7}$

electrons are in the bottom of the diagram. If an electron is removed, the atom becomes ionized (i.e. hole state) and thus the vacancy is filled by an electron from outer shells according to the selection rules. This process at least gives rise to the emission of characteristic X-ray photons. However, there is an alternative or complementary process known as Auger effect, which takes place when the emitted photon is absorbed by another bound electron which is then emitted as a free electron.

The preeminent characteristics of K-series are the K_{α_1,α_2} doublet and K_{β_1,β_2} lines. These lines are shown in figure (1-1) and they conform to the selection rules for dipole radiation as given in equation (1.12). The energy of K_α doublet is given by the approximate formula[1]

$$E = KR_\infty hc(Z - \lambda_m)^2 \tag{1.13}$$

Where $\lambda_m \approx 1$ for K-shell, $K = \frac{3}{4} = \left(\frac{1}{1^2} - \frac{1}{2^2}\right)$, i.e. Lyman series, since for K_α there is a transition between $n = 2$ to $n = 1$. This type of expression is known as Moseley's law which implies that $E \propto Z^2$. A plot of the X-ray energies versus atomic number for $K_\alpha, K_\beta, L_\alpha, L_\beta$ and M is shown in figure (1-2). The plot confirm the Moseley's law for K_α and K_β. In case of L-series, the most intense lines are expected to be those are originated from the subshell that contains more electrons, that is L_3-subshell. The L_{α_1,α_2} line corresponding to atomic transitions[1] $L_3 \rightarrow M_5$ and $L_3 \rightarrow M_4$, respectively, as shown in figure (1-1). Other intense lines are the L_{β_1} and L_{β_2} corresponding to transitions $L_2 \rightarrow M_4$ and $L_3 \rightarrow N_5$, respectively. Moseley law also holds for L series[5]. That is clearly seen in figure (1-2). The L_{β_1} lines follow a formula similar to equation (1.13) with $\lambda_m = 7.4$ and $K = \frac{1}{2^2} - \frac{1}{3^2} = \frac{5}{36}$ [5].

1.1.2 Fluorescence Yield

The probability of X-ray emission from a specific ionized atomic shell is called *the fluorescence yield* symbolized as ω_s where s stands for K, L, M shell etc. In case of

[1]The arrows indicate the direction of vacancy migration.

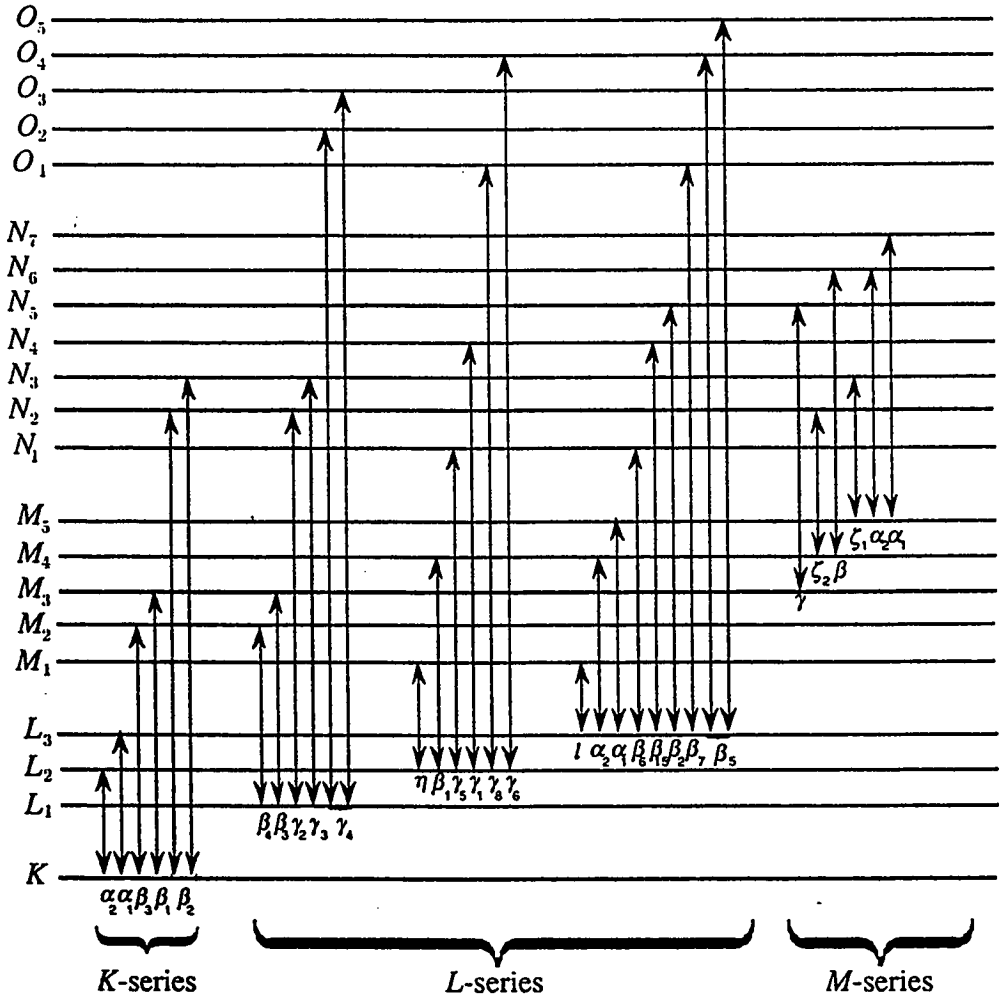

Figure 1-1: Energy levels for a singly-ionized atom. The diagram contains all the lines except a few weak quadrupole transitions.

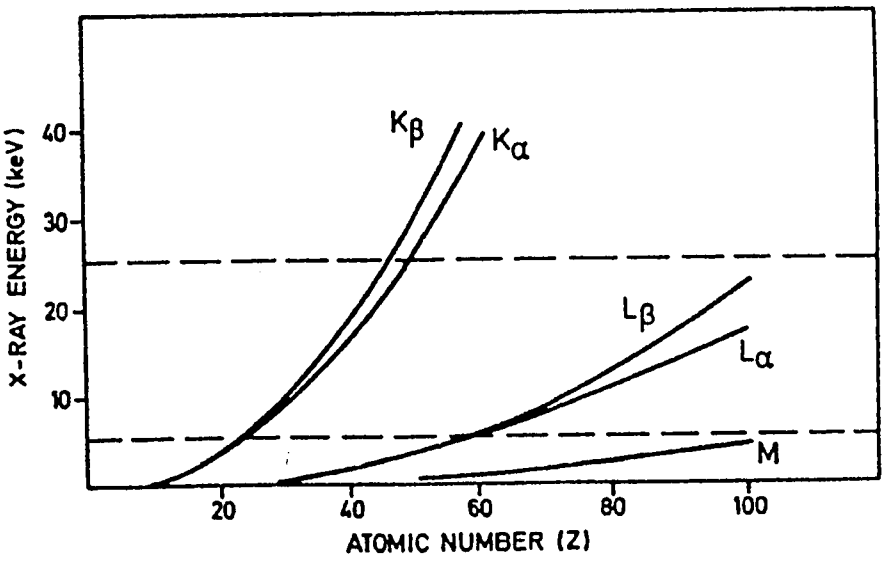

Figure 1-2: *K*-, *L*-, and *M*-series lines, illustrating Moseley's law. (Taken from JOHANSSON and CAMPBELL, 1988.)

K shell, vacancy refilling and de-excitation undergoes within about 10^{-6} seconds[6] emitting either X ray or Auger electron or both. Therefore the fluorescence yield can be written as

$$\omega_K = \frac{N_K}{N_K + A_K} \tag{1.14}$$

Where N_K is the number of X-ray photons emitted from *K* series, A_K is the number of *K*-Auger electrons. Obviously that $0 \leq \omega_K \leq 1$, since it represents a probability.

However, from equation (1.14) one can notice that ω_s is dimensionless but it depends on the type of the atom. In fact the fluorescence yield is strongly Z-dependent as shown in figure (1-3). A semi-empirical formula for ω_K is provided by BAMBYNEK *et al.*[7] to account for precise measurements given as

$$\left(\frac{\omega_K}{1-\omega_K}\right)^{\frac{1}{4}} = \sum_{i=0}^{3} B_i Z^i \tag{1.15}$$

where the coefficients B_is' are listed in table (1.2). The values of ω_K given by equation (1.15) agree with the theoretical values obtained by CHEN *et al.*[8] using calculations

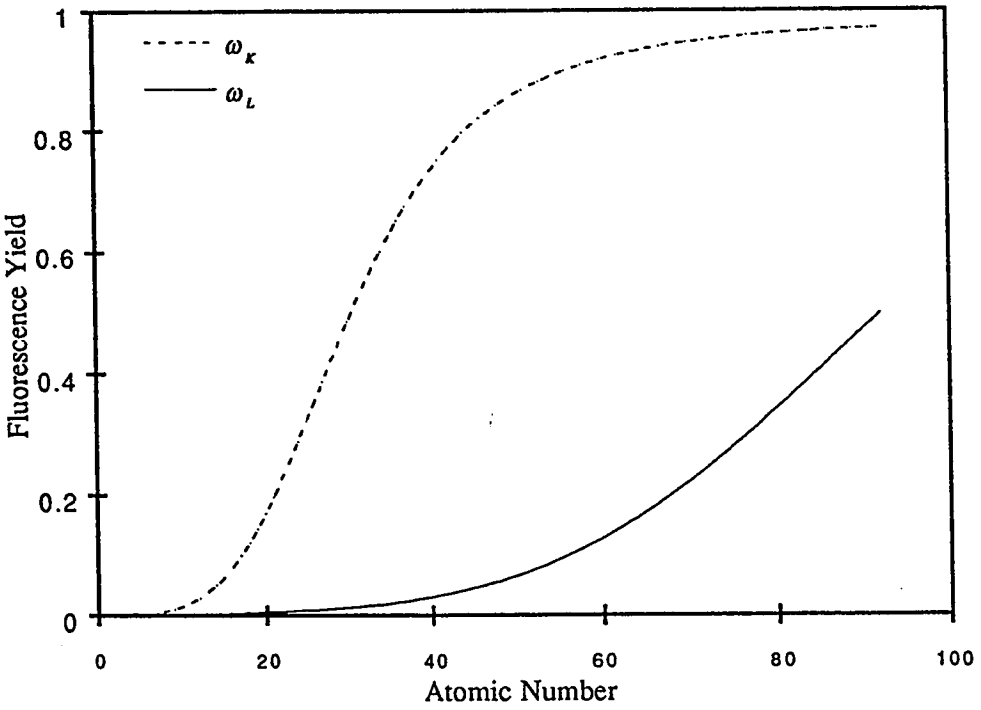

Figure 1-3: The K- and L-shell fluorescence yields as a functions of atomic number Z.

based on Dirac-Hartree-Slater bound wave functions. The deviations in the fitted ω_K are estimated as 3-5 % for $Z = 10$ to 20, 1-3 % for $Z = 20$ to 30, 0.5-1 % for $Z = 30$ to 40, and 0.3-0.5 % for $Z > 40$[6]. In order to avoid the deviation at low Z, an analytical formula has been obtained[1]

$$\omega_K = \frac{Z^4}{a_K + Z^4} \tag{1.16}$$

Where $a_K = 1.12 \times 10^6$[1]. Equation (1.16) arises from the fact that if the radiating atom is considered as a classical oscillator losing energy by radiative damping the relaxation time $\tau \propto \nu^{-2}$[1]. But from Moseley's law, $\nu \propto Z^2$,thus $\tau \propto Z^{-4}$. Therefore the transition probability $\propto Z^4$ which leads to equation (1.16).

For L shell, the fluorescence yield is much more complicated than K shell because there are three subshells each has its own fluorescence yield. Moreover, the radiationless

Table 1.2: Coefficients for evaluation of K- and L-shell fluorescence yields.

Coefficients	K-shell	L-shell
B_o	$(3.70 \pm 0.52) \times 10^{-2}$	0.17765
B_1	$(3.112 \pm 0.044) \times 10^{-2}$	2.98937×10^{-3}
B_2	$(5.44 \pm 0.11) \times 10^{-5}$	8.91297×10^{-5}
B_3	$-(1.25 \pm 0.07) \times 10^{-6}$	-2.67184×10^{-7}

transitions are not only unrestricted for Auger effect but also for transitions among the subshells known as Coster-Kronig transitions. COHEN[9] has generated a set of values for ω_L as a function of Z, fitted using expression similar to equation (1.15) for $30 \leq Z \leq 96$, given by

$$\left(\frac{\overline{\omega}_L}{1-\overline{\omega}_L}\right)^{\frac{1}{4}} = \sum_{i=0}^{3} B_i Z^i \tag{1.17}$$

The coefficients are listed in table (1.2), $\overline{\omega}_L$ is the effective fluorescence yield given by

$$\overline{\omega}_L = \frac{X(L_1) + X(L_2) + X(L_3)}{n_1 + n_2 + n_3} \tag{1.18}$$

Where $X(L_i)$ is the effective fluorescence yield for the ith-subshell and n_is' are called the vacancy distributions, where $\sum_{i=1}^{3} n_i = 1$. The probability of vacancy occupied by non-radiative transition among the subshells, i.e. Coster-Kronig transition for $\Delta n = 0$, is incorporated within $X(L_i)$. Coster-Kronig effect is responsible for the bulk of the de-excitation width of L_1 vacancy. Let f_{ij} denotes the Coster-Kronig transition probability between the ith and jth subshells, a general formula can be obtained for $X(L_i)$ given as

$$X(L_i) = [n_i + f_{i-1,i} n_{i-1} + (f_{i-2,i} + f_{i-2,i-1} f_{i-1,i})]\omega_{L_i} \tag{1.19}$$

Where i runs form 1 to 3 corresponding to L_1, L_2, and L_3 subshells. Note that $f_{ii} = 0$, to ignore the Coster-Kronig transition within the same subshell.

The L_3-subshell fluorescence yield follows equation (1.16) with $a = 1.02 \times 10^8$[1], therefore at certain Z, L_3-subshell fluorescence yield is lower than that for K-shell. This is true also for L_1 and L_2 fluorescence yields. A set of experimental fluorescence

yield for K and L subshells are fitted and interpolated by KRAUSE[10]. These values are considered as a main source for experimental (or semi-empirical) fluorescence yields. In the other hand, the theoretical values of CHEN *et al.*[8, 11] offer a data base which enhances those of KRAUSE for K shell. However a noticeable disagreements are found for L subshells which make the situation difficult to rely on one of them alone. This is because there is no absolute conclusion that can be drawn due to the difficulties of obtaining L-subshell fluorescence yields using both experimental and theoretical techniques. Though SARKADI and MUKOYAMA[12] recommend to use the decay parameters of CHEN *et al.*, due to the fact that their f_{12} Coster-Kronig rate for gold, which is 0.074, very low compared to KRAUSE's estimation, which is 0.140, supporting the results of the synchrotron radiation measurements carried out by JITSCHIN *et al.*[13]. But still the other values of KRAUSE are closer to those estimated by JITSCHIN *et al.*[13].

1.1.3 Relative Intensities of X-Ray Lines

The intensity or emission rate for any X-ray line expresses the probability of the transition that produces it, therefore, the relative intensities can be considered as the relative probabilities of the transitions. The allowed and forbidden transitions are distinguished according to selection rule given in equation (1.12). For magnetic dipole transitions, corresponding to $\Delta l = 0$, it must be mentioned that, similar to optical spectra, a few cases are observed though it is a forbidden transition. for example a $K \rightarrow L_1$ transition is reported for excited gold atoms beside the K_{α_2} peak as shown in figure (1-4)[5, 14]. When $\Delta n = 0$, that is Coster-Kronig transition, the absence of these lines refers to the dependence of the intensity of unrestricted transitions ν^4, which is extremely small as indicated by EINSTEIN[5], because the energy differences among the subshells are very small (can be considered as degenerate or nearly degenerate states[12]).

A general rule is always followed to estimate the relative intensities for singly-ionized atoms, states that the relative intensities for lines originated from *common* initial shell

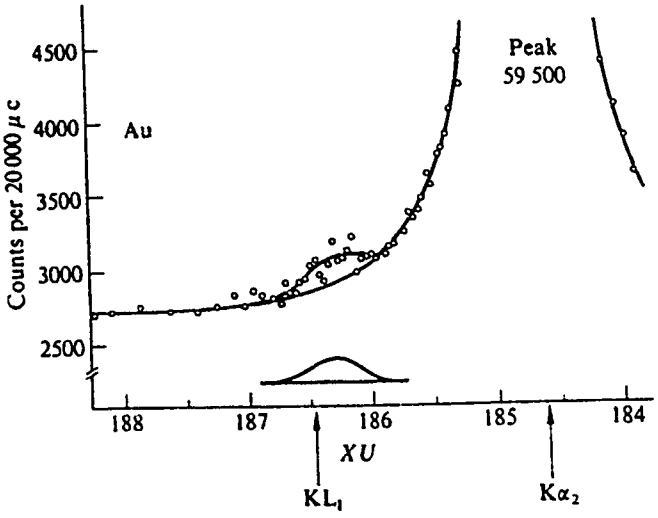

Figure 1-4: The $K \rightarrow L_1$ magnetic dipole transition in gold. (Taken from DYSON, 1990.)

or subshell are constant and independent of mode of excitation. Whereas the relative intensities for lines originated from *different* shells or subshells are not constant and depend strictly on the mode of excitation. Mode of excitation means type, energy, and charge of particle causes the ionization. This is because each shell or subshell has certain probability of ionization (i.e. ionization cross section) that depends on the mode of excitation. However, as soon as a vacancy is created in a given shell or subshell, the vacancy refilling process takes place according to a set of statistically-constant transition options that are characteristic for the atom only. This is confirmed by SALEM *et al.*[15] when they studied the relative intensities for K, L_1, L_2, and L_3 shells using different exciters, namely electrons and photons at different bombardment energies. They demonstrated that the relative intensities for specific shell or subshell is independent of excitation particle. Additionally, CHEN *et al.*[16] obtained the ratios of $L_{\gamma_1} : L_\eta$ (both are originated from L_2 subshell) for Pb, Au, and Pt by using proton bombardment at various energies. They demonstrated that the ratios of $L_{\gamma_1} : L_\eta$ are constant and independent of excitation energies of the protons as shown in figure (1-5). On the other hand, the ratio of $L_{\gamma_1} : L_{\gamma_{2,3}}$ was not found to be constant. This is

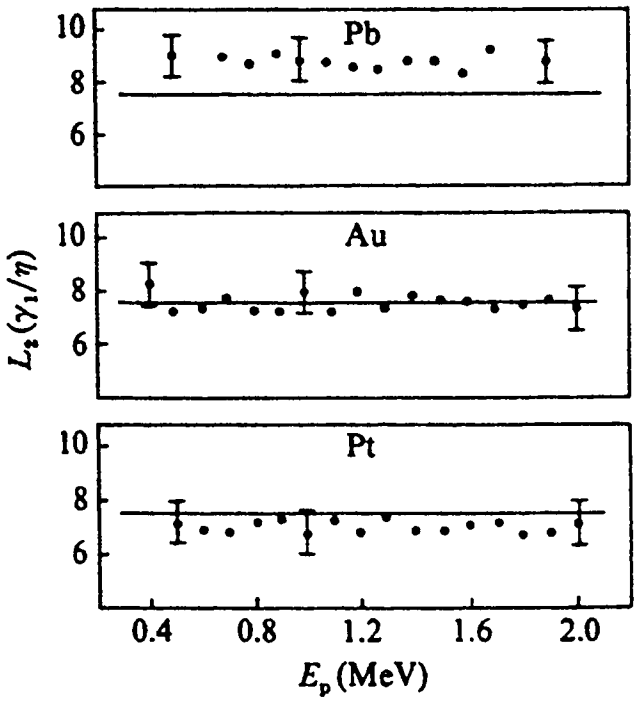

Figure 1-5: Ratio of L_{γ_1} : L_η line intinsities as a function of proton bombarding energy. (Taken from DYSON, 1990.)

however expected according to the previous argument, because L_{γ_1} and $L_{\gamma_{2,3}}$ originate from different subshells, L_1 and L_2 subshell, respectively. Physically the change in the ratio L_{γ_1} : $L_{\gamma_{2,3}}$ is attributed to the change in the impact parameter of the proton as bombardment energy changes with respect to L_1 and L_2, which tends to change the ionization cross section of certain subshell[1].

Experimentally, the relative intensities can be obtained by estimating the peak areas for the lines in X-ray spectrum corrected for the detection efficiency and the background. However, the difficulties arise in the presence of overlapped lines when the typical detector resolution is larger than the energy differences of X-ray lines. Moreover, the background would add more difficulties since background subtraction involves information losing that would limit the precision of the measurements especially for low intensity lines. A collective work is offered by SALEM *et al.*[15] involves a careful least-square-fit for a numerous published experimental data for different ex-

citation processes, namely, the radioactive sources, or sources ionized by photons or electrons bombardment. It gives a data base for K- and L-subshell relative intensities but it is limited for relatively intense group of X-ray lines ignoring many other smaller lines. Also it does not offer the relative intensities for L lines originated from different subshells which is a critical demands in analytical applications such as the *PIXE* analysis.

Theoretically, the situation is more difficult. The decay scheme for ionized atom is very sophisticated and one must take into account many complex effects. One of these effects is Coster-Kronig transition that can affect the transitions of all shells in the atom including the K shell. For L shell, the effect becomes more complicated because of the effect of Coster-Kronig transitions and Auger effect in M and N shells cause a radical redistribution of electrons in a shell prior to radiation. As an example, for atoms whose $Z > 37$ atoms, the $L_1 \rightarrow L_2$ transition ejects Auger electron from M_3 subshell. The process is represented by $L_1 \rightarrow L_3M_3$. This transition has three consequences[1]:

1. The L_3 lines are enhanced at the expense of L_1 lines.

2. These transitions take place in atom that is already ionized in M_3 subshell and a slight displacement in energy occurs, appears as satellites of the main line.

3. The extra vacancy in M shell enhances M-line spectrum with modification in the effective charge because the vacancy in L shell reduces the screening effect by approximately one unit of charge, therefore, M lines corresponding to $Z + 1$ element instead of Z[1].

Various theoretical approximations are used to calculate the emission rates for K and L lines. The earlier work was done by SCOFIELD for K shell[17] and L shell[18, 19] by finding the total decay rate of a vacancy state using relativistic wave function based on Dirac-Hartree-Slater calculations for isolated atoms in their initial and final states, including the exchange effect of wave overlapping from different subshells. In

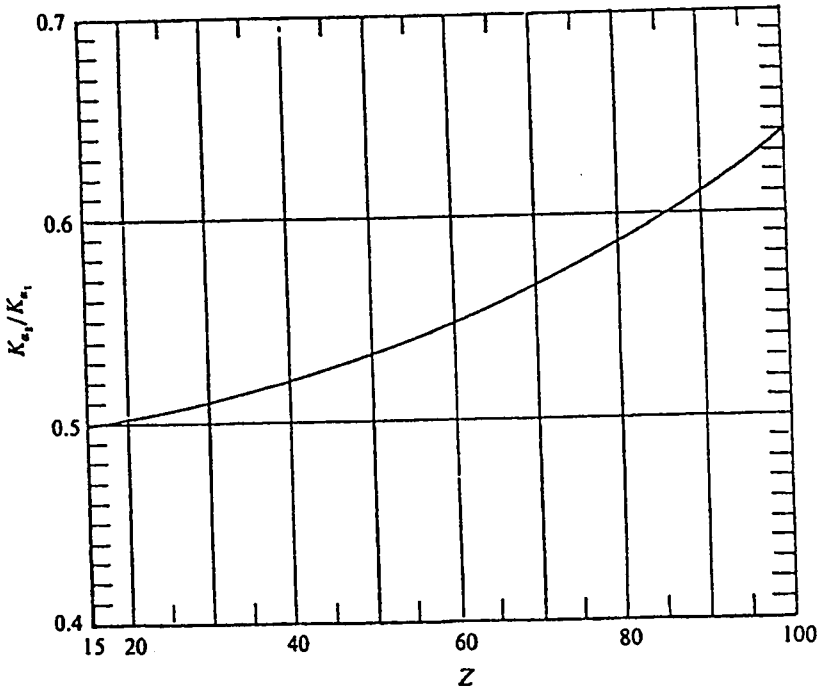

Figure 1-6: The ratio K_{α_2} : K_{α_1} expressed as a ratio of numbers of photons as a function of Z. (Taken from DYSON, 1990.)

the calculations the electrons in the initial and final states are treated as moving in the same central potential which is given by the neutral-atom occupations of the subshells.

In earlier calculations[18], the effects of the relaxation of the electronic cloud after filling the initial vacancy is omitted, and hence the predicted ratio K_β/K_α differs systematically than the observed values. Accordingly these effects is included in later calculations[17, 19] and good agreement with experimental values given by SALEM *et al.*[15] is observed except the region $21 \leq Z \leq 32$ where the $3d$ subshell is filling. This discrepancy is confirmed by PERUJO *et al.*[20] by measuring the ratio K_β/K_α for proton-induce X-ray emission from thin targets in the $22 \leq Z \leq 32$ region. The discrepancy in this region is attributed to spectral overlaps between the K_α of element Z and the K_β of element $Z-1$ which contributes negatively to experimental values of K_β/K_α ratio. For L shell, there is inadequate state of knowledge for de-excitation quantities, The obvious difficulty of unfolding the many overlapping components has

limited the precision of experimental studies. However available information supports SCOFIELD's predictions but accurate conclusions have not been drawn yet[6].

One might work in the opposite direction and attempt to measure the ionization cross sections (either experimentally or theoretically) for the atomic shells and subshells and then obtain the relative intensities out of them. This involves converting the ionization cross section to other quantities by using some decay parameters including the fluorescence yields and Coster-Kronig transitions, which are not precisely known. However, COHEN and HARRIGAN[21] offer an extensive tabulation of L-subshell relative intensities by utilizing the ionization cross section derived by the *ECPSSR* theory[2]. In this work, 16 X-ray line are considered namely, $L_l, L_\alpha, L_\eta, L_{\beta_1}$ to $L_{\beta_6}, L_{\beta_{9,10}}$,and L_{γ_1} to L_{γ_6}, at various bombardment energies for protons and α-particles. The fluorescence yield of KRAUSE[10] and the relative intensities of SALEM *et al.*[15] are employed to link the L X-ray lines produced from different subshells as a function of projectile bombardment energy and element atomic numbers. This work provides a useful data base for *PIXE* analyst if protons are used as bombarding particles. However, the relative intensities for X-ray lines originated from different subshells have not been examined experimentally yet. Moreover, the *ECPSSR* theory is still subjected to test and its validity has not been confirmed yet for L subshells, especially for α-particle bombardments. Finally it remains to state that the intensities of L shell are higher than those of K shell and more complex in nature, this is because L shell contains more electrons than K shell, 8 electrons in L shell instead of 2 electrons in K shell.

1.2 Basic Principles of RBS and PIXE

When a beam of ions interpenetrates through the target media, various reactions take place. However, there are mainly three types of reactions classified microscopically into

[2]The theory is disscused comprehensively in chapter 2

1. Interaction of the ion with the atomic electrons. One of the consequences of this interaction is the characteristic X-ray emission, abbreviated as *PIXE* (Particle-Induced X-ray Emission).

2. Elastic scattering of the ion by the Coulomb fields of the target nuclei. This interaction is called Rutherford Backscattering, and denoted as *RBS*.

3. Inelastic scattering or direct reaction between the incident ion and the target nuclei, producing nuclear radiations. The analysis of this reaction is called nuclear reaction analysis, denoted as *NRA*.

For the purpose of inner-shell ionization cross section measurements, one has to consider the first two reactions since both of them are frequently utilized for such measurements. *PIXE* and *RBS* can be detected simultaneously with one setup using proper detectors for each. The third reaction must be minimized because it produces undesired backgrounds and interferences. This imposes an upper limit to the beam energy such that it must be less than the threshold energy of the nuclear excitation. In many cases, the threshold energy is comparable to the Coulomb-barrier heights of the target nuclei. Additionally, the minimum energy transferred from the ion to the bound electron must be more than or comparable to the binding energy of the electron. The later condition holds for ions having energies in the MeV range.

1.2.1 Rutherford Backscattering

The backscattering process takes place when the incident particle is deflected elastically through a large angle by the Coulomb field of the target nucleus. The process is depicted in figure (1-7) which shows a particle with mass, charge, velocity, and impact parameter M_1, Z_1, v_o, and b, respectively, approaching a target nucleus with mass and charge M_2 and Z_2, respectively. The target nucleus is typically considered as a point charge and initially at rest in the laboratory frame. The particle experiences the

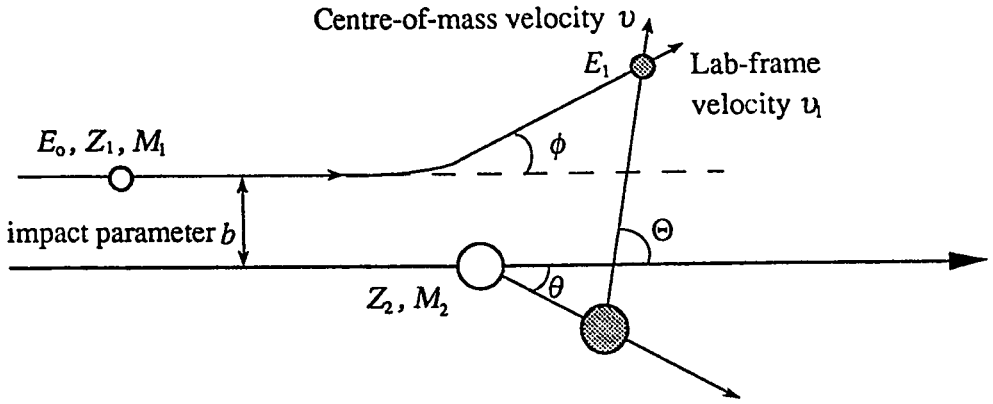

Figure 1-7: The deflection of the charged particle due to the Coulomb field of the nucleus in lab and centre-of-mass frame.

repulsive field of the nucleus and scatters through angle ϕ and velocity v_1. In centre-of-mass frame, the particle scatters through angle Θ with initial and final relative velocity v.

The scattering is assumed to be totally elastic, i.e. there is no significant momentum transfer to the target nucleus, otherwise, the nucleus will be excited, and then de-excites by emitting γ rays or other nuclear radiations. In case of protons and α particles, accelerated up to few MeV, the maximum energy transfer to a target nucleus in a single encounter is given by[22]

$$\epsilon_{max} = \frac{4M_1M_2}{(M_1 + M_2)^2} E_o \tag{1.20}$$

Where E_o is the energy of the proton or α-particle. Figure (1-8) shows the ratio ϵ_{max}/E_o as a function M_2 for both protons and α particles. The ratio reaches its maximum (i.e. $\epsilon_{max}/E_o = 1$) when $M_1 = M_2$, then it falls rapidly as M_2 increases. The stable light nuclei (small M_2) have wide energy gab between ground state and first excited state because the transferred energy appears as a recoiling kinetic energy. Whereas, for heavy nuclei (large M_2), the energy gab is narrow with respect to that for light nuclei. Therefore, it is convenient to restrict the upper limit of the incidence energy to be lower than the Coulomb barrier height of the target nucleus in order to minimize, as

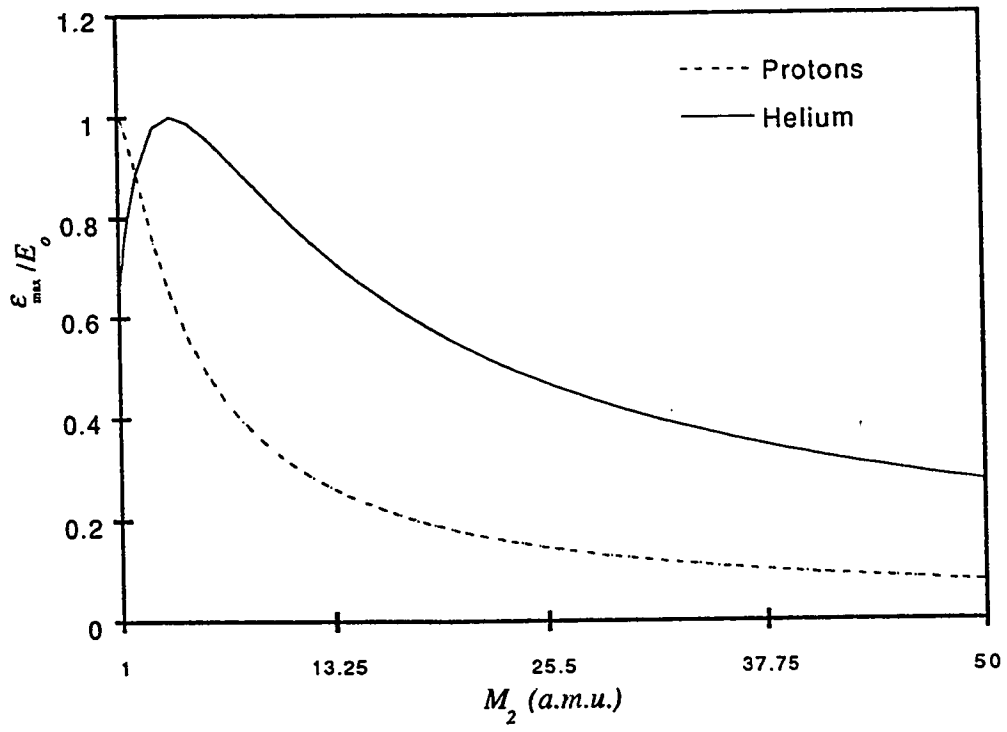

Figure 1-8: The ratio of maximum energy transfer to ion energy (ϵ_{max}/E_o) for protons and α particles as a function of the target nucleus mass (M_2).

possible, the nuclear excitation.

RBS is a substantial process that is widely utilized in measuring the ionization cross section by light ion impacts. Therefore, to utilize *RBS* one must interpret the *RBS* spectrum precisely. This can be achieved by understanding all parameters discussed below.

Scattering Cross Section (Rutherford Formula)

Many workers have derived the *RBS* cross section classically[23, 24, 25, 26]. But here the formula will be derived quantum mechanically using Born approximation. This approximation is valid as long as the interaction potential $V(r)$, which is the Coulomb central potential, is regarded as a perturbed term in the total Hamiltonian of the

system. In another word

$$E_o \gg V(r) = \frac{Z_1 Z_2 e^2}{r}$$

For the inner-shell ionization process, the impact parameter b is comparable to the inner-shell electronic radius, which is in order of Å, thus r is in order of Å too, and hence the maximum value of $V(r)$ is of the order of keV while E_o is of the order of MeV. Accordingly $E_o \gg V(r)$. The use of Born approximation implies that the contribution of partial waves that posses high angular momenta can be neglected. This condition is true as long as the energy of the incident particle is restricted to few MeV. For a system depicted in figure (1-7) in centre of mass frame, the cross section for elastic scattering by the Coulomb field is given by[3][27]

$$\left(\frac{d\sigma}{d\Omega}\right)_R = \frac{M^2}{4\pi^2\hbar^4}\frac{v_f}{v_i}\left|\langle\psi_f\left|V(r)\right|\psi_i\rangle\right|^2 \tag{1.21}$$

Here M is the reduced mass. v_i and v_f are the initial and final velocities in centre-of-mass frame, respectively. ψ_i and ψ_f are the incident and scattered plane wave functions, respectively, given by

$$\psi_i \sim \exp(i\mathbf{p}_i \cdot \mathbf{r}/\hbar) \text{ and } \psi_f \sim \exp(i\mathbf{p}_f \cdot \mathbf{r}/\hbar) \tag{1.22}$$

Where $\mathbf{p}_i$ and $\mathbf{p}_f$ are the initial and final relative momentum vectors, respectively. For elastic scattering one can deduce that

$$|\mathbf{p}_i| = |\mathbf{p}_f| = p \tag{1.23}$$

Which implies that the change in momentum is in the direction only not in the magnitude as shown in figure (1-9). Thus $v_f/v_i = 1$ in equation (1.21). The matrix element

[3]The detailed derivation of this formula is justified in section 2.2.1. Note that cgs system units are used through this discussion.

$\langle \psi_f | V(r) | \psi_i \rangle$ can be calculated functionally as

$$\begin{aligned} \langle \psi_f | V(r) | \psi_i \rangle &= \int \psi_f^*(\mathbf{r}) V(r) \psi_i(\mathbf{r}) d\mathbf{r} = \int e^{i(\mathbf{p}_i - \mathbf{p}_f)/\hbar \cdot \mathbf{r}} \frac{Z_1 Z_2 e^2}{r} d\mathbf{r} \\ &= Z_1 Z_2 e^2 \int_0^{2\pi} d\varphi \int_0^{\pi} \sin\vartheta d\vartheta \int_0^{\infty} r^2 dr \frac{e^{i(\mathbf{p}_i - \mathbf{p}_f)/\hbar \cdot \mathbf{r}}}{r} \end{aligned}$$

Since there are no preferences in the phase space, thus one can choose the direction of momentum change vector $\mathbf{p}_i - \mathbf{p}_f$ in figure (1-9) to be in z-direction of $\mathbf{r}$. Thus

$$(\mathbf{p}_i - \mathbf{p}_f) \cdot \mathbf{r} = |\mathbf{p}_i - \mathbf{p}_f| \, r \cos\vartheta$$

Hence

$$\langle \psi_f | V(r) | \psi_i \rangle = 2\pi Z_1 Z_2 e^2 \int_0^{\pi} \sin\vartheta d\vartheta \int_0^{\infty} r^2 dr \frac{e^{i|\mathbf{p}_i - \mathbf{p}_f| r \cos\vartheta/\hbar}}{r}$$

Applying the integral yields[4]

$$\langle \psi_f | V(r) | \psi_i \rangle = \frac{4\pi Z_1 Z_2 e^2 \hbar^2}{|\mathbf{p}_i - \mathbf{p}_f|^2} \tag{1.24}$$

The magnitude of $|\mathbf{p}_i - \mathbf{p}_f|^2$ can be reformulated by using equation (1.23), figure (1-9), and tringometric relations, to obtain

$$|\mathbf{p}_i - \mathbf{p}_f|^2 = 4p^2 \sin^2 \frac{\Theta}{2} \tag{1.25}$$

Make use of equation (1.25) into equation (1.24) yields

$$\langle \psi_f | V(r) | \psi_i \rangle = \frac{4\pi Z_1 Z_2 e^2 \hbar^2}{4p^2 \sin^2 \frac{\Theta}{2}} \tag{1.26}$$

Substituting equation (1.26) into equation (1.21), noting that $p^2/2M$ is nothing but the projectile kinetic energy E, one obtains the scattering cross section in centre of

[4]Evaluation of this type of integrals is presented in appendix A.

mass frame as

$$\left(\frac{d\sigma}{d\Omega}\right)_R = \left(\frac{Z_1 Z_2 e^2}{4E}\right)^2 \frac{1}{\sin^4 \frac{\Theta}{2}} \tag{1.27}$$

Equation (1.27) is similar to Rutherford formula that was derived using classical approach. This formula is valid in the laboratory frame, but only when $M_1 \ll M_2$[25]. It can transformed using the relation between the scattering angle in centre-of-mass frame Θ and the scattering angle in lab frame ϕ, obtained from figure (1-9) and the geometric sketch in figure (1-10)

$$\tan\phi = \frac{\sin\Theta}{\frac{M_1}{M_2} + \cos\Theta} \tag{1.28}$$

Therefore, the transformation of this formula from centre-of-mass frame to lab frame yields[25]

$$\left(\frac{d\sigma}{d\Omega}\right)_R = \left(\frac{Z_1 Z_2 e^2}{4E}\right)^2 \frac{4}{\sin^4\phi} \frac{\left\{\sqrt{1-\left(\frac{M_1}{M_2}\sin\phi\right)^2} + \cos\phi\right\}^2}{\sqrt{1-\left(\frac{M_1}{M_2}\sin\phi\right)^2}} \tag{1.29}$$

Since $M_1 < M_2$, it follows from equation (1.28) that ϕ is unrestricted. Moreover, for $M_1 \ll M_2$, equation (1.29) can be expanded in the power series[25]

$$\left(\frac{d\sigma}{d\Omega}\right)_R \approx \left(\frac{Z_1 Z_2 e^2}{4E}\right)^2 \left[\sin^{-4}\frac{\phi}{2} - 2\left(\frac{M_1}{M_2}\right)^2 + \cdots\right] \tag{1.30}$$

Where the first omitted term is in order of $(M_1/M_2)^4$. Note that at the limit $M_1/M_2 \to 0$, then it follows from equation (1.28) that $\phi \to \Theta$, and equation (1.30) will have the same form of equation (1.27).

Equation (1.30) uncovers the functional dependence of the Rutherford scattering differential cross section[25]

The validity of Rutherford formula is only restricted for $M_1 \ll M_2$. However even when M_1 is comparable to M_2, Rutherford formula holds but at limited upper value of bombardment energies. For instance, CHENG *et al.*[28] indicated that the 170°

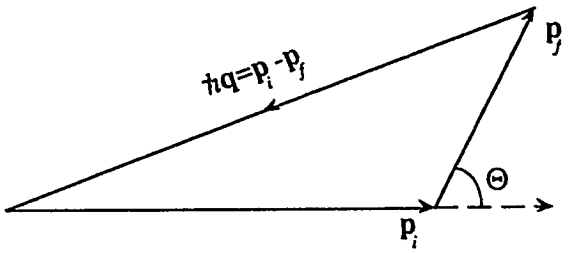

Figure 1-9: Momentum diagram for Rutherford scattering.

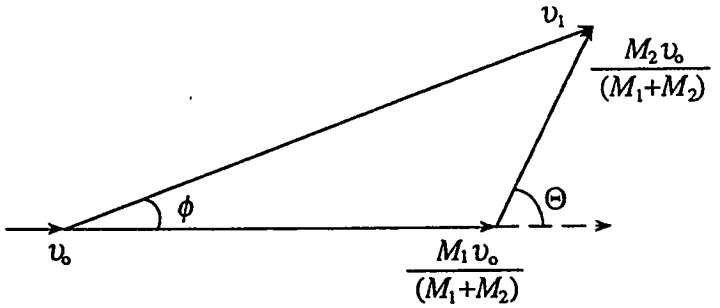

Figure 1-10: Schematic diagram shows the relation between the scattering angles in centre-of-mass frame Θ and lab frame ϕ.

backscattering cross sections for α particles from oxygen remain Rutherford-like up to $E_\alpha = 2.35$ MeV. Additionally, some sort of resonance peaks are found, for example, in the range 3-4 MeV, when the ration σ_R/σ_{exp} is sketched versus the bombardment energy[28]. Some attention is paid, nowadays, to obtain formulas for departures from Rutherford backscattering when M_1 is comparable to M_2, for example the attempt of BOZOIAN[29]

Kinematic Factor

For an elastic scattering in lab frame the kinematic factor K is defined as

$$K = \frac{E_1}{E_o} = \frac{v_1^2}{v_o^2} \tag{1.31}$$

Where E_o and E_1 are the projectile energy before and after scattering in lab frame, respectively. An expression for K can be obtained using classical conservation laws

for energy and for both parallel and perpendicular components of the momentum with respect to the direction of incidence. Thus conservation law of energy implies

$$\frac{1}{2}M_1v_o^2 = \frac{1}{2}M_1v_1^2 + \frac{1}{2}M_2v_2^2 \tag{1.32}$$

And the conservation of momentum implies

$$M_1v_o = M_1v_1\cos\phi + M_2v_2\cos\theta \tag{1.33}$$

$$0 = M_1v_1\sin\phi - M_2v_2\sin\theta \tag{1.34}$$

Eliminating θ and then v_2, one finds

$$\frac{v_1}{v_o} = \pm\left(\frac{\sqrt{M_2^2 - M_1^2\sin^2\phi} + M_1\cos\phi}{M_2 + M_1}\right)$$

Therefore, the kinematic factor in equation (1.31) is given by

$$K_{M_2} = \left(\frac{\sqrt{1 - \left(\frac{M_1}{M_2}\sin\phi\right)^2} + \frac{M_1}{M_2}\cos\phi}{1 + \frac{M_1}{M_2}}\right)^2 \tag{1.35}$$

Obviously that K_{M_2} has its lowest value when $\phi = \pi$, where K_{M_2} is

$$K_{M_2} = \left(\frac{M_2 - M_1}{M_2 + M_1}\right) \tag{1.36}$$

For a given beam detected at fixed angle ϕ, K_{M_2} depends only on M_2. In another word, K_{M_2} depends on the elemental composition within the sample. This property is very useful to analyse multi-elemental samples out of *RBS* spectrum.

Projectile Slowingdown

Incident ions rapidly dissipate their energies within the sample through inelastic encounters with the atomic electrons. The momentum of MeV ions is much greater in magnitude than electron's. Since at least, the proton is 1836 times more massive than the electron, thus for a single encounter and according to equation (1.20) only a small fraction of the proton's (or the α particle's) energy is lost and a small value of the momentum is transferred to the bound electron, therefore its direction is scarcely altered.

The encounters between ions and electrons are attributed to the electrostatic attraction. For small angular deflection (i.e. small momentum transfer)

$$\phi = \frac{\Delta p}{p} \ll 1 \tag{1.37}$$

Where Δp is the change in momentum obtained from impulse approximation

$$\Delta \mathbf{p} = \int_{-\infty}^{\infty} \mathbf{F} dt = \frac{1}{v} \int_{-\infty}^{\infty} -\nabla V(\mathbf{r}) dx \tag{1.38}$$

Where x is the coordinate of the system as depicted in figure (1-11). Bohr stated that the energy loss of a particles with $v > c/137$ (Bohr velocity) can be found from impulse approximation. Since the momentum is transferred to an electron of mass m by a charged particle Z_1 has velocity v and impact parameter b as shown in figure (1-11) thus Δp is given by[26]

$$\Delta p = \frac{2 Z_1 e^2}{bv}$$

Thus the change in the kinetic energy is

$$\Delta E = \Delta \left(\frac{p^2}{2m} \right) = \frac{2}{m} \left(\frac{Z_1 e^2}{bv} \right)^2 \tag{1.39}$$

For a sample contains n electrons per unit volume ($n = Z_2 N$, Where N is the atomic

density), the energy transferred to the electron in a shell of radius b is given by[26]

$$-\frac{dE}{dx}db = 2\pi b\,db\,n\,\Delta E \tag{1.40}$$

Where dE/dx is the energy loss per unit path, thus

$$\int_{b_{\min}}^{b_{\max}} -\frac{dE}{dx}db = \frac{4\pi}{m}\left(\frac{Z_1 e^2}{v}\right)^2 N Z_2 \ln\frac{b_{\max}}{b_{\min}}$$

Where $b_{\min}$ corresponds to direct head on collision (i.e. b approaches zero) at which the maximum energy transfer is $\Delta E_{\max} = 2mv^2$, and $b_{\max}$ corresponds to minimum energy transfer which is just the binding energy of the electron $I \sim Z_2 \times 10$ eV, thus $\Delta E_{\min} = I$. Make use of these values yields[26]

$$\frac{dE}{dx} = \frac{-4\pi Z_1^2 Z_2 N e^4}{mv^2}\ln\frac{2mv^2}{I} \tag{1.41}$$

This relation holds only for ions at considerable energies below the relativistic limit.

The stopping power $S(E)$ defined as

$$S(E) = -\frac{1}{\rho}\frac{dE}{dx} \tag{1.42}$$

Where ρ is the density of the sample. The atomic stopping power is given by

$$\epsilon(E) = -\frac{1}{N}\frac{dE}{dx} = \frac{A}{N_A}S(E) \tag{1.43}$$

Where A and N_A are the atomic mass number and Avogadro number, respectively

The range of an ion has energy E_o through a bulk sample is given by the following numerical integral

$$R = \int_0^{R_o} dx = \int_{E_o}^{0} -\frac{dE}{(dE/dx)} \tag{1.44}$$

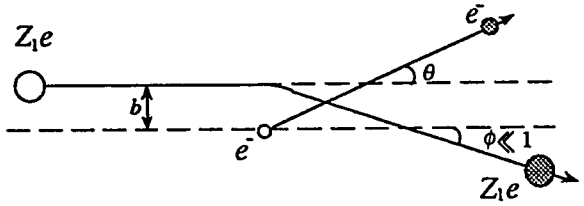

Figure 1-11: Schematic diagram for a positively charged-ion deflection by the electrostatic field of the atomic electron.

A family of dE/dx curves for α particle in various elements is shown in figure (1-12) for a broad energy range[26]. The figure shows the atomic stopping power $\epsilon(E)$ in units of eV·cm^2/10^{15}atoms, for Au, Ag, Cu, and Al. The maximum values in the curves correspond energies where the particle velocities approach the mean velocity of the atomic electrons. At low energy, the values of dE/dx decrease because α particles have an average charge less than +2 due to charge exchange between the incident ion and the surrounding electrons[26].

A comparison between theoretical and experimental stopping power is shown in figure (1-13). Through measured values at low energies exhibit a wide spread, however, there is very good agreement in the 1-4 MeV energy range[30] that seems adequate for this project.

Rutherford Backscattrering Spectra

In practice, the parameters regarding the detecting angle ϕ, beam type Z_1 and M_1, and beam energy E_o are fixed. The only parameters that *RBS* spectrum for a given sample depends on are

1. The elemental compositions of the sample. This is obvious from equation (1.29) for the differential cross section and equation (1.35) for the kinematic factor.

2. The Profile thickness of the sample.

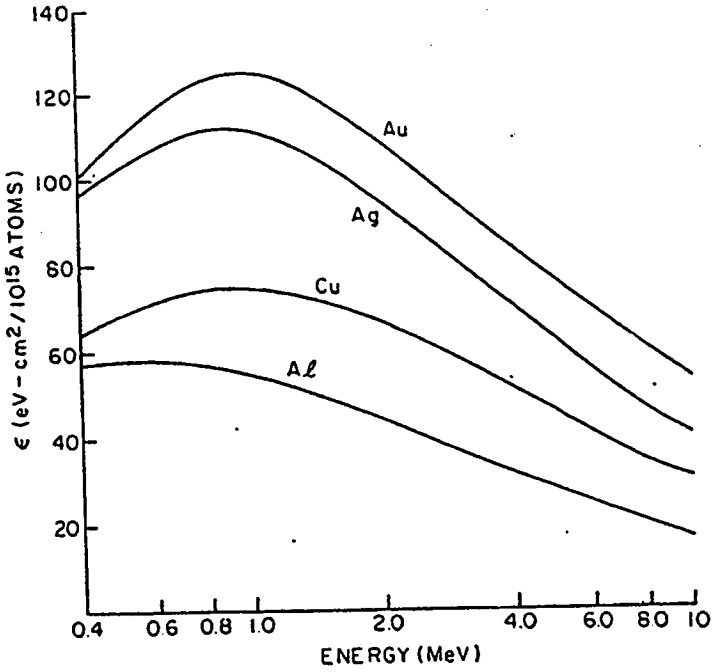

Figure 1-12: Stopping power curves for α particles in various elements as a function of energy. (Taken from FELDMAN *et al.*,1982.)

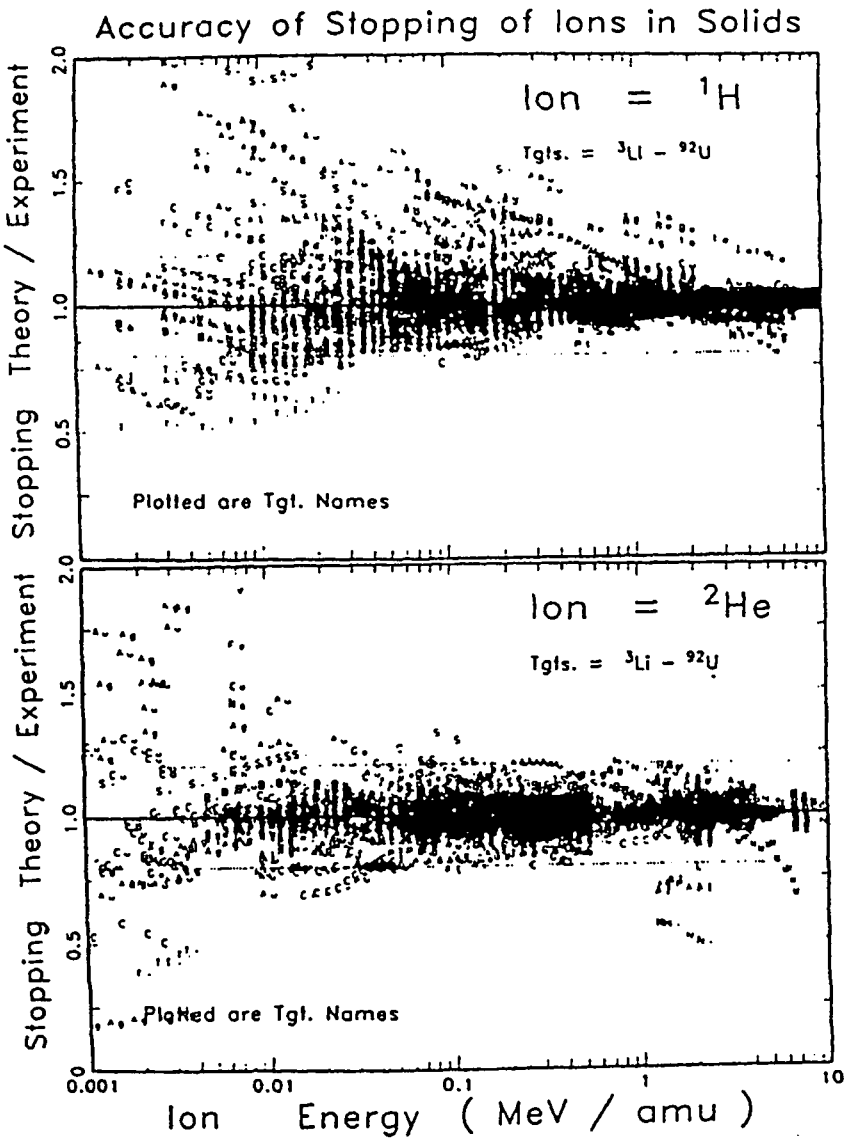

Figure 1-13: Comparison between theoretical and experimental stopping powers for protons and α particles in all solids. (Taken from ZIEGLER *et al.*, 1985.)

When a sample contains two types of atoms which differ in their masses by a small amount ΔM_2, the detected pulses for backscattered ions differ in energy by amount ΔE_1 . This difference in energy is desired to be larger than the detector resolution in order to distinguish the ions which are scattered from each type of the atoms. For fixed M_1, ΔM_2 gives the maximum change in K_{M_2} when $\phi = 180°$ as shown in equation (1.36). Additionally, equation (1.30) implies that the cross section reaches its maximum when $\phi = 180°$, which means the detection process becomes very efficient. Practically it is not possible to place the detector exactly at $\phi = 180°$ because it will obstruct the path of the incident particles. The detector is thus normally placed at some steep backward angle. In this project ϕ is fixed at 164°.

The energy difference between scattered particles by two different materials M_2 and $M_2 + \Delta M_2$ can be obtained directly using equation (1.31) as

$$\Delta E_1 = E_o \left(\frac{dK_{M_2}}{dM_2} \right) \Delta M_2 \tag{1.45}$$

Obviously ΔE_1 can be enlarged by increasing E_o. However, the upper limit for the beam energy must avoid nuclear resonance and knock-out reactions.

If an energetic ion impinges on a thick sample, it will suffer energy loss as it traverses through the atomic layers. The energy of a backscattered particle at certain depth t in a thick sample is given by[26]

$$E_1(t) = K_{M_2} \left\{ E_o - t \left(\frac{dE}{dx} \right)_{E_o} \right\} + \frac{t}{\cos\phi} \left(\frac{dE}{dx} \right)_{E_1} \tag{1.46}$$

Where the subscripts on dE/dx refer to the energy at which dE/dx is calculated. Equation (1.46) assumes a constant dE/dx which is true when $E_o \geq 1$ MeV as shown in figure (1-12). The first term in equation (1.46) gives the energy of the ion at depth t, whereas the second term gives the energy of the ion after scattering from depth t and angle ϕ. Additionally, equation (1.46) indicates that $E_1(t)$ is linear function of t. for thin samples, $t \to 0$, equation (1.46) reduces to equation (1.31). The effect of multiple

scattering contribution to thick-target yield is neglected, however there are attempts to include this effect theoretically, especially for protons, at scattering angles close to 180°[31].

A variation in the thickness by δt corresponds to a variation in the energy by δE_1. This can be obtained directly from equation (1.46) as

$$\delta E_1 = \left\{ \frac{(dE/dx)_{E_1}}{\cos\phi} - K_{M_2} \left(\frac{dE}{dx} \right)_{E_o} \right\} \delta t \tag{1.47}$$

This indicates that the depth resolution is determined by the energy resolution of the detector δE, dE/dx, and geometry. Typical depth resolution is in order of 30-100 Å. At higher depths energy straggling will set a limit on depth resolution[26].

The yield of backscattered particles Y from thin layer of atoms Δt is given by[26]

$$Y = \dot{\Omega} Q N \Delta t \left(\frac{d\sigma}{d\Omega} \right)_R \tag{1.48}$$

Where Ω is the solid angle subtended by the detector, Q is the total incident charge, and $N\Delta t$ is the number of target atoms/cm^2 in the layer. Practically equation (1.48) can be employed to obtain profile depth and thickness of thin films.

For a thick samples (bulk targets), the particle could scatter from any layer at depth t. Thus the expected *RBS* spectrum is continuous to low energy. This is illustrated experimentally in figure (1-14) for 2.0 MeV α particles scattered from thick Si substrate. For a thick homogeneous sample which contains two elements of masses M and m, where $M > m$, with different kinematic factors K_M and K_m, respectively, then the resultant spectrum has steplike as shown in figure (1-15), and the spectrum of the bulk target extends to zero energies. As a matter of fact, the spectrum experimentally will not extend to zero energy because near zero energy the yield disappears in a large background noise. Also the yield will not be flat topped, due to the E^{-2} dependence of the scattering cross section.

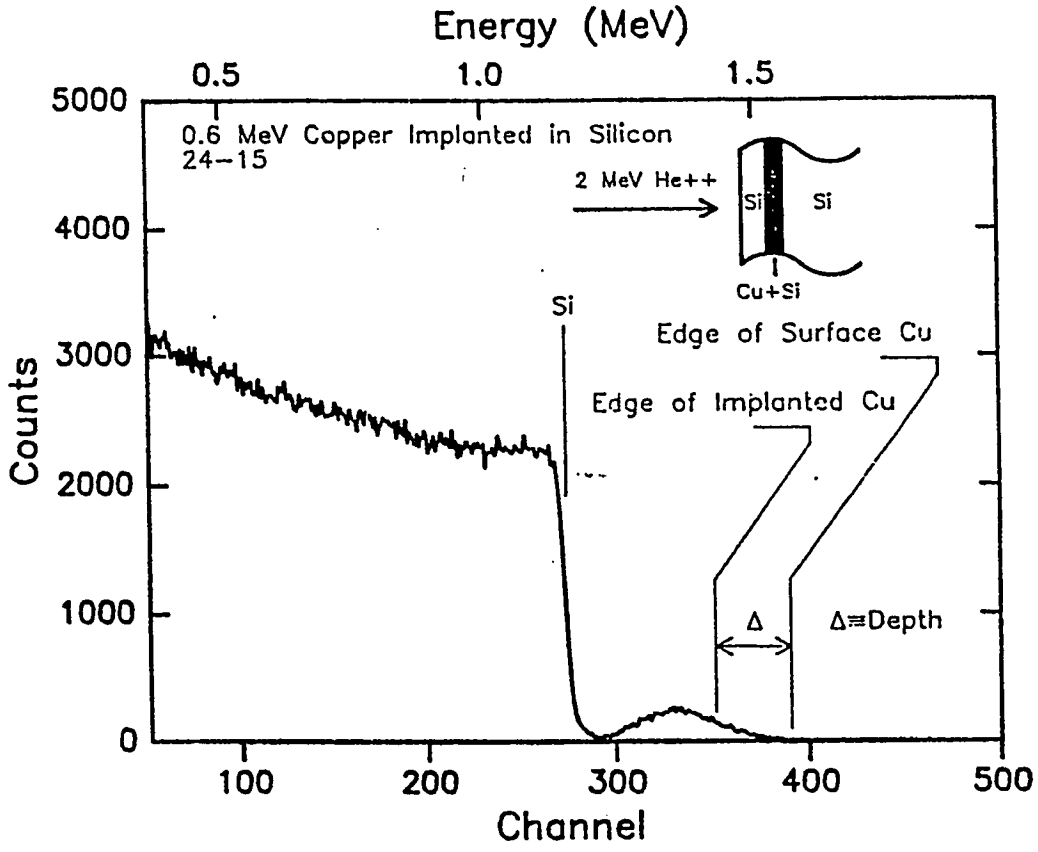

Figure 1-14: The *RBS* spectrum for 2.0 MeV He^{++} in bilayer sample composed of Si layer and Cu implanted in Si and bulk Si substrate.

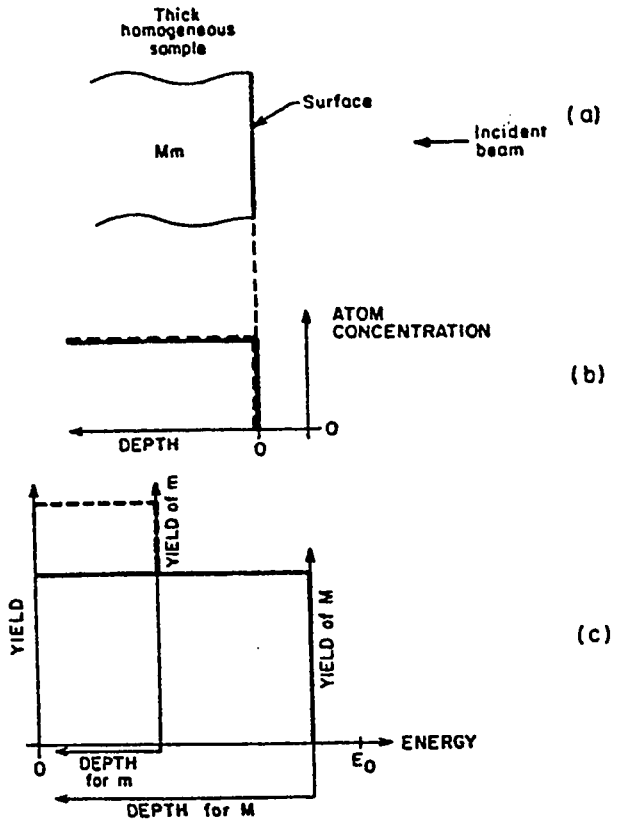

Figure 1-15: The signals of thick sample composed of two different elements. (Reproduced from CHU *et al.*,1978.)

One of the main applications of *RBS* spectrometry is the analysis of thin films and layered structures. A thin film could be composed of a uniform mixture of two or more elements or multi-layer of several elements. For the first case, a certain criteria are deduced from the derived relations under the consideration that the elements have different masses:

1. Since kinematic factor depends on mass as equation (1.35) indicates. Therefore, from equation (1.31) and equation (1.46), the yield of heavy masses appears at high energies in the *RBS* spectrum; and the yield from light masses appears at low energies[25].

2. According to equation (1.29) and equation (1.48), high atomic number elements give high yield; low atomic number elements give low yield[25].

Thus, the spectrum from two elements consists of two signals, each has certain energy and yield according to its mass and atomic number. This is illustrated in figure (1-16). If the masses and the atomic numbers for two elements are close, one expects an overlapping to occur between the two signals. Note that in figure (1-16), the substrate signal is omitted.

The *RBS* energy spectrum of multi-layered elemental film, can be summarised in the following example. Suppose three elements, A and B as a thin layers and S as a substrate (bulk), with masses M_A, M_B, and M_S, respectively, such that $M_B > M_A > M_S$. Figure (1-18a) shows the spectrum for the thin film when the thickness of B and A are relatively small. Since B is heavier than A, then its signal will be at higher energy position and has relatively higher yield (this arises from the fact that heavy elements have high atomic numbers). For the same reason element B is followed by A and then S. An example from this project is shown in figure (1-17). The figure shows the *RBS* spectrum for 2 MeV α particles scattered from 50.3 $\mu g/cm^2$ HoF_3 thin film deposited on moderate-thickness Nuclepore substrate. The *RBS* yields and energies from Ho, F, and the substrate confirm the previously mentioned expectations.

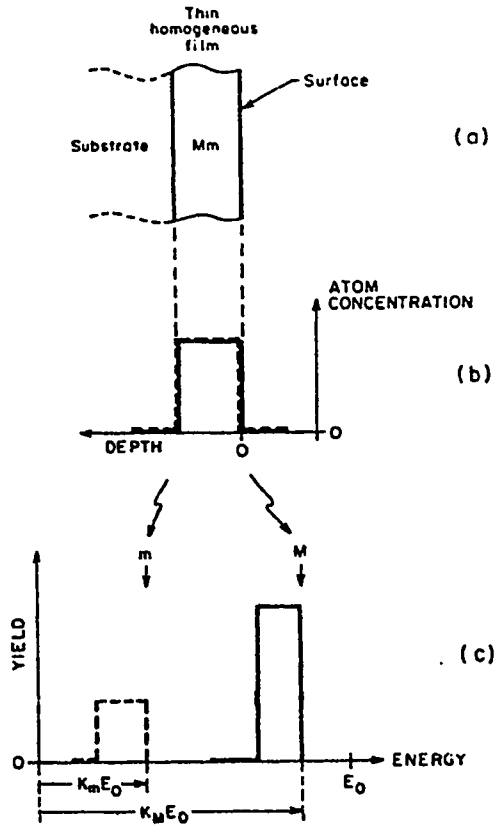

Figure 1-16: The signals of thin sample composed of two different elements. (Reproduced from CHU *et al.*,1978.)

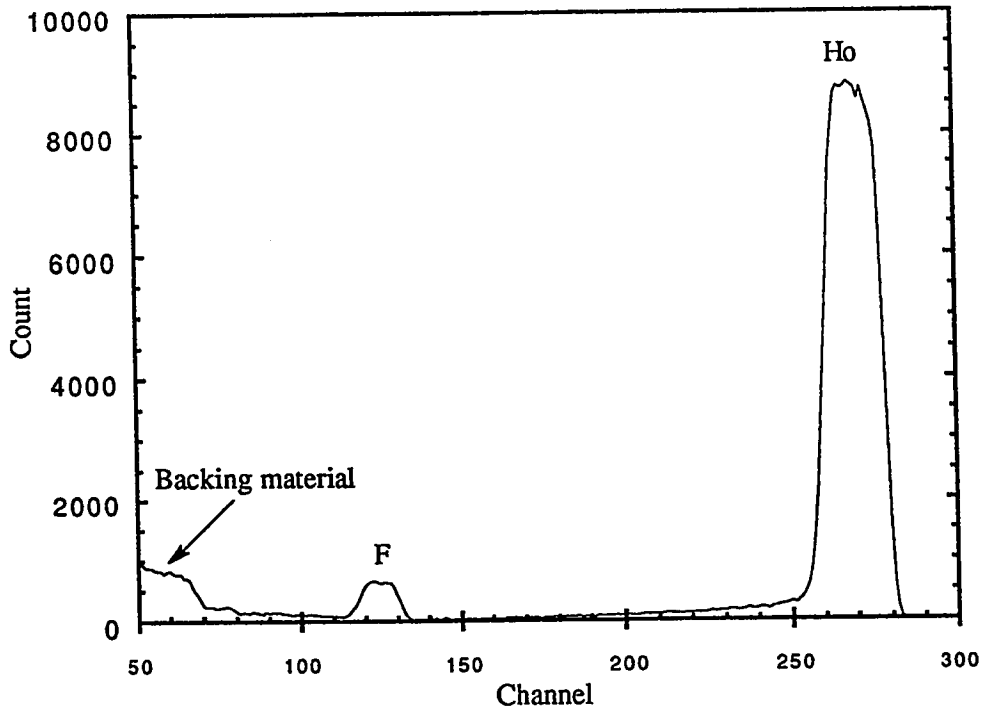

Figure 1-17: The *RBS* spectrum produced by 2.0 MeV α-particle bombardments on $\mu g/cm^2$ HoF_3 thin film deposited on Nuclepore backing.

Now, if the thin film was fabricated such that layer B is noticeably thicker than A, then according to equation (1.46) the energy width of signal B increases as the width is increased. This increment of width occur by a shift to the low energy region and overlapping between the two signals A and B occurs if the thickness of B is large enough. The overlapping appears as a high yield region relative to the yield of both A and B as it is shown in figure (1-18*b*).

Same argument satisfies when the thickness of layer A is thicker than B. However, the width shift for signal A is toward the high energy region. This because layer A is in the front of layer B which is shifted towards the low energy region due to the obscureness and attenuation of the beam (that arrives to B) by the thick layer A. Thus overlapping occurs as shown in figure (1-18*c*).

The experimental results confirm the theoretical calculations and *RBS* spectrometry is quite successful and powerful for material analysis since the spectrum can be fitted and analysed theoretically.

1.2.2 Particle Induced X-Ray Emission (PIXE)

In this process the X rays are induced by the impact of energetic ions due to the Coulomb interaction between the incident ion and inner-shell bound electron, giving rise to vacancy. This vacancy is consequently filled by an outer shell electron, and the atom is subsequently de-excites by emitting a characteristic X ray. Moreover, there is a probability for Auger electron emission. The process is depicted in figure (1-19) and the mechanism is similar to that shown in figure (1-11). The X-ray energy depends on the electronic shell structure in the atom and hence on the type of the atom itself. Accordingly, in multi-elemental samples, each element can be traced and identified by referring to its characteristic X-ray lines.

The study of X rays produced by light ions bombardments has received a great impetus by the development of analytical techniques. The ion beam is usually obtained from a conventional accelerator with a current of few nano amperes which is usually

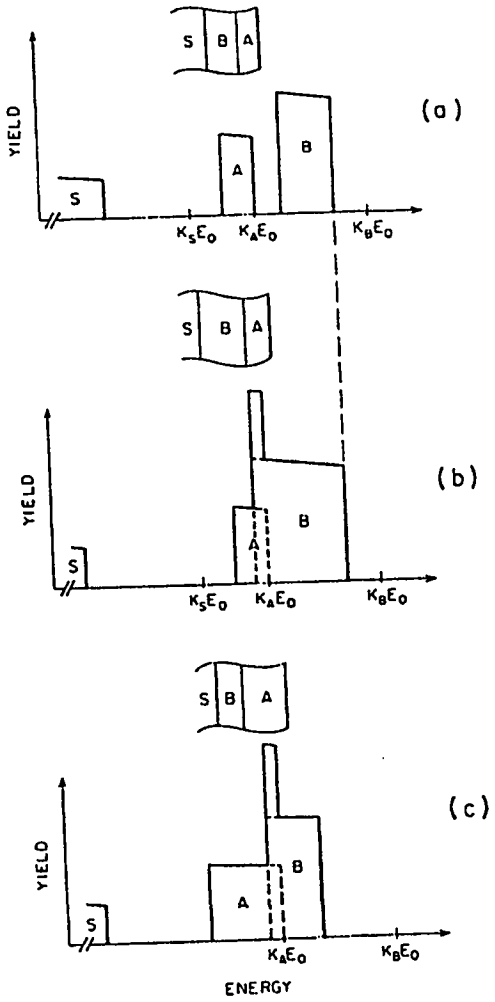

Figure 1-18: Schematic representation of the backscattering spectrum of a bilayered film on a substrate *S*. (Reproduced from CHU *et al.*,1978.)

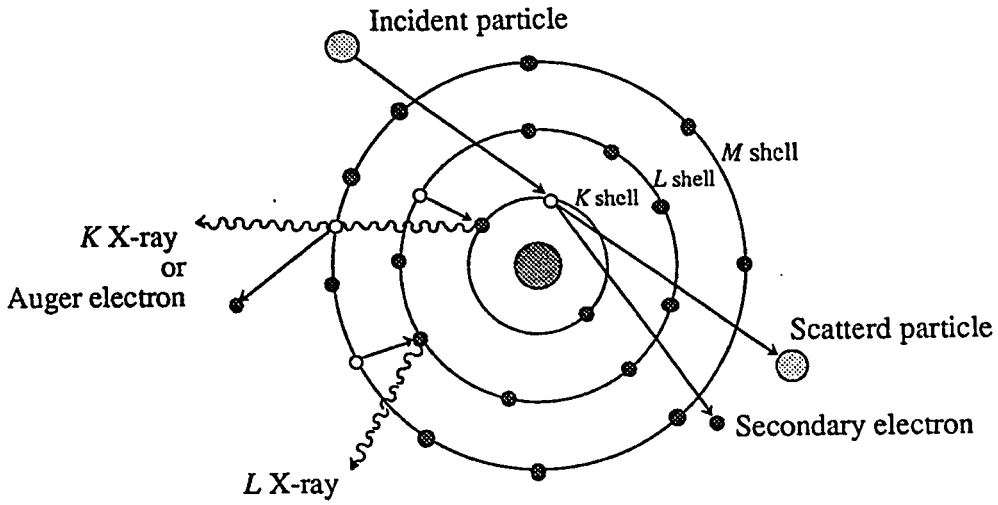

Figure 1-19: Schematic diagram shows the ion-atom interaction and consequential possible processes.

sufficient. Compared to the other excitation processes, *PIXE* has relatively high cross section. Therefore, the characteristic X rays are produced in abundance with relatively low background and only a small amount of sample's material is required for the analysis. Under favourable conditions it is possible to detect 1-2 part per million over a wide range of elements. The process is classified as non-destructive and surface contaminants, such as oxide layers, do not affect the analysis since *PIXE* is usually insensitive for elements with $Z < 13$. For thick target samples one is able to detect through few micro-meter depth, which is the typical range of light ions in solids, taking into account the energy loss of the ion and self absorption effects. A typical *PIXE* spectrum for aerosol pollution sample, collected from 20 m^3 of air, is shown in figure (1-20).

In *PIXE* analysis a high resolution detector is normally used. The necessity of good energy resolution detector in *PIXE* arises from the complex nature of *PIXE* spectrum, since it involves many overlapped peaks. For instance, in K X rays of transition elements, $20 \leq Z \leq 30$, the K_β of element Z overlaps the K_α of element $Z+1$. Also in this region, the K_α of peak for specific element interferes with the escape

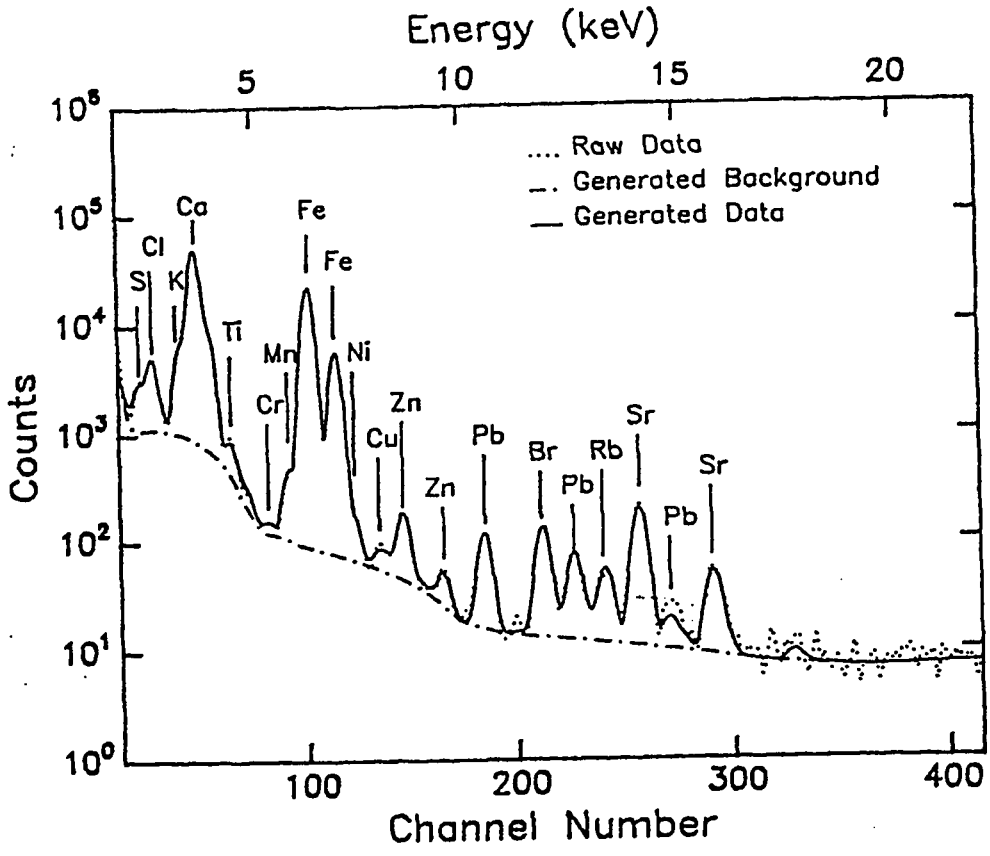

Figure 1-20: PIXE spectrum of aerosol pollution sample collected from 20 m^3 of air in Dhahran.

peak of the K_α of another element whose Z is two or three units greater[6]. Moreover, there is a possibility of overlaps of the K X rays of light elements with L X rays of heavy ones. For example, if our samples (Ho, Er, and Tm) contaminated by impurities, such as Fe, Cu, Zn, and Co, there will be an overlapping between the K X-ray lines of the impurities and the L X-ray lines of our samples. Finally, at very low energies even M X rays can enter the picture[6]. Since *PIXE* is a trace element technique, spectra tend to be crowded and there are many peaks whose energy differences is less than the typical resolution of the detectors. These point out the need for a computer code that fits entire spectra relying on a data base of X-ray energies and relative intensities for lines which contribute to the spectra. The most important parameter obtained from *PIXE* spectrum is the line peak area (line intensity) from which the elemental concentration within the sample can be obtained using appropriate standardization. Moreover, the estimations of production and ionization cross sections depend on measuring accurately the peak areas.

PIXE Yield Calculation

The most popular *PIXE* sample are thin films deposited on backing material. Usually backing materials consists of elements that are insensitive for *PIXE* analysis (i.e. elements whose $Z \leq 13$). However backing materials contributes only to the background. Thick samples can be analysed using *PIXE* technique but the analysis is more difficult because the calculations must be corrected for projectile slowingdown and self-absorption effects.

PIXE Yield for Thin Targets

For a thin target of thickness t μgm/cm^2, the yield is given by[32]

$$Y = \frac{tN_A\Omega Q\epsilon}{4\pi ew\cos\theta}\sigma_p(E) \tag{1.49}$$

Where Ω is the solid angle subtended by the detector, Q is the accumulated charge, ϵ is the detector efficiency, N_A is Avogadro number, w is the elemental atomic weight for multi-elemental sample $w = \sum_i w_i$ where i runs for all elements within the sample, e is elementary charge, θ is the angle between the beam and the sample normal, and $\sigma_p(E)$ is the X-ray production cross section as a function of projectile energy. In order to obtain concentrations, *PIXE* system must be calibrated for a given elements versus related X-ray yield per unit concentration, and obtain the calibration curve. Normally the calibration is made by using measured yields from thin standards (known concentration) samples.

PIXE Yield for Thick Targets

If secondary effects are ignored, the thick target yield for an element j of concentration C_j mg/Kg can be written as[33]

$$Y_j = \frac{C_j N_A}{w} \frac{\Omega Q \epsilon}{4\pi e} \int_{E_p}^{0} \sigma_p^x(E) \frac{dE}{S(E)} \exp\left\{-\mu \int_{E_p}^{E} \frac{dE'}{S(E')} \frac{\cos\theta_i}{\cos\theta_o}\right\} \tag{1.50}$$

Where E_p is the projectile energy (MeV), $\sigma_p^x(E)$ is X-ray production cross section (cm^2), $S(E) = \sum_j S_j C_j$ is the composite stopping power of the matrix (MeV cm^2/gm), where subscript j stands for the jth element of the matrix, $\mu = \sum_j \mu_j C_j$ is the composite mass attenuation coefficient of the matrix (cm^2/gm), C_j is the jth element relative concentration by weight, θ_i and θ_o are the angles of the incident beam and detector axis with respect to matrix normal, respectively. The thick target yield can be simply represented as

$$Y = CM \tag{1.51}$$

Here we dropped the subscript j, Y denotes the X-ray yield, C is the element concentration, and M is the calculated yield per unit concentration.

The analysis usually include the use of internal standards and the use of standard reference materials to provide a measured calibration curve for standard experimen-

tal conditions. A known amount of non-interfering element (commonly yttrium or ruthenium) is added to the sample. The concentrations of the elements are obtained with respect to the concentration of the standard, by calculating the expected yield. Equation (1.51) becomes for internal standard

$$C_e = C_{st}\left(\frac{Y_e}{Y_{st}}\right)\left(\frac{M_{st}}{M_e}\right) \tag{1.52}$$

Where the subscripts st and e denote the standard and element, respectively. The advantages of using standard materials are to avoid the uncertainties of the current integration, geometric factor, and detection efficiency.

1.2.3 Background in PIXE spectra

X-ray production cross section is generally quite large according to nuclear physics standards. Therefore, only very small amount of matter produces relatively large number of characteristic X-ray pulses, that enhances trace element detection. However, in addition to the characteristic X-ray peaks from trace elements, *PIXE* spectrum is influenced by a background that is originated from several sources during the excitation process.

Projectile Bremsstrahlung

Generally, when a charged particle is decelerated, It emits an electromagnetic radiation. In the case of charged projectiles penetrating through atomic media, the deceleration is due to the Coulomb fields, and consequently a bremsstrahlung radiation is emitted with energies distributed from zero to the projectile's kinetic energy. This process produces the majority of the detected background. Using heavy charged particles, the effect of bremsstrahlung is much lower. This is because the bremsstrahlung intensity is proportional to the square of the acceleration. In other words, it is proportional to $(F/m)^2$[6] where F denotes the Coulomb force that acts on the charged particle of mass

m. Since the Coulomb force that acts on the electron is equivalent to the force that acts on a proton, the intensity of proton bremsstrahlung is lower than that of electron by $(1836)^2$ times.

The bremsstrahlung cross section for a projectile of energy E_p with atomic and mass number Z_1 and A_1, respectively, penetrates through a sample that contains atoms of atomic and mass numbers Z_2 and A_2, respectively, is given by[6]

$$\left(\frac{d\sigma}{d\Omega}\right)_x = \frac{cA_1Z_1^2Z_2^2}{E_pE_x}\left(\frac{Z_1}{A_1} - \frac{Z_2}{A_2}\right)^2 \tag{1.53}$$

Where c is a slowly varying constant and E_x is the energy of the radiated photon. Thus at low Z elements, one expects low bremsstrahlung radiations which fortunately enhance the detection and analytical method.

The yield according to equation (1.53) gives rise to high energy tail in the spectrum[6]. Additionally, equation (1.53) suggests that the yield decreases as projectile's energy increases which is contrary to those of the characteristic X-ray yield and other background processes. Moreover, it is obvious that the ratio $Z/A \simeq 0.5$ for the majority of elements heavier than hydrogen, therefore, for α-particle bombardments the expected yield according to equation (1.53) goes to zero.

Secondary Electron Bremsstrahlung (SEB)

Secondary electron bremsstrahlung was first considered by FOLKMANN[34]. The process is schematically shown in figure (1-21a), where the projectile ejects an electron from a target atom at point A. This electron is decelerated due to the nuclear Coulomb field of other atoms to produce bremsstrahlung at point B. This radiation is called *secondary electron bremsstrahlung* (*SEB*) or knock-out bremsstrahlung[35].

The *SEB* spectrum is characterised by the quantity $T_{\max} = 4m_eE_p/M_p$, where m_e denotes the rest mass of electron, E_p and M_p are the energy and the mass of the projectile, respectively, and $T_{\max}$ is the maximum energy that can be transferred in head-on

collision from the projectile to a free electron at rest. Therefore, the bremsstrahlung of energy higher than T_{max} must be produced by inner-shell electrons. As the number of free and outer-shell electrons is generally much larger than those of inner-shell electrons, the intensity of *SEB* is expected to decrease rapidly above T_{max}.

In the case of a finite target thickness, secondary electrons can escape out of the target before producing the bremsstrahlung. This effect is expected to be larger with increasing the projectile energy and with decreasing the target thickness. For heavy atoms the screening of the nucleus by atomic electrons substantially reduces the *SEB* cross section[35].

Quasi-Free Electron Bremsstrahlung (QFEB)

This process is illustrated in figure (1-21*b*), where a projectile of velocity v_p and energy $E_p = \frac{1}{2}Mv_p^2$ approaches a target atom. The outer-most shell electrons have velocities $v \ll v_p$. Therefore, these electrons in the particle's frame system can be considered as approaching the projectile with energy $T_r = \frac{1}{2}m_e v_p^2$. Hence they are scattered by the Coulomb field of the projectile and produce bremsstrahlung. This process is called *quasi-free electron bremsstrahlung (QFEB)*. It occurs in the projectile's system and not in the target's system. Accordingly, the X-ray source is the projectile itself, which is moving in the target frame. The wave length shift due to the Doppler effect must be taken into account. Note that the maximum energy of this process must be T_r which is of the order of $E_p/1836$ for protons and $E_p/7344$ for α particles.

Atomic Bremsstrahlung (AB)

In this process the incident projectile ejects an inner-shell electron, this electron is then recaptured by the atom, consequently, the electron emits a photon of continuum spectrum. The emission of photon in this case depends on the internal structure of the target atom. This process is called *atomic bremsstrahlung (AB)*[35]. The process is illustrated in figure (1-21*c*). The ejected electron must leave the atom at very

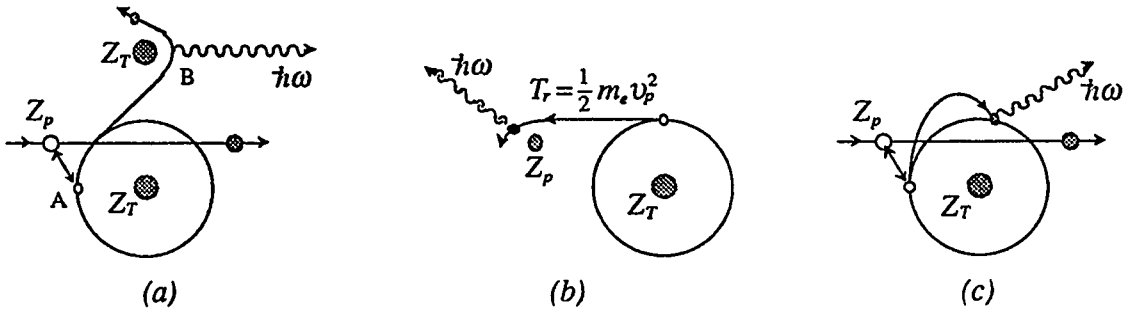

Figure 1-21: Three schematic representation of (*a*) Secondary electron bremsstrahlung (*SEB*), (*b*) Quasi-free electron bremsstrahlung (*QFEB*), and (*c*) Atomic bremsstrahlung (*AB*); Z_p and Z_T represent the atomic numbers of the projectile and the target atom. (Reproduced from ISHII & MORITA, 1990.)

low energy (i.e. the energy transferred from the projectile to the bound electron is comparable to the binding energy), so the atom become capable to recapture the ejected electron. The wave function of the final state of the electron in this process is equal to that of initial state. If the final state is not bound state, but continuum, the process then is an ionization accompanied by a characteristic emission of photon or Auger electron.

Nuclear Reaction Background

If the projectile is scattered inelastically by the nuclear Coulomb field, the target nucleus is excited and de-excites to the ground state by emitting γ rays. However he γ-ray spectrum becomes broadened due to Compton scattering with the detector's material and it appears as a continuous background at high energy region.

Moreover, there is a possibility that *PIXE* spectrum includes some γ-ray lines due to Coulomb excitations of the nuclei. It was found in our study that Tm $L_{\beta_{2,15}}$ line (at 8.467 keV) is larger than expected. This is referred to the fact that ^{169}Tm γ ray, which is emitted from 8.41 keV level, overlaps Tm $L_{\beta_{2,15}}$ line.

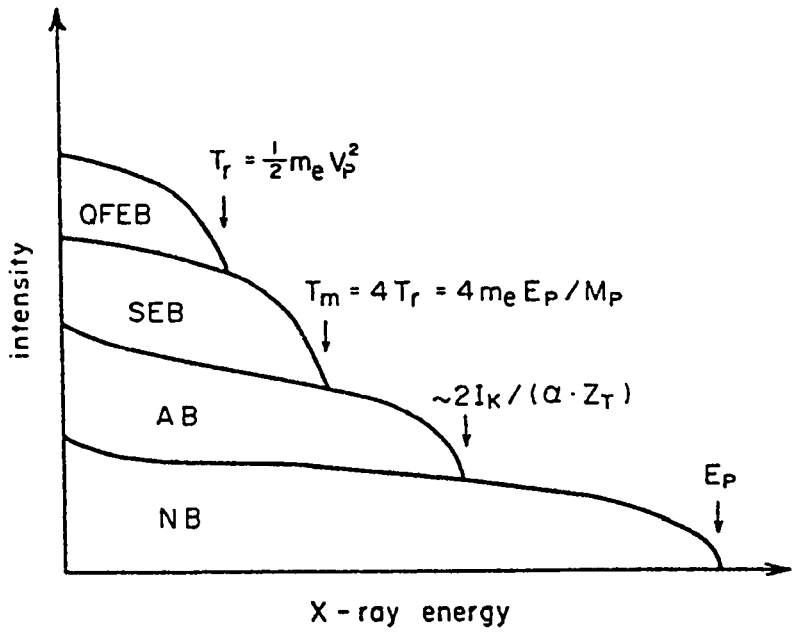

Figure 1-22: Schematic representation of a layer structure in a continuous X-ray spectrum. Note that the ordinate is in logarithmic arbitrary scale. (Taken from ISHII & MORITA, 1990.)

Charge Build-Up Effect

In the case of a target material is being insulator, the region of the target bombarded by ion beam is positively charged. The charge accumulates until a discharge process occurs to an earthed point as a consequence of insulation break down. The process is accompanied by continuous X-ray emission that appears at high energy region ($\sim$ 10–30 keV). One can overcome this effect by using the electron gun that emits electrons from a heated filament in order to neutralize the positive charge build-up on the sample. The beam current must be reduced as possible to make the neutralization process effective.

Figure (1-22) shows a schematic representation of a layer structure in a continuous X-ray spectrum as a result of all processes mentioned before, to demonstrate the relative intensity and domain for each effect.

1.2.4 Sensitivity

Because of the fluctuations of the continuum background, the detection limit of *PIXE* is usually determined by the relation

$$N_P \geq 3\sqrt{N_B} \tag{1.54}$$

Where N_P denotes the counts of the characteristic X-ray peak, and N_B denotes the counts of continuum background in interval covered by FWHM of the peak. This relation implies that the characteristic peak must be at least three times larger than the background fluctuation in order to be identified accurately. The background however depends on the composition of the target and therefore it is not possible to give any general expression for the sensitivity. On the other hand if the background is well known, the sensitivity can be calculated directly from X-ray production cross section. One can conclude from equation (1.54) that the sensitivity can be improved by increasing the counts of the characteristic peaks, since the relative statistical fluctuation of the entire spectrum decreases as counts increase. Because the counts are affected by the experimental parameters, such as detector efficiency, geometric factor, accumulated charge ... etc., the minimum detectable concentration, denoted as *MDC*, satisfies the following releation[6]

$$MDC \propto \sqrt{\frac{\Delta E}{\Omega Q t}} \tag{1.55}$$

Where ΔE is the detector resolution (eV), Ω is the solid angle, Q is the accumulated charge (μC), and t is sample thickness (mgm/cm^2). JOHANSSON[6] estimated the *MDC* for $\Delta E = 165$ eV, $\Omega = 0.003 \times 4\pi$, $Q = 10\,\mu$C, and $t = 0.1$ mgm/cm^2. The plot of *MDC* versus the atomic numbers is shown in figure (1-23) at 1-3 MeV protons, for K shell ($Z < 40$) and L shell ($Z > 40$). The main feature obtained from the figure is that *MDC* varies as proton energy and atomic number are varied. There are minima at certain atomic numbers which indicate that the sensitivity is maximum at these points. The sensitivity decreases around the maximum points because of the drop of

the fluorescence yield as Z decreases, and the drop of the X-ray production cross section as Z increases.

The atomic numbers corresponding to maximum sensitivity depend on the projectile energy. Therefore, one can adjust the beam energy in order to detect certain element properly. Hence one also can construct another pattern of sensitivity that gives projectile energy versus atomic number at various concentrations as shown in figure (1-24). Each shaded area in figure (1-24) represents specific concentration. For instance, to detect light elements, low energy protons $\sim$ 1 MeV is sufficient. This arises from the fact that the production cross section at low energy projectile is much larger for light elements than heavy ones. Additionally, a low energy projectile has a lower background. For $Z > 40$, the K X-ray production cross section becomes very small giving low sensitivity, thus one can make use of L X rays instead.

The above discussion is limited for protons. However the situation is similar for α particles. For $Z < 25$, it turns out that both protons and α particles almost give the same sensitivity, where for heavier elements α particles give a considerable lower sensitivity[6].

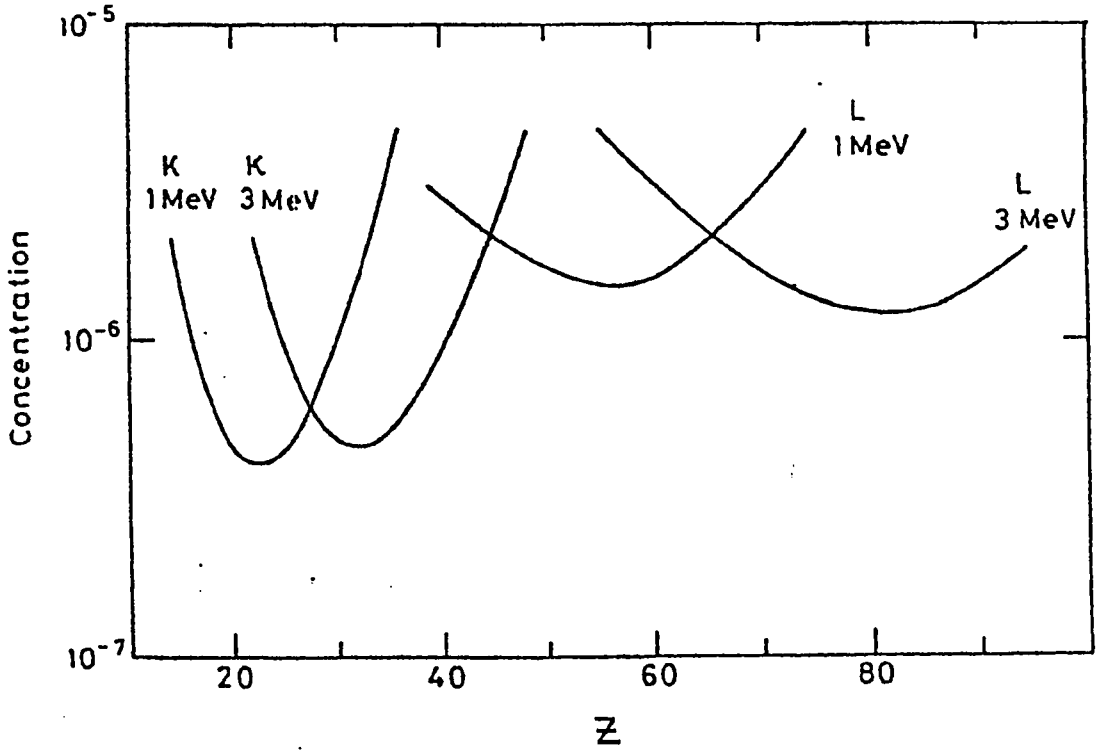

Figure 1-23: Minimum detectable concentration as a function of atomic number for proton energies 1 and 3 MeV.

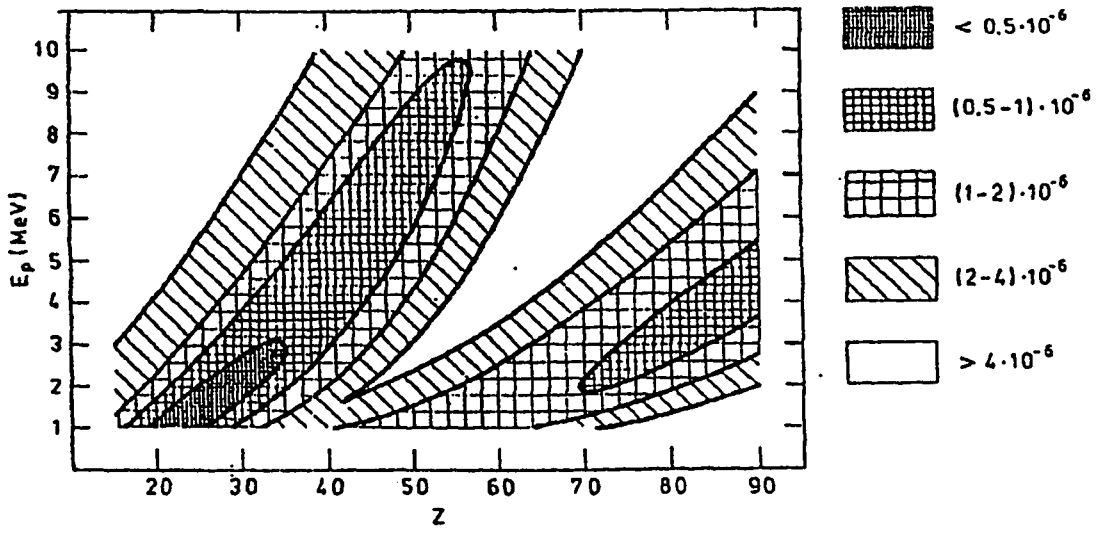

Figure 1-24: Minimum detectable concentration as a function of atomic number and bombarding energy. (Taken from JOHANSSON & CAMPBELL, 1990.)

Chapter 2

Inner-Shell Ionization Cross Section

This study concerns in the ionization that is created by α-particle impact for which Coulomb excitation results in inner-shell ionization with a subsequent emission of X rays. The first order theories, which are utilized to calculate the ionization cross sections, describe the ion-atom collision process in a general manner. Consequently, this chapter offers a general view for the main concepts of calculating the ionization cross section theoretically and experimentally. However, more attention is paid for the ionization induced by α-particle bombardment.

2.1 Inner-Shell Vacancy Creation by Light-Ion Impact

This is to offer an insight into the dynamics governing inner-shell excitation. One must distinguish between projectiles that act as a bare Point-charge particles in the impact leading to inner-shell ionization and those do not. And one should set apart slow and fast collisions relative to the response time of the inner-shell electron to be excited[36].

Projectiles that act as mass points of charge $Z_1 e$ excite target inner-shell electrons

via the Coulomb interaction between the projectile nucleus and the target electrons, and hence cause Coulomb excitation of the inner shells. This excitation always dominates other interaction processes when the projectiles move as bare nuclei through the target[36]. Indeed, even a slow projectile carrying an electronic structure acts as a bare charged particle provided that its K-shell radius, a_{1K} is large compared to target K-shell radius a_{2K}[36]. Thus, the projectile's electrons will be found mainly outside the interaction region, leaving the projectile nucleus to excite inner-shell target electrons as a bare charged particle.

The condition $a_{1K} \gg a_{2K}$ imposes that $Z_1 \ll Z_2$, where Z_2 is target charge. This arises from the fact that the radius of the S shell, $S = K, L, M, \ldots$ etc., is given by

$$a_{is} = \frac{a_o}{Z_{is}} \tag{2.1}$$

where the subscript i stands for 1 the projectile, 2 for the target. a_o denotes the Bohr radius, Z_{is} is the effective (screened) charge for the S shell as it is indicated in (1.4) and equation (1.5). The condition of deep penetration follows from the circumstance that the impact parameters which mostly contribute to the ionization have values $\simeq q_o^{-1}$ where q_o is the minimum momentum transfer given by

$$\hbar q_o = \frac{I_s}{v_1} \tag{2.2}$$

Where I_s is the binding energy of the S-shell electron, v_1 is the velocity of the projectile. Therefore, slow projectiles, for which $q_o^{-1} \ll a_{2K}$, must penetrate deeply into the K shell. Usually the binding energy of S-shell electron is expressed in terms of the dimensionless parameter θ_s as follows

$$\theta_s = \frac{n^2 I_{2s}}{Z_{2s}^2 R_\infty} \tag{2.3}$$

The parameter θ_s measures the nonhydrogenic aspect of the S-shell ionization energy.

R_∞ is Rydberg constant ($R_\infty = \frac{1}{2}$ a.u.= 13.6 eV). For K shell, θ_K grows slowly with Z_2 from $\simeq 0.6$ for light elements to $\simeq 0.9$ for heavy elements whereas for L-shell, θ_L grows from 0.4 to 0.8. Denoting the mean velocity of S-shell as:

$$v_{2s} = Z_{2s} v_o \tag{2.4}$$

where v_o is the Bohr velocity, the condition $q_o^{-1} \ll a_{2K}$ implies $v_1 \ll \frac{1}{2}\theta_K v_{2K}$. Thus, when $Z_1 \ll Z_2$, all projectiles act as a bare point charge at velocities $v_1 \ll \frac{1}{2}\theta_K v_{2K}$. At higher velocities stripping of the projectile electrons can occur, hence, the projectile acts as a bare point charge.

In case of slow projectiles with Z_1 greater or comparable to Z_2, they carry their electronic clouds inside the target K shell and thus they act as ions or atoms. They excite K- and L shell through the exchange forces set up by the Pauli exclusion principle in the overlapping electron clouds, as well as by Coulomb excitation[36]. This excitation is characterized as being Pauli excitation of atoms in collision. Thus, at low velocities $v_1 \ll v_{2s}$, Pauli excitation overshadows Coulomb excitation. At higher velocities, $v_1 > v_{2s}$, the response time of the bound electrons is too long compared to the collision time to allow the Pauli principle to influence the ionization process, and Coulomb excitation dominates. Both excitation process, Coulomb and Pauli are drastically differ in basic way. Pauli excitation causes multi-vacancies that leads to complex-nature spectrum with broaden peaks. Whereas, Coulomb excitation consistently causes single vacancy and leads to spectral lines whose energies represent vacancy-refilling transitions, and whose intensities represent the transition probabilities.

The convenient demarcation between slow and fast collisions is set by the time it takes for the projectile to traverse target inner-shell, $\simeq a_{2s}/v_1$, compared to the characteristic time of the target S-shell electron $\simeq 2\pi a_{2s}/v_{2s}$. This condition is obtained when the parameter;

$$\xi_s \equiv \frac{n}{(q_o a_{2s})} = \frac{v_1}{\frac{1}{2}\theta_s v_{2s}} \ll 1 \tag{2.5}$$

Fast collisions or high-velocity conditions prevail when $\xi_s \gg 1$.

It is customary to express the projectile-velocity dependence of the cross sections through the reduced velocity parameter:

$$\eta_s \equiv \frac{v_1^2}{v_{2s}^2} = \left(\frac{\xi_s \theta_s}{2}\right)^2 = \frac{m}{M}\frac{E}{Z_{2s}^2 R_\infty} \tag{2.6}$$

The parameter η_s is proportional to the projectile's energy. Note that

$$\eta_K = \frac{40 E_1(\text{MeV})}{Z_{2K}^2 M_1(\text{a.m.u.})}$$

The demarcation $\xi_s \simeq 1$ separates the domain of low velocities and of high velocities.

Other effects, that must be taken into account during the excitation process, is stated as follows:

1. Polarization of the electronic clouds of the target atom by the electrostatic field of the projectile.

2. Relaxation time of the atom after the excitation and transition.

3. Energy loss of the projectile due to the deflection by target nuclear field.

These effects can perturb the system. Regarding or disregarding these effects is discussed according to their contribution to the ionization cross section.

2.2 Theoretical Models

Mainly, three theoretical models are set to calculate inner-shell ionization cross section. Early theories on the dependence of the cross section on the energy of the projectile, atomic number of the projectile and target atoms lead to some fair agreement with experimental studies. Nevertheless, early theories do not provide totally the observed features of the cross section. There is at least one result that satisfies the experiments.

The cross section reaches a maximum when the projectile energy $E_p = A_p(M/m)I_i(Z)$, where A_p is the mass number of the projectile, M and m are the masses of projectile and the electrons respectively, and $I_i(Z)$ is the electron binding energy in the target atom. The theories also predict the scaling law[6]

$$\sigma_{Z_pA_p}(E_p, Z) = Z_p^2\sigma_{11}(\frac{E_p}{A_p}, Z) \tag{2.7}$$

Where $\sigma_{Z_pA_p}(E_p, Z)$ is the cross section of the projectile of atomic and mass numbers Z_p and A_p, and Z is the atomic number of target atoms. Thus for α particles, the cross section in terms of proton cross section is given as

$$\sigma_\alpha(E_\alpha, Z) = 4\sigma_{proton}(\frac{E_\alpha}{4}, Z)$$

However, JOHANNSON claims that the this law breaks down for ions heavier than helium, since multiple vacancies are created by the direct ionization and projectile pick-up which tends to change the cross section drastically[6]. More recently, several corrections were incorporated on the old theories, but they are still subjected to experimentation. The theories are Semi-Classical Approximation (*SCA*) introduced by BANG and HANSTEEN[37], Plane Wave Born Approximation (*PWBA*) by HENNEBERG[38] and then by MERZBACHER and LEWIS[4], and binary encounter approximation (*BEA*) by GARCIA[39].

The first two of these are high energy formulations, in the sense that they are expected to be valid only for incident particle energies much larger than the binding energies of the electrons. Proceeding to the details of these theories, it is convenient to understand the mechanism of inner shell vacancy creation by heavy charged particles bombardment.

2.2.1 Plane Wave Born Approximation (PWBA)

At high energy, many partial waves contribute to the scattering. To avoid the angular momentum decomposition, it is useful to apply Born approximation. The approximation will hold when the interaction potential is very weak compared to the energy of the incident particle[27]. This is true when the incident particle energy is few MeV where the interaction potential in our case is given by

$$\frac{ze^2}{r} \ll E \text{ (MeV)}$$

Where z is the atomic number of the projectile, r denotes the distance between the bound electron and the projectile[1]. In addition, Born approximation requires that the energy transfer from the incident particle to the bound electron to be very small or comparable to the binding energy of the electron. In our situation, we have massive particles with velocity less than or comparable to the velocity of the orbital electron. The maximum energy that a heavy particle of mass M and velocity v can transfer to electron of mass m and velocity u is given by

$$T_m = \frac{2Mm}{(M+m)^2}(Mv - mu)(v + u)$$

If $M \gg m$ and v is comparable to u, then T_m can be reduced to

$$T_m = \frac{4Mm}{(M+m)^2}E \approx \frac{4m}{M}E \tag{2.8}$$

where E is the energy of the projectile. From equation (2.8), T_m is in order of few keV, which is in the same order of magnitude of inner-shell electron binding energy. In fact, it has been found experimentally that the cross-section reaches its maximum

[1]In this section, the relative coordinate system is used, therefore the distinct supscribts are not involved in this discussion. Alternatively, the distinction between projectile and target atom parameters will be characterised by small letters for projectile and capital letters for target atom.

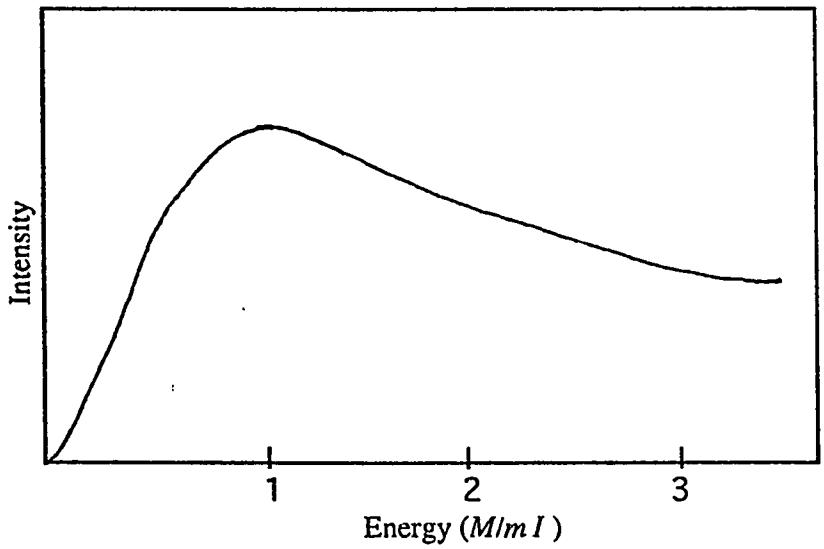

Figure 2-1: Intensity of inner-shell ionization as a function of incident particle energy. The abscissa is in unit of $(M/m)I$.

when $T_m \approx I_s$, where I_s is the binding energy of the electron in S shell, $S = K$, L, M...etc. As energy increases the cross-section falls off roughly as $1/E$, as shown in figure (2-1)[4].

The Born approximation implies that one could neglect the distortion of the wave function of the projectile by the atomic electrons. The validity of this condition can be demonstrated by the following inequality[4]

$$\frac{ze^2}{\hbar v} \ll 1 \tag{2.9}$$

One may thus exclude very slow collisions and collisions with light elements, when $Z <$ 10, to keep condition (2.9) valid. Moreover, slow collision includes the undesirable Pauli excitation. Thus to restrict the discussion on Coulomb excitation and to exclude Pauli excitation one have to consider fast collisions. Another effect that can be neglected is the nuclear Coulomb field. This is true if the electron radius a_n is large compared with

the distance of closest approach d, i.e.

$$\frac{d}{a_n} \ll 1 \tag{2.10}$$

Where

$$d = \frac{zZe^2}{E}$$

and

$$a_n = \frac{n^2\hbar^2}{Ze^2m}$$

Thus for $Z = 50$ the ratio $d/a_n = 0.03$. Somehow condition (2.10) does not hold well. This would be expected as an important error source.

The scattering process using Born approximation is considered as a transition between two states. There is an initial state (continuous incident plane wave function and bound electron) and final state (continuous outgoing plane wave function and ejected electron). Consider a projectile of atomic number z and coordinates $\mathbf{R}$ relative to the nucleus, incident on atom has atomic number Z and ejects electron at S shell whose position coordinates relative to the nucleus is $\mathbf{r}$, as illustrated in figure (2-2). Accordingly, it is possible to use Fermi-golden rule, which indicates that the transition rate is given by

$$R_{i\to f} = \frac{2\pi}{\hbar} \left|\langle \Psi_f | V(\mathbf{r},\mathbf{R}) | \Psi_i \rangle\right|^2 \rho(E_f) \tag{2.11}$$

Where $V(\mathbf{r},\mathbf{R})$ is the Coulomb potential between the incident particle and the electron in S shell, given by

$$V(\mathbf{r},\mathbf{R}) = \frac{ze^2}{|\mathbf{r}-\mathbf{R}|} \tag{2.12}$$

And Ψ_i and Ψ_f are the total initial and total final wave functions of the system, respectively given by[27]

$$\Psi_i(\mathbf{r},\mathbf{R}) = \frac{1}{\sqrt{V}} e^{i\mathbf{p}_i\cdot\mathbf{R}/\hbar}\psi_n(\mathbf{r}) \tag{2.13}$$

and

$$\Psi_f(\mathbf{r},\mathbf{R}) = \frac{1}{\sqrt{V}} e^{i\mathbf{p}_f\cdot\mathbf{R}/\hbar}\psi_{n'}(\mathbf{r}) \tag{2.14}$$

where $\mathbf{p}_i$ and $\mathbf{p}_f$ are the initial and final momenta, ψ_n and $\psi_{n'}$ are the initial bound and final continuum wave functions, respectively. $\rho(E_f)$ is state density at final state, i.e. number of accessible states per unit energy at final state, given by

$$\rho(E_f) = g_{j_s}\frac{Vd^3p_f}{(2\pi\hbar)^3}\delta(\frac{p_f^2}{2m} - \frac{p_i^2}{2m}) \tag{2.15}$$

Where g_{j_s} is constant given by

$$g_{j_s} = \begin{cases} 2j_s + 1 & \text{for massive particles} \\ 2j_s & \text{for massless particles} \end{cases} \tag{2.16}$$

Note that the unit volume in phase space is nothing but h^3. The delta function in equation (2.15) expresses energy conservation, i.e. the total energy $E = p_i^2/2m$. Here m denotes the reduced Mass. Accordingly equation (2.11) can be written as

$$R_{i\to f} = \frac{2\pi}{\hbar}\int \frac{g_{j_s}Vd^3p_f}{(2\pi\hbar)^3}\frac{1}{V^2}\left|\left\langle\psi_{n'}(\mathbf{r})e^{i\mathbf{p}_f\cdot\mathbf{R}/\hbar}\right| V(\mathbf{r},\mathbf{R})\left|\psi_n(\mathbf{r})e^{i\mathbf{p}_i\cdot\mathbf{R}/\hbar}\right\rangle\right|^2\delta(\frac{p_f^2}{2m} - E)$$

Let M_{if} to be the scattering amplitude, i.e.

$$M_{if} = \left\langle\psi_{n'}(\mathbf{r})e^{i\mathbf{p}_f\cdot\mathbf{R}/\hbar}\right| V(\mathbf{r},\mathbf{R})\left|\psi_n(\mathbf{r})e^{i\mathbf{p}_i\cdot\mathbf{R}/\hbar}\right\rangle = \int \psi_{n'}^*(\mathbf{r})e^{i(\mathbf{p}_i-\mathbf{p}_f)\cdot\mathbf{R}/\hbar}V(\mathbf{r},\mathbf{R})\psi_n(\mathbf{r})d\mathbf{r}d\mathbf{R}$$

Therefore the transition rate becomes

$$R_{i\to f} = \frac{g_{j_s}}{4\pi^2\hbar^4V}\int d\Omega\,|M_{if}|^2\int_0^\infty p_f^2dp_f\,\delta(\frac{p_f^2}{2m} - E)$$

By applying the integral over final momenta, yields

$$R_{i\to f} = \frac{g_{j_s}m}{4\pi^2\hbar^4V}p_f\,|M_{if}|^2\,d\Omega \tag{2.17}$$

Equation (2.17) expresses the transition rate per unit solid angle. In practical sense, one is seeking the flux of one particle per second in centre of mass frame, which is nothing but v_i/V, where v_i is the initial relative velocity and V is the volume in coordinate space. Therefore the differential cross section is the transition rate divided by the flux, hence equation (2.17) yields

$$d\sigma = \frac{g_{j_s} m}{4\pi^2\hbar^4}\frac{p_f}{v_i}\left|M_{if}\right|^2 d\Omega$$

But $p_f = mv_f$, using the above equation one ends up with

$$d\sigma(\Omega) = \frac{g_{j_s} m^2}{4\pi^2\hbar^4}\frac{v_f}{v_i}\left|\int \psi^*_{n'}(\mathbf{r})e^{i\mathbf{q}\cdot\mathbf{R}}V(\mathbf{r},\mathbf{R})\psi_n(\mathbf{r})d\mathbf{r}d\mathbf{R}\right|^2 d\Omega \tag{2.18}$$

Where $\mathbf{q}$ is the momentum-change vector given by

$$\hbar\mathbf{q} = \mathbf{p}_i - \mathbf{p}_f \tag{2.19}$$

One can carry out the integral over the particle coordinate $\mathbf{R}$ using the same procedures given in appendix A and hence integrate over the solid angel, yields

$$\sigma = \frac{2g_{j_s} z^2}{q^5}\left(\frac{e^2}{\hbar v_i}\right)^2\left|\int \psi^*_{n'}(\mathbf{r})e^{i\mathbf{q}\cdot\mathbf{r}}\psi_n(\mathbf{r})d\mathbf{r}\right|^2 \tag{2.20}$$

Which gives the cross-section at a certain momentum and energy transfer. Therefore, the cross-section must be integrated over all possible momenta and energy transfer. Thus

$$d^2\sigma(\mathbf{q},\epsilon) = \sigma d\mathbf{q}d\epsilon = 4\pi q^2\sigma dq d\epsilon$$

Using equation (2.20) yields

$$d^2\sigma(\mathbf{q},\epsilon) = 8\pi z^2\left(\frac{e^2}{\hbar v_i}\right)^2\frac{g_{j_s}dq}{q^3}\left|\int \psi^*_{n'}(\mathbf{r})e^{i\mathbf{q}\cdot\mathbf{r}}\psi_n(\mathbf{r})d\mathbf{r}\right|^2 d\epsilon \tag{2.21}$$

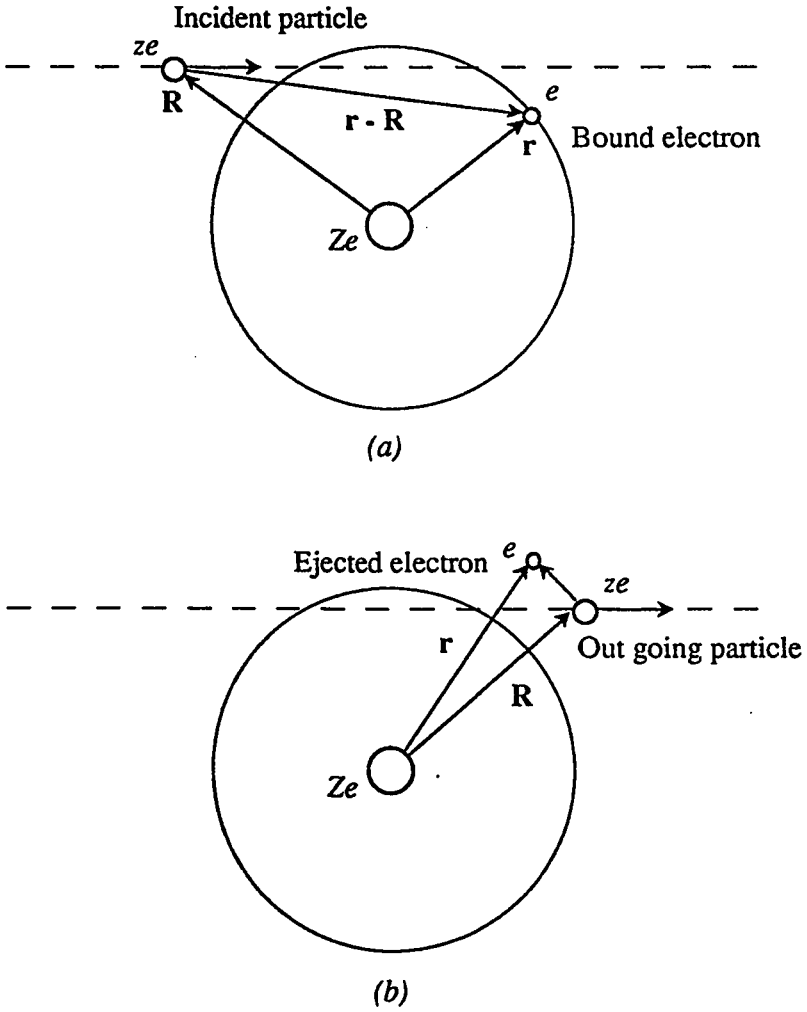

Figure 2-2: Schematic diagram for the system (a) befroe collision and (b) after collision.

The evaluation of cross section using equation (2.21) involves evaluation of the *form factor* $F_{nn'}$ (the matrix element for initial and final states), given by

$$F_{nn'}(q) = \int \psi^*_{n'}(\mathbf{r}) e^{i\mathbf{q}\cdot\mathbf{r}} \psi_n(\mathbf{r}) d\mathbf{r} \tag{2.22}$$

A problem in the evaluation of the form factor arises from the final continuum wave function since the behaviour of continuum wave function under the influence of outer

screening is not well known precisely. For initial wave function, the screened hydrogenic wave function derived from Hartree-Fock-Slater self-consistent field method, either non-relativistic (solution of Schrödinger equation) or relativistic (solution of Dirac equation) wave function can be used.

Using Schrödinger equation, The electron that undergoes excitation has stationary states of energy E' determined by

$$-\frac{\hbar^2}{2m}\nabla^2\psi - \frac{Z_s e^2}{r}\psi + V_s(r)\psi = E'\psi$$

Where Z_s is the effective nuclear charge given in equation (1.4) and equation (1.5), V_s is the interaction potential between the electron at S shell and outer shell electrons. Therefore the binding energy of the electron at S shell is given by

$$I_s = \frac{Z_s^2 R_\infty}{n^2} - V_s \tag{2.23}$$

It is convenient to express equation (2.21) and the form factor in equation (2.22) using dimensionless parameters. Here we introduce the screening parameter in equation (2.3) as

$$\theta_s = \frac{n^2 I_s}{Z_s^2 R_\infty} \tag{2.24}$$

Note that if there is no screening $V_s = 0$, and from equation (2.23) and equation (2.24) $\theta_s = 1$. The continuous wave function of the ejected electron can be characterized by the wave number K of the hydrogenic wave functions such that

$$T - V_s = \frac{\hbar^2 K^2}{2m} \tag{2.25}$$

Where T is the kinetic energy of the electron at infinity. The energy transferred ϵ is consumed to compensate the binding energy and the available energy appears as a kinetic energy. From equation (2.23) and equation (2.25) one obtains the energy

transferred to the electron as

$$\epsilon = T + I_s = \frac{\hbar^2 K^2}{2m} + \frac{Z_s^2 R_\infty}{n^2} \tag{2.26}$$

Now one can introduce another set of dimensionless parameters to scale the cross section

$$W = \epsilon/(Z_s^2 R_\infty) \quad ; \quad k = a_s K \quad ; \quad Q = a_s^2 q^2/Z_s^2 \tag{2.27}$$

Where $a_s = a_o/Z_s$ (a_o is Bohr radius). Equation (2.26) now appears as

$$W = k^2 + \frac{1}{n^2} \tag{2.28}$$

Therefore if a hydrogenic wave functions are employed, then the cross section in equation (2.21) and the form factor in equation (2.22) can be expressed as a homogeneous function of k, Q, and W. Thus equation (2.21) becomes

$$\sigma_s = 4\pi z^2 g_{j_s} \left(\frac{e^2}{\hbar v_i}\right)^2 \frac{a_o^2}{Z_s^2} \int_{W_{\min}}^{W_{\max}} dW \int_{Q_{\min}}^{Q_{\max}} \frac{dQ}{Q^2} |F_{SW}(Q)|^2 \tag{2.29}$$

Introducing the S shell reduced velocity parameter η_s, given in equation (2.6), in another form as

$$\eta_s = \left(\frac{v_i}{v_s}\right)^2 = \frac{m_e E}{M Z_s^2 R_\infty} = \left(\frac{\hbar v}{Z_s e^2}\right)^2 \tag{2.30}$$

Substituting in equation (2.29), the S shell ionization cross section becomes

$$\sigma_s = \frac{4\pi z^2 a_o^2 g_{j_s}}{Z_s^4 \eta_s} f_s(\eta_s, \theta_s) \tag{2.31}$$

where $f_s(\eta_s, \theta_s)$ called reduced universal cross section, is given by

$$f_s(\eta_s, \theta_s) = \int_{W_{\min}}^{W_{\max}} dW \int_{Q_{\min}}^{Q_{\max}} \frac{dQ}{Q^2} |F_{SW}(Q)|^2 \tag{2.32}$$

Introducing another form $F_s(\eta_s/\theta_s, \theta_s)$ given by

$$F_s(\frac{\eta_s}{\theta_s}, \theta_s) = \frac{\theta_s}{\eta_s} f_s(\eta_s, \theta_s)$$

and

$$\sigma_{os} = \frac{4\pi z^2 a_o^2 g_{j_s}}{Z_s^4}$$

Hence a popular formula of σ_s is given by

$$\sigma_s = \sigma_{os}\theta_s^{-1} F_s(\frac{\eta_s}{\theta_s}, \theta_s)$$

The maximum and minimum energy transfer are obtained from equation (2.19) as

$$q_{\text{min}}^{\text{max}} = \frac{\sqrt{2mE}}{\hbar} \pm \frac{\sqrt{2m(E-\epsilon)}}{\hbar} = \frac{\sqrt{2m}}{\hbar}(\sqrt{E} \pm \sqrt{E-\epsilon})$$

or

$$q_{\text{min}}^{\text{max}} = \frac{\sqrt{2mE}}{\hbar}\left(1 \pm \sqrt{1-\frac{\epsilon}{E}}\right) \tag{2.33}$$

Since $\epsilon \ll E$, one can expand $\sqrt{1-\frac{\epsilon}{E}} \approx 1 - \frac{\epsilon}{2E}$, Therefore

$$q_{\text{max}} = \frac{\sqrt{8mE}}{\hbar}\left(1 - \frac{\epsilon}{4E}\right) \approx \frac{\sqrt{8mE}}{\hbar} \tag{2.34}$$

And

$$q_{\text{min}} = \frac{\sqrt{8mE}}{\hbar}\frac{\epsilon}{2E} \approx \sqrt{\frac{m\epsilon^2}{2E\hbar^2}} \tag{2.35}$$

Thus Q_{min} can be obtained using equation (2.35)

$$Q_{\text{min}} = \frac{W^2}{4\eta_s} \tag{2.36}$$

Whereas one can set $Q_{\text{max}} = \infty$. In order to obtain W_{min}, one must note that for minimum energy transfer the kinetic energy of the ejected electron is zero. Therefore,

from equation (2.26), $\epsilon = I_s$. Using equation (2.24) and equation (2.28) $W_{\min}$ is given by

$$W_{\min} = \frac{\theta_s}{n^2} \tag{2.37}$$

So $f_s(\eta_s, \theta_s)$ becomes as

$$f_s(\eta_s, \theta_s) = \int_{W_{\min}}^{\infty} dW \int_{Q_{\min}}^{\infty} \frac{dQ}{Q^2} |F_{SW}(Q)|^2$$

An explicit expressions for the form factor for both K and L shell as a function of Q and k were obtained by BETHE and WALSKE[4] using non-relativistic wave functions.

A comparison between the theoretical and the experimental values has been made for ionization by proton bombardment. The experimental calculations involve determination of X-ray production after subtracting the contribution of the background and correcting for Auger effect by dividing by the fluorescence yield. Figure (2-3) shows the calculated (solid line) and estimated (points) K- shell ionization cross section by protons for various elements Ni, Ag, Ta, and Pb, at all possible screening parameters[4]. They exhibit good agreement at low η_K. while for L shell, the ionization cross sections for Ta, Au, Pb, and U by protons are shown in figure(2-4). Unlike the K Shell, somehow considerable deviation is observed. In figure(2-5) the universal cross section is illustrated using the approach[4]

$$f_K(\eta_K, \theta_K) \approx \theta_K f_K(\frac{\eta_K}{\theta_K^2}, 1)$$

Thus from equation (2.31)

$$\frac{\theta_K Z_K^4 \sigma_K}{z^2} \approx 8\pi a_o^2 \frac{\theta_K^2}{\eta_K} f_K(\frac{\eta_K}{\theta_K^2}, 1)$$

so that $(\theta_K Z_K^4 \sigma_K)/z^2$ is common function of the variable η_K/θ_K^2. Note that for K shell, $g_{jK} = 2$. The left hand side has to be independent of Z. The general trend of the calculated values agrees with the estimated ones. However when $\frac{\eta_K}{\theta_K^2} \rightarrow 1$, the deviation

becomes appreciably large. Additionally, the dependence of the cross section on the type of the projectile appears as $\sigma_s \propto z^2$ only, which is called the scaling law.

By means of this approximation (*PWBA*), KHANDELWAL *et al.*[40] and CHOI *et al.*[41] published the ionization cross section by proton and α-particle impact versus the scaled parameters. Latter, BENKA and KROPF[42] estimated the cross section at the exact integration limits in equation (2.29) or equation (2.32), for both energy and momentum transfer parameters. The minimum energy transfer $W_{\min}$ is similar to that in equation (2.37), but instead of setting $W_{\max} = \infty$, they found that[42]

$$W_{\max} = \left(\frac{M}{m}\right)\eta_s \tag{2.38}$$

Here M and m are the mass of the projectile and the electron,respectively. In case of momentum transfer parameter Q, the exact values of $q_{\max}$ and $q_{\min}$ in equation (2.33) are employed instead of using approximations in equation (2.34) and equation (2.35). Thus one can directly obtain the exact values of $Q_{\min}$ and $Q_{\max}$ as[42]

$$Q_{\min}^{\max} = \left(\frac{M}{m}\right)^2 \eta_s \left[1 \pm \left(1 - \frac{m}{M}\frac{W}{\eta_s}\right)^{\frac{1}{2}}\right]^2 \tag{2.39}$$

Excluding the relative coordinate system. Unlike the previous approximation, the cross section here with the exact integration limits is not universal for different projectiles because of the explicit dependence of $W_{\max}$, $Q_{\max}$, and $Q_{\min}$ on the mass of the projectile.

Considering the atomic fine structure, a separate expressions of the form factors for L_1, L_2, and L_3 subshells are provided instead of total L-shell form factor[40, 41, 42]. The K-shell and L-subshell ionization cross-section values for proton impact, calculated by BENKA and KROPF[42] using the exact integration limits for momentum and energy transfer, agree with those values calculated by KHANDELWAL *et al.*[40] and CHOI *et al.*[41], who utilized the approximate integration limits in their calculations, within

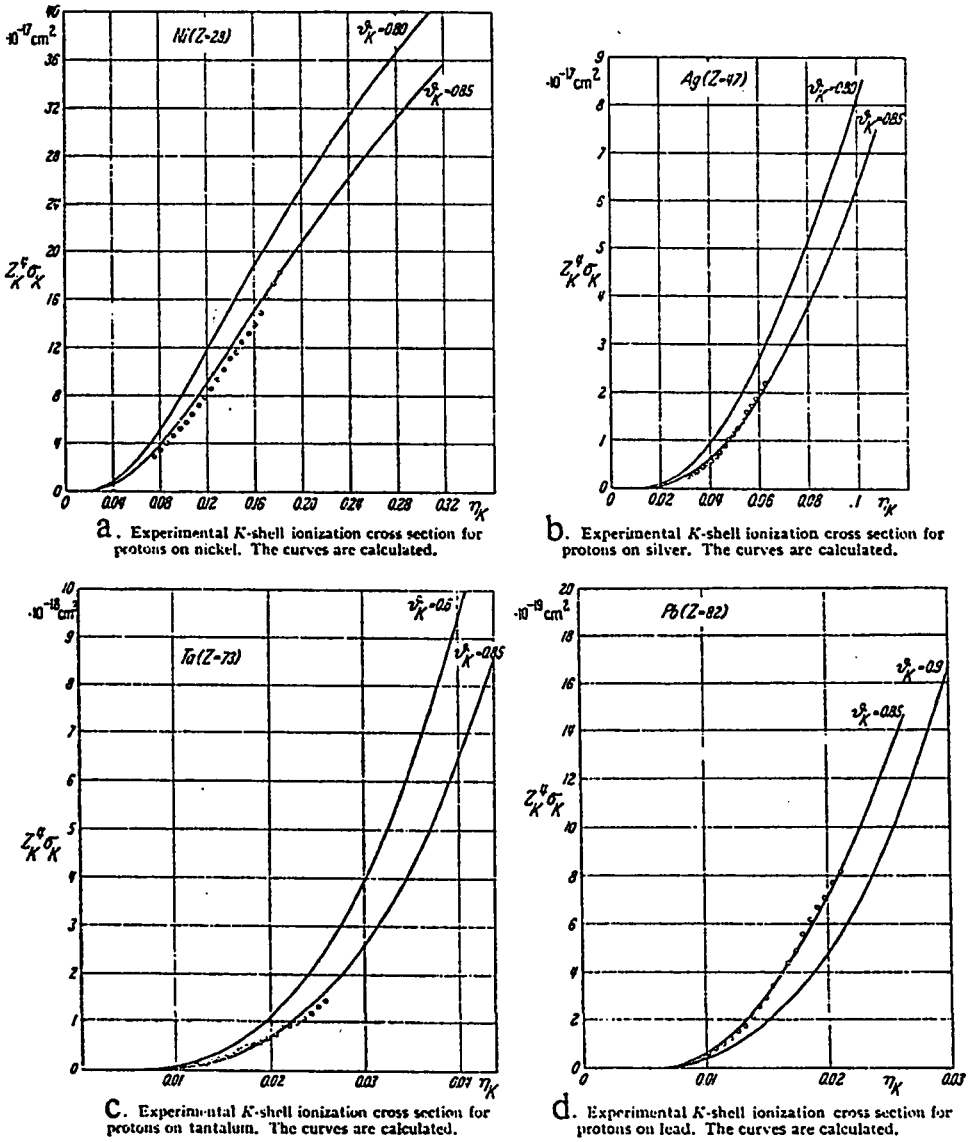

a. Experimental K-shell ionization cross section for protons on nickel. The curves are calculated.

b. Experimental K-shell ionization cross section for protons on silver. The curves are calculated.

c. Experimental K-shell ionization cross section for protons on tantalum. The curves are calculated.

d. Experimental K-shell ionization cross section for protons on lead. The curves are calculated.

Figure 2-3: The experimental K-shell ionization cross section for protons on (a) nickle, (b) silver, (c) tantalum, (d) lead. The curve is calculated. (Taken from MERZBACHER & LEWIS, 1958.)

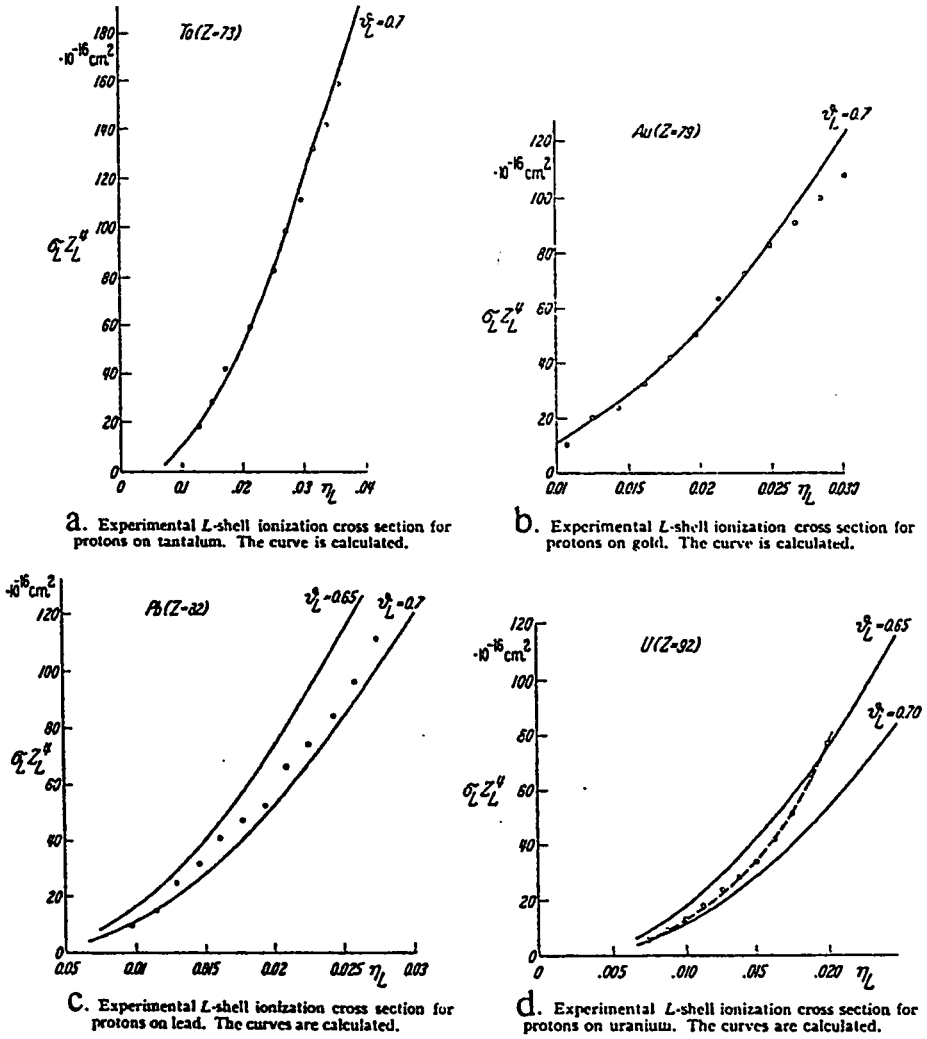

a. Experimental L-shell ionization cross section for protons on tantalum. The curve is calculated.

b. Experimental L-shell ionization cross section for protons on gold. The curve is calculated.

c. Experimental L-shell ionization cross section for protons on lead. The curves are calculated.

d. Experimental L-shell ionization cross section for protons on uranium. The curves are calculated.

Figure 2-4: The experimental L-shell ionization cross section for protons on (a) tantalum, (b) gold, (c) lead, (d) uranium. The curve is calculated. (Taken from MERZBACHER & LEWIS, 1958.)

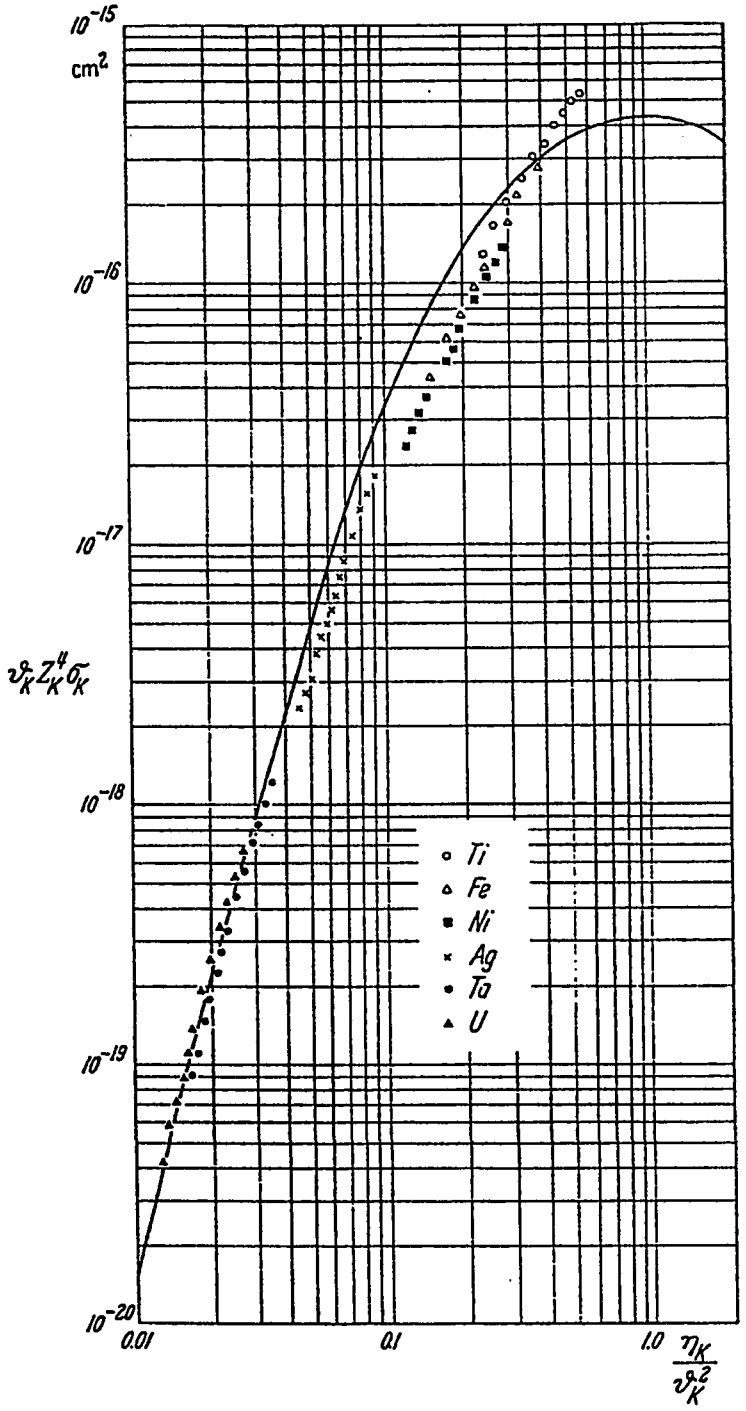

Figure 2-5: Composite graph of experimental and calculated K-shell ionization cross section. (Taken from MERZBACHER & LEWIS, 1958.)

$\pm 0.5\%$ for K shell and $\pm 1\%$ for L subshells when $\eta > 0.1$ for all targets. However, at low incident energy of protons, the cross sections when estimated at exact integration limits became significantly smaller than those calculated by approximate limits[42]. The exact-limit cross sections are comparable with the experimental values.

The *PWBA* provides a flexible frame work for further modifications. For instance the condition (2.10) is insufficient to ignore the Coulomb deflection effect, especially for projectiles whose charge is greater than protons. Moreover the electronic cloud polarization by the projectile's Coulomb field and its perturbational consequences must be accounted in the calculations.

2.2.2 Semi-Classical Approximation (SCA)

The *SCA* method was introduced with the aim to study the effects of projectile deflection and deceleration in atomic Coulomb excitation by assuming classical projectile trajectories and entering the classical impact parameter b into the formalism. The ionization probability may be defined as:

$$I(\theta_{proj}, E_1) = \frac{\text{Ionization cross section}}{\text{Scattering cross section}} = \frac{d\sigma_{ion}/d\Omega_{proj}}{d\sigma_{scatt}/d\Omega_{proj}} \tag{2.40}$$

where θ_{proj} and E_1 denote the projectile scattering angle and energy, respectively. The decisive parameter may be written as the ratio of two lengths[43]

$$k = \frac{4\pi d}{\lambda} = \frac{2Z_1 Z_2 e^2}{\hbar v_1} \gg 1 \tag{2.41}$$

where $d = Z_1 Z_2 e^2/(M_1 v_1^2)$ is half the distance of closest approach in a head-on collision. Z_1 and Z_2 are the atomic numbers of the projectile and target atoms, respectively and v_1 is the initial velocity of the projectile. The *SCA* model is characterized by the following conditions[43]:

1. The center of force, in this case is a point change moving along a classical trajectory. This is illustrated in figure (2-6).

2. Only a single active electron is considered in this approximation.

3. The electronic states are represented by a hydrogen-like wave function.

4. The threshold ionization energy is substituted by the experimental binding energy.

Quantum mechanically, the total electronic system is described by a set of Z_2-electron states

$$H_{el}(Z_2)\psi_k(r_1, r_2, \ldots, r_{Z_2}) = E_k\psi_k(r_1, r_2, \ldots, r_{Z_2}) \tag{2.42}$$

The perturbation is induced by a bare charged particle moving along a classical trajectory $\mathbf{R}_b(t)$ with respect to the target nucleus and it is represented by the potential:

$$V(t) = \sum_{l=1}^{Z_2} \frac{-Z_1 e^2}{|\mathbf{r}_l - \mathbf{R}_b(t)|} \tag{2.43}$$

The excitation amplitude, deduced from time-dependent perturbation theory is given by [43]

$$a_{fi} = -\frac{i}{\hbar}\int_{-\infty}^{\infty} dt e^{i(E_f - E_i)t/\hbar} \left\langle \psi_f \left| \sum_{l=1}^{Z_2} \frac{-Z_1 e^2}{|\mathbf{r}_l - \mathbf{R}_b(t)|} \right| \psi_i \right\rangle \tag{2.44}$$

The Z_2-electron wave function is assumed to be the asymmetrized sum of products of single-electron wave function "Slater determinant":

$$\psi_i = \frac{1}{\sqrt{Z_2!}} \sum_{permutation} (-1)^p \prod_i \phi_{\alpha_i}(\mathbf{r}_i) \tag{2.45}$$

where $\{\alpha_i\}_i$ a fixed set of occupied states. Limiting the discussion to use Slater-determinants for the function ψ_k in equation (2.42), the amplitude becomes exactly

$$a_{fi} = -\frac{i}{h}\int_{-\infty}^{\infty} dt e^{i\omega t}\left\langle \phi_f(\mathbf{r})\left|\frac{-Z_1 e^2}{|\mathbf{r}-\mathbf{R}_b(t)|}\right|\phi_i(\mathbf{r})\right\rangle \tag{2.46}$$

Where $\omega = (E_f - E_i)/\hbar$,the wave functions ϕ_f and ϕ_i are the one-electron states in the self-consistent field, as only single-electron excitation is possible in the first order theory (condition 2). This is true since KOOPMAN[44] justifies that the self-consistent fields are unchanged in the ground and excited states. The ionization cross section for projectile scattered through b and $b + db$ is given by:

$$\sigma_s = 2\pi\int_0^{\infty} bI(b)db \tag{2.47}$$

Where $I(b)$ is the ionization probability given by

$$I(b) = \int_0^{E_{\max}} dE_f \frac{dI(b)}{dE_f} \tag{2.48}$$

And

$$\frac{dI(b)}{dE_f} = |a_{fi}(t\to\infty)|^2 \tag{2.49}$$

The relation between scattering angle and impact parameter in the Coulomb potential is[26]

$$\sin\frac{\theta_{proj}}{2} = \frac{d}{\sqrt{d^2+b^2}} \tag{2.50}$$

The problem remains in evaluating equation (2.46). The main advantage of hydrogen-like wave functions is that they are represented by a well known analytical expressions, while the more realistic description is based on numerical procedures[43]. The proper screened charge of the target nucleus in the hydrogen-like wave function must be used as expressed in equation (1.4) and equation (1.5). The continuum states (final state) is much more complex since there are an ionized atom and an ejected electron. However,

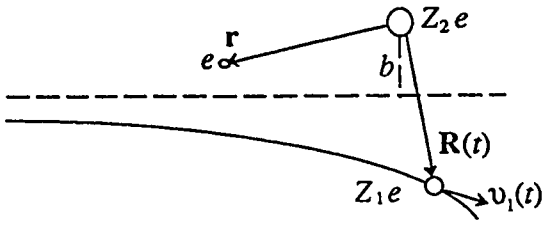

Figure 2-6: Classical picture of the bare nucleus-atom collision.

for the continuum electron, one can make use of a screened Coulomb wave function, normalized to one electron, given by[45]

$$\psi_{\infty l} = \sqrt{\frac{m}{\hbar}}\frac{2^{l+1}}{(2l+1)}e^{\pi Z_s^*/2\kappa}\kappa^{l+\frac{1}{2}}\left|\Gamma(l+1+\frac{iZ_s^*}{\kappa})\right|r^l e^{i\kappa r}$$

$$\times_1 F_1(l+1+\frac{iZ_s^*}{\kappa};2l+2;2i\kappa r)Y_{lm}(\theta,\phi) \qquad (2.51)$$

Here, ${}_1F_1(a;b;c)$ is the confluent hypergeometric function, κ is the wave number of the ejected electron, l is the orbital angular momentum quantum number of the ejected electron. Z^* is the effective charge.

To evaluate the amplitude in equation (2.46), there are two well-known methods to obtain separation between projectile (time) and electronic coordinates They are as follows:

1. Make use of multiple expansion in spherical polar coordinates

$$\frac{1}{|\mathbf{r}-\mathbf{R}|} = \sum_{L,M}\frac{4\pi}{2L+1}Y_L^{M*}(\hat{\mathbf{R}})Y_L^M(\hat{\mathbf{r}})\begin{cases}\frac{r^L}{R^{L+1}}, & r<R\\ \\ \frac{R^L}{r^{L+1}} & r>R\end{cases}$$

Where $\hat{\mathbf{R}}$ and $\hat{\mathbf{r}}$ represents the spherical polar coordinates for projectiles and electron in a coordinate from whose origin is the target nucleus. This method is called *the Coordinate Space formulation*[43].

2. The second method is based on the Fourier transform of the Coulomb interaction, i.e.

$$\frac{1}{|\mathbf{r}-\mathbf{R}|} = \frac{1}{2\pi^2}\int \frac{d^3q}{q^2} e^{i\mathbf{q}\cdot(\mathbf{r}-\mathbf{R})} \tag{2.52}$$

This is called Bethe integral[43]. For obvious reasons, this method is called momentum space approach[43]. Using this approach, the analysis become very close to *PWBA*. In fact, this approach demonstrates how the *SCA* may be viewed as a limit to the *PWBA*. The form factor in equation (2-20) can be evaluated over the transferred momentum space coordinates if the wave function is expressed by hydrogenic wave function.

Both approaches have been extensively used. One of the advantages of *SCA* is its flexibility, since one can utilize different classical trajectories, such as straight lines or hyperbola. Moreover, one can incorporate relativistic wave functions in the calculations. It is found by KOCBACH[43] that the major contribution to the ionization cross section corresponds to very small scattering angles. Therefore, the straight-line (constant velocity) *SCA* has been very useful for many purposes. Straight-line trajectory implies that the deflection of the projectile by the Coulomb field of the target nucleus is neglected. The evaluation of projectile factor is very simple for such trajectories since the scattering angle is very small. From equation (2.50), $\theta_{proj} \approx 2d/\sqrt{d^2+b^2}$. The total cross sections for straight-line trajectory, using momentum space approach is given by[43]

$$\frac{d\sigma}{dE_f} = 8\pi \frac{Z_1^2 e^4}{\hbar^2}\frac{M_1}{E_1}\int_q \frac{dq}{q^3}\sum_L (2L+1)\left|F_{fi}^L(q)\right|^2 \tag{2.53}$$

which are equivalent to those obtained from *PWBA* when of course identical wave functions are used in the two approximations.

2.2.3 Binary Encounter (Impulse) Approximation (BEA)

In this approximation, the viewpoint taken is that the dominant interaction producing the transition is a direct energy exchange between the incident charged particle and

bound electron. The role of the nucleus of the target atom is simply that of establishing the momentum distribution of the electron. The collision is thus viewed as the collision of the incident particle, momentum $\mathbf{k}_1$, with a free electron of momentum $\mathbf{k}_2$. The term binary Encounter Approximation (*BEA*) arises from this step. The cross section is then summed over all momentum exchange $\mathbf{q} = \mathbf{k}_1 - \mathbf{k}_2$, compatible with an energy exchange ϵ. This result is integrated over all allowed energy exchanges, and finally weighted by the distribution of electron momenta associated with the bound states[39, 46]. The form of impulse approximation which has been applied corresponds to a "restricted" impulse approximation, since momentum and energy conservation have been required in the binary encounter between the incident particle and the electron[46].

Recalling that the exact quantum mechanical expression for the collision of two free charged particles is identical to the classical result, thus all steps in the above procedure, except the determination of the distribution of the initial bound electron momenta, can be carried out classically. The cross section for incident particle with velocity v_1 is given by[46]

$$\sigma_I(v_1) = N_i \int_0^\infty \sigma_i^s(v_1, v_2) P(v_2) dv_2 \tag{2.54}$$

Where $P(v_2)$ is the speed (momentum) distribution of the bound electrons, N_i is the number of equivalent electrons having binding energy I, and

$$\sigma_i^s = \int_{I_s}^{E_1} \frac{d\sigma}{d\epsilon} d\epsilon \tag{2.55}$$

The integration in equation (2.55) is obtained in closed form by GARCIA[39]. This model has also been modified to approximate the nuclear repulsion effect on the incident particle. If hydrogenic velocity distributions are used in equation (2.54), the results have been shown to obey a scaling law, and a universal behaviour is obtained for the cross section as a function of the incident energy expressed in units of the binding

energy i.e.,

$$I_s^2\sigma_I = Z_1^2 f(\frac{E_1}{\lambda I_s}, \lambda) \tag{2.56}$$

Where Z_1 is charge of the incident particle, $\lambda = M_1/m_e$. Accordingly, a plot of $I_s^2\sigma_I/Z_1^2$ versus $E_1/\lambda I_s$ should yield the same results for all target atoms. These are to be compared to the Born scaling factors η and θ defined in equation (2.30) and equation (2.24). One can note that

$$\theta_K^2(Z_K^4\sigma_K/Z_1^2) = I_K^2\sigma_K/Z_1^2 \tag{2.57}$$

and

$$\eta_K/\theta_K = (m_e/M_1)(E_1/I_K) = \frac{E}{\lambda I_K} \tag{2.58}$$

A general comparison of *PWBA* and *BEA* with experimental *K*-shell X-ray cross section by proton impact is shown in figure (2-7). The dashed curve represents the *PWBA* predictions, solid curve represents *BEA* predictions, and the points represents the experimental measurements. The figure shows that the cross section of *BEA*, as well as that of *PWBA*, reaches its maximum when $E = I_K(M/m)$, which is being proved experimentally from the general tendency of the experimental points in the figure. However, the *BEA* predictions are closer to the experimental points than the *PWBA* predictions when $(E/I_K)(m/M) < 0.2$. Whereas the *PWBA* being closer for $(E/I_K)(m/M) > 0.2$. This is referred to the basic assumption of the *PWBA*, that is the interaction between the incident particle and the atom is weak and can be treated as a perturbation as justified by equation (2.9). This assumption breaks down at low velocities since the condition in equation (2.9) does not hold at low velocities. On the other hand, the *BEA* treats this interaction exactly in the sense that the bound electron is viewed as a free particle of definite momentum, scattering with incident particle. GARCIA *et al.*[39] stated that the adiabatic "relaxation" and polarization of the remaining electrons during the ionization must be taken into account in the *PWBA* description. For high velocity incident particles and high-Z target atoms this relaxation is likely to be

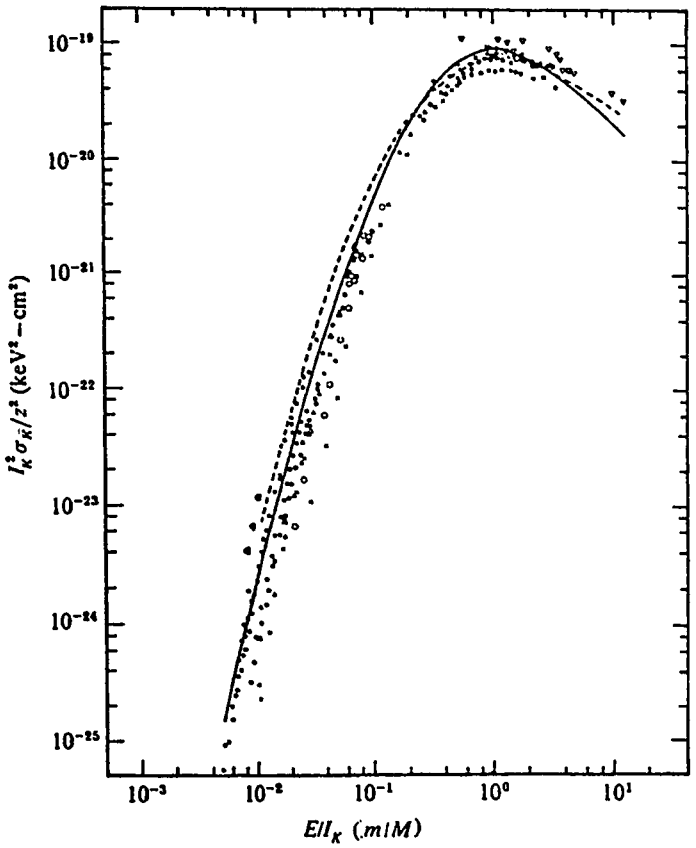

Figure 2-7: Cross sections for inner-shell ionization as a function of $(E/I_K)(m/M)$. (Taken from GARCIA *et al.*, 1973.)

unimportant for K-shell ionization, but may not be the case for L shells [46]. A proper theoretical framework for these adiabatic changes could be obtained by starting with a perturbed stationary state (*PSS*) method. The *BEA* gives the same tendency for K-shell ionization by α-particle impact, but near the peak of the curve the α-particle data tend to lie above the *BEA* prediction, whereas the proton data tended to be below this curve. In fact the α-particle data lie within 20% of the theory[46].

For L-shell measurements, the complicated structure (three subshells) of the L shell as compared to K-shell makes comparison with theory slightly more difficult. The comparisons are made in term of the reduced parameters $I_L^2\sigma_L/Z_1^2$ versus $E/I_L(m/M)$. Figure (2-8) shows such comparison a number of elements. The behaviour here is

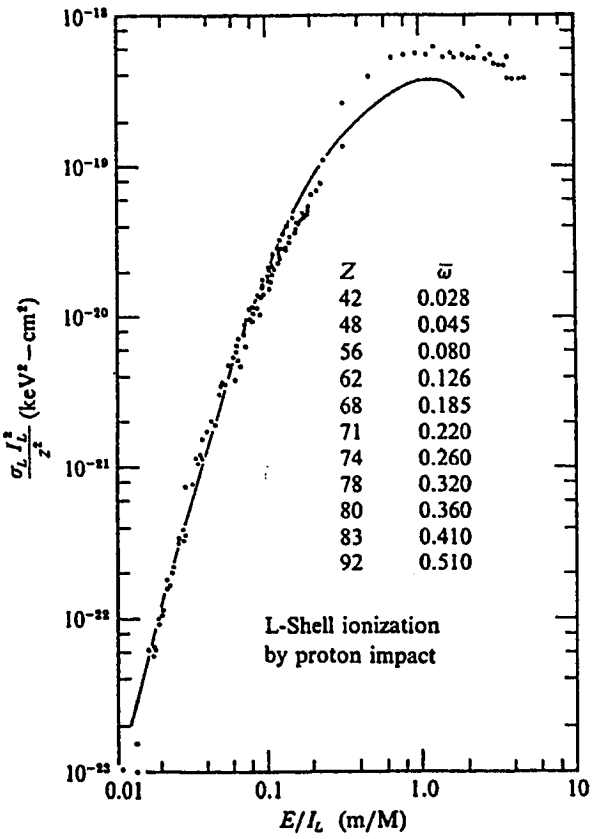

Figure 2-8: Total L-shell ionization cross section by proton impact as a function of $(E/I_L)(m/M)$. (Taken from GARCIA *et al.*, 1973.)

similar to that of the K-shell data. The *BEA* curve is identical to that in figure (2-7), but multiplied by four, which is the ratio of total number of electrons in L shell to the total number of electrons in K shell. Unlike figure(2-7), the *BEA* curve lies below the experimental data in figure (2-8) . The deviation between the *BEA* theory and experimental data near the threshold to fast collision region as shown in figure (2-8).

The deviation between the *BEA* theory and experiments is referred to the electronic velocity distribution, which is not the same for s states as for p states[46]. The *PWBA* approximation provides the best simple theoretical framework for describing these events. *BEA* is a simpler model and provides simple expression and scaling laws, but it is less flexible as a general framework. In addition, there are attempts to employ

the impulse approximation to evaluate the electron-electron excitation and ionization in energetic ion-atom collisions[47, 48]. In short, the *PWBA* approach seems to be the promissing one provided that some corrections are introduced on the theory. Thses corrections are disscussed next.

2.2.4 Relativistic Effect in Ion-Atom Collision

In *PWBA* the target atom is represented by a product of screened-hydrogenic (SH) wave functions as shown in equation (2.45). There is spacious evidence that products of single-electron wave functions, specifically of SH wave functions, give K-shell ionization cross section that agree within a few percent with those calculated based on Hartree-Slater-Dirac (HSD) wave functions[49]. The product of single electron wave functions also appears to suffice for the calculation of L-shell cross sections, although differential cross sections based on SH wave functions were found to be larger by a factor of 2-5 than those calculated with HSD wave functions at small energy transfer[50] corresponding to high projectile velocities (cf. equation (2.2)) or large impact parameters where deviations from the calculations based on SH wave functions can be expected. BRANDT and LAPICKI[49] pointed out that the integrated cross sections, for Al^{13} bombarded by protons, differ by no more than $\sim$ 35%. Also the variation due to the choice of the wave functions diminishes rapidly with increasing Z_2, as it is illustrated in figure (2-9) for proton bombardment. Moreover, electron correlations, which are not included in HSD approach tend to close the gap between calculations with HSD and SH wave functions[49].

Many approximations were adopted in order to incorporate the relativistic effect. However, such approximate methods are inadequate since they mimic the relativistic effects by a change of the average quantities that characterize inner shells. Such approaches can reproduce numerical calculations with relativistic wave functions only when $v_1 \simeq v_{2s}$ and the impact parameter b is comparable to a_{2s}[49].

When ionization takes place deep inside the inner shell, the relativistic effect can

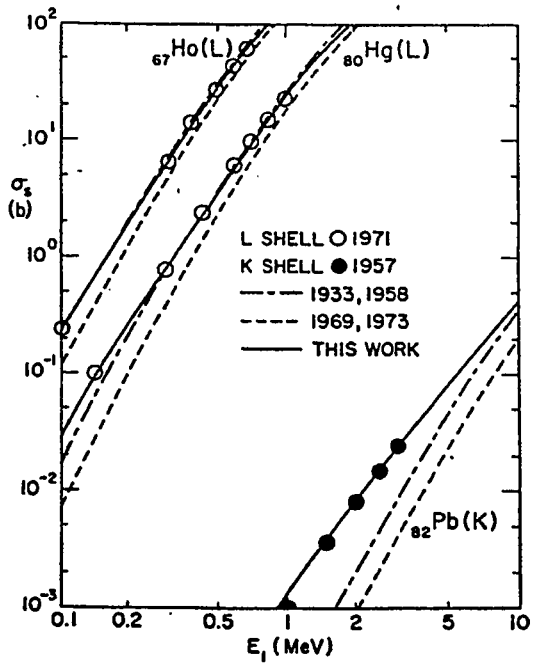

Figure 2-9: Calculated K-shell and L-shell ionization cross section in *PWBA* with relativistic wave functions for the indicated elements (circles) and with non-relativistic wave functions (dashed lines). The solid lines represent the *PWBA* corrected for relativistic effects as given in equation (2.65). (Taken from BRANDT and LAPICKI, 1979.)

become significant even for L shell of light atoms. A relativistic change in the binding energy, the mean velocity, or the electronic orbital radius, confoundedly under estimates this effect. In *SCA*, the relativistic effect correction was based on the observation that the effect has its origin mainly in the replacement of the bound state $\sim e^{-r}$ by the Dirac radial part $\sim r^{\gamma-1}e^{-r}$, where $\gamma^2 = 1-(Z_2/137)^2$. This is due to the relativistic increase of mass which leads to a change in momentum[43]. For *BEA*, the relativistic correction is based on approximating the relativistic electron-momentum distribution to obtain the relativistic ionization cross section σ^R and hence calculate the ratio σ_s^R/σ_s^{NR}. However, this method is not possible in the *PWBA*. The relativistic effect in *PWBA* can be taken into account by evaluating the relativistic relative velocity of the projectile, given by[51]

$$v_1 = \frac{1}{\alpha}\sqrt{1-\frac{1}{(1+E_1/M_1c^2)^2}} \tag{2.59}$$

Where v_1 is given in atomic units, α is the fine structure constant. The relativistic electron mass calculated by BRANDT and LAPICKI[49] is given by

$$m_s^R(\xi_s) = \int_0^\infty m^R(\alpha b)W_s(bq_{os})bq_{os}d(bq_{os}) \tag{2.60}$$

Where q_{os} is minimum momentum transfer, b denotes the impact parameter, W_s is weight function derived strictly in the slow collision limit ($\xi_s \ll 1$) but it is still valid for fast collision regime. $m^R(x)$ is given by

$$m^R(x) = [1+(Z_{2s}/2xc^2)^2]^{\frac{1}{2}} + Z_{2s}/2xc^2$$

Following equation (2.60), the relativistic target electron mass correction $m_s^R(\xi_s)$ is given by[49]

$$m_s^R(\xi_s) \simeq (1+\beta y_s^2)^{\frac{1}{2}} + y_s \tag{2.61}$$

Where β is slowly varying parameter. When $\beta = 1.1$, equation (2.61) agrees with the numerical integration of equation (2.60) to within 3 %[49]. The function y_s is given

by[49]

$$y_{K,L_1} = \frac{0.40(Z_{2s}/c)^2}{n\xi_{K,L_1}} \quad \text{and} \quad y_{L_2,L_3} = \frac{0.15(Z_{2L}/c^2)^2}{\xi_{L_2,L_3}} \tag{2.62}$$

The parameters ξ_s and η_s, must be corrected to be ξ_s^R and η_s^R, respectively. They are given by[49]

$$\xi_s^R = \left(m_s^R\right)^{\frac{1}{2}} \xi_s \tag{2.63}$$

$$\eta_s^R = m_s^R \eta_s \tag{2.64}$$

Thus, the cross section now is given by

$$\sigma_s^{PWBAR} = \sigma_s^{PWBA}(m_s^R \eta_s, \theta_s) \tag{2.65}$$

BRANDT and LAPICKI[49] indicated that the cross sections caculated using this procedure agree with those calculated using relativistic wave functions.

2.2.5 Polarization and Binding Effects

The calculations in section 2.2.1 were carried out under the assumption of fast collision events. These calculations do not account for the behaviour of the system at slow collision. Note that, as discussed in section 2.1, slow and fast collisions are defined relative to the ratio of the collision time to the response time of the electron in the target atom and they are represented by ξ_s as given in equation (2.5)[36, 52]. At fast collisions, $\xi_s \gg 1$, the collision time is shorter than the response time of the electron in the target atom, thus it does not react significantly due to the perturbational effect of the projectile. Whereas, when slow collisions are considered, $\xi_s \ll 1$, the situation is different, the electron response time is shorter or comparable to collision time, and hence the perturbational effects become more pronunciational. The effect appears as a polarization in the electronic cloud as the projectile approaches the target atom due to the Coulomb field of the projectile tends to make the electron more tightly bound during the collision.

The increased binding then reduces the probability of ionization. This effect increases with decreasing projectile velocity and lower target atomic number. Such a mechanism would explain the deviation from Z_1^2 scaling rule, following from first order Born approximation[43]. The Z_1^2 dependence is attributed to the dipole component $\propto R^{-2}$ of the projectile-electron interaction. However, as a consequence of the polarization effect, a quadruple component $\propto R^{-3}$ of the interaction polarizes the motion of the electron and gives rise to the Z_1^3 dependent term[49].

The polarization and binding correction is treated on the basis of the perturbed stationary-state approach (PSS)[53, 54]. The PSS is based on the expansion of the wave function into the basis of instantaneous eigenfunctions of the time dependent Hamiltonian. The detailed derivation is carried out by BRANDT and LAPICKI[49] and new corrections are obtained for the binding parameter θ_s and the reduced velocity ξ_s^R. The binding parameter θ_s is replaced by

$$\theta_s \rightarrow \theta_s \zeta_s \tag{2.66}$$

Where ζ_s is projectile velocity dependent function derived in the PSS theory, given by[49]

$$\zeta_s = 1 + \left(\frac{2Z_1}{Z_{2s}\theta_s}\right)(g_s - h_s) \tag{2.67}$$

where

$$g_s(\xi_s) = \frac{\sum_{i=0}^{8} a_n \xi_s^n}{(1+\xi_s)^{l+9}} \tag{2.68}$$

Where a_n's are coefficients shown in table (2.1) for K, L_1, L_2, and L_3 shells, l is the angular momentum quantum number for a given shell, $l = 0$ for K and L_1, and $l = 1$ for L_2 and L_3 subshells. h_s is given by[49]

$$h_s = \frac{2n}{\theta_s \xi_s^3} I\left(\frac{C_s n}{\xi_s}\right) \tag{2.69}$$

Where C_s is a cut-off parameter, which is the ratio p_s/a_{2s}, where p_s is the effective

polarizational impact parameter. The numerical values of C_s are

$$C_s = \begin{cases} 1.50 & \text{For } K \text{ and } L_1 \text{ shells} \\ 1.25 & \text{For } L_2 \text{ and } L_3 \text{ shells} \end{cases} \tag{2.70}$$

Defining $x = C_s n/\xi_s$, the function $I(x)$ is given by [55]

$$I(x) = \begin{cases} \frac{3}{4}\pi(\ln x^{-2} - 1) & \text{For } 0 < x \leq 0.035 \\ \exp(-2x)(0.031 + 0.21x^{\frac{1}{2}} + 0.005x & \\ -0.069x^{\frac{3}{2}} + 0.324x^2)^{-1} & \text{For } 0.035 < x \leq 3.1 \\ \frac{2\exp(-2x)}{x^{1.6}} & \text{For } 3.1 < x \leq 11 \\ 0 & \text{For } x > 11 \end{cases} \tag{2.71}$$

The change in binding energy is obtained from first-order perturbation theory, given by[51]

$$\langle \Delta I_s \rangle = \frac{2Z_1 I_s}{Z_{2s}\theta_s}[g_s - h_s] \tag{2.72}$$

In case of the reduced velocity parameter, the correction due to binding effect implies that ξ_s is replaced by[49]

$$\xi_s \rightarrow \xi_s/\zeta_s \tag{2.73}$$

However, ξ_s is replaced by ξ_s^R (equation(2.63)) due to the relativistic effect, thus ξ_s^R is given by

$$\xi_S^R = [m_s^R(\xi_s/\zeta_s)]^{\frac{1}{2}}\xi_s \tag{2.74}$$

Where $m_s^R(\xi_s/\zeta_s)$ is the relativistic electron mass correction, corrected for the binding effect, obtained in equation (2.61) and equation (2.62) after replacing ξ_s by ξ_s/ζ_s. The

Table 2.1: The coefficients a_n's for evaluating the function $g_s(\xi_s)$.

Coefficients	K shell	L_1 subshell	L_2 and L_3 subshell
a_0	1	1	1
a_1	9	9	10
a_2	31	31	45
a_3	98	49	102
a_4	12	162	331
a_5	25	63	6.7
a_6	4.2	18	58
a_7	0.515	1.97	7.8
a_8	0	0	0.888

cross section corrected for relativistic (R) and binding effect (PSS) is given by:

$$\sigma_s^{PSSR} = \sigma_s^{PWBA}\left([m_s^R(\xi_s/\zeta_s)]^{\frac{1}{2}}\xi_s, \zeta_s\theta_s\right). \tag{2.75}$$

2.2.6 Projectile Coulomb Deflection Correction (C)

In quantum-mechanical *PWBA* and *SCA*, the projectile is described, respectively, as a plane wave or as a classical particle moving along a straightline trajectory. These approximations become inadequate when the projectile moves so slowly that the plane wave is appreciably distorted by the Coulomb field of the target nucleus or the classical particle is significantly deflected into a hyperbolic trajectory[56]. In consequence, with decreasing ion velocity, the experimental cross sections for inner-shell vacancy in ion-atom impact become significantly smaller than theoretical predictions.

For *SCA*, a new deflection factor has been found by direct comparison of the straightline σ_{SL} and hyperbolic σ_{HYP} trajectory calculations[43]. The numerical factor has been approximated by ANHOLT[57] as

$$C_c(q_o d) = \frac{1}{0.22 + 0.78e^{1.9\pi q_o d}} \tag{2.76}$$

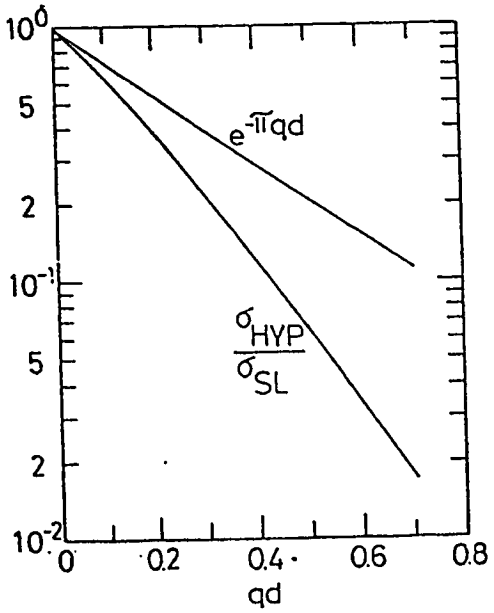

Figure 2-10: Coulomb trajectory correction factros for K-shell ionization cross sections. The quantities σ_{SL} and σ_{HYP} denote the cross sections for the straightline and hyperbolic trajectory case, respectively. (Taken from KOCBACH *et al.*, 1980.)

Figure (2-10) shows the ratio σ_{HYP}/σ_{SL} versus the dimensionless parameter $q_o d$ where q_o and d are the minimum momentum transfer and half-distance of closest approach, respectively. Note that the ratio is significantly large as $q_o d \rightarrow 0$.

For *PWBA*, the Coulomb deflection factor is derived quantum-mechanically out of the first Born approximation. The factor C_c in this case is given by[56]

$$C_c = \frac{\sigma^{CWBA}}{\sigma^{PWBA}} \tag{2.77}$$

Where *CWBA* indicates Coulomb-wave Born approximation. C_c has a universal character since it scales *PWBA* cross section to *CWBA* cross section for any inelastic collision. The cross section σ^{CWBA} involves Coulomb wave function instead of plane wave function, by adding a nuclear part $(Z_1 Z_2 e^2/R)$ to the unperturbed Hamiltonian

$$\left(\frac{-\hbar^2}{2m}\nabla_R^2 + \frac{Z_1 Z_2 e^2}{R}\right)\psi_{if}(\mathbf{R}) = E_{if}\psi_{if}(\mathbf{R}) \tag{2.78}$$

Where $\mathbf{R}$ is the coordinates of the projectile with respect to the target nucleus. Z_1 and Z_2 are the projectile and target nucleus atomic numbers, respectively, and $\psi_{if}(\mathbf{R})$ is the projectile distorted wave function. Note that the screening effect for internuclear interaction is neglected here. The transition amplitude is thus given by

$$a_{if} \propto \int\int \psi_f^*(\mathbf{R})\phi_f^*(\mathbf{r})V(\mathbf{r},\mathbf{R})\psi_i(\mathbf{R})\phi_i(\mathbf{r})d\mathbf{r}d\mathbf{R}$$

Where $V(\mathbf{r},\mathbf{R})$ is the perturbed potential given in equation (2.12). However, LAPICKI and LOSONSKY[56] indicated that since the Coulomb deflection effect becomes more pronounced at low velocities, it is possible to utilize the quantum mechanical Coulomb-deflection factor in the scaling of straight line semi-classical calculations. Following this treatment, C_c was given at low velocity limit, as a complicated combination of modified Bessel function of imaginary order and their derivatives, given as[49]

$$C_c(x) = \exp(-\pi x)\left\{x\left(\frac{dK_{ix}(y)}{dy}\right)_{y=x}\right\}^2 \tag{2.79}$$

Where $K_{ix}(y)$ is the Bessel function of imaginary order, $x = \tau dq_{os}$, and $\tau = 1 + T_f/I_{2s}$, where I_{2s} is the is the binding energy of the electron[2]. T_f denotes the final energy of the ejected electron. $q_{os} = I_{2s}/(v_1\hbar) = \omega_{2s}/v_1$ is minimum momentum transferred to shell S, and $d = Z_1Z_2e^2/(Mv_1^2)$ is the half distance of closest approach in a head-on collision with $M^{-1} = M_1^{-1} + M_2^{-1}$. Note that the parameter $q_{os}d$ is the ratio of the characteristic time in Coulomb scattering d/v_1 to the electronic transition time ($\approx \hbar/I_{2s} = \omega_{2s}^{-1}$) and thus measures the adiabaticity of the collision. At $x \ll 1$, equation (2.79) can be simplified to[49]

$$C_c(x) = \exp(-\pi x) \tag{2.80}$$

[2]In references [49] and [56], the binding energy I_{2s} is express by $\hbar\omega_{2s}$. Here ω_{2s} indicates the shell orbital frequency and ω_{2s}^{-1} denotes the electronic transition time. However, since atomic units (a.u.) is used in [49] and [56], thus $\hbar \equiv 1$ and hence $I_{2s} = \omega_{2s}$. In order to purge confusion, one can just change I_{2s} by ω_{2s}.

When $T_f \ll I_{2s}$ then $\tau \to 0$ and hence $x = dq_{os}$, therefore $C_c = \exp(-\pi dq_{os})$, which is the same expression that was proposed in *SCA*[43].

Equation (2.79) or equation (2.80) do not account for the Coulomb deflection factor for all possible energy transfer. Therefore, C_c must be integrated overall values of τ. Note that when $T_f \to 0$, $\tau \to 1$. It is known that $T_f^{\max} \simeq \frac{4m_e}{M_1}E_1$, however, it is possible to set $\tau \to \infty$ as an upper limit. It is confirmed from equation (2.53) that the differential cross section for straight line trajectory is proportional to $\left(\frac{1}{q_{os}\tau}\right)^{10+2l}$[49], thus in the slow collision limit, the Coulomb deflection factor for ionization of an S Shell becomes[49]

$$C_s^c(q_{os}d) = \int_1^\infty \frac{C_c(\tau dq_{os})}{\tau^{10+2l}} d\tau$$

The integral yields[49]

$$C_s^c(q_{os}d) \simeq \frac{C_\gamma(dq_{os})}{1 + \gamma\pi dq_{os}/(9+2l)} \tag{2.81}$$

Where $\gamma = 1$ if $C_\gamma(dq_{os})$ is given by equation (2.80) and $\gamma = 2$ if $C_\gamma(dq_{os})$ is given by equation (2.79).

BRANDT and LAPICKI[49] indicated that the Coulomb deflection factor when $\gamma = 1$ gives better agreement with experimental data than that when $\gamma = 2$, which implies that the Coulomb factor derived from equation (2.80) is more realistic than that derived from equation (2.79), although equation (2.80) being an approximation of equation (2.79). Adding this Coulomb deflection factor to the *PWBA* in equation (2.31); yields the *PWBAC* (Plane Wave Born Approximation corrected for Coulomb deflection)

$$\sigma^{PWBAC} = C_s^c(q_{os}d)\sigma^{PWBA} \tag{2.82}$$

If the Coulomb correction factor $C_s^c(q_{os}d)$ in equation (2.82) is incorporated in σ^{PSSR} as given by equation (2.75), a new expression denoted by σ_s^{CPSSR} is obtained

$$\sigma_s^{CPSSR} = C_s^c(q_{os}d\zeta_s)\sigma_s^{PWBA}([m_s^R(\xi_s/\zeta_s)]^{\frac{1}{2}}\xi_s, \zeta_s\theta_s) \tag{2.83}$$

Which expresses the ionization cross section calculated by *PWBA*, corrected for relativistic effect (R), the influence of the projectile on the electronic orbits using PSS theory, and the Coulomb deflection due to target nuclear field (C). BRANDT and LAPICKI[58] pointed out that the *CPSSR* theory applies to collision systems such that $Z_1/Z_2 \leq \frac{1}{2}\theta_s$. where θ_s reaches its minimum ($\simeq 0.4$) for L shell. Thus *CPSSR* theory is valid as long as $Z_1/Z_2 \leq 0.2$.

2.2.7 Projectile Energy-Loss Correction (E)

The *CPSSR* theory is tested by BRANDT and LAPICKI[58] with large body of experimental K and L-shell data that was available at that time for protons and deuterons. It was found that *CRSSR* theory agrees on the average within 30%. This scatter is attributed to the uncertainties in the measurements of fluorescence yield and Coster-Kroing transition probability to convert the production cross section to ionization cross section or vice versa.

Figure (2-11) displays some 2300 measured cross sections are inferred from K X-ray production cross sections for protons in target covering $10 \leq Z_2 \leq 92$. The ordinate gives the ratio of $\sigma_K^{\exp}/\sigma_K^{CPSSR}$. The Coulomb deflection factor in σ_K^{CPSSR} is calculated using equation (2.80) into equation (2.81), where $\gamma = 1$. The abscissa is given in units of $\zeta_K \Delta_K$, where Δ_K is minimum fractional energy loss of the projectile during K-shell ionization in the centre-of-mass system with reduced mass $M^{-1} = M_1^{-1} + M_2^{-1}$. The value of Δ_K is given by[58]

$$\Delta_K = \frac{\omega_{2K} M_1}{M E_1} \tag{2.84}$$

The upper scale in figure (2-11) gives the reduced velocity variable $\xi_K^R/\zeta_K \propto v_1$.

From the figure, the points scatter rarely by no more than a factor of two about the ideal value of one. Some 90% of the data agrees with the *CPSSR* prediction to within 30%[58]. The data approaches unity for $\xi_K > 1$, but falls systematically below the predictions when $\xi_K < 1$. BRANDT and LAPICKI attributed this trend to the finite

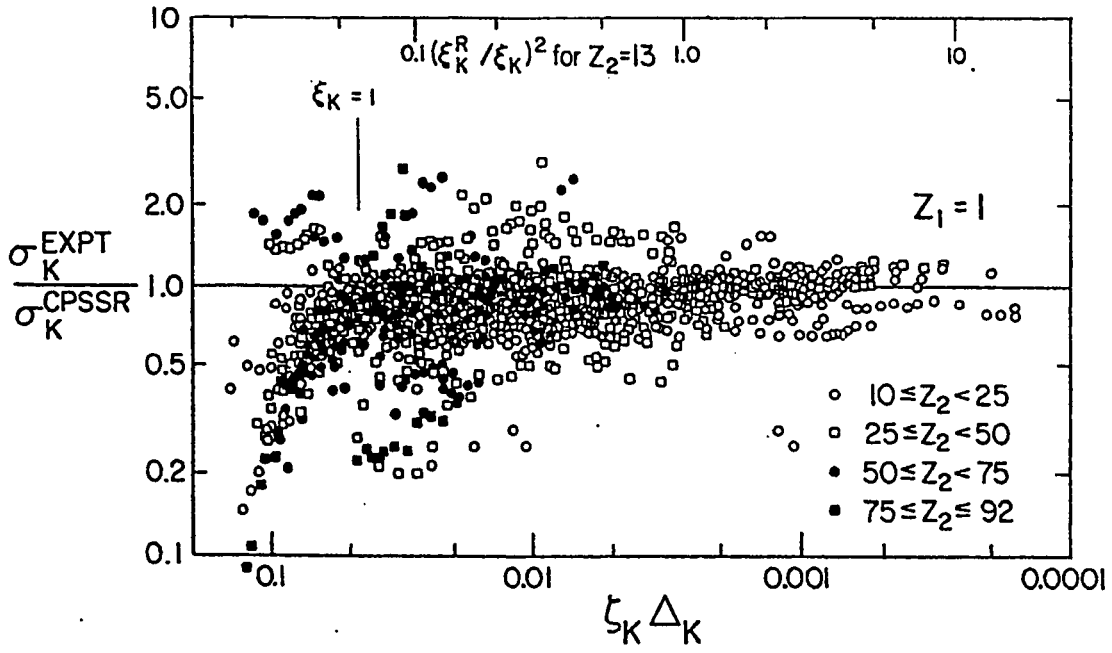

Figure 2-11: Ratios of experimental and theoritical cross sections for K-shell ionization by protons versus $\zeta_K \Delta_K$, the effective relative projectile energy loss. (Taken from BRANDT and LAPICKI, 1979.)

kinetic-energy loss suffered by the projectile in the inner-shell excitation process[58]. These calculations of BRANDT and LAPICKI[58] are based on the assumption that the energy transfer $\epsilon \ll E$, where E being the energy of the projectile. Thus the maximum and minimum momentum transfer in equation (2.33) are approximated and presented in equation (2.34) and equation (2.35) which included in the calculations. In fact it follows from equation (2.35) that

$$q_{\min} = \frac{\epsilon}{\hbar}\sqrt{\frac{m}{2E}} = \frac{\epsilon}{\hbar v} \tag{2.85}$$

Where $E = \frac{1}{2}mv^2$, is the projectile energy. Since the energy transferred ϵ is comparable to the binding energy for ejected electron in S shell, I_{2s}, thus one can replace ϵ by I_{2s} in equation (2.85), yields

$$\hbar q_{\min} \approx \frac{I_{2s}}{v} \tag{2.86}$$

Which is the same expression given by BASBAS *et al.*[36] in equation (2.2) and employed by BRANDT and LAPICKI[49, 56, 58] in their calculation of *CPSSR*.

However, the use of approximate integration limits in the cross section calculation yields reasonable calculations at high velocity projectiles since it involves small energy transfer i.e., the condition $\epsilon \ll E$ holds, and the minimum momentum transfer can be approximated, as shown in equation (2.34) to equation (2.35), with a disregarded small error. Nevertheless, this is not true at low velocity projectile (when $\xi_s \ll 1$) whereas the condition $\epsilon \ll E$ does not accurately meet the approximation requirements. This is verified by BENKA and KROPF[42] when they tabulate the *PWBA* cross sections by protons using the exact integration limits, as given in equation (2.38), and equation (2.39) in section 2.2.1, and compare them with the *PWBA* value calculated by KHANDELWAL *et al.*[40] and Choi *et al.*[41] using the approximate integration limits. It was found that the cross sections calculated using exact integration limits is roughly five times smaller than those calculated by approximate integration limits at low velocity and this difference falls rapidly until it diminishes at high velocity region. This is il-

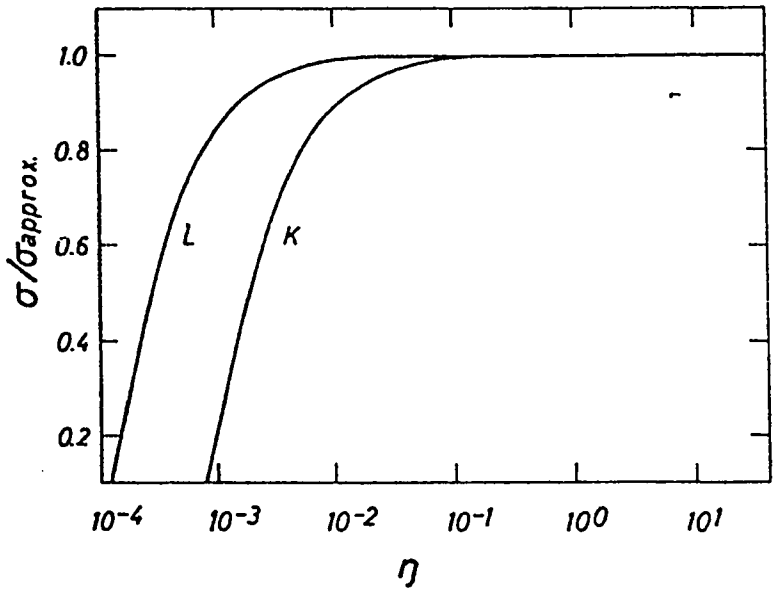

Figure 2-12: Ratio of *PWBA* values calculated for Cu K and L shells with exact limits for the minimum and maximum momentum transfer to those calculated with approximate limits. (Taken from BENKA and KROPF, 1978.)

lustrated in figure (2-12) which displays the ratio of *PWBA* cross sections calculated using exact integration limit by BENKA and KROPF[42] to those calculated using approximate integration limits by CHOI *et al.*[41] versus the reduced velocity parameter $\eta \propto v_1^2$ for Cu K and L shell. The previous discussion gives a consequent explanation for the departure of the experimental data points from theoretical predictions at low velocity region in figure (2-11) which has the same trend shown in figure (2-12), that strongly ensures the importance of energy loss effect and the meaning of using the exact integration limits especially at low energy regions.

Therefore BRANDT and LAPICKI[58] stated that, at slow collisions the relative projectile energy loss cannot be neglected, because at low projectile velocities the inelastic cross sections are inversely proportional to high powers of q. Specifically, the differential *PWBA* ionization cross section for direct ionization of the target shell S with regard to the final kinetic energy of the ejected electron, $T_f = \epsilon - I_{2s}$, takes a

simple analytical forms. When the energy-loss effect is included they can be written as[58]

$$\frac{d\sigma^{EPWBA}}{dT_f} = \frac{d\sigma^{PWBA}}{dT_f}\left[\left(\frac{q_o}{q_{\min}}\right)^{\nu+1} - \left(\frac{q_0}{q_{\max}}\right)^{\nu+1}\right] \tag{2.87}$$

where the letter E in the superscript signifies that the q integration was performed between the exact limits for $q_{\min}$ and $q_{\max}$, q_o denotes the approximated minimum momentum (when $\epsilon \ll E$) given in equation (2.86), and $\nu = 9 + 2l_2$, where l_2 is the angular momentum quantum number for the shell of interest, $l_2 = 0$ for K and L_1 shell, and $l_2 = 1$ for L_2 and L_3 subshell. Integrating equation (2.87) over all final states T_f yields the ionization cross section in closed form[58]

$$\sigma_s^{EPWBA} = f_s(z_s)\sigma_s^{PWBA} \tag{2.88}$$

With

$$z_s = \sqrt{1 - \frac{\theta_s}{n^2 M \eta_s}} \tag{2.89}$$

And[58]

$$f_s(x) = \frac{2^{-\nu}}{(\nu - 1)}\left[(\nu x - 1)(1 + x)^\nu + (\nu x + 1)(1 - x)^\nu\right] \tag{2.90}$$

where $\nu = 9 + 2l_2$. Upto this point, this development is exact[58].

The Coulomb deflection effect becomes important in reducing the ionization probability just in low-velocity range where also the energy-loss effect can diminish the ionization cross sections noticeably. The Coulomb deflection factor $C_s^c(q_{os})$ is obtained in section 2.2.6, equation (2.81), as a function of $q_{os}d$ where q_{os} is the same approximated momentum transfer used by BRANDT and LAPICKI in their treatment, given in equation (2.2). Thus the argument $q_{os}d$ of the Coulomb-deflection factor must be corrected in the presence of energy loss, the Coulomb deflection factor C_s^c therefore is changed by C_s^{EC} and given by[58]

$$C_s^{EC}\left(\frac{2q_{os}d}{z_s(1 + z_s)}\right) = \nu\varepsilon_{\nu+1}\left(\frac{2\pi q_{os}d}{z_s(1 + z_s)}\right) \tag{2.91}$$

Which corresponds to the choice $\gamma = 1$ in equation (2.81), $\varepsilon_m(y)$ is the exponential integral of order m given by

$$\varepsilon_m(y) = \int_1^\infty x^{-m} e^{-xy} dx$$

or

$$\varepsilon_m(y) = \frac{e^{-y}}{y+m}\left[1 + \frac{m}{(y+m)^2} + \frac{m(m-2y)}{(y+m)^4} + \frac{m(6y^2 - 8my + m^2)}{(y+m)^6} + \cdots\right]$$

Equation (2.91) is called the hyperbolic energy loss function and $f_s(z_s)$ in equation (2.89) and (2.90) is called the straight line energy-loss function, and they are combined in one equation given by[58]

$$f_s^{EC}(z_s, q_{os}d) = C_s^{EC}\left(\frac{2q_{os}d}{z_s(1+z_s)}\right) f_s(z_s)(1+\delta_s) \tag{2.92}$$

where δ_s is the error in the factorization[58].

2.2.8 The ECPSSR Theory

The *CPSSR* cross section for direct ionization of an S shell is given in equation (2.83). The effect of energy loss with Coulomb deflection factor in equation (2.92) must take into account the relativistic and perturbed stationary-state effects by replacing θ_s with $\zeta_s\theta_s$ and replacing η_s with $m_s^R(\xi_s/\zeta_s)\eta_s$ for z_s in equation (2.89). Therefore, the new parameter z_s is symbolized as z_s^R and given by[51, 58]

$$z_s^R = \sqrt{1 - \frac{\zeta_s\theta_s}{n^2 M m_s^R(\xi_s/\zeta_s)\eta_s}} = \sqrt{1 - \frac{4}{M\zeta_s\theta_s}\left(\frac{\zeta_s}{\xi_s}\right)^2 \frac{1}{m_s^R(\xi_s/\zeta_s)}} \tag{2.93}$$

Thus the Coulomb deflection factor in equation (2.91) becomes

$$C_s^{ECPSSR}(\zeta_s q_{os}d) = \nu\varepsilon_{\nu+1}\left(\frac{2\pi d q_{os}\zeta_s}{z_s^R(1+z_S^R)}\right) \tag{2.94}$$

Finally, the *ECPSSR* cross section for direct ionization of an S shell is given by

$$\sigma_s^{ECPSSR} = C_s^{ECPSSR}\left(\frac{2dq_{os}\zeta_s}{z_s^R(1+z_s^R)}\right) f_s(z_s^R)\sigma_s^{PWBA}(\xi_s^R/\zeta_s, \zeta_s\theta_s) \qquad (2.95)$$

The function $f_s(z_s^R)$ depends on the choice of the integration limits in the evaluation of the universal cross section given by equation (2.32). COHEN and HARRIGAN[51] used the exact integration limits in equation (2.37), (2.38), and (2.39), with $f_s(z_s^R) = 1$, in their tabulated *ECPSSR* calculations for proton and helium bombardments at various energies. Moreover, the relativistic effect that is used in the calculations can be disregarded if a relativistic Hartree-Slater-Dirac (HSD) wave functions are used in the calculations of the form factor given by equation (2.22) in the original *PWBA*. This is carried out by CHEN and CRASEMANN[55] in their tabulated relativistic *PWBA* with binding (B) and Coulomb deflection (C) effects corrections, denoted as *RPWBA-BC*. The calculation of *ECPSSR* agrees with *RPWBA-BC* within 1.2% for medium elements.

The data points in figure (2-11) are statistically analysed by dividing them into a group for certain values of $\zeta_K\Delta_K$. The mean value of each group of points is plotted in figure (2-13) midway within the abscissa interval and marked with an error bar determined by 95% confidence limit, corresponding to twice the standard deviation for the group. The curve in the figure represents the ratio $\sigma_K^{ECPSSR}/\sigma_K^{CPSSR} = (C_s^{ECPSSR}/C_s^c)f_s(z_s^R)$. The curve clearly reproduces the trends of the K-shell ionization measurements by protons for target elements $10 \leq Z_2 \leq 92$. The theory of *ECPSSR* and experiment agree, on the average, to within $\pm 10\%$ instead of $\pm 30\%$ for the *CPSSR*[58]. Later, and usibg more experimental measurements, PAUL[59] and MUHR[60], after careful statistical analysis, found out that the *ECPSSR* theory describes the K-shell ionization cross section by protons very well. An average agreement within $\pm 6\%$ is observed.

Moreover, SARKADI[61] showed, by studying L X rays produced by proton impact

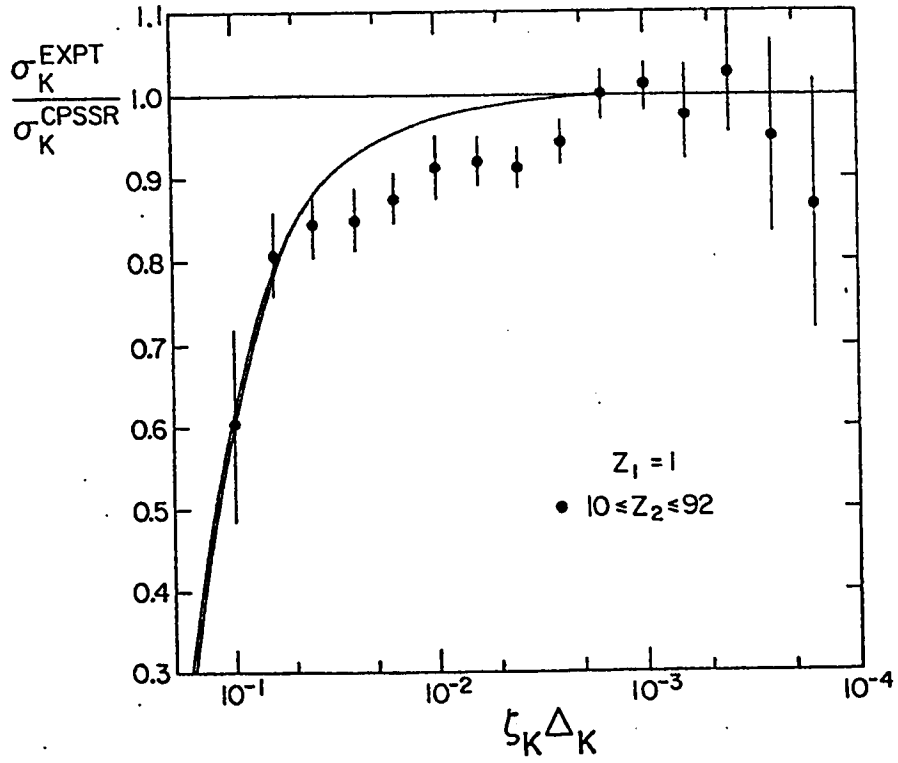

Figure 2-13: Ratios of experimental and theoritical cross sections for K-shel after a statistical analysis. The ratios equal to one when the energy loss effect had been negligably small. (Taken from BRANDT and LAPICKI, 1979.)

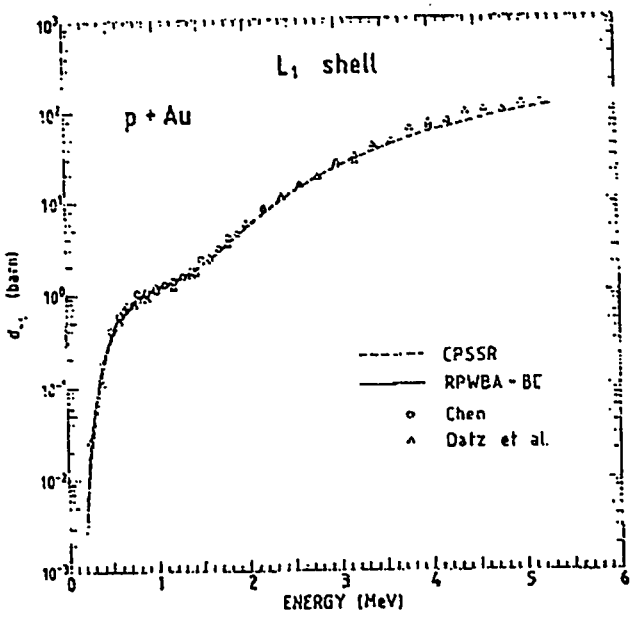

Figure 2-14: Experimental and theoretical L_1-subshell ionization cross section for protons on Au. (Taken from SARKADI, 1983.)

on gold, that the *ECPSSR* theory works very well and it is possible to describe successfully X-ray production of L shell and its three sub-shells. A comparison between theory for L X-ray induced by protons impact on gold are shown in figures (2-14), (2-15), and (2-16). One of the most characteristic features of the L-shell ionization by charged particles is the presence of bump in the energy dependence of L_1-subshell ionization cross section, as shown in figure (2-14). This bump is related to the extra node of the $2s_{\frac{1}{2}}$ radial wave function and the theory successfully predicts it. More recent study for proton induced L X-ray emission on rare earth elements was done by FERNÁNDEZ *et al.*[62] showed that the *ECPSSR* theory under-estimate the measure cross section at low energies, 400 keV-700 keV.

The theory is subjected to investigations for ion bombardment heavier than protons. For K shell, generally good agreement is observed for α-particle bombardments[63]. This is demonstrated by MUKOYAMA and SARKADI[63] and shown in figure (2-17) for K-shell ionization cross section induced by α particles on Fe. The experimental cross

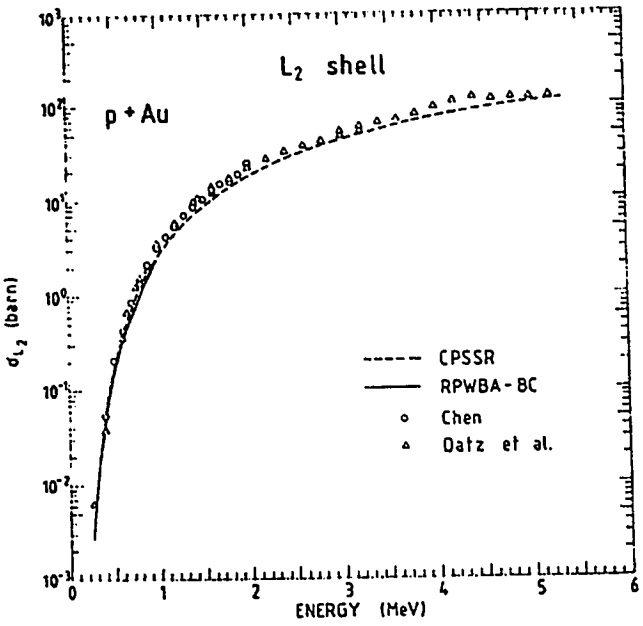

Figure 2-15: Experimental and theoretical L_2-subshell ionization cross section for protons on Au. (Taken from SARKADI, 1983.)

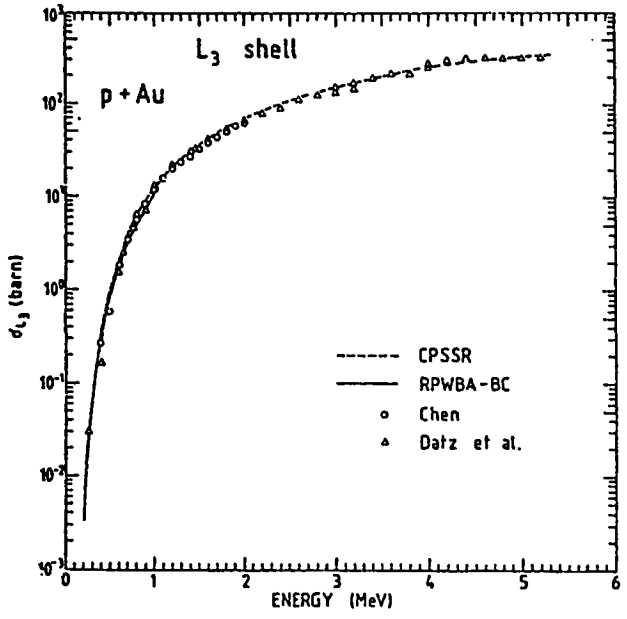

Figure 2-16: Experimental and theoretical L_3-subshell ionization cross section for protons on Au. (Taken from SARKADI, 1983.)

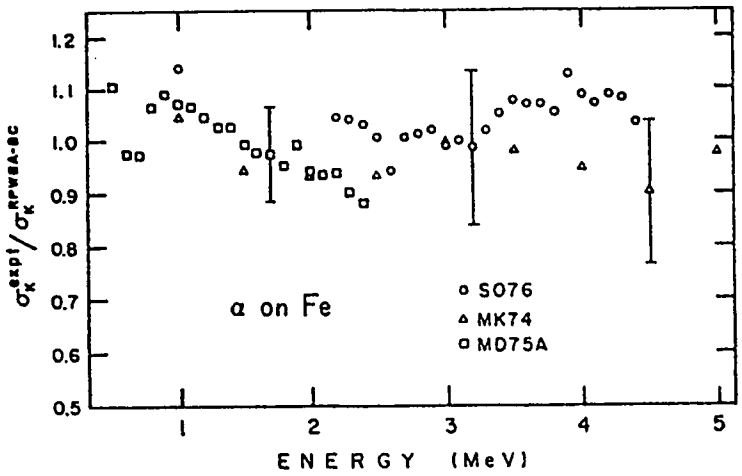

Figure 2-17: Comparison of K-shell ionization cross section data with theoretical calculations of *RPWBA-BC* for α particles on Fe. (Taken from MUKOYAMA and SARKADI, 1981.)

section is normalized by *RPWBA-BC* estimated by using the method of BRANDT and LAPICKI[49]. The deviations, are within the experimental errors shown in the error bars. However, these small deviations are attributed to the fact that the energy loss correction factor is not incorporated yet in the *RPWBA-BC*.

Additionally, YU[64] measured K-shell production cross section by α particles on thin sample C, O, and F as a function of ion energy, using windowless Si(Li) detector. These measurements are compared with other experimental measurements, the *ECPSSR* theory, and the *PWBA* theory as shown in figure (2-18). For carbon, both the *PWBA* and *ECPSSR* theories underpredict the data by 15-25% for ion energies greater than 3.5 MeV, but overpredict the data by 40-80% below 1.0 MeV. For oxygen, the *ECPSSR* theory slightly underpredicts the data by $\sim$ 20% for energies above 1.5 MeV. For fluorine, the data agrees quite well with the *ECPSSR*. YU[64] attributes the discrepancies to the fluorescence yields taken from KRAUSE[10] which do not take into account the effect of multiple ionization of target atoms. However, it must be noted that the effect of multiple vacancies becomes significant as projectile's mass and charge increase.

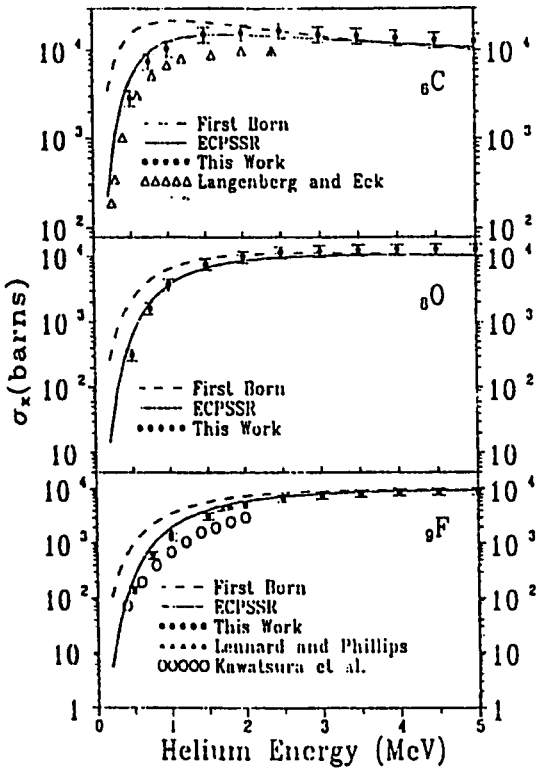

Figure 2-18: The *K*-shell X-ray production cross section for α particles incident on carbon, oxygen, and fluorine as a functions of projectile energy. The data is compared with the *PWBA* and the *ECPSSR*. (Taken from YU, 1993.)

The preferable test for the validity of the *ECPSSR* and other theories is to study the L-subshell ionization cross sections by α-particle and heavier-ion impacts. The L-shell offers a particularly sensitive ground for testing the direct Coulomb ionization theories because it consists of three subshells with different atomic parameters for each. Experimental L-subshell ionization cross section for α-particle bombardments on thin targets of Hf, Ta, W, Re, Os, Ir, Pt, Au, and Bi are obtained by SEMANIAK *et al.*[65] and compared with the predictions of the *ECPSSR* and *SCA*. The data is shown in figure (2-19) and the abscissa gives the relativistic reduced velocity $\xi^R_{L_2}$ as it is given in equation (2.63). The *SCA* is corrected for relativistic effect using the relativistic wave function within the form factor in equation (2.46), Coulomb deflection by adopting the classical hyperbolic projectile trajectory, and binding effect by using united atom limit[3] and including the recoil term in the ionization amplitude[65]. For the L_1 subshell, the data agrees within 30-40% with *SCA* values in the whole range of reduced velocity and with *ECPSSR* predictions for higher velocities $\xi^R_{L_1} \geq 0.3$. While for lower velocities, the *ECPSSR* theory underestimate the data systematically up to factor 2. A similar general trend is observed for L_3 subshell. However the agreement in the case of L_3 is much better (within $\pm$10-30%). The largest discrepancies between experimental values and theoretical predictions are found for L_2 subshell, at $\xi^R_{L_2} \approx 0.2$ where the theories underestimate the data up to a factor 3-4. These discrepancies decrease gradually as reduced velocity increases. For $\xi^R_{L_2} \geq 0.3$, very good agreement with the *SCA* is observed within the experimental uncertainties, while the *ECPSSR* theory remains underestimates the data by $\sim 20 - 30\%$ for $\xi^R_{L_2} \geq 0.5$[65].

Additionally, CAI *et al.*[2] studied the α-particle induced L-subshell ionization on thin $_{71}$Lu, $_{13}$Ta, and $_{79}$Au samples. They concluded that the experimental cross sections for L_1 subshell are 10-20% smaller than those of the *ECPSSR* theory for Lu and Ta. In contrast, for the heavy element Au, the experimental cross sections are larger than those

[3]United atom limit primarily includes correcting the electron binding energy to be for atom Z_1+Z_2 instead of Z_2 only. And an electronic wave function for $Z_1 + Z_2$ is used in the calculations instead of Z_1.

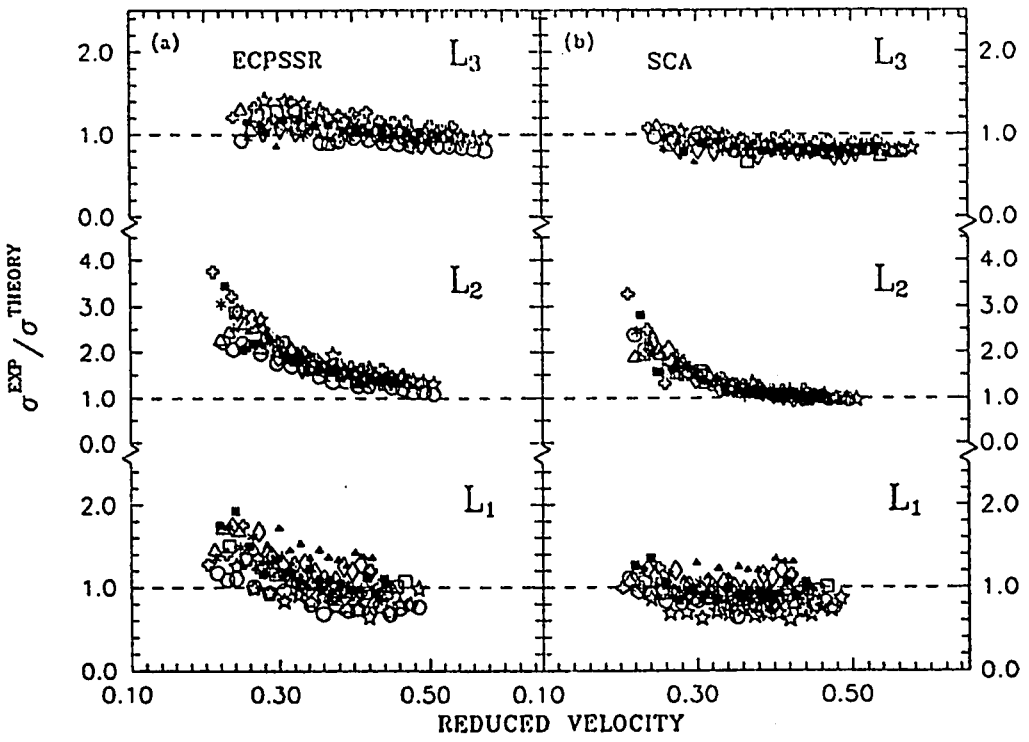

Figure 2-19: Ratios $\sigma^{exp}/\sigma^{theory}$ for the *ECPSSR* (left) and *SCA* (right) theories versus the relativistic reduced velocity parameter for $^4He^{++}$ ion impact. The symbols used to mark the the different elements. See text for the involved elements. (Taken from SEMANIAK *et al.*, 1993.)

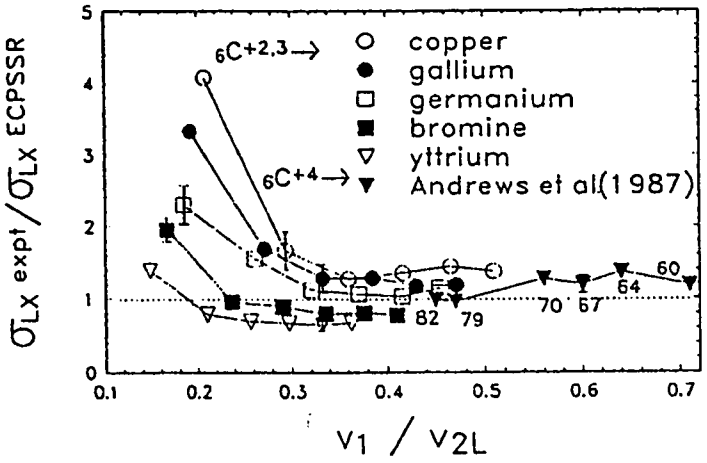

Figure 2-20: Ratios of the measured L-shell X-ray production cross section with that predicted by the *ECPSSR* theory versus v_1/v_{2L}. (Taken from METHA *et al.*)

of the *ECPSSR* theory by 10-20%. For L_3 subshell, a 15% agreement between theory and experiment is observed. In case of L_2 subshell, at low velocities the experimental values are 70% larger than the *ECPSSR* predictions, but the discrepancy decreases as the reduced velocity increases[2], i.e. the same tendency that was shown by SEMANIAK *et al.*[65] as given in figure (2-19). It seems that the case L_2 subshell is not possible to describe by the direct ionization theories.

Similar tendency was observed by METHA *et al.*[66], when they obtained the total L-shell production cross section by $_6C^{+2,5}$ bombardment, on Ga, Ge, Br, and Y thin samples. The cross section was normalized to the *ECPSSR* and plotted versus the factor v_1/v_{2L}, where $v_{2L} = (Z_2 - 4.15)/2$ as shown in figure (2-20). At low velocities of the projectile, the *ECPSSR* theory underestimates the cross sections whereas at high velocities good agreement between theory and experiment was observed. A remarkable feature from figure (2-20) is that the discrepancies at low velocities, decrease systematically as target atomic number increases.

This breakdown feature of the *ECPSSR* for α-particle and heavier ion bombardments at low velocities needs further explorations. However, the binding and relativistic corrections incorporated in the *PWBA* formalism have similar but opposite effects on

the measured subshell ionization cross sections. Hence, both relativistic and binding effect are incapable of explaining the observed low energy discrepancies. METHA *et al.*[66] indicated that the discrepancy needs to be treated in terms of multiple ionization and screening effects. These effects might become effective at high velocities as indicated by SARKADI[61]. However, the discrepancies increases when the difference between Z_1 and Z_2 is relatively small. The discrepancy drains away as $Z_1 \ll Z_2$. This can be inferred directly from the fact that the K-shell ionization cross sections by α particles on Fe agree well with the theory as shown in figure (2-17) whereas they deviate at low velocities for light elements such as $_6$C, $_8$O, and $_4$F as shown in figure (2-18).

SARKADI and MUKOYAMA[61, 63] proposed another effect that would cause the discrepancies at low energy and heavy projectiles called the subshell coupling effect. As the atomic number of the projectile is raised, its perturbational field becomes strong that induces secondary intra-shell transitions among the different subshells. Therefore, the strength of the coupling between the ionization amplitudes of the different subshells increases and the picture of the independent ionization of the subshells fails[61]. Hence, one cannot neglect the electron correlation effects and the ionization of each subshell cannot be treated independently. The success of the direct theory for protons, as shown in figures (2-14), (2-15), and (2-16) is referred to the small perturbation and the reliability of the atomic parameters [61]. Thus a correction factor must be incorporated in the *ECPSSR* formalism to solve this discrepancy.

2.2.9 Subshell-Coupling Effects in L-Subshell Ionization

The investigation of the L-shell ionization cross sections indicates that the ionization of one subshell cannot be regarded as independent from the ionization of the other subshells, especially for strong perturbation caused by heavier ions. Secondary intra-shell transitions may be induced between the subshells by the projectile in the same collision resulting in a redistribution of the vacancies created by the primary direct ionization (vacancy sharing)[67]. The probability of such transitions is a strong function

of the atomic number of the projectile, while it is small for light ions. It may values around unity for ions as heavy as oxygen[67]. The vacancy sharing process tends to equalize the subshell cross section. For low-velocity collisions the number of the vacancies produced in the L_2 subshell by the direct ionization is smaller by one order of magnitude than in the other two subshells. A small amount of vacancy transfer from L_1 and L_3 to L_2 subshell may alter the cross section of the latter shell significantly[67].

To model the coupled state effect, the *SCA* is used by employing classical trajectory and impact parameter as explained in section 2.2.2 and considering only terms contain L-subshell amplitudes[68]. In direct ionization process, the transition from undisturbed ith substate to final state f takes place from pure atomic state. In contrast to this, the subshell coupling mechanism considers transition from mixed state that evolves in time from the ith state as a result of dynamical coupling with other L substates. The mixed state is defined by a set of L-substate occupation amplitudes, $a_{n_L}(t)$, where n_L is a shorthand notation for the quantum numbers l, j, and m_j. The time evolution is governed by the following eight coupled equations

$$\frac{da_{n_L}}{dt} = -\frac{i}{\hbar}\sum_{n'_L}\left\langle \psi_{n'_L}\left|\frac{-Z_1e^2}{|\mathbf{r}-\mathbf{R}(t,b)|}\right|\psi_{n_L}\right\rangle e^{i\omega_{n'_Ln_L}t}a_{n'_L}(t) \tag{2.96}$$

Where $\omega_{n'_Ln_L} = (E_{n'_L} - E_{n_L})/\hbar$. All the parameters are introduced previously in section 2.2.2. An initial condition for a_{n_L} is given as

$$a_{n_L}(t=-\infty) = \delta_{n_L,i} \tag{2.97}$$

Which indicates that there are no transitions among the subshells when the projectile is far away from the target atom. Note that, as indicated in section 2.2.2, $t = 0$ corresponds distance of closest approach at given impact parameter b. The transition amplitude from the mixed state to the final state is given from time-dependent perturbation theory, similar to equation (2.46), however the coupled equation amplitude

$a_{n_L}(t)$ is incorporated, thus

$$a_f = -\frac{i}{\hbar}\int_{-\infty}^{+\infty} dt \sum_{n_L} e^{i\omega_{fn_L}t}\left\langle \psi_f \left| \frac{-Z_1e^2}{|\mathbf{r}-\mathbf{R}(t,b)|}\right| \psi_{n_L}\right\rangle a_{n_L}(t) \tag{2.98}$$

Where $\omega_{fn_L} = (E_f - E_{n_L})/\hbar$. The replacement of the L-substate occupation amplitude in equation (2.98) by $a_{n_L}(t) = \delta_{n_L,i}$ leads to the first-order approximation for direct ionization process

$$a_f^{(1)}(t=\infty) = -\frac{i}{\hbar}\int_{-\infty}^{+\infty} dt e^{i\omega_{fi}t}\left\langle \psi_f(\mathbf{r}) \left| \frac{-Z_1e^2}{|\mathbf{r}-\mathbf{R}(t,b)|}\right| \psi_i(\mathbf{r})\right\rangle \tag{2.99}$$

The cross section for vacancy production in state i is given by[12]

$$\sigma_i = 2\pi\int_0^{\infty} dbb\sum_f |a_f(t=+\infty)|^2 \tag{2.100}$$

The correction factor due to coupling effects is thus given by

$$C_{L_i}^{IS} = \sigma_{L_i}^{\prime(c)}/\sigma_{L_i}^{\prime(1)} \tag{2.101}$$

Where $\sigma_{L_i}^{\prime(c)}$ is a cross section calculated by solving the couple equations, equation (2.96), (2.97), (2.98), and equation(2.100). $\sigma_{L_i}^{\prime(1)}$ is the first-order approximation cross section for direct ionization calculated by solving equation (2.99) and equation (2.100). The prime indicates that these quantities are results of model-like calculations containing the following simplification[12, 67]

1. Only some dominant transitions with a limited number of final states are chosen to characterize the ionization process. The dominant transitions are those take place with minimum energy transfer at low-velocity collisions, where the coupling effects are expected to be large[12, 67].

2. For a similar reason the angular momentum of the electron in the final state is restricted to be $l_f = 0$ and 1.

3. In the multiple expansion of the $1/|\mathbf{r}-\mathbf{R}(t,b)|$factor[4] in the perturbing potential, terms higher than quadruple are neglected.

4. A screened non-relativistic hydrogenic wave functions are used to calculated the matrix element $\left\langle \psi_m \left| \frac{-Z_1e^2}{|\mathbf{r}-\mathbf{R}(t,b)|} \right| \psi_n \right\rangle$.

5. Since the coupling effect is large at low-velocity domain, thus the Coulomb deflection effect must be accounted in the calculations by choosing hyperbolic trajectory (Kepler orbit) for the projectile path and neglect of the target recoil effect.

The correction factor that is given in equation (2.101) is used as a multiplicative correction factor to the *ECPSSR* or other accurate first-order cross sections. Thus the effect of collision-induced intrashell transitions (IS) when included in the *ECPSSR* theory in the form of a correction factor yields

$$\sigma_{L_i}^{ECPSSR-IS} = C_{L_i}^{IS}\sigma_{L_i}^{ECPSSR} \tag{2.102}$$

The solution of the coupled equations automatically gives account of the binding effect i.e.,

$$I_i \rightarrow I_i + \Delta I_i \tag{2.103}$$

Where ΔI_i is given by

$$\Delta I_i = e^{i\omega_{fi}t}\left\langle \psi_f \left| \frac{-Z_1e^2}{|\mathbf{r}-\mathbf{R}(t=0,b)|} \right| \psi_i \right\rangle \delta_{if} = \left\langle \psi_i \left| \frac{-Z_1e^2}{|\mathbf{r}-\mathbf{R}(t=0,b)|} \right| \psi_i \right\rangle \tag{2.104}$$

This gives a correction factor reflecting purely the subshell couplings i.e., the effect connected with the non-diagonal matrix elements.

[4]The multiple expansion for $\frac{1}{|\mathbf{r}-\mathbf{R}|}$ is given as[49]

$$\frac{1}{|\mathbf{r}-\mathbf{R}|} = \frac{1}{R} + \frac{\mathbf{R}\cdot\mathbf{r}}{R^3} + \frac{1}{2}\left(\frac{3(\mathbf{R}\cdot\mathbf{r})^2}{R^5} - \frac{r^3}{R^3}\right) + O(\frac{r^3}{R^4})$$

The terms represent monopole, dipole, and quadrupole terms that contribute to the ionization.

The existence of such effect is demonstrated by SARKADI and MUKOYAMA[12] when they studied the ratio $\sigma_{L_2}/\sigma_{L_3}$ calculated from first order theories for direct ionization for proton impact on gold. The reasons of studying $\sigma_{L_2}/\sigma_{L_3}$ ratio are the ratio of cross sections can be measured with much higher accuracy than absolute cross sections. Also, the L_2-to-L_3 ratio is a smooth function of the projectile energy since both states are $2p$ states with difference in the binding energy only[12]. A noticeable disagreement is found between theory and experiments. However, when the coupling effect is incorporated in the calculations, a prominent agreement is found[12]. Consequently, the effect is not negligible even for proton impact, where the first-order descriptions are generally assumed to be valid, though the disturbing effects do not exist, but the subshell coupiings are expected to be weak[67].

To derive a scaling function on the basis of obtained correction factor for the *ECPSSR* theory, the reduced velocity parameter ξ_{L_i} , which is an important scaling parameter for the *ECPSSR*, was considered as a variable to express the energy dependence of the correction for the different targets. SARKADI and MUKOYAMA[67] have defined their ξ_{L_i} as[5]

$$\xi_{L_i} = \frac{2Z_{2L}}{nI_{L_i}}\sqrt{\frac{m}{M_1}R_\infty E} \tag{2.105}$$

Moreover, the subshell coupling effect can be regarded as generalized binding effect similar to that is shown in equation (2.67) in the *ECPSSR* description. Thus in an anology of equation (2.67), SARKADI and MUKOYAMA[67] parametrized the correction factor defined by equation (2.101) in the form

$$C_{L_i}^{IS}(\xi_{L_i}) = 1 + n\frac{Z_{2L}R_\infty}{I_{L_i}}u_{L_i}(\xi_{Li}) \tag{2.106}$$

[5]The ξ_{L_i} which is introduced by SARKADI and MUKOYAMA in reference [67] is less than the original ξ_{L_i} which was defined by BASBAS *et al.*[36] and given in equation (2.5), by a factor n i.e.,

$$\xi_{L_i}^{SM} = n\xi_{L_i}^{B}$$

Here $n = 2$ for L shell. the superscript SM indicates that the value of ξ was defined by SARKADI and MUKOYAMA and B indicates that the value of ξ was defined by BASBAS and used many references[36, 49, 58, 69]. The distinction superscript will be omitted through this discussion.

Here $I_{L_i} \propto \theta_{L_i} Z_{2L}^2$, as shown in equation (2.3). In contrast to equation (2.67), equation (2.106) gives a multiplicative correction factor which can be applied directly to the cross section[67].

SARKADI and MUKOYAMA calculated the coupled-state effects for helium induced L-shell ionization on elements with atomic numbers $60 \leq Z_2 \leq 92$ and bombarding energies 0.6-6 MeV with the use of the correction factors obtained from the coupled-states model. Plotting the values as a function of the reduced velocity, it turns out that they followed a universal curve for each of the three subshells. For example, figure (2-21) shows the case of the L_2 subshell. The lonely highest point in the figure belongs to $Z_2 = 92$, the deviation is probably due to rapidly increasing relativistic effect with increasing target atomic number[67]. The obtained universal curves are approximated by the following polynomials in the range $0.2 \leq \xi_{L_i} \leq 0.8$, for the L_1 subshell

$$u_{L_1}(\xi_{L_1}) = 8.8 - 85.6\xi_{L_1} + 228.2\xi_{L_1}^2 - 241.1\xi_{L_1}^3 + 89.4\xi_{L_1}^4 \tag{2.107}$$

For the L_2-subshell

$$u_{L_2}(\xi_{L_2}) = \begin{cases} 11.5 + 12.4\xi_{L_2} - 135.4\xi_{L_2}^2 & \text{If } 0.2 \leq \xi_{L_2} \leq 0.3 \\ 33.5 - 193.7\xi_{L_2} + 413.4\xi_{L_2}^2 & \\ -393.8\xi_{L_2}^3 + 141.7\xi_{L_2}^4 & \text{If } 0.3 < \xi_{L_2} \leq 0.8 \end{cases} \tag{2.108}$$

For the L_3-subshell

$$u_{L_3}(\xi_{L_3}) = \begin{cases} -1.4 + 16\xi_{L_3} - 57.9\xi_{L_3}^2 & \\ +57.3\xi_{L_3}^3 & \text{If } 0.2 \leq \xi_{L_3} \leq 0.55 \\ -2.2 + 4.4\xi_{L_3} - 2.6\xi_{L_3}^2 & \text{If } 0.55 < \xi_{L_3} \leq 0.8 \end{cases} \tag{2.109}$$

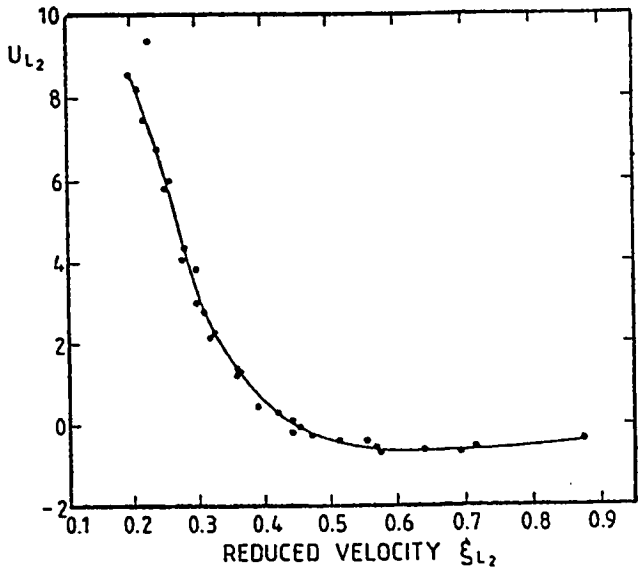

Figure 2-21: The $u_{L_2}(\xi_{L_2})$ universal function. The points are results of the coupled-state calculations, the curve has been drawn using the polynomials fitting given in the text. (Taken from SARKADI and MUKOYAMA, 1991.)

SARKADI and MUKOYAMA[67] have compared the *ECPSSR* theory with experimental measurements for α-particle induced L-shell ionization for 503 data points. For L_1 subshell a good agreement is observed with the *ECPSSR*, however, the agreement becomes slightly worse when the effect of the collision-induced intra-shell collision (IS) is included as shown in figure (2-22). For L_2 subshell, the IS effect gives drastic improvement but the deviations remain hold as shown in figure (2-23). For L_3 subshell the modification have less effect compared to the L_1 and L_2 subshell, both models, *ECPSSR* and *ECPSSR-IS*, give a reasonable description of the experimental data for L_3 subshell, as shown in figure (2-24)[67].

Similar trends are observed by SEMANIAK *et al.*[65], when the IS correction is applied for the data described in figure (2-19), but for L_2 subshell the data points become more consistent but the *ECPSSR-IS* remains under estimate the experimental values. Moreover, the L_1 subshell becomes worst as shown in the left (a) of figure (2-25)[65]. Therefore, it seems that the discrepancy remains for L_2 subshell and another

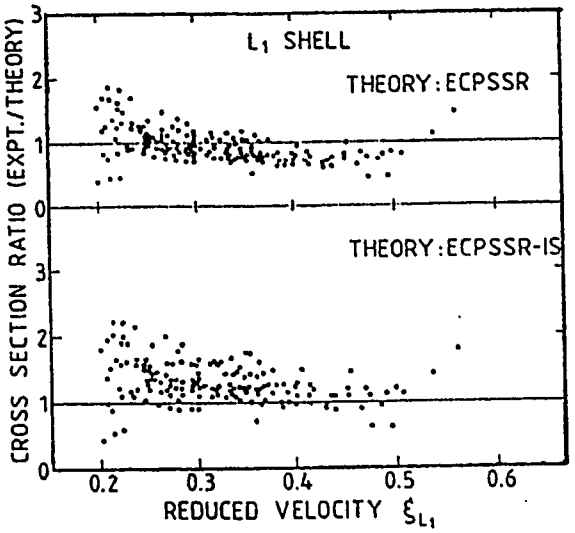

Figure 2-22: Ratios of experimental and theoretical L_1-subshell ionization cross section for α-particle impact as a function of the reduced velocity. In the upper part the theoretical values have been calculated using the *ECPSSR* model. In the lower part the *ECPSSR* theory has been corrected to include the effect of the collision-induced intrashell transition (*ECPSSR-IS*). (Taken from SARKADI and MUKOYAMA, 1991.)

problem is arisen for L_1-subshell, when the IS corrections are incorporated.

One important remark, can be obtained from previous discussion, that good agreement can be observed when the subshell quantum number is increased. VIGILANTE *et al.*[70] have suggested that the *ECPSSR* theory overestimates the binding effect and one must "saturate" the binding correction with decreasing velocity at a value corresponds to the binding energy of the united atom (UA) approximation. SARKADI and MUKOYAMA[67] accounted this effect by using the $g_{L_i}(\xi_{L_i})$ function only to interpolate between the separated and united atom binding energies instead of using its absolute value thus [67]

$$\epsilon_{L_i} = 1 + \frac{I_i(Z_1 + Z_2) - I_i(Z_2)}{I_i(Z_2)} g_{L_i}(\xi_{L_i}) \tag{2.110}$$

At low velocities $g_{L_i}(\xi_{L_i}) \approx 1$, and thereby $\epsilon_{L_i} I_{L_i}(Z_2) \approx I_{L_i}(Z_1 + Z_2)$. Whereas at high velocities $g_{L_i}(\xi_{L_i}) \approx 0$, and thus $\epsilon_{L_i} \approx 1$[67]. The cross sections calculated using equation (2.110) agreed almost exactly with those obtained with the UA approximation

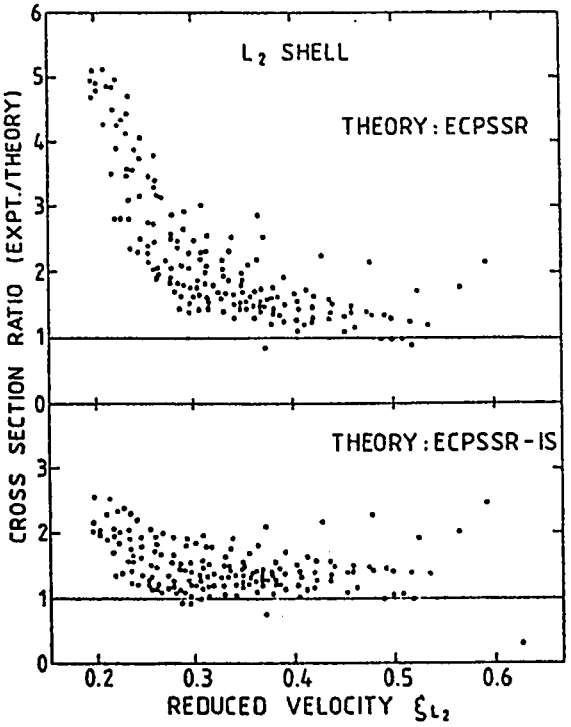

Figure 2-23: Ratios of experimental and theoretical L_2-subshell ionization cross section for α-particle impact as a function of the reduced velocity. In the upper part the theoretical values have been calculated using the *ECPSSR* model. In the lower part the *ECPSSR* theory has been corrected to include the effect of the collision-induced intrashell transition (*ECPSSR-IS*). (Taken from SARKADI and MUKOYAMA, 1991.)

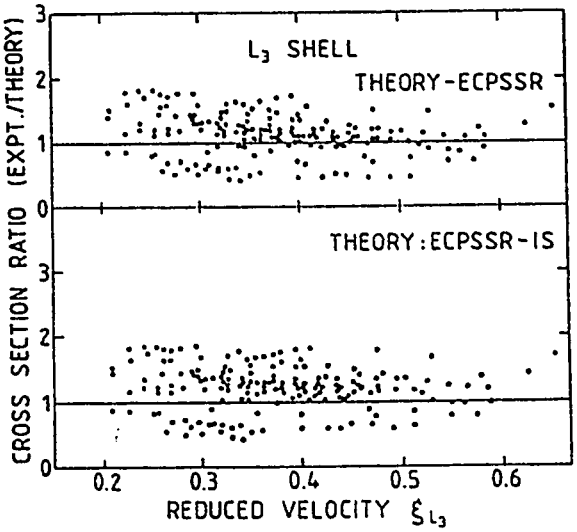

Figure 2-24: Ratios of experimental and theoretical L_3-subshell ionization cross section for α-particle impact as a function of the reduced velocity. In the upper part the theoretical values have been calculated using the *ECPSSR* model. In the lower part the *ECPSSR* theory has been corrected to include the effect of the collision-induced intrashell transition (*ECPSSR-IS*). (Taken from SARKADI and MUKOYAMA, 1991.)

of Vigilante *et al.*[70] at low velocity range, and slightly different from the *ECPSSR* values at higher velocities [67]. When the UA correction is applied to the data shown in figure (2-22), (2-23), and (2-24), only minor changes (1-2%) are observed for L_1 subshell The change is larger for L_2 and L_3 subshell, typically 10% and 20%, respectively, as shown in figure (2-26)[67]. A similar trends are observed when the *ECPSSR-IS-UA* is applied for data points shown in figure (2-19), causes significant changes of ionization cross sections, up to 20-30% for L_2 and L_3 and 10% for L_1 subshell as shown in the right of figure (2-25). The theory predicts the data within $\pm$15% for L_3 subshell and 20-30% for L_2 subshell[65].

In general the model describes the L_2 subshell cross section much better. However, for L_1 the discrepancies are not reduced within the *ECPSSR-IS-UA* model. The reason is attributed to the use of screened hydrogen-like (SH) wave function in the *ECPSSR* formalism[65]. SARKADI and MUKOYAMA have shown that the use of a Dirac-Hartree-Slater (DHS) instead of SH wave function causes changes of the cross sections for the

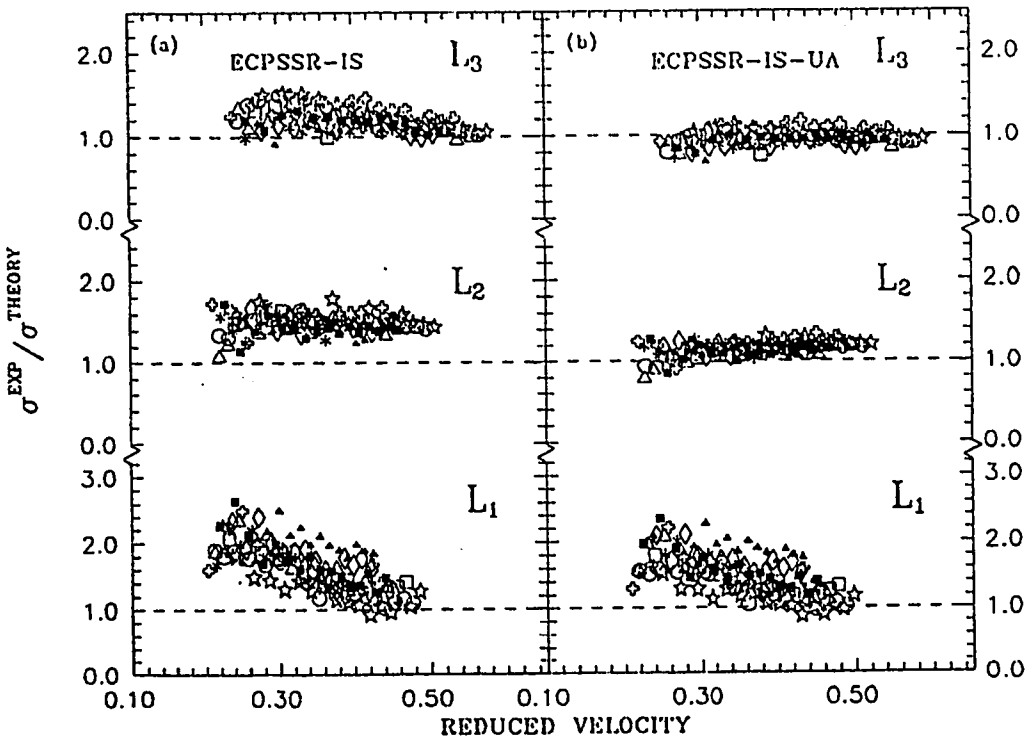

Figure 2-25: Ratios $\sigma^{exp}/\sigma^{theory}$ for the *ECPSSR-IS* (left) and *ECPSSR-IS-UA* (right) theories versus the relativistic reduced velocity parameter for $^4He^{++}$ ion impact.

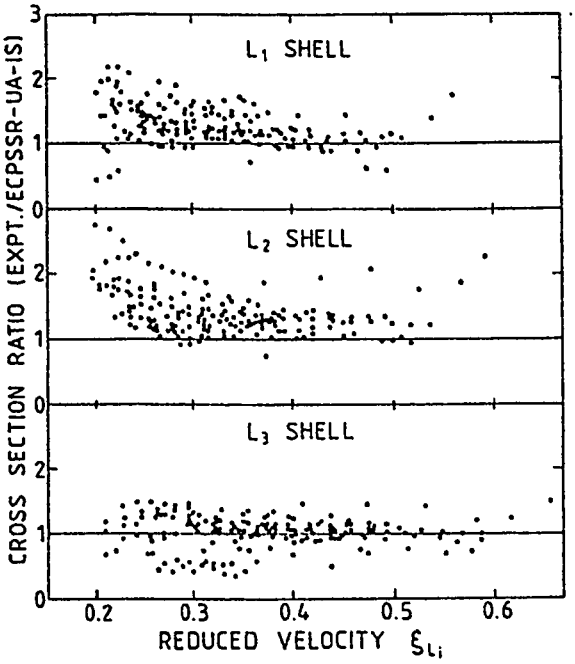

Figure 2-26: Ratios of experimental and theoretical L-subshell ionization cross section for α-particle impact as a function of the reduced velocity. In the upper part the theoretical values have been calculated using the *ECPSSR* model, corrected to include the effects of collision-induced intrashell transition and united atom (*ECPSSR-IS-UA*). (Taken from SARKADI and MUKOYAMA, 1991.)

L_1 subshell up to 60% for the lowest velocities measured[12, 67]. However, there is a necessity of more accurate measurements for L-subshell ionization by helium impact to firm a clear conclusions.

2.3 Experimental Measurement Techniques

Many details of the atomic excitation accompanying the vacancy production by ion impact can be studied by examining the spectral distributions of the X-ray and Auger-electron lines. By summing over all modes of de-excitation, one can obtain a number which is proportional to the probability of producing the original vacancy. The X-ray emission is almost completely dominated by one-photon electric dipole radiation whose selection rule is given in equation (1.12). So that the accessible final states are

severely restricted by the usual dipole selection rule. Auger emission, on the other hand, proceeds via e^2/r_{ij} (scalar) interaction repulsion which is unrestricted process, since the ejected electron may in principle have any angular momentum, and thus the number of states accessible to the residual atomic system is unrestricted. These remarks lead to the correct conclusion that the X-ray spectrum should be relatively simple, with the Auger spectrum perhaps richer in information[46].

The majority of inner-shell ionization cross section data is obtained out of total X-ray production cross sections, since X-ray detector systems are less complex than those of Auger.

The X-ray spectrum associated with energetic ion-atom impact can be detected and analysed experimentally by means of conventional nuclear instruments, namely, appropriate detector, preamplifier, amplifier, voltage bias supply, and single- or/and multi-channel analyser. The multi-channel analyser makes the analysis practically easier since one capable to view the total pulse height spectrum within the desired energy range, which represented by a channels, set by choosing convenient amplification gain. A high resolution detector is often required. Usually Si(Li) detectors offer proper detection capability that suits the complex nature of X-ray spectra. Therefore they widely utilized for such measurements. Data is always recorded and transferred from detector system to a computer using suitable interfacial procedure in order to carry out the analysis that involves the analytical fitting of the spectrum and peak area calculations. This is one of the most important step since the ionization cross section estimations depend rigorously on the peak areas.

2.3.1 Analytical Fitting of X-Ray Spectrum

To construct the model pulse height spectrum for a given element, the first requirement is the relative intensities of its various X-ray lines, denoted by R^i_{jk} for the relative intensity of jth line with respect to the most intense kth reference line for the ith element.

This quantity must be practically corrected for detector efficiency[6] and self-absorption effect if thick samples are used. Thus for thin samples at particular arrangement, the practical relative intensity is given by

$$R'^{i}_{jk} = R^{i}_{jk}\frac{\varepsilon(E^{i}_{j})}{\varepsilon(E^{i}_{k})} = \left(\frac{L^{i}_{j}}{L^{i}_{k}}\right)\left(\frac{\varepsilon(E^{i}_{j})}{\varepsilon(E^{i}_{k})}\right) \tag{2.111}$$

Where $\varepsilon(E)$ denotes the detector efficiency as a function of X-ray line energy. Note that $R'^{i}_{kk} = 1$. In the case of specimen of moderate thickness or one that stops the beam entirely (i.e. thick sample), R'^{i}_{jk} in equation (2.111) has to be further adjusted to account the matrix effects, by incorporating an extra multiplicative factor T^{i}_{j} to describe the transmission of the photons through the successive depth in the sample, given by

$$T^{j}_{i} = \int_{E_o}^{E_f}\frac{\sigma^{x}_{p}(E)}{S(E)}dE\exp\left\{-\mu\int_{E_f}^{E}\frac{dE'}{S(E')}\frac{\cos\theta_i}{\cos\theta_o}\right\} \tag{2.112}$$

Where the parameters involved are defined in equation (1.50). For thick samples those stop the beam entirely, the integration limit $E_f = 0$. The existence of the X-ray production cross section $\sigma^{x}_{p}(E)$ in equation (2.112) lends difficulties to obtain the experimental relative intensities in equation (2.111) for thick and moderate thickness samples, since the X-ray production cross section is a quantity has to be measured. This difficulty can be avoided by fitting each X-ray line independently (i.e. without using reference line) or alternatively employing thin samples.

The X-ray spectrum yield from the ith element that contains n X-ray lines is then

$$Y_i(E) = A_k\sum_{j=1}^{n} g_j(E^{i}_{j}, E)R'^{i}_{jk} \tag{2.113}$$

Where A_k is the peak area parameter of the main line to be determined from the least-square-fitting program, and $g_j(E^{i}_{j}, E)$ is the detector line shape. The simplest form for

[6]The efficiency here includes the absorption effect of the external parameters such as the optional filter, absorber, air path, and beryllium window of the Si(Li) detector.

the line shape is a Gaussian with width and centroid σ_j and μ_j, respectively, which are related linearly to the X-ray line energy E_j^i. The obvious low energy tailing of peaks in Si(Li) detectors warrants incorporation of some kind of description of this distortion. One choice is to employ exponential tails. The width, centroid, and tailing parameters are determined for a particular experimental system.

The characteristic X-ray contribution to the *PIXE* spectrum for a sample consists of N elements is then

$$Y_{fit}(E) = \sum_{i=1}^{N} Y_i(E) + B(E) \tag{2.114}$$

Where $B(E)$ denotes the generated background. Although there are serious attempts to model the *PIXE* background, as shown in section 1.2.3, however, the background depends crucially on energy and charge of the projectile, and the atomic number of the target atom or the matrix. Therefore, a universally applicable background model does not yet exist[6]. Thus, after fitting the X-ray lines according to data base involves elements in the matrix, the centroids and widths of X-ray lines, and the distortion parameters such as low energy tailing, the background is then fitted analytically by altering the fitting parameters until the best fit is achieved. Usually polynomial functions with floating order is employed to fit the background, given by[32]

$$B(E) = S \exp\left\{\sum_{l=0}^{m} a_l (E - E_o)^l\right\} \tag{2.115}$$

Where S is the term that describes the detector efficiency and self absorption, m is the order of the polynomial, and E_o is a constant. The parameters a_l are varied during the least squares fit. The polynomial background is very flexible for such continuum spectrum, but there have been occasions when the polynomial background has failed to produce a satisfactory background, especially when the background contains some peaks due to satellites, statistical fluctuations, and escape peaks of the detector. In many cases the peaks result from satellites, which are located beside or overlapped with the parent characteristic lines, and statistical fluctuations can be ignored or smoothed

by adopting iterative procedure whose algorithm examines the height of the spectrum compared to the average of points either side[32]. This is achieved by testing whether the count C_i

$$C_i > \frac{1}{2}(C_{i-1} + C_{i+1}) = m_i \tag{2.116}$$

If C_i is greater than the mean m_i then it is replaced by the mean[32]. This procedure removes peaks and progressively reduces the spectrum to background continuum.

In case of escape peaks, the effect that originates them is well known, thus they can be stripped directly through the fitting process. The escape peaks arise from the escape of silicon K X ray following photo-electric interaction close to the front surface of the detector. This cause the Si(Li) detector to detect its own K X ray when it penetrates through the Si crystal. Addition escape peaks arise when the X-ray photon for certain element experiences Compton scattering close to the front surface of the Si crystal causes the photon to lose part of its energy and then it is detected and recorded at low energy with respect to the parent line in the pulse-height spectrum. Although the escape peak intensity is only 1% or less of its parent peak, it has a potential for causing confusion. For example the iron K_α escape peak at 4.65 keV overlaps the titanium K_α line at 4.51 keV. This is regarded as one of experimental difficulties that limits the precision of peak area estimation. Additionally the escape peaks violate the fitting accuracy for the background. The silicon escape peak is always accounted through fitting procedures in up-to-date programs.

Practically the background can be suppressed using suitable filter in front of the window of the detector. One of the filters is the digital filter which is a mathematical operator when applied sequentially at each channel in the spectrum suppress the continuum at low energy region, passes the intermediate energy band that contains the characteristic peaks, and is not sensitive to the high energy band that contains channel-to-channel fluctuations due to counting statistics[6]. Another type called Mylar filter (has the formula $C_{10}H_8O_4$) can be used to attenuate low energy X rays so that one can analyse elements heavier than chlorine. And finally, a filter made of graphite with a

small pin hole in the centre, allows a small percentage of low energy X rays through. With this filter, all elements from aluminium to uranium can, in principle, be detected in a single measurement.

The parameters involved in equation (2.113) and equation (2.114) are altered during the fitting until the best values which minimize the reduced *chi-squared* test are obtained. The reduced chi square is given by[71]

$$\chi_R^2 = \frac{1}{f}\sum_{i=1}^{m}\left(\frac{Y_{fit} - Y_{\exp}}{\sigma}\right)^2 \tag{2.117}$$

Where m denotes number of channels, f is the number of degrees of freedom, defined by $f = m - p$, where p is the number of parameters which are varied during the fitting, and σ is the standard deviation, given for Gaussian distribution to be $\sigma = \sqrt{Y_{\exp}}$[72]. Thus equation (2.117) may be written as

$$\chi_R^2 = \frac{1}{f}\sum_{i=1}^{m}\frac{(Y_{fit} - Y_{\exp})^2}{Y_{\exp}} \tag{2.118}$$

The perfect case for χ_R^2 would be 1, if the model is not quite appropriate, then the value of χ_R^2 will grow with spectral intensity.

Subsequent to the fitting, the peak area parameter for the kth reference line of the ith element in equation (2.113) A_k^i is estimated with uncertainty $\pm\sigma$, given for Gaussian peaks[72]

$$\sigma = \sqrt{A_k^i} \tag{2.119}$$

Noting that the uncertainty in measuring the peak area must account the uncertainty in the fitting as well. This may be obtained from the residual of the fitting, defined as

$$Ris = \sum_{i=1}^{m} Y_{fit} - Y_{\exp} \tag{2.120}$$

Accordingly, it is expected that $\sigma \geq \sqrt{A_k^i}$.

Finally, it must be emphasized that for measuring the inner-shell ionization cross section purposes, it is favourable to get the *PIXE* spectrum for each element independently, if it is possible. This is to avoid the complexity of multi-element *PIXE* spectrum, the possible peak overlapping, and the high background, which limit the accuracy of the fitting and hence the results.

2.3.2 X-Ray Production Cross-Section Measurements

The line peak area obtained from X-ray spectrum, A_k^i can be utilized to estimate the production and the ionization cross section of the particular line. In this project, attention however is paid to estimate the cross section for total shell or subshell that originates the particular line. Therefore must be corrected to involve the contribution of the other lines those are originated from the same shell or subshell. This is done by dividing the line peak area by the branching ratio which gives the X-ray yield for the total shell as follow

$$N_s^x = \frac{A_k^i}{B_k} \tag{2.121}$$

Where the subscript $S = K$, L_1, L_2, or L_3. The quantity N_s^x is S-shell X-ray yield and B_k is the branching ratio of the kth X-ray line.

The yield given in equation (2.121) can be used to estimate the production cross section. The technique depends on the type of the sample, whether it is thick or thin.

Thick Target Measurements

The production cross section determination through thick target measurements is suggested through the use of the formula of MERZBACHER and LEWIS[4], derived from the fact that the X-ray yield is given as

$$N_s^x(R_\circ) = \frac{n\Omega\varepsilon}{4\pi}\int_0^{R_\circ} \exp\left\{-\frac{\mu}{\cos\theta}(R_\circ - R)\right\}\sigma_s^x\left(E(R)\right)dR$$

Where n denotes number of target atoms per cm^3, μ is the absorption coefficient of the target for its own characteristic X ray, Ω is the solid angle subtended by the detector, ϵ is the detector efficiency, θ is the angle between the detector and the normal of the sample, and R_o is the total range of the projectile in the sample. Here the production cross section change because of the dependence of the energy of the projectile on the residual range R. By differentiating the above expression one thus obtain

$$\sigma_s^x(E) = \frac{4\pi}{n\Omega\varepsilon}\left\{\frac{dN_s^x(E)}{dE}\frac{dE}{dR} + \frac{\mu}{\cos\theta}N_s^x(E)\right\} \tag{2.122}$$

Where dE/dR is the energy loss per unit path given in equation (1.41). The formula accounts the variation of the production cross section with the variation of the energy of the projectile due to the energy loss as it traverses through the sample. Additionally the formula accounts the self-absorption effect by incorporating the absorption coefficient.

Thus one can obtain the production cross section at particular energy by estimating the X-ray yield as a function of the energy of the projectile and then finding the slope of the X-ray yield at this particular energy.

Thin Target Measurements

For a thin target of thickness t μgm/cm^2 the X-ray yield at a given particle energy E, is given by[73]

$$N_s^x = \varepsilon Q \Delta n \sigma_s^x(E)\frac{\Omega}{4\pi} \tag{2.123}$$

Where Q is number of incident charge, and Δn is the number of target atoms per cm^2.

In the other hand, the number of incident particles is determined through measurement of the number of particles scattered at angle ϕ, given as[73]

$$N^p = Q\Delta n\left(\frac{d\sigma}{d\Omega}\right)_R \Omega' \tag{2.124}$$

Where Ω' is the solid angle subtended by the particle detector and $(d\sigma/d\Omega)_R$ is the

differential scattering cross section that is given by Rutherford formula in equation (1.29). Combine equation (2.123) and equation (2.124), one obtains

$$\sigma_s^x(E) = \frac{4\pi}{\varepsilon}\frac{\Omega'}{\Omega}\frac{N_s^x}{N^p}\left(\frac{d\sigma}{d\Omega}\right)_R \tag{2.125}$$

All quantities in equation (2.125) can be calculated and measured so that the production cross section $\sigma_s^x(E)$ can be determined.

It is obvious that thin target measurements are much easier than thick target measurements. The advantage of thin target measurements is the possibility of utilizing both *PIXE* and *RBS* simultaneously. Thus, the accumulated charge and target areal density are irrelevant in the calculations which improves the accuracy of the measurements. This shows why it is favourable to use thin targets in such measurements rather than thick targets.

2.3.3 X-Ray Ionization Cross-Section Measurements

The X-ray production is just one consequences of the atomic relaxation processes following the ionization in the inner shells. Hence, the X-ray production cross section does not offer the ionization probability unless it is corrected to involve the other radiation less processes, such as Auger effect, and vacancy migration among shells.

The Auger effect can be accounted by dividing by the fluorescence yield. Whereas for transitions among the subshells can be accounted by merging the Coster-Kronig probabilities for all possible transitions.

For K shell ionization, the vacancy refilling processes involves just X-ray or Auger-electron emission. Consequently the direct ionization cross section for K shell can be directly obtained as

$$\sigma_K^i(E) = \frac{\sigma_K^x(E)}{\omega_K} \tag{2.126}$$

Where ω_K is the K shell fluorescence yield, and $\sigma_K^p(E)$ is K-shell X-ray production cross section.

Similar argument applies for L_1 subshell, though, the vacancy migration effect for vacancy created in K shell and transferred to L_1 subshell could be accounted. Thus the L_1-subshell direct ionization cross section is given by

$$\sigma^i_{L_1}(E) = \frac{\sigma^x_{L_1}(E)}{\omega_{L_1}} - \eta_{K\to L_1}\sigma^i_K(E) \tag{2.127}$$

Where ω_{L_1} is the L_1-subshell fluorescence yield, and $\eta_{K\to L_1}$ is the probability of magnetic dipole transition, induced when a vacancy has been created in K shell, given by

$$\eta_{K\to L_1} = \frac{B_{KL_1}}{\omega_K} \tag{2.128}$$

Where B_{KL_1} is the branching ratio for the $K \to L_1$ transition.

In case L_2 subshell, the decay scheme become more sophisticated. This is because besides to direct ionization to L_2, there is a probability for vacancy immigration from $L_1 \to L_2$ via Coster-Kronig effect. Moreover, for a vacancy created in K shell, there is a significant probability for vacancy migration from K shell to L_2 subshell, represented by the X-ray line K_{α_2} for radiative transition and related Auger-electron lines. Additionally, for a vacancy created in K shell, it can induce the $K \to L_1$ magnetic dipole vacancy transition and consequently it can induce the $L_1 \to L_2$ Coster-Kronig transition. Therefore, subtracting the contribution of all effects, the cross section for L_2 subshell by direct ionization is given by

$$\sigma^i_{L_2}(E) = \frac{\sigma^x_{L_2}(E)}{\omega_{L_2}} - f_{12}\sigma^i_{L_1}(E) - \eta_{K\to L_2}\sigma^i_K(E) \tag{2.129}$$

Where ω_{L_2} is the L_2-subshell fluorescence yield, f_{ij} denotes the Coster-Kronig transition probability, and $\eta_{K\to L_2}$ denotes the $K \to L_2$ vacancy migration probability, given by

$$\eta_{K\to L_2} = \frac{(B_{K_{\alpha_2}} + f_{12}B_{KL_1})}{\omega_K} \tag{2.130}$$

Where $B_{K_{\alpha_2}}$ is the branching ratio for K_{α_2} line.

For L_3 subshell, same effects occur however in more complicated scheme. The direct ionization cross section must be corrected for Auger emission, Coster-Kronig transition, and vacancy migration from other lower shells, those has been already ionized. Furthermore, one must take into account the two-step $L_1 \rightarrow L_2 \rightarrow L_3$ Coster-Kronig transition, as well as the $L_1 \rightarrow L_3$ and the $L_2 \rightarrow L_3$ transitions. Therefore the direct ionization cross section for L_3 subshell can be written as

$$\sigma^i_{L_3}(E) = \frac{\sigma^x_{L_3}(E)}{\omega_{L_3}} - f_{23}\sigma^i_{L_2}(E) - (f_{13} + f_{12}f_{23})\sigma^i_{L_1}(E) - \eta_{K\rightarrow L_3}\sigma^i_K(E) \qquad (2.131)$$

Where ω_{L_3} is the L_3-subshell fluorescence yield, and $\eta_{K\rightarrow L_3}$ denotes the $K \rightarrow L_3$ vacancy migration probability, given by

$$\eta_{K\rightarrow L_3} = \frac{\left\{B_{K\alpha_1} + f_{23}B_{K\alpha_2} + (f_{13} + f_{12}f_{23})B_{KL_1}\right\}}{\omega_K} \qquad (2.132)$$

Where $B_{K\alpha_1}$ is the branching ratio for K_{α_1} line.

The values of $\eta_{K\rightarrow L_1}$, $\eta_{K\rightarrow L_2}$, and $\eta_{K\rightarrow L_3}$ are calculated by PURI *et al.*[74] using different approach, involving the decay widths of radiative and non-radiative transitions. In order to avoid this composite scheme, the values in equation (2.128), equation (2.130), and equation (2.132) are recommended and easier for estimation, since they entail the same available data base that is always employed in X-ray analysis. In many literatures[2, 65, 69, 62], the effect of vacancy migration from K shell are neglected or ignored. This is however true for estimating the L-subshell ionization cross section for heavy elements $Z > 60$ by α particles, since in this case $\sigma^i_K \ll 1$. PURI *et al.*[74] tabulated these values using their scheme. For holmium $Z = 67$, $\eta_{K\rightarrow L_1} \simeq 0.031$, $\eta_{K\rightarrow L_2} \simeq 0.30$, and $\eta_{K\rightarrow L_3} \simeq 0.52$. The values successively increase, nevertheless, the theoretical ionization cross sections, at particular energy of the projectile, increase rapidly when going from L_1 subshell to L_3 subshell with respect to K shell. Therefore there are no significant contributions to the uncertainty when the vacancy migration effects are disregarded.

Chapter 3

Experimental Arrangement

3.1 Irradiation Probes

Thin film standards (Provided by MICROMATTER Co. U.S.A.) are employed for this study. The samples and their areal density are listed in table (3.1). The first three elements in the list are used to measure their L X-ray ionization cross section by α-particle impact. The others are utilized to calibrate the system and to obtain an analytical expression for the efficiency and geometric factor.

The purity, dimensions, and shapes of standards were achieved under a certain restrictions required for convenient determination. These standards are prepared by vacuum deposition resulting in highly uniform deposit. In most cases the standards present an element free of interfaces and thin enough to ignore thickness effects, which makes the analysis easier and more accurate as previously explained.

The elements are deposited on 25 mm-diameter Nuclepore polycarbonate membrane filter (approximately 1mg/cm^2 thick), and mounted by 1 mm-thick polycarbonate rings. A schematic diagram for these standards is shown in figure (3-1). These standards are kept before and after use within tight-closing plastic bags to maintain them from the exterior effects, such as humidity, temperature, and dust. The uncertainty in the thickness was estimated by the manufacturer to be within $\pm 0.5\%$.

Table 3.1: Thin-standard targets and their characteristics.

Element	Combound	Atomic number Z	Areal density $\mu gm/cm^2$
Holmium	HoF_3	67	37.4
Erbium	ErF_3	68	36.8
Thulium	TmF_3	69	37.4
Copper	CuS_x	29	41.7
	Cu	29	47.5
Germanium	Ge	32	48.5
Nickel	Ni	28	44.5
Iron	Fe	26	74.6
Strontium	SrF_2	38	33.2
Yttrium	YF_3	39	30.7
Niobium	Nb_2O_3	41	39.3
Molybdenum	MoO_3	42	33.9
Selenium	Se	34	51.3
Manganese	Mn	25	49.9
Vanadium	V	23	46.5
Cobalt	Co	27	50.9
Rhodium	Rh	45	43.8
Palladium	Pd	46	50.2
Silver	Ag	47	46.0
Rubidium	RbI	37	20.0
Titanium	Ti	22	52.7
Chlorine	NaCl	17	30.7

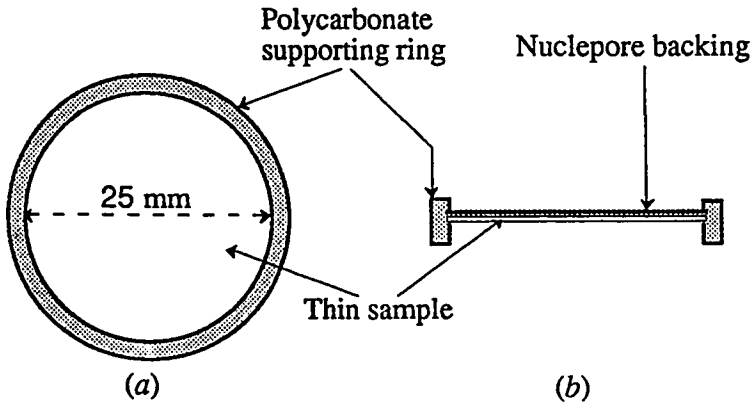

Figure 3-1: Schematic diagram for the thin standards shows the shape, the dimension, and the composition.(a) front view and (b) top view.

3.2 Beam-Handling System

In this experiment two types of ion beams are handled. A 2.5 MeV-proton beam utilized for calibration purposes of the system, and from 1 to 6 MeV α-particle beams utilized to measure the L X-ray ionization cross section for holmium, erbium, and thulium. The beam is accelerated, transported, and focused via a state-of-art 3 MV General Ionix Tandetron accelerator of *Energy Research Laboratory* (*ERL*) at *University of Petroleum and Minerals* (*UPM*). A layout of the accelerator is shown in figure (3-2). The accelerator is described in detail elsewhere[75]. For the sake of continuity, a brief summary of the accelerator facility will be given in the following:

3.2.1 The Injector Assembly

On the low energy side of the Tandetron a dual-leg injector provides two ion sources for the production of virtually all ions of the periodic table. One leg is accommodated to with duoplasmatron-type source (model 358), mainly used for light elements. Negatively charged hydrogen can be directly extracted from the ion source whereas helium is used with positive extraction. To provide negative helium ion injection with high efficiency, the ion source is interfaced to a recirculation lithium charge-exchange canal, followed by a 7° electrostatic deflector to removal of neutral and unwanted positive ion beams.

The other injector leg is accommodated with a cesium sputtering source (model 860B) depending on surface ionization. It is used for the production of heavy ion and followed by an einzel lens and preacceleration tube.

Each of the two injectors is designed to produce and accelerate ions of different species up to about 80 keV. The beam are steered and focused to low-energy end of the accelerating tube by lenses and a 30° injector magnet. The injector magnet has a maximum field of 1 T[75].

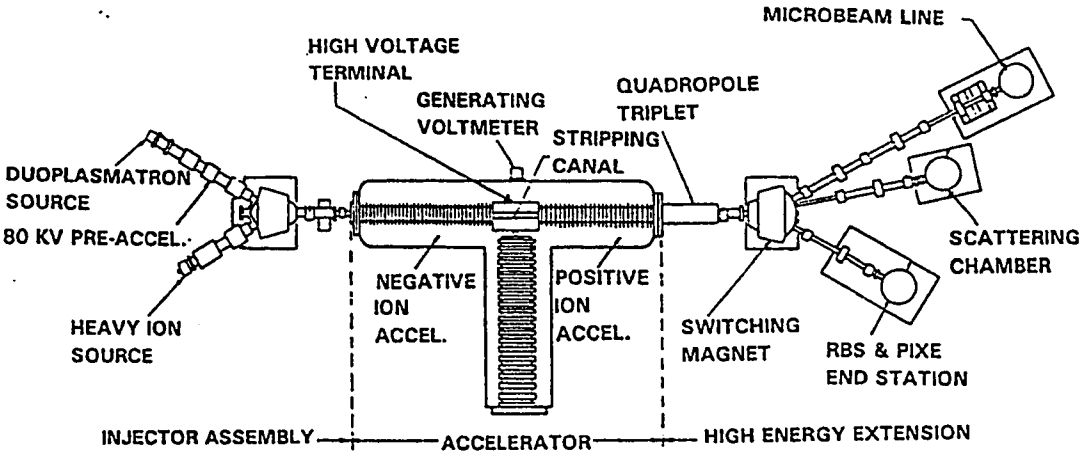

Figure 3-2: System layout for a 3 MV high current Tandetron accelerator, showing all different sections.

Duoplasmatron Ion Source

The details of up-to-date ion source technologies are explained elsewhere[76]. In this experiment, however, only one ion source is employed to obtain proton and α-particle beam, which is the duoplasmatron. Typical duoplasmatron ion source is shown in figure (3-3). In this ion source, the ions are produced by abstracting gas molecules and then ionizing them by means of electron plasma produced by an arc discharge between a hot filament cathode and an anode plate surface[77, 76]. The electronic plasma is confined by both axial magnetic field and an electrode which is maintained at a potential between the cathode and anode potential, which enhances the probability of an electron's colliding gas molecules before striking the anode. The field also has a focusing effect on the produced ions. As a consequences of pressure differences, the ions flows out through an aperture in the anode plate and then by means of suitable potential differences between the extraction electrode and anode plate, the positive ion is extracted.

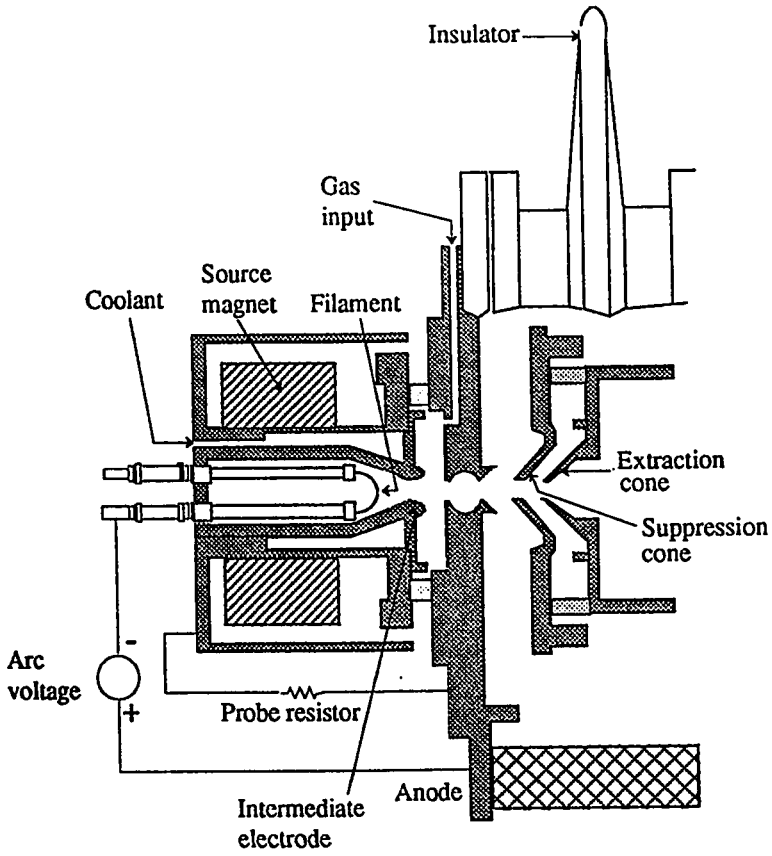

Figure 3-3: Sketch diagram of duoplasmatron ion source. (Reproduced from AL-JALAL, 1991.)

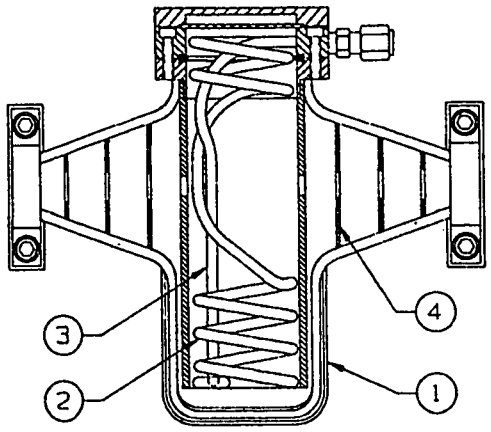

Figure 3-4: The charge exchange canal. (1) Lithium reservior, (2) heater, (3) Thermocouple, (4) Baffels.

Charge-Exchange Canal

The charge exchange canal is shown in figure (3-4). It consists of a reservoir filled with lithium. Upon heating a lithium vapour is formed in the upper part of the canal. On passage through the canal positive ions pick up electrons and are converted into negative ions. A number of parallel baffles reduces the escape of lithium vapour out of the canal. Most of the lithium vapour condenses on the baffles and flows back into the reservoir. In this way lithium is continuously circulated in the canal and hence vacuum contamination and lithium consumption are kept to a minimum. Lithium has been chosen as a canal charge because of its easy handling, safety compared to other alkali metals and good negative ion yield. The melting point of the lithium is optimal in maintaining control of both the central reservoir and condenser temperature.

3.2.2 Accelerator Sector

The acceleration tube together with terminal gas stripper assembly, and the 3 MV highly-regulated solid state power supply are located inside a pressure vessel filled with sulphur hexafluorine gas (SF_6) normally at 135 psi. For the utmost in reliability and low noise levels, the system has no moving parts except the pumps[75]. A gas

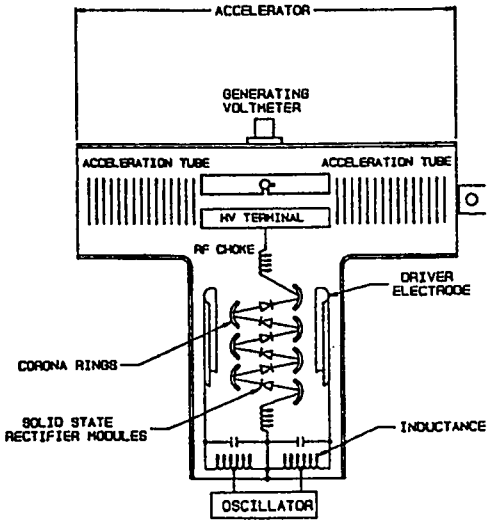

Figure 3-5: Internal view of the accelerator sector shows the basic components of the accelerator.

stripping region located in the terminal housing, between the low and the high energy halves of the accelerator tube, removes electrons from high energy ions. The negative ions from the low-energy acceleration tube lose electrons in the stripper and become positive so that they are accelerated a second time down the high-energy end of the acceleration tube.

The hart of the Tandetron is parallel fed Cockroft-Walton type high voltage power supply. It is based on an 5 kW-circuit RF oscillator operating at approximately 40 kHz. As shown in figure (3-5), driver electrodes are formed like half-cylinder shape and they capacitively feed the RF power to coupling rings. A voltage multiplier cascade rectifies the RF power and generates the high voltage. An advantage of this design is the proven reliability due to the absence of moving parts inside the pressure tank.

In the high current version, a turbo pump is located in the high voltage terminal to circulate the gas flowing out of the stripper canal. In this way 95% of the stripper gas is circulated and the gas load of the accelerator tube is minimized. This reduces radiation and unwanted charge exchange processes inside the tubes.

3.2.3 The High-energy Extension

On the high energy side of the accelerator the ion beam bases through an electrostatic quadruple-triplet lens for focusing purposes. A switching magnet analyses the ion on mass and charge-state and deflects the ion beam into the desired beamline.

Five ports are available on the analysing magnet of the high energy end of the accelerator for setting up experiments. These ports are located at +30°, +15°, 0°, -15°, and -30°, respectively, with respect to the beam line of the accelerator. Presently these ports are utilized for *NRA*, *μPIXE*, and *PIXE* and *RBS* simultaneously.

The terminal voltage was calibrated by AL-JUWAIR *et al.*[75] using several resonance and threshold nuclear reactions. Among the reactions are: $^{19}F(p,\gamma)^{16}O$ at E_R = 340.45, 484, and 872.1 keV; $^{27}Al(p,\gamma)^{28}Si$ at E_R = 992 keV; $^{7}Li(p,n)^{7}Be$ at $E_{threshold}$ = 1880.5 keV[75]. The relation between the displayed reading of the terminal voltage gauge and the energy of the ion of charge Z is given by

$$V_{Term} = \frac{E(\text{keV}) - E_{inj}(\text{keV})}{Z+1} \tag{3.1}$$

Where E denotes the acceleration energy, and E_{inj} denotes the injection energy given by

$$E_{inj} = E_{ext} + E_{pre} \tag{3.2}$$

Where E_{ext} denotes the extraction energy, and E_{pre} denotes the preacceleration energy. Presently E_{ext} = 17 keV, and E_{pre} = 30 keV, thus E_{inj} = 47 keV. The denominator in equation (3.1) means that the ion of charge Z is accelerated $(Z+1)$ times. So for protons $(Z = 1)$, it will be accelerated twice, once by negative extraction to the terminal as H^-, and once after stripping at the terminal as H^+. Similarly, for α particles $(Z = 2)$, they will be accelerated three times. Once by negative extraction to the terminal as He^-, and twice after stripping at the terminal as He^{++}.

3.3 Target Chamber

The target chamber was originally installed as an automated *RBS* chamber with a remotely controlled goniometer, but modified to include a *PIXE* setup. The schematic diagram for the chamber setup is shown in figure (3-6). The chamber has been accommodated at the -30° port with respect to beam line. The Si(Li) was brought as close as possible to the target (11 cm) by means of a stainless steel well with a window at the end close to the detector. The window was made from a Kapton foil of 3 mg/cm^2 thickness which allows soft X rays to pass through and at the same time withstands repeated venting and pumping of the *PIXE/RBS* chamber to a pressure of about 10^{-6} torr.

A beam collimator was constructed from high-purity aluminium with the collimator mutable ends made from graphite at various hole sizes in order to control the final beam spot diameter on the target. The beam spot diameter is selected to be 2.6 mm. In addition, a 2μm-thick beam diffuser, made from aluminium foil and used for proton beams, was constructed and installed after the switching magnet to obtain a homogeneous beam spot at the target. A homogeneous beam is essential for quantitative *PIXE* analysis. Beam uniformity is checked visually during every run by observing the beam spot on a ZnS foil.

The external absorber which is used to attenuate low energy X rays was constructed from graphite. A hole of 1 mm in diameter limits the intensity of these X rays and thus eliminates pile-up problems from these lines and constrains the majority of X-ray photons to incident on the active area of the Si(Li) detector crystal to avoid the edge effects, which reduces the distortion in peak shaping and minimizes the tailing effect. Additionally, pinhole absorber reduces the bremsstrahlung at low energy by secondary electrons which are not isotropic with respect to the solid angle. High intensities from the low energy X rays result from low atomic number elements which are major elements in most matrices. The goniometer is controlled by IBM PC computer and equipped with precise stepper motors for controlling the position of the sample holder

in three dimensions. The desired beam-spot position on the target is tested by sending a laser beam through the beam line and the collimator, then the desired coordinates of the spot are obtained and fed to the computer, such that the goniometer memorizes the position at various run. A 3.4 mm-width and 4.5 mm-length rectangular aperture is placed in front of surface barrier detector SSB to reduce the solid angle of the detector and minimize the dead-layer effects of the SSB detector.

The same computer is interfaced to a Nuclear Data ND62 multi-channel analyser which is used with the computer for data acquisition and analysis. The system was designed not only for simultaneous analysis of "normal" *RBS* and *PIXE*, but also with the capability of performing Rutherford scattering at "grazing" angle and "channelling" at the same time. However, The major activity is concentrated on simultaneous normal *RBS* and *PIXE* measurements.

3.4 Data Acquisition System

A schematic diagram illustrating the *PIXE/RBS* data acquisition system configuration is shown in figure (3-7). X rays from *PIXE* are measured with a detection system based on a Si(Li) detector. In *RBS*, the backscattered particles are measured with a solid-state surface barrier (SSB) detector system. The output of each of the two detectors is fed to standard NIM-model electronic equipment including a preamplifier and the associated linear amplifier. The linear output of the amplifier is digitized by an analogue to digital converter (ADC) and processed by the on- line computer to produce simultaneously *PIXE* and *RBS* energy spectra. The system remotely controls the goniometer and electronics for sample positioning, and charge accumulation[78].

Practically the electronic systems are designed to maintain linear relationship between the energy of the radiation and the charge signal created in the detector. The electronic parameters such as high voltage power supply, gain of the amplifier, and pulse shaping time are adjusted after heedful investigation to acquire a highly qualified

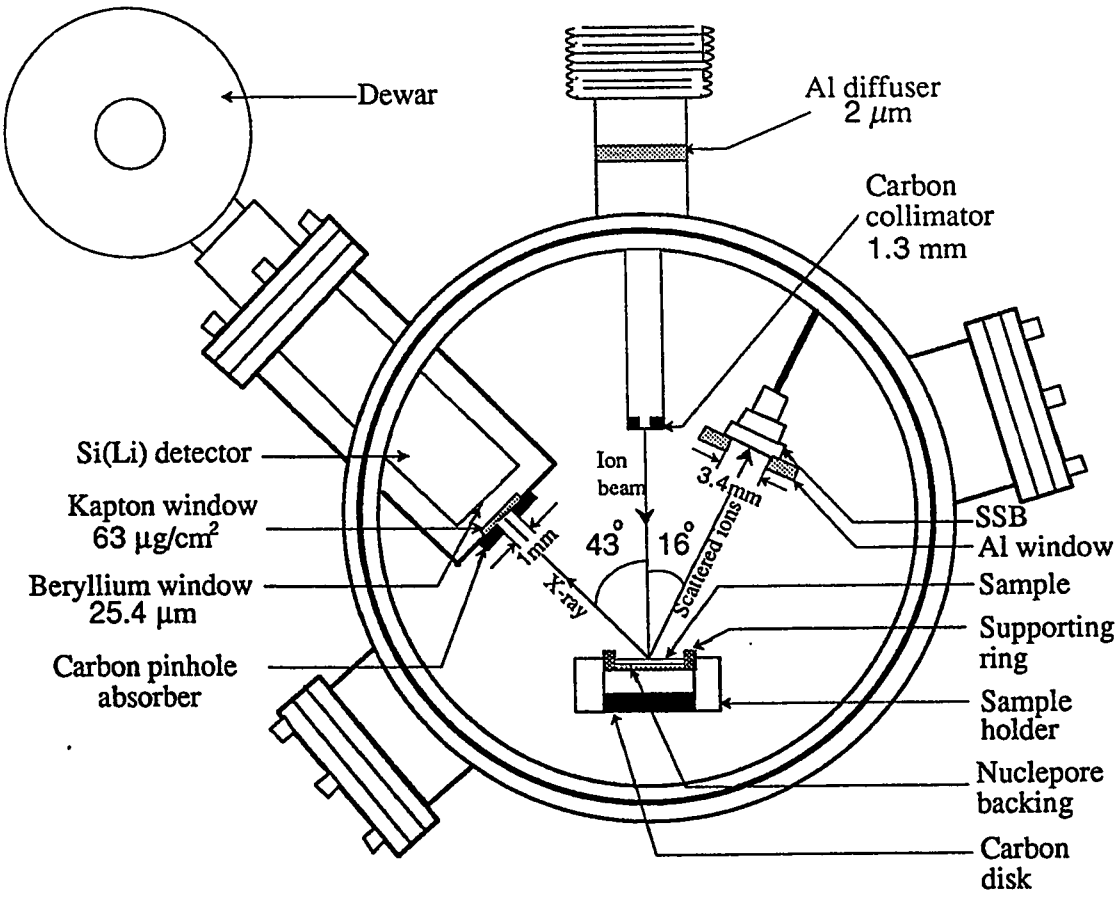

Figure 3-6: Schematic diagram shows the *PIXE/RBS* setup at the Tandetron accelerator laboratory.

and efficient operation mode of the system and capability to view the concerned part of the energy spectra with achieving the optimum peak resolution and minimizing the undesired effects like pile-up and detector dead time. A listing for all electronic parameters are shown in table (3.2) for *PIXE* setup, table (3.3) for *RBS* setup, and table (3.4) for both *PIXE/RBS* setup.

3.4.1 Solid-State Surface Barrier Detector (SSB)

Typically, the surface barrier detector (SSB) is a diode made with high-quality single-crystal silicon with a very thin evaporated gold (40 $\mu g/cm^2$) contact on an etched n-type silicon wafer. The gold evaporation forms the front rectifying contact of the diode, and the rear ohmic contact is composed of 40 $\mu g/cm^2$ of evaporated aluminium. This is depicted in figure (3-8).

When a reverse-bias voltage is applied to the diode, an electric field is created in the depletion region. Thus the incident radiation entering from n-type side and stops in the depletion region releasing free electron-hole charge carriers. Consequently these charge carriers are collected by the electric field resulting in a potential drop across the junction, which is conveyed to the preamplifier.

The thickness of the crystal within the SSB must be designed to stop protons and α particles in the depletion layer. Thus from figure (3-9), which displays range-energy curve for various charged particles in silicon, shows that 100 μm thickness meet this requirement for 2.5 MeV protons and 1to 6 MeV α particles. The model of SSB detector that is employed in this experiment (see table 3.3) satisfies this requirement.

The SSB detectors are sensitive to light. Since the energy of the visible light ranges from 2-4 eV which exceeds 1.1 eV energy gap in silicon. Therefore, the detector generates large noise when exposed to light. Thin gold coating is insufficient to stop ambient light. So it is important to operate the SSB detector in the light-tight chamber[79].

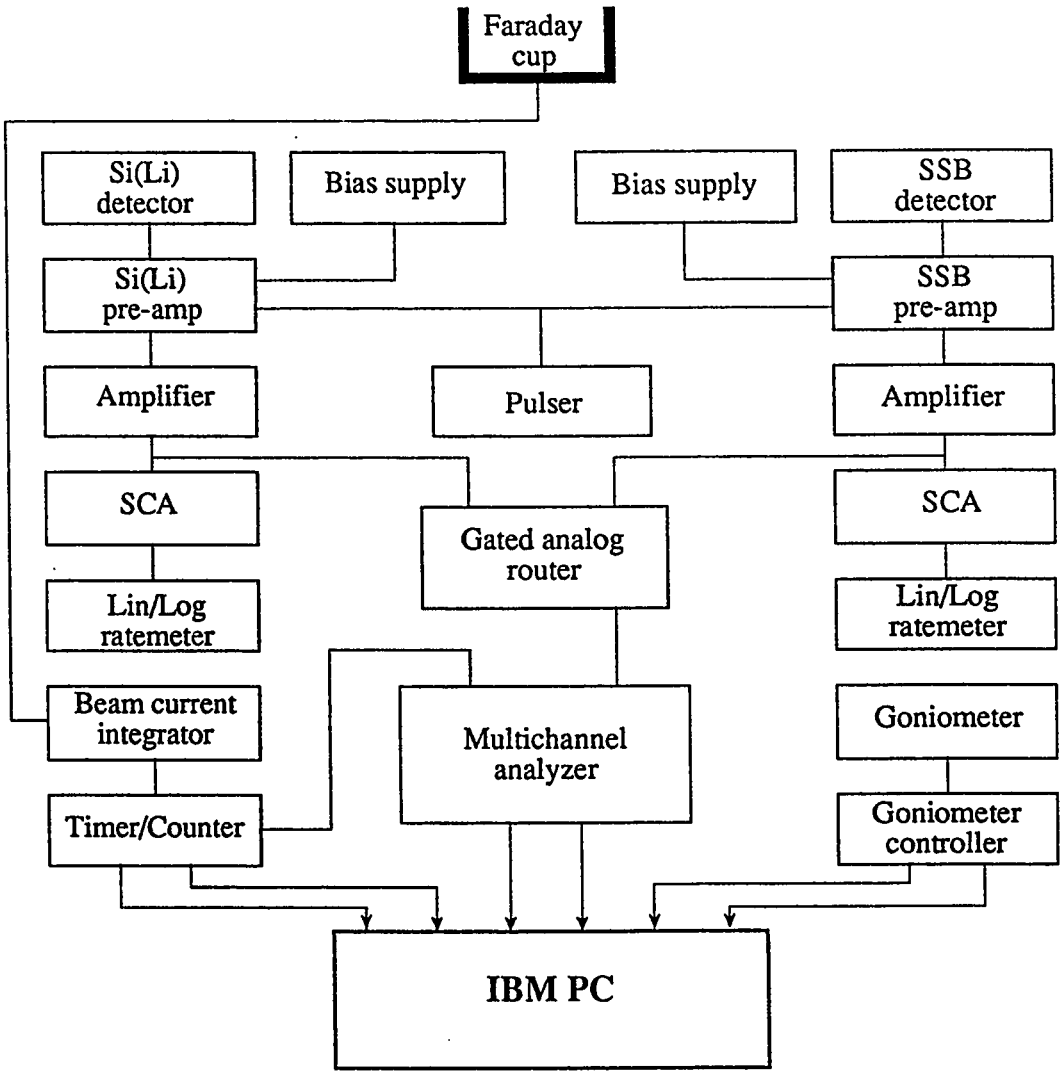

Figure 3-7: A block diagram of the *PIXE/RBS* data acquisition system at Tandetron accelerator laboratory. (Reproduced from HALLAK and DAOUS, 1992.)

Table 3.2: The data acquisition system for *PIXE*.

Electronic	Model	Parameters	Adjustments
Si(Li) detector	*EG&G ORTEC*		
	SLP-10180	Resolution	190 eV for Mn K_α
		Active area	314 mm^2
		Sensitive depth	5.35 mm
		detectro-window distance	5 mm
		Be window thickness	25.4 μm
		Gold layer	$\sim$ 200 Å
		Silicon dead layer	0.1 μm
Preamplifier	hypridized		
High voltage bias supply (HV)	TENNELEC TC 950	Output	-1500 V
Amplifier	*EG&G ORTEC* 577	Output	Back conn. neg. delayed unipolar pulse
		Coarse gain	200
		Fine gain	0.74
		Pulse shaping time	10 μsec

Table 3.3: The data acquisition system for *RBS*.

Electronic	Model	Parameters	Adjustments
SSB detector	*EG&G ORTEC*		
	A-016-100-100	Depleted	Partially
		Max resolution	16 keV for ^{241}Am
			$E_\alpha = 5.486$ MeV
		Active area	100 mm^2
Preamplifier	*EG&G ORTEC* 142B	Output conn.	Junction E
		H.V. conn.	Bias
High voltage bias supply (HV)	TENNELEC TC 908	Output	+500 V
Amplifier	TENNELEC TC 241	Output	back conn. +ve unipolar
		Coarse gain	50-200
		Fine gain	0.74
Single-Channel analyzer (SCA)	TENNELEC TC 450	UL	10
		LL	0.3
		Mode	Norm
		DC/AC	DC
LIN/LOG Rate meter	TENNELEC TC 527	Linear range	1 M
		Time constant	0.3 sec
		Prescale	× 10

Table 3.4: The common data acquisition system for *PIXE/RBS*.

Electronic	Model	Parameters	Adjustments
Gated Analog Router (GAR)	Nuclear Data (ND)	Mode	2
		Memory field	512
		Preset time	LT
		Base	9
		Multiplier	10^4
Timer/Counter	*EG&G ORTEC* 773	Master/Slave	Master
		m	1
		n	4
		Counter mode	Counter
Digital Current Integrator (DCI)	*EG&G ORTEC* 439	Multiplier	3
		Current(Amp)	10^{-9}
		Coul/pulse	10^{-10}
Analog-to-digital converter ADC	Combined in the MCA		
Multi-Channel Analyzer (MCA)	Nuclear Data ND62		

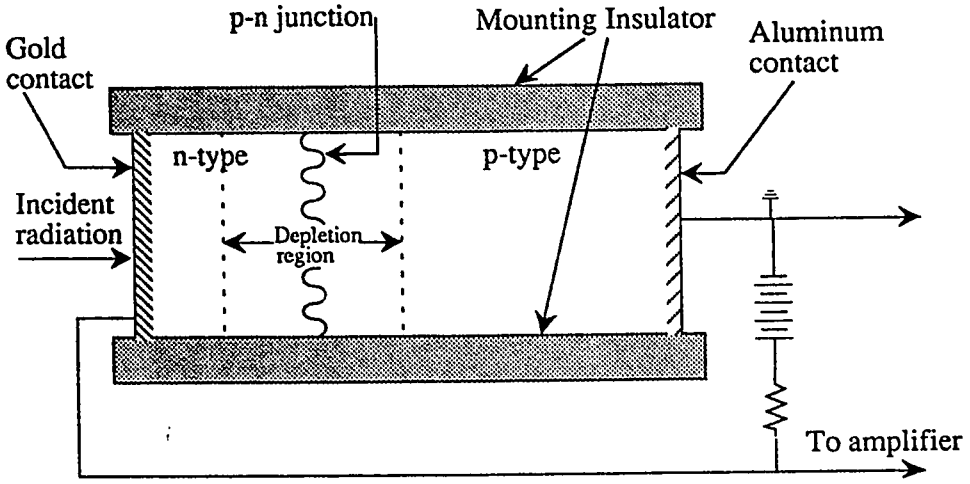

Figure 3-8: A schematic cross-section view for a typical solid-state surface barrier detector.

3.4.2 Lithium-Drifted Silicon X-Ray Detector

If lithium is diffused into silicon p-n junction in the previous configuration, the depletion region will be increased that maximizes the productivity of the configuration to detect photons. The Si(Li) detector provides the spectroscopist with a highly-sensitive premium performance research tool for detecting X rays produced with nuclear accelerator, radioactive sources, or X-ray tubes. The energy range of detection is from less than 1 keV to 60 keV, depending on the resolution of the detector and the thickness of the end-cap window.

The Si(Li)X-ray detector consists of a lithium drifted silicon crystal, cryogenic high-gain, low-noise hybridized preamplifier, and liquid nitrogen dewar. The X-ray photons are detected via three interaction mechanisms which the photons most often undergo in the silicon crystal. These mechanisms are photoelectric effect, Compton scattering, and pair productions and. Each mechanism is characterised by a linear absorption coefficient that vary rigorously with the energy of the photon. Figure (3-10) shows the linear absorption coefficients for the three mechanisms versus the photon energy for silicon and germanium. The figure verifies that the germanium ($Z = 32$) is further efficient than silicon ($Z = 14$). This is referred to the conclusive dependence of the

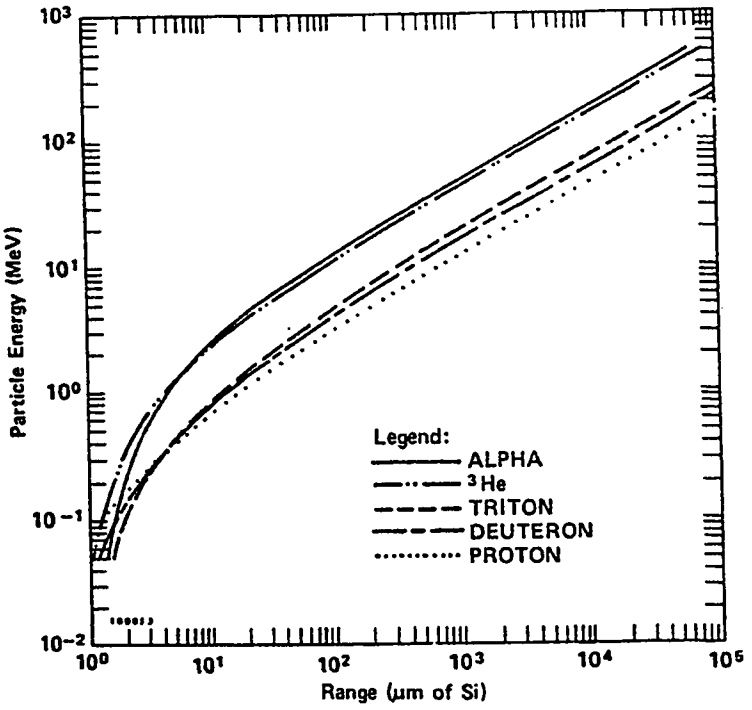

Figure 3-9: Range-Energy curves for charged particles in silicon. (Taken from *EG&G ORTEC*, 1991/92.)

linear absorption coefficients on the atomic number of the medium, for example the linear absorption coefficient for the photoelectric effects varies roughly as Z^4. However, the germanium detectors have a grave disadvantage, that the germanium has absorption edge at 11.8 keV which produces a sudden alteration in the efficiency around this energy. Moreover, for lithium-drifted, Ge(Li), detectors must be cooled to liquid nitrogen temperature (77° K), either in operative mode or not, otherwise the lithium will diffuse out of the germanium crystal. For Si(Li) detectors, in the other hand, the effect of liquid nitrogen is to hold the noise at low level, and there is no any damage would happen to the crystal when the dewar is out of liquid nitrogen.

Despite its low efficiency compared to NaI(Tl) scintillation detector[1], Si(Li) detector is favourable in this experiments because of its high resolution, measured for potassium K_α line (5.6 keV) to be 190 eV (compared to few keV for NaI(Tl) scintillation detector). This is because the pulses which are produced in the Si(Li) detector are conveyed to the preamplifier directly. In the other hand the pulses which are produced in the NaI(Tl) detector experience many stages, such as the photocathode and the photomultiplier tube, before conveyed them to the preamplifier. This consequently increases the statistical deviations for the counting system and hence reduces the quality of detector resolution. Figure (3-11) shows a schematic diagram for the configuration and the geometry of the Si(Li) detector system that is employed in this experiment.

3.4.3 Preamplifier

A preamplifier is specifically designed to accept the signal from a detector with minimum shaping in order to preserve the maximum signal-to-noise ratio[79]. Since the input signal at the preamplifier is generally weak, preamplifiers are normally mounted as close as possible to the detector so as to minimize cable length. In this way, pick-up of stray electromagnetic fields is reduced and cable capacitance, which decreases the signal-to-noise ratio, is minimized.

[1] Because Si has lower atomic number than NaI.

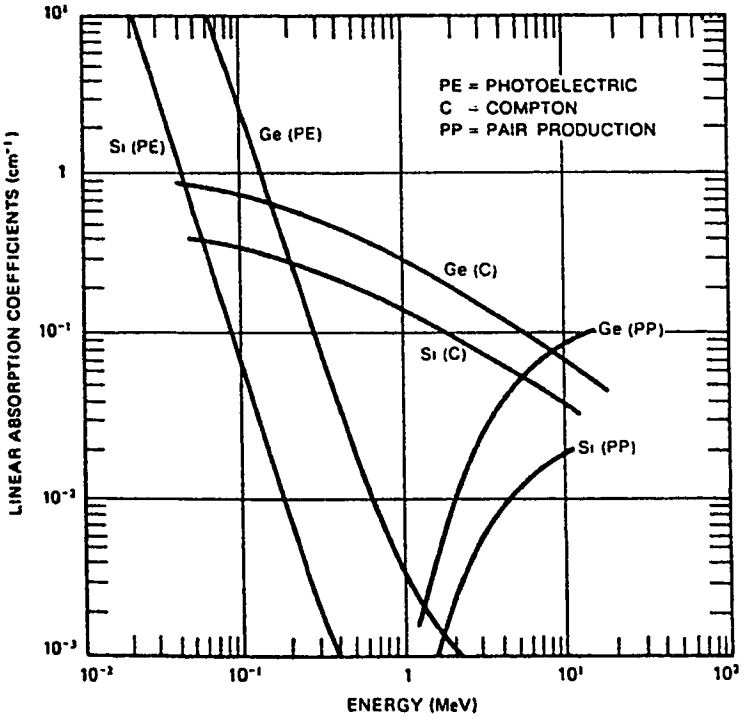

Figure 3-10: Linear absorption coefficients versus Gamma-Ray energy for Si and Ge. (Taken from *EG&G ORTEC*, 1991/92.)

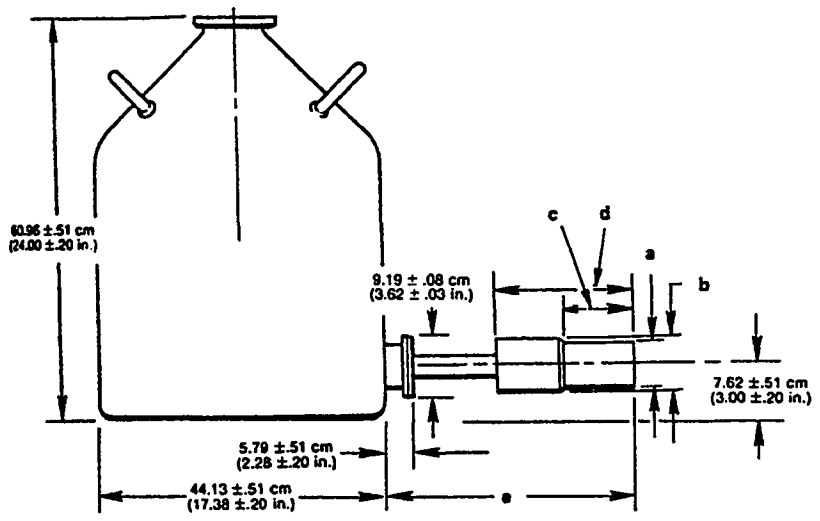

Figure 3-11: A schematic diagram for the configuration and the geometry of the Si(Li) detector system. (Taken from *EG&G ORTEC*, 1991/92.)

The three basic types of preamplifiers are voltage sensitive, current sensitive, and charge sensitive. The first type requires that the detector capacitance to be independent of the bias voltage and other parameters which does not meet the situation for SSB and Si(Li). The second type is accommodated with low input impedance and designed to convert fast current pulses to voltage pulses. However for a current pulses lasting from 10^{-9} to 10^{-5} seconds, which is the situation for SSB and Si(Li) detectors, the current sensitive preamplifier is inefficient and the third type, charge sensitive preamplifier, is designed to perform this task efficiently. Therefore the charge sensitive preamplifiers are employed in this experiment for both SSB and Si(Li) detectors[79].

3.4.4 Linear Amplifier

The linear pulse-shaping amplifier performs several key functions. Its primary purpose is to magnify the amplitude of the preamplifier output pulse from the millivolt range into the 0.1- to 10-V range without losing pulse height information. This facilities accurate pulse amplitude measurements with analog-to-digital converters (ADC), and single-channel pulse-height analyser (SCA). In addition, the amplifier shapes the pulses to optimize the energy resolution, and to minimize the risk of overlap between successive pulses. Most amplifiers also incorporate a baseline between pulses is held rigidly at ground potential in spite of change in counting rate or temperature. The adjustable pulse shaping time of the amplifier allows to reduce the pile up effects due to addition of two pulses following each other within the selected pulse shaping time. Pulse shaping also optimize signal to noise ratio[80].

Frequently, the requirement to handle high counting rates is in conflict with the need for optimum energy resolution. With many detector-preamplifier combinations, achieving the optimum energy resolution requires long pulse widths. On the other hand, short pulse widths are essential for high counting rates. In such cases a compromise pulse width must be selected which optimizes the quality of information collected during the measurement[79].

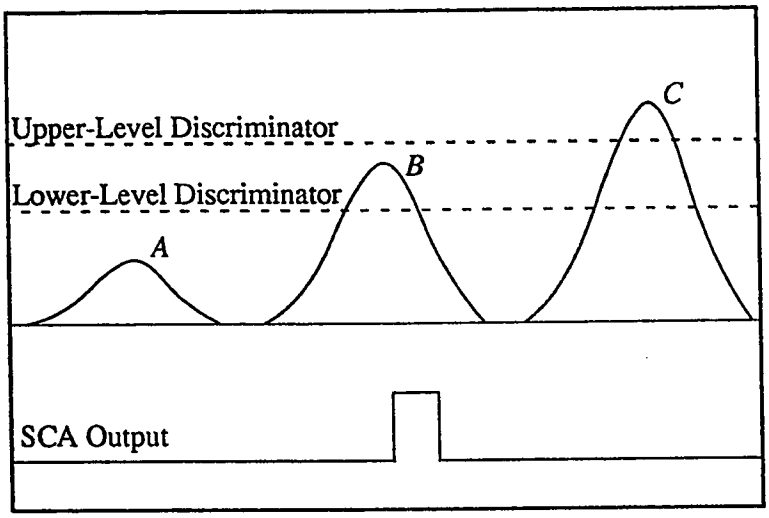

Figure 3-12: A diagram displays the single-channel analyser function. (Reproduced from *EG&G ORTEC*, 1991/92.)

3.4.5 Single-Channel Analyser (SCA)

The single channel analyser is a device which sorts incoming analog signal according to their amplitudes. The function of SCA is summarized in figure (3-12). It contains a lower level discriminator below which signals are blocked as revealed in the figure for pulse *A*. In addition, there is also an upper level discriminator above which signals are rejected as revealed in the figure for pulse *C*. Thus only signals which fall between these two levels, as the case for pulse *B* in figure (3-12) generate a standard positive logic signal at the output of the single channel analyser[77, 79].

3.4.6 Analog-to-Digital Converter (ADC)

The analog-to-digital converter measures the maximum amplitude of an analog pulse and converts that value to a digital number. The digital output is a proportional representation of the analog amplitude at the ADC input.

For sequential arriving pulses, the digital outputs from the ADC are fed to a dedicated memory, or a computer, and sorted into a histogram that represents the spectrum of input pulses heights. If the input pulses come from an energy spectroscopy

amplifier, our case, the histogram corresponds to the energy spectrum observed by the associated detector. When the output of a time-to-amplitude converter is connected to the ADC input, the histogram represents the time spectrum that measured by the time-to-amplitude converter[79].

In this experiment, the ADC and the histograming memory are combined in an ND62 Nuclear Data multi-channel analyser.

3.4.7 Digital Current Integrator (DCI)

The digital current integrator was designed to accurately measure dc or the average value of pulse current, such as accelerator beam currents, detected by Faraday cup. It digitizes the input current by producing an output pulse for specific values of input charge. In the model was utilized in this experiment, a front-panel switch permits the selection of three different amounts of charge (10^{-10}, 10^{-8}, or 10^{-6}, Coulomb) required to produce an output pulse. The instrument has a digitizing rate from 0-10 kHz to provide wide dynamic range on each setting and high-resolution readout without meter interpolation[79].

3.4.8 Log/Lin Rate Meter

The Log/Lin Ratemeter provides two mode of operation, linear and logarithmic. The linear mode has 11 full-scale ranges from 10 to 10^6 counts/sec in 1-3-10 steps. The 5-decades log mode covers the ranges from 10 to 10^6 counts/sec in a single span. These selections permit logical operation of the instrument when measuring low, medium, or high steady pulse rates or when monitoring rates that vary through a wide range[79].

3.5 Data-Reduction Codes

For a shorter-time performance and literal analysis, a series of computer codes, available at Tandetron accelerator laboratory (TAL), are employed to automate the system and

analyse the collected data. These codes can be interfaced and transferred from certain format to another using special conversion codes. A brief summary of the codes will be given in the following.

3.5.1 Tandetron Operating System (TOS)

This code is written to control the operation of the accelerator. It is installed to IBM PC computer. The code controls the goniometer controller, the timer/counter panel, and the multi-channel analyser by means of interfacing routine inherent in the code. Sample position and total accumulated charge are fed to the computer. After sending the ion beam to the sample, and using run command in the computer, the computer directly resets the timer/counter and the multi-channel analyser for a new run. Each one Coulomb is considered as one cycle. The run keeps on until the desired charge accumulation is achieved. Afterward, the run will be halted and the data which are stored in the MCA will be transferred to the computer and stored in a TOS-format diskette.

A modifications was implemented to the original code[81] in order to perform a combined data collection from the *RBS* and *PIXE* set-up. This allows the analyst to investigate both data in shorter time and in efficient manner.

3.5.2 Material Analysis by X-Ray Emission (MAXE)

This code is created to attain an analytical system for combined *RBS* and *PIXE* analysis and it can handle data that is stored in TOS format. The code is based on a data library of element-specific X-ray energies and their relative intensities in *PIXE,* throughout using the energy-channel and peak-FWHM calibration parameters[81]. The MAXE code capable to offer optimal fit over all energy ranges of *PIXE* spectrum including low-energy region. It can also perform spectral deconvolution and peak separation and background subtraction. The code involves many utilities, including the ability for positive identification of peaks present in the spectrum. Therefore, in this experiment,

this code is primarily employed to preview the energy spectrum and to identify its X-ray peaks prior to analysis[81].

3.5.3 Rutherford Backscattering Analysis Code (RUMP)

This code operates along with GENPLOT code and employs its utilities for analysis. The RUMP code makes use of the theoretical relations for Rutherford backscattering process, derived in section 1.2.1, to simulate the *RBS* spectrum. Parameters such as layer thickness, elemental compositions, elemental ratios, and ion beam type and its energy are fed to the computer to execute the simulations. The simulation parameters regarding thickness of layers and other built-in parameters, obtained from the theoretical derivations of *RBS*, are varied during the fitting to obtain quantitative results. Optimization is done according to a maximum likelihood chi-squared value, so that the best fit values of parameters and their uncertainty can be determined[82, 83].

Accordingly, The code will be utilized to obtain the peak area of the scattered ions from the elements of interest. The experimental data originally stored in TOS format, therefore, a convergent file called "dataconv.exe" convert TOS format into RUMP format automatically. Then the data can be analysed and fitted.

3.5.4 The PIXAN-PC Package

This program was created by CLAYTON[32] at the Australian Atomic Energy Commission Research Establishment. The package consists of two major programs, BATTY and THICK, written in FORTRAN 77. The first program, BATTY, deals with the implementation of the spectrum analysis and estimates the element peak area. The second program, THICK, calculates the X-ray yields for both thin and thick samples. These programs are complementary and together they provide the data necessary to evaluate PIXE spectra. For our experiment, only BATTY is needed.

The program BATTY performs the spectral fitting using the same procedures mentioned in section 2.3.1. Additionally there is a built-in ability to strip the escape peak

of silicon. The database that the program reads from them are DSET2, which embodies the element energies and relative intensities, and DESET3, which embodies the attenuation and stopping power data mainly used for thick samples only. Thus The effective data set in this case is only DSET2. The program employs two techniques for the background fitting, which are polynomial, as given in equation (2.115), and iterative background, as given in the test representation in equation (2.116).

Modifications to the program BATTY, were done by Tandetron group[78], included, changing the detector parameters to suit the detection system of in the TAL. For example, the parameters for the determination of the Si(Li) efficiency, that is currently used in this experiment, were changed by estimating its relevant efficiency using the method that explained by COHEN[84, 78]. Additionally, investigation of the different fit parameters were also performed. This included the mode of background fitting, the shape of characteristic peaks, the energy-channel relationship, the parameters that determine the detector resolution at different energies, and the parameters for a possible shift in the energy calibration. On some occasions, the data bases for the fundamental parameter were modified to include L X rays of some heavy elements[78]. The peak-shape model adopted in the program is Gaussian peak, that may be distorted by a low energy exponential tail. The program model the fact that the non-Gaussian response is proportionally greater for the K_β lines than for the K_α[32]. Accordingly the tailing is modelled by an exponential tail with a step function being placed between K_α and K_β only. Thus the peak-shape function that is incorporated in equation (2.113) is given by

$$g_j(E, E_j) = \exp\left[-\frac{(E-\mu_j)^2}{2\sigma_j^2}\right] + P_5 \exp\left[P_6^2(E-\mu_j)\right] + P_7\Theta(E) \qquad (3.3)$$

Where σ_j is the resolution of the detector for the jth line expressed by the FWHM, and it is given as

$$\sigma_j = P_1 + P_2 E_j \qquad (3.4)$$

And μ_j is the centroid of the jth line given as

$$\mu_j = P_3 + P_4 E_j \tag{3.5}$$

The set $\{P_k\}_{k=1}^{7}$ are varied during the least square fit. Initial estimates for P_1 to P_4 are read into the program and they are listed in table (3.5). Initial values for P_5 to P_7 are provided by the program. The function $\Theta(E)$ is a step function defined as

$$\Theta(E) = \begin{cases} 1 & \text{If } E_{K_\beta} > E > E_{K_\alpha} \\ 0 & \text{Elsewhere} \end{cases}$$

The parameter In order to keep the slope of the exponential tail to be positive the parameter P_5 is set it to be zero when $E > \mu_j$. The analytic approach that is given in equation (3.4) and equation (3.5), is favoured due to at least two advantages that compensate for the computational overhead incurred:

1. The slight electronic drifts which alter the energy calibration between sample and standard runs are automatically catered for by basing the peak construction on the calibration relation (equation (3.5)) and allowing parameters P_3 and P_4 to be variables determined by the fitting procedures; the same is done for the parameters P_1 and P_2 of equation (3.4).

2. The relative intensities of the various lines of a given element in the analytical model may be corrected in straightforward manner for effects of the uncertainty in efficiency measurements.

A user interface program, called PASS (*PIXE* Analysis Software System), was written in C language by the Tandetron group[78] and is used for automating-file organizations and analysis program operation for PIXANPC. The raw *PIXE* data files are primarily obtained in TOS format. A subroutine called PIXCON was written to convert data files from TOS format to PIXANPC format which enable the analyst to use

Table 3.5: The initial estimations for the fitting parameters.

Parameters	Initial values
P_1	0.06864
P_2	0.00361
P_3	0.008602
P_4	0.996312
P_5	Determined by the fitting
P_6	Determined by the fitting
P_7	Determined by the fitting

PIXANPC with proper mode of operation.

The essential parameters those are fed to BATTY control file include background fitting technique, optional absorber type, elemental compositions, and energy of the fitting. After execution, the program displays the plot of the raw data, generated data, and generated background as well as the chi-squared of the fitting. Thus one can alter the parameters in the control file until a likelihood chi-square value is obtained. The peak areas of the reference lines for each element and the floating parameters, such as energy-channel calibration, peak centroid, and detector resolution, are stored in the output file. Originally, The program BATTY was composed to read the elements and their total L X rays relative intensities with respect to one reference line which is usually L_α line. For the case of this experiment, one must however be careful since the relative intensities among L subshells exhibit a significant dependence on the type of the projectile and its energy. This dependence is not precisely known so far. In the other hand the relative intensities among lines those belong to particular subshell are independent of the energy and type of the projectile, according to the previous discussion in section 1.1.3. Therefore, the data set DSET2 is modified to make BATTY reads the relative intensities for each subshell-line group or each line group whose lines belong to a common subshell. These groups are fitted according to their relative intensities to one reference line. Table (3.6) shows these groups, the rference line for each, and the common subshell which they belong to. The relative intensities are taken from the experimental values of SALEM *et al.*[15]. This modification does not requires

Table 3.6: The groups of the X-ray lines, their reference lines, and common subshells.

Group	Common subshell	Refrence line
L_α		
L_l		
L_{β_6}	L_3 subshell	L_α
$L_{\beta_{2,15}}$	L_3 subshell	$L_{\beta_{2,15}}$
L_{β_1}		
L_η	L_2 subshell	L_{β_1}
L_{β_3}		
L_{β_4}	L_1 subshell	L_{β_3}
L_{γ_1}		
L_{γ_5}	L_2 subshell	L_{γ_1}
$L_{\gamma_{2,3}}$		
L_{γ_4}	L_1 subshell	$L_{\gamma_{2,3}}$

any additional changes in DSET3 since only thin samples are employed, additionally each element is analysed separately.

Chapter 4

Results and disscusion

4.1 System Calibration

This is the first step in the determination of the ionization cross sections. System calibration involves finding the geometrical factor and efficiency of X rays as prerequisite for the estimation of the production cross sections shown in equation (2.125). Moreover, estimating the peak area requires a precise energy-channel calibration of the Si(Li) detector system.

4.1.1 Geometrical factor and Efficiency Calibration

For K-shell ionization cross sections by proton bombardment, the *ECPSSR* theory provides values agree with the experimental data within $\pm 6\%$, as previously mentioned. Thus one can utilize this attribute to obtain the geometrical factor and efficiency employing the ionization cross sections which are derived from the *ECPSSR* theory. Therefore from equation (2.125) one can directly obtain

$$\gamma(E) = \frac{1}{\varepsilon(E)}\frac{\Omega'}{\Omega} = \frac{1}{4\pi}\frac{N^p}{N_s^x}\left(\frac{d\sigma}{d\Omega}\right)_R^{-1}\sigma_s^x(E)$$

Here $\gamma(E)$ denotes the combined efficiency and geometrical factor. Its energy dependence is a consequence to the energy dependence of the efficiency. For K-shell, the production cross section is related to the ionization cross section through equation (2.126). Hence the calibration factor $\gamma(E)$ is given by

$$\gamma(E) = \frac{\omega_K}{4\pi} \frac{N^p}{N_K^x} \left(\frac{d\sigma}{d\Omega}\right)_R^{-1} \sigma_K^i(E) \tag{4.1}$$

Experimentally, the values of the peak areas N_K^x, as well as N^p, are obtained from K-shell ionization induced by 2.5 MeV protons incident on a set of thin film standard elements listed in table (3.1). The reason of choosing 2.5 MeV protons is that the energy dependence of the cross sections for these elements exhibit a broad maximum around 2.5 MeV[6]. Therefore, small deviations in the energy of the proton beam does not alter the values of the cross sections or peak areas significantly. Additionally, these elements have high sensitivity of detection by 2.5 MeV protons as illustrated in figure (1-23). Therefore, high X-ray yield can be achieved which reduces the statistical fluctuations of the *PIXE* spectra and consequently more precise peak areas can be obtained.

Each sample was bombarded by 1 μC of protons. The peak area N_K^x was obtained using the code PIXANPC through fitting the K_α line as a reference line and model the K_β line using the relative intensities provided by SALEM *et al.*[15]. Figure (4-1) and figure (4-2) show a typical *PIXE* spectra for Fe and Cu, respectively, which modelled and fitted using the code PIXANPC. The K_α peak area was converted to total K-shell yield using the branching ratios obtained from SALEM *et al.*[15]. The backscattering peak area N^p was obtained using the code RUMP. Figure (4-3) and figure (4-4) shows a selective *RBS* spectra for the same samples Fe and Cu, respectively. For the *RBS* spectra, there are no peak overlapping or background continua. Therefore, the peak area, N^p, for each sample was obtained by just finding the area under the relevant peak directly without making any simulation and modelling for the spectrum. The fluores-

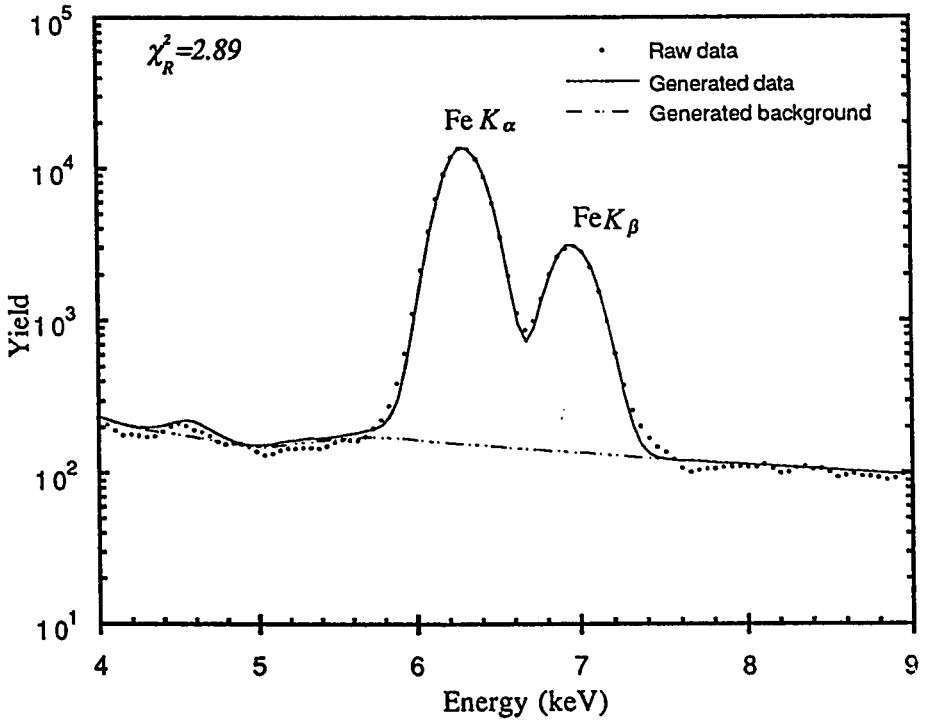

Figure 4-1: The *PIXE* spectrum for 2.5 MeV protons on iron thin film.

cence yields of KRAUSE[10] were adopted in equation (4.1) to convert the production cross section into ionization cross section. The Rutherford formula in lab-frame system given in equation (1.29) was used to calculate the backscattering differential cross section at $\phi = 164°$. The *ECPSSR* ionization cross sections of COHEN and HARRIGAN[51] were embraced in equation (4.1).

Table (4.1) lists the elements and their K_α energy in keV, X-ray yields, backscattering yield, and the normalization factor γ. A plot of γ versus the K_α energy is shown in figure (4-5). The error bars were calculated from the uncertainties of the different parameters involved in equation (4.1). The uncertainty in the fluorescence yields was pointed out by KRAUSE[10] to be within $\pm 3\%$, and the uncertainty in the ionization cross section is $\pm 6\%$. The statistical uncertainties in the backscattering peak areas were obtained using equation (2.119)[72], whereas the statistical uncertainties in the

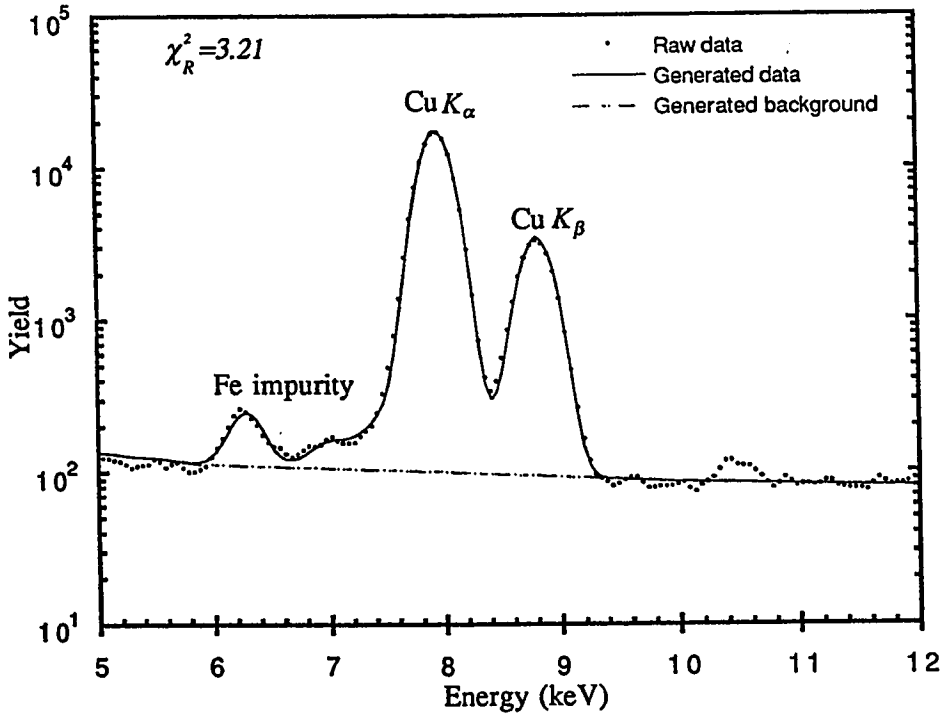

Figure 4-2: The *PIXE* spectrum for 2.5 MeV protons on copper thin film.

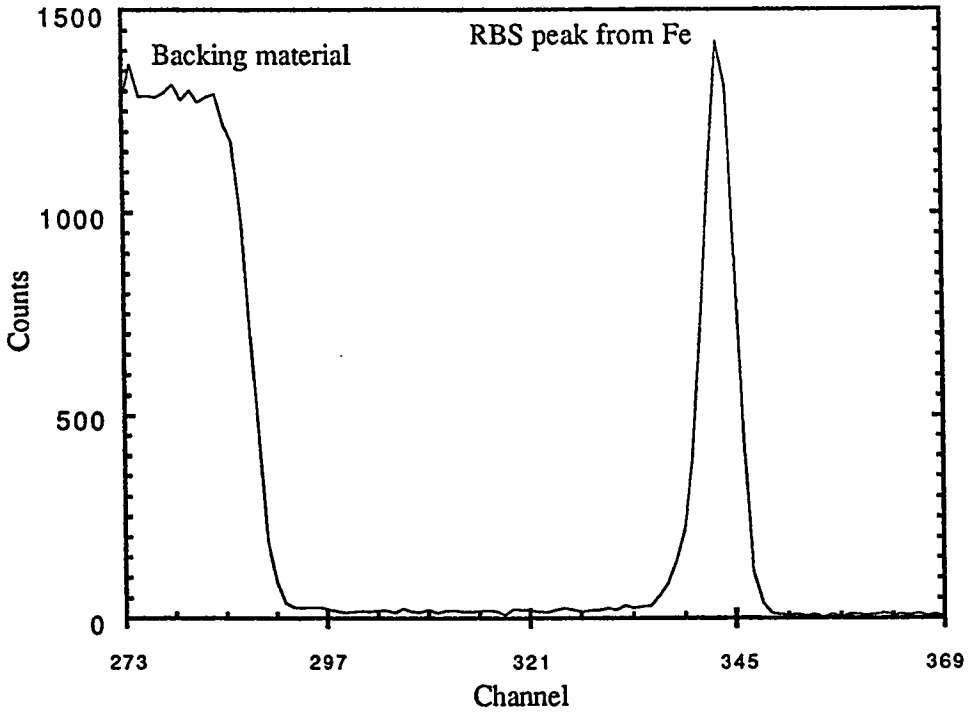

Figure 4-3: The *RBS* spectrum for 2.5 MeV protons on iron thin film.

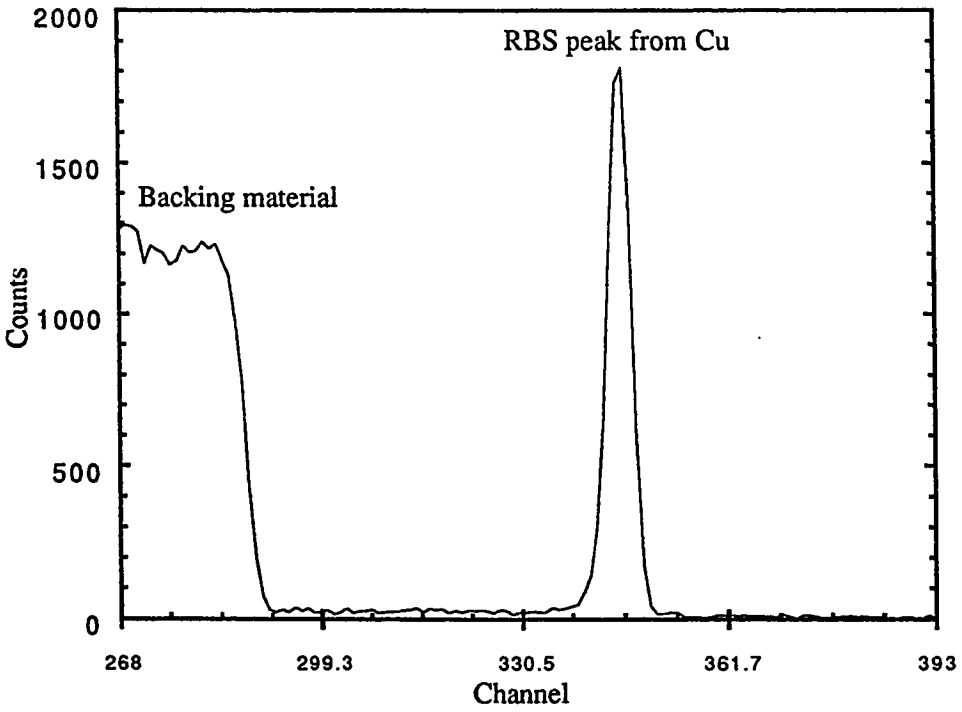

Figure 4-4: The *RBS* spectrum for 2.5 MeV protons on copper thin film.

X-ray yields were provided by the code PIXANPC. Thus the total uncertainty for γ is just the square root of the sum of squares of partial errors. In order to use this factor in further calculations at various X-ray energies, a polynomial fitting is performed as shown in figure (4-5). The polynomial is given by

$$\gamma(E_x) = \sum_{n=0}^{9} a_n E_x^n \tag{4.2}$$

Where the coefficients a_n's are listed in table (4.2), E_x denotes the X-ray energy in keV. The residual of the fitting is shown in figure (4-6). The fitting can reproduce the data points within ±5%. The maximum uncertainty of the estimated values is 7.4% whereas the minimum uncertainty is 6.8%. The energy region in which γ will be employed, for L-subshell ionization cross section measurements, is between 5-10 keV. The average error in this region is approximately 7.1%.

4.1.2 Si(Li) Calibration

The code PIXANPC recognizes the positions of the peaks according to their energies. Pulse-height spectra are obtained as a yield versus channel numbers. Therefore, each channel number must be converted into the corresponding X-ray energy in order to enable the code to recognize the positions of the peaks. This was performed by comparing the peak centroids (in channel number) with the corresponding energies for the *PIXE* spectra of 2.5 MeV protons on Zn and Fe, and collecting the X-ray spectra from X-ray emitters of, ^{55}Fe and ^{207}Bi, which yield ^{55}Mn and ^{207}Pb X rays, respectively, by electronic capture.

Table (4.3) shows the X-ray lines, their energies, and the corresponding channel numbers. The relation between energy in keV and channel number is verified in figure (4-7). The electronic system was designed to achieve a linear relation between the photon energy and its pulse height. This is shown from the linear fitting of the data

Table 4.1: Measured parameters for calculating the normalization factor γ.

Element	Z	E_{K_α} (keV)	N^p	N^x	$\gamma(E)$
Cu	29	08.046	8101.0 ± 90.01	121777.32 ± 348.97	01.776559 ± 0.120910
Ge	32	09.885	9149.0 ± 95.65	099066.24 ± 314.75	01.050234 ± 0.071380
Ni	28	07.477	7834.0 ± 88.51	123895.69 ± 351.99	02.227359 ± 0.151650
Fe	26	06.403	6933.0 ± 83.26	091447.21 ± 302.40	04.670601 ± 0.318670
Cu	29	08.046	7175.5 ± 84.71	108413.53 ± 329.26	01.767568 ± 0.120510
Sr	38	14.100	1433.0 ± 37.85	003891.04 ± 062.38	00.770668 ± 0.056919
Y	39	14.960	1386.0 ± 37.23	002984.93 ± 054.63	00.737927 ± 0.055007
Nb	41	16.612	1211.0 ± 34.80	002349.48 ± 048.47	00.477370 ± 0.036203
Mo	42	17.476	1546.5 ± 39.33	001752.26 ± 041.86	00.629051 ± 0.047564
Ge	32	09.885	1811.0 ± 42.56	017682.49 ± 132.98	01.164698 ± 0.083247
Cu	29	08.046	1605.0 ± 40.06	023487.19 ± 153.26	01.824952 ± 0.131160
Se	34	11.220	1981.0 ± 44.51	013732.17 ± 117.18	00.923008 ± 0.065771
Fe	26	06.403	1557.5 ± 39.47	017616.42 ± 132.73	05.446687 ± 0.392720
Mn	25	05.890	1441.0 ± 37.96	015050.93 ± 122.68	07.805419 ± 0.566120
V	23	04.950	1099.0 ± 33.15	009757.92 ± 098.78	15.907525 ± 1.181100
Co	27	06.929	1718.0 ± 41.45	023818.48 ± 154.33	03.361596 ± 0.240630
Ni	28	07.477	1229.0 ± 35.06	018205.23 ± 134.93	02.378037 ± 0.174240
Rh	45	20.213	2022.5 ± 44.97	001270.48 ± 035.64	00.523851 ± 0.039832
Pd	46	21.121	2878.0 ± 53.65	001303.79 ± 036.11	00.566213 ± 0.042426
Ag	47	22.159	2627.0 ± 51.25	000850.77 ± 029.17	00.618670 ± 0.048145
Ti	22	04.510	1202.0 ± 34.67	011944.30 ± 109.29	18.811836 ± 1.384400
Cl	17	02.622	0571.0 ± 23.90	012458.98 ± 111.62	36.610832 ± 2.913200

Table 4.2: The coefficients of the polynomial fitting for the factor γ as a function of X-ray energy.

Coefficients	Values
a_0	-1.326837×10^2
a_1	1.942645×10^2
a_2	-8.427544×10^1
a_3	1.823953×10^1
a_4	-2.317549
a_5	1.843326×10^{-1}
a_6	-9.313538×10^{-3}
a_7	2.908364×10^{-4}
a_8	-5.12392×10^{-6}
a_9	3.897146×10^{-8}

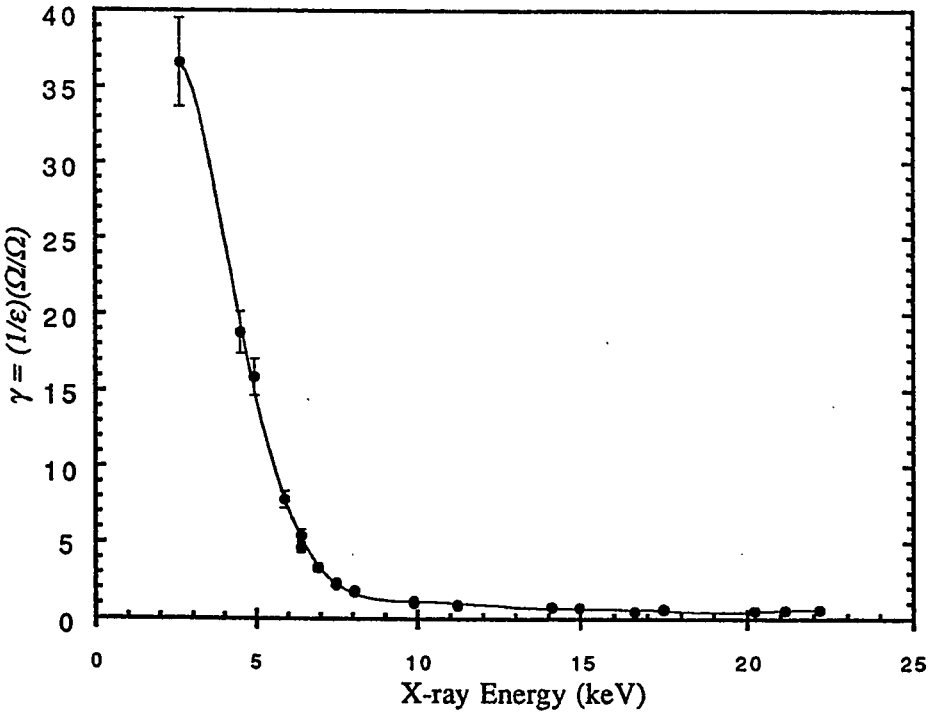

Figure 4-5: A plot of the normalization factor γ as a function of X-ray energy. The points are the experimental points and the curve is the polynomial fitting.

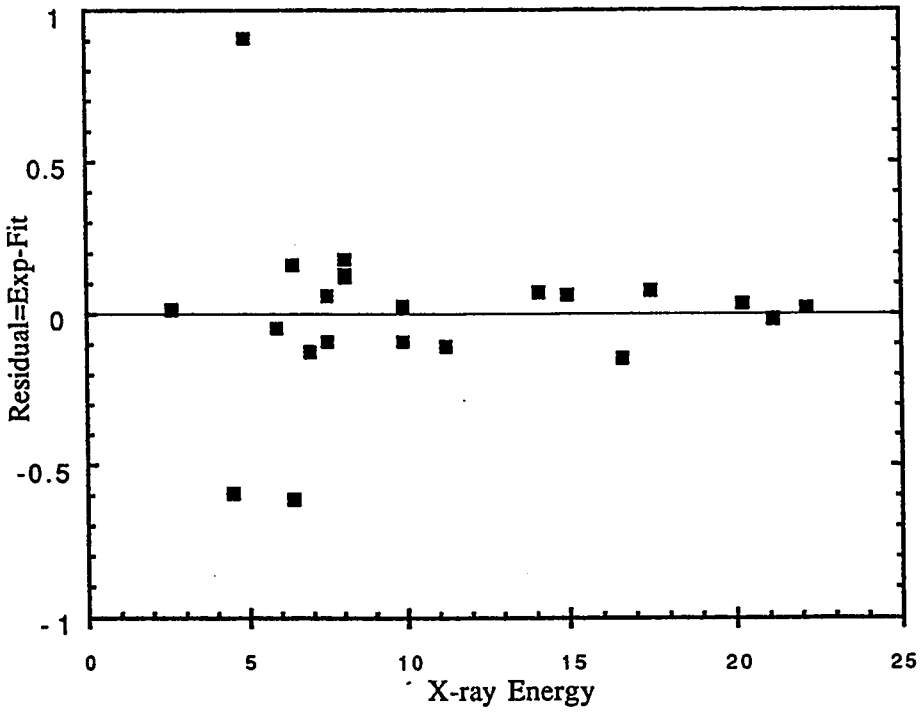

Figure 4-6: The residual of the fit of data points which are shown in the previous figure.

Table 4.3: The X-ray lines, channel number, and their energies for Si(Li) energy-channel calibration.

Element	Centroid	Energy (keV)
Zn K_α	305.80	08.630
Zn K_β	339.00	09.570
Fe K_α	227.00	06.398
Fe K_β	249.90	07.057
Mn K_α	210.15	05.894
Pb L_α	375.40	10.554
Pb L_β	449.10	12.612

points figure (4-7), which is represented by the following relation

$$E_x(\text{keV}) = 0.028057Ch + 0.030683 \tag{4.3}$$

Where E_x is the photon energy in keV, and Ch denotes the channel number obtained for each peak centroids. The small deviations for some points in the figure are attributed to the variation of the counting statistics at that point. This effect is compensated when the parameters P_1 and P_2 in equation (3.4) and parameters P_3 and P_4 in equation (3.5), are varied during the fitting using PIXANPC.

4.2 Spectral Fitting and Peak Area Determination

4.2.1 Yield Measurements

Thin film standards of Ho, Er, and Tm are used to measure L-subshell ionization cross section by helium impact. The specifications of these samples are listed in table (3.1). Since these samples belong to rare earth group, they are chemically unstable and they can interact easily, for example with moist air. Thus they were deposited as a stable compound in the form of tri-fluorine. A well focused and energetically well defined α-

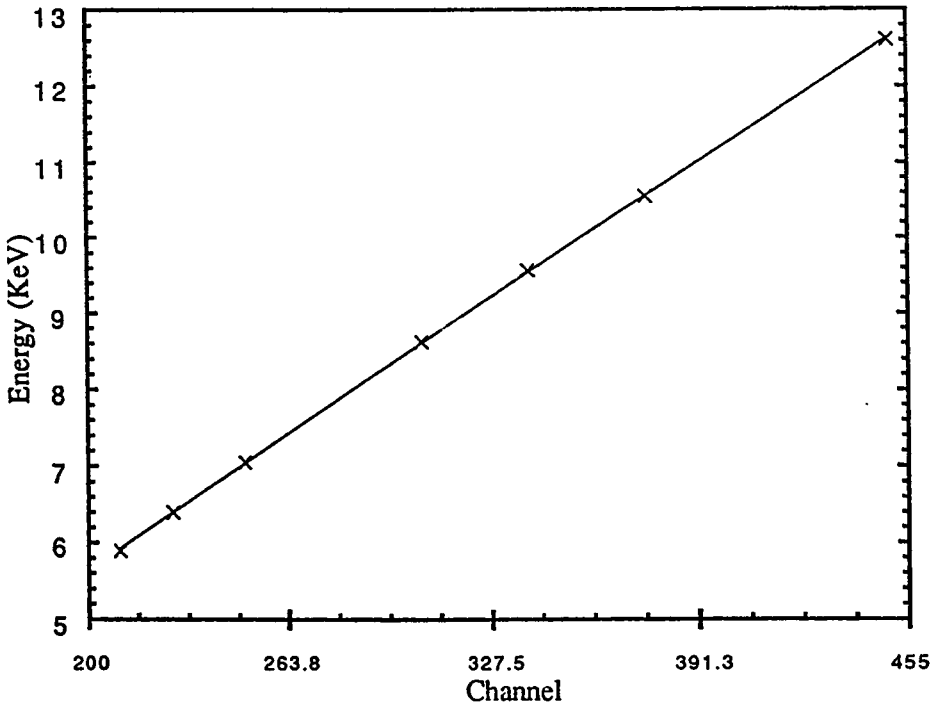

Figure 4-7: The energy versus channel calibration for the handled setup. The straight line is the least square fit of the data points.

particle beam, obtained from the Tandetron accelerator, was led through the precisely adjustable beam slits. The shaped beam was directed towards the sample located in the vacuum chamber. The samples were irradiated by 1 to 6 MeV α particles with 0.2 MeV increment. The irradiation continued till approximately 10 μC charge accumulations were achieved at energies less than 4 MeV and 5 μC charge accumulations at energies greater than 4 MeV. This is because the X-ray yield at low energies is relatively small. Thus to improve the statistic of the spectrum and to reduce the error in the measurements, a longer irradiation time is required. Whereas at high energies, the X-ray yield is very high and the peaks stands sharply in the pulse height spectra. The beam current was limited to 3 nA in order to avoid pile-up and dead time effects of the detector.

The produced X-ray spectra were transferred from the ND62 multichannel analyser to IBM PC computer and the spectra of *PIXE* and *RBS* are stored there simultaneously. The X-ray spectra were analysed and fitted using the PIXANPC code, by following the same procedures and line group divisions explained in section 3.5.4. A selective X-ray spectra are shown in figure (4-8) for 1.2 MeV α particles on Ho, figure (4-9) for 3 MeV α particles on Er, and figure (4-10) for 6 MeV α particles on Tm. Note that the fluorine X-ray lines are out of the detection range of the Si(Li) detection system. Unlike the proton spectra in figure (4-1) and figure (4-2), the α particle impact spectra have much lesser background, even at low energy side. This is due to the absence of projectile bremsstrahlung as directly justified from equation (1.53). Additionally, the secondary-electron bremsstrahlung radiations are very low because of two facts; firstly the secondary electron production is very low because the inner-shell ionization cross section for α particles is very small compared to proton's, this can be observed from the low X-ray yield rates by α particles bombardment compared to those by protons; secondly the energy transferred from the α particles to surrounding and bound electron at individual collision is approximately four times smaller than from the protons, as concluded from section 1.2.3. Therefore, the secondary electron bremsstrahlung is

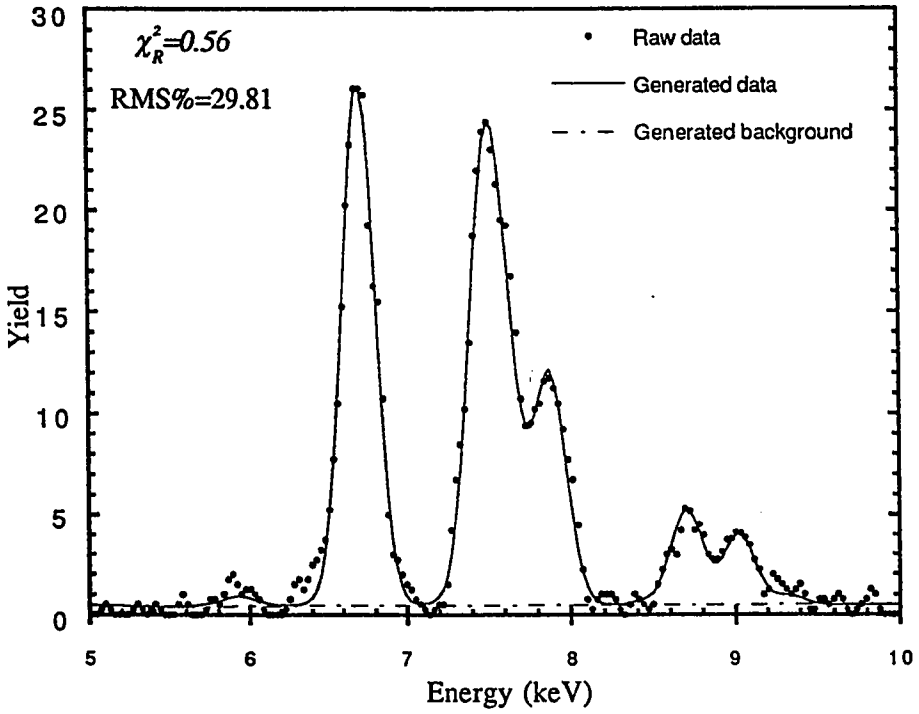

Figure 4-8: The X-ray spectrum produced by 1.2 MeV α-particle bombardments on Ho.

expected to be low and limited towards the low energy side and increases slowly as α-particle energies increase.

In general, the L X-ray spectra of all elements have the same compositional model, of course, with different line intensities. At low bombardment energies, an appreciable number of satellite and noise lines appear. These lines diminishes at high energies due to the high X-ray yield that improves the statistics of the peaks and conquers the distorting lines. Typical line positions are shown in figure (4-11). The figure shows these lines after separating the unresolved lines using Gaussian line-shape model.

On the other hand, *RBS* spectra are much simpler than those of *PIXE* spectra, as shown in figure (4-12), (4-13), and figure (4-14) which correspond to simultaneous collection to the *PIXE* spectra shown in figures (4-8) to (4-10), respectively. The peaks

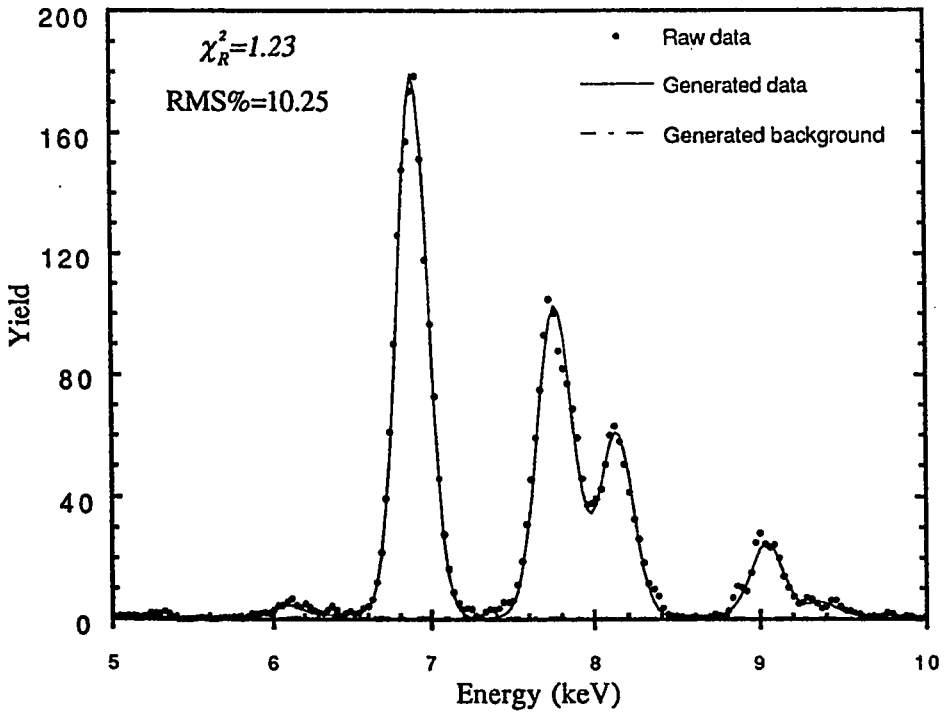

Figure 4-9: The X-ray spectrum produced by 3 MeV α-particle bombardments on Er.

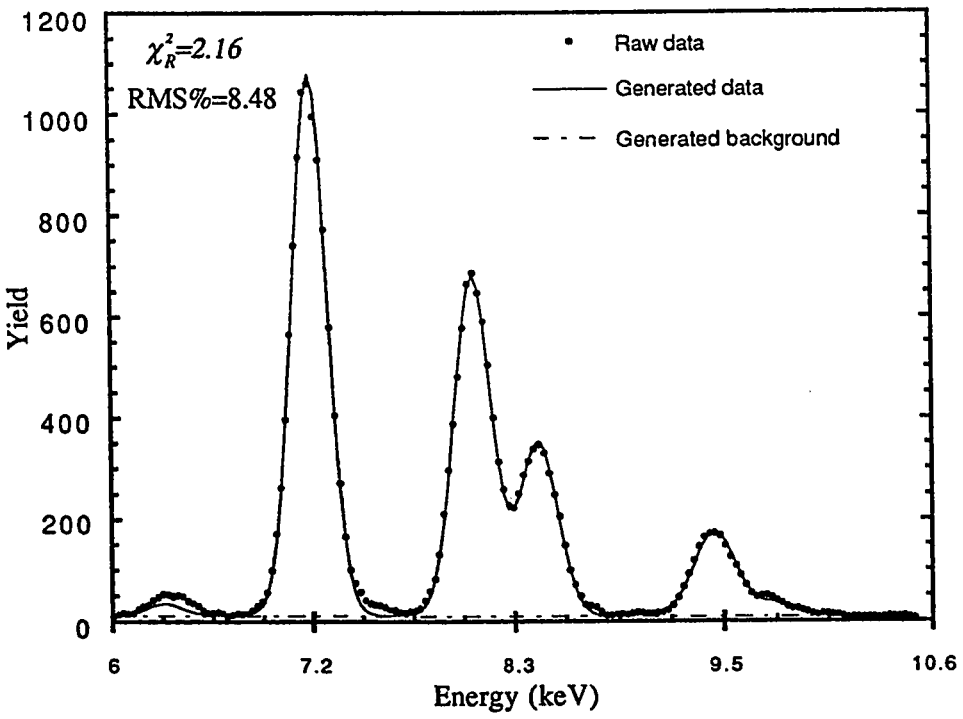

Figure 4-10: The X-ray spectrum produced by 6 MeV α-particle bombardments on Tm.

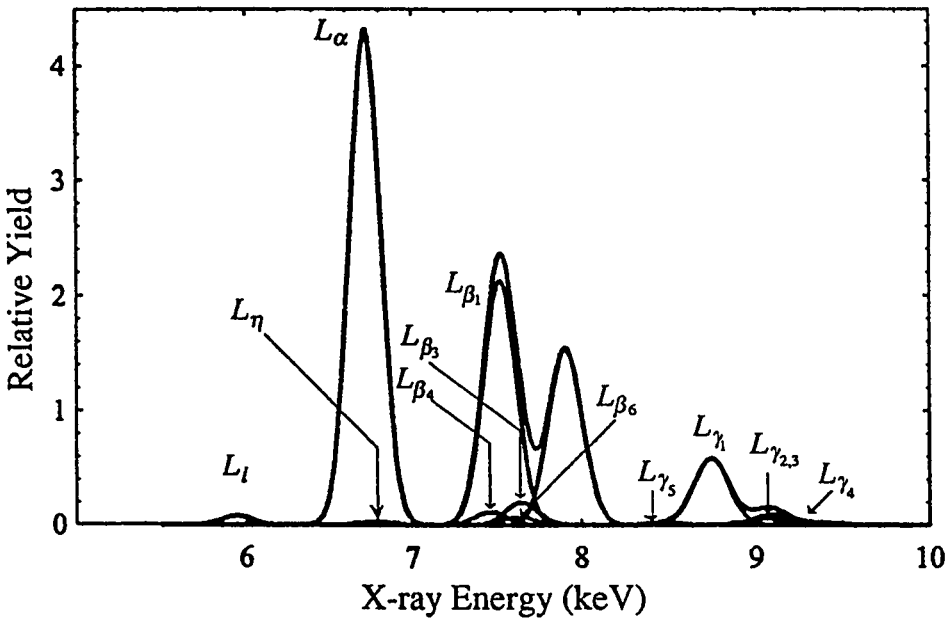

Figure 4-11: The principal L X-ray lines for Ho, after separating the unresolved lines using Gaussian line shape model.

which result from the backscattering process from Ho, Er, and Tm are well resolved from the fluorine peak that lies at low energy side with respect to the peak of elements of interest. No significant background was reported in *RBS* spectra, however the code RUMP able to subtract the contribution of the noise automatically after applying the summation under the peak. No resonance peaks were noted in the *RBS* spectra for all samples except at bombardment energy 4.4 MeV. The resonance peak that appears for bombardment energy 4.4 MeV lies at low energy side, channel number 51 over the backing material spectrum for all samples (i.e. due the interaction of the α particles with the Nuclepore backing material). Therefore it does not affect the peak of backscattered α particles from elements of interest. The shifts of the *RBS* peaks towards the high energy region, as the bombardment energy increases, was accounted by reducing the gain of the amplifier in order to keep the peaks within the detection range. The settings of the amplification gain at particular energy range are shown in table (4.4).

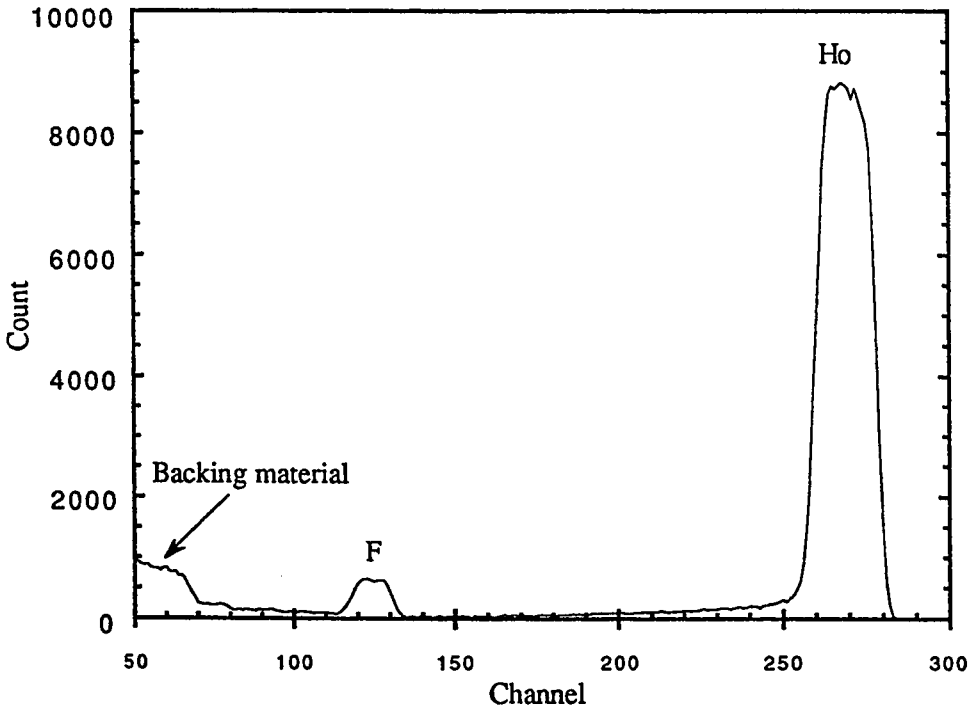

Figure 4-12: The *RBS* spectrum produced by 1.2 MeV α-particle bombardments on HoF_3 thin film deposited on Nuclepore backing.

Table 4.4: The settings of the coarse amplification gain for the SSB detector at particular bombardment energy range.

Coarse gain	Energy range (MeV)
200	$1 \leq E_\alpha \leq 2$
100	$2 < E_\alpha \leq 4$
50	$4 < E_\alpha \leq 6$

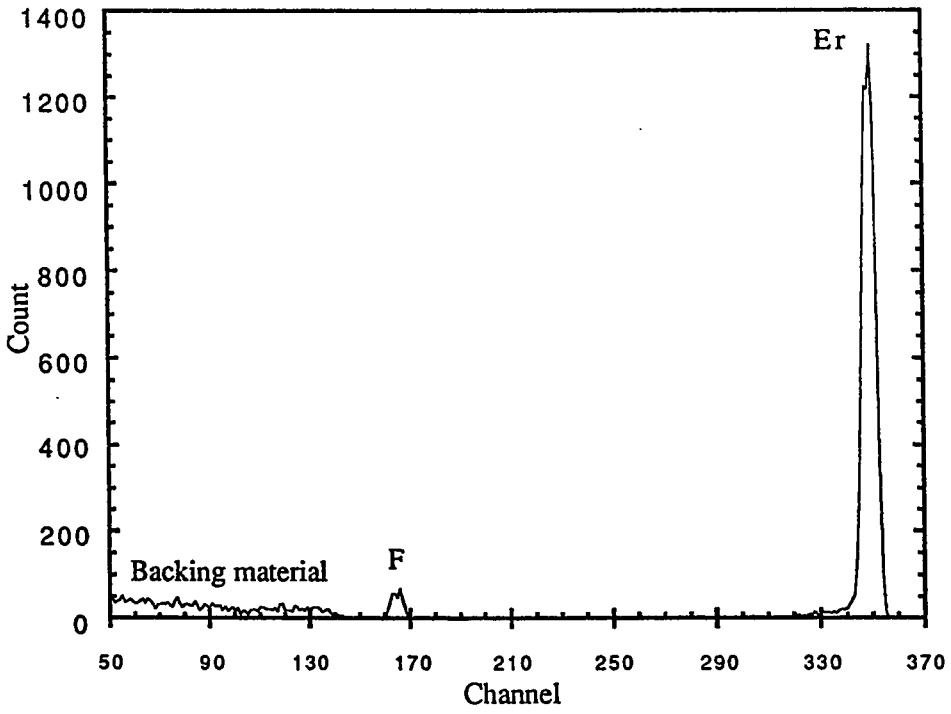

Figure 4-13: The *RBS* spectrum produced by 3 MeV α-particle bombardments on ErF_3 thin film deposited on Nuclepore backing.

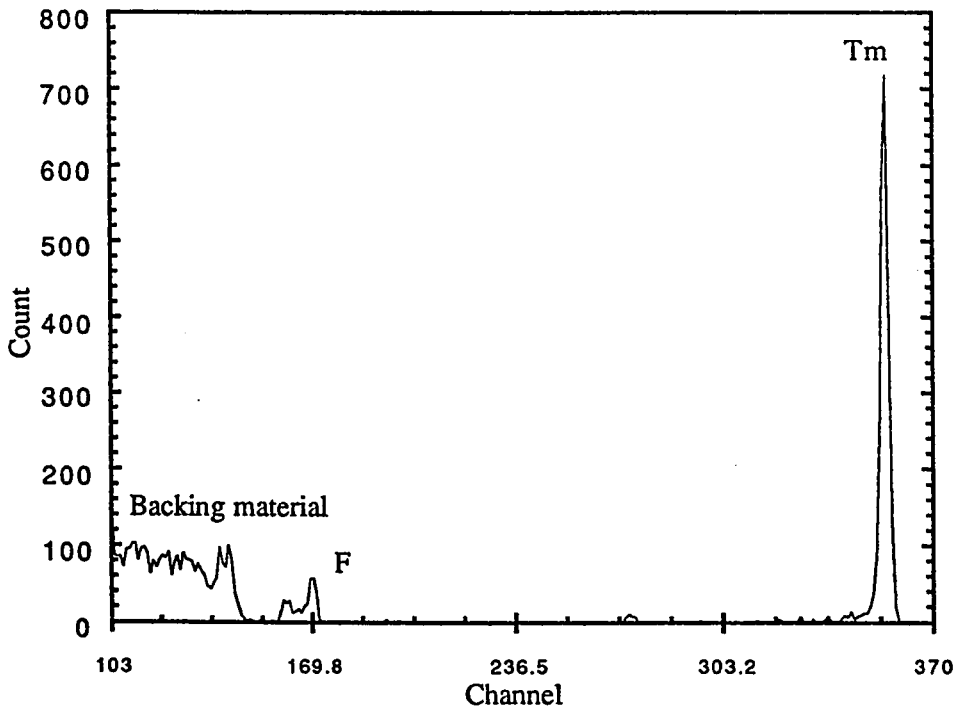

Figure 4-14: The *RBS* spectrum produced by 6 MeV α-particle bombardments on TmF_3 thin film deposited on Nuclepore backing.

The peak areas of the lines L_α, L_{β_1}, $L_{\beta_{2,15}}$, L_{β_3}, L_{γ_1}, and $L_{\gamma_{2,3}}$, as well as the peak area of the backscattered α particles were measured. The L_α peak area values were used to obtain the cross sections for L_3 subshell. For L_2 subshell, the peak area values of L_{β_1} were adopted for cross section calculations instead of L_{γ_1}, despite many literatures have used the peak area values of L_{γ_1} for the cross section calculations[61, 65, 2, 73]. Our justification is that the uncertainties in measuring the L_{γ_1} yields are larger than those of L_{β_1} yields, as listed in the tables and shown in figures (4-15), (4-16), and (4-17) for Ho, Er, and Tm, respectively. For L_1 subshell, the $L_{\gamma_{2,3}}$ were adopted in the cross section calculations instead of using the most intense line in the L_1 subshell group, that is L_{β_3} line. This is due to the fact that the L_{β_3} line lies in a region contains a crowded unresolved lines with higher or comparable intensities with respect to L_{β_3} as shown in figure (4-11). This limits the accuracy of the peak area values. Unlike $L_{\gamma_{2,3}}$ line, the weighted coupling of the lines L_{β_3} and L_{β_4} does not offer a proper Gaussian response, since the energy difference between L_{β_3} and L_{β_4} lines (180-205 eV) is comparable to the resolving power of the detector and comparatively larger than that of L_{γ_2} and L_{γ_3} lines (37-59 eV). Therefore, the weighted coupling of the lines L_{β_3} and L_{β_4} does not meet exactly the employed fitting model.

The normalized yields (count/particle) for L_α, L_{β_1}, and $L_{\gamma_{2,3}}$ are listed in table (4.5) for Ho, table (4.6) for Er, and table (4.7) for Tm. Figures (4-18), (4-19), and (4-20) show the plot of the normalized yields of L_α, L_{β_1}, and $L_{\gamma_{2,3}}$ for the three elements, Ho, Er, and Tm, respectively, versus the bombardment energy. Obviously the yields gradually decrease as the atomic number increases. This is exactly as predicted by the first order theories since the ionization cross sections inversely proportional to the inverse square of the target atomic number. Also the difference in the yield between the X-ray lines are not significantly changed since the decay parameters for Ho, Er, and Tm do not alter appreciably. The error bars here are estimated from the uncertainties of the both backscattering and X-ray yields. The yields here are not corrected for the detector efficiency.

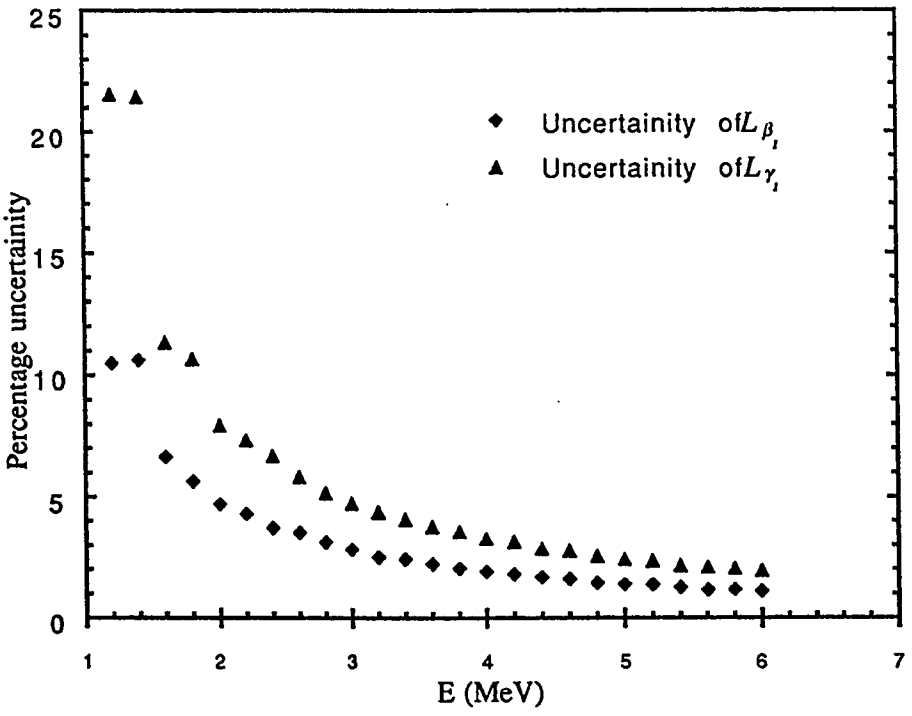

Figure 4-15: The uncertainties in L_{β_1} and L_{γ_1} yield measurements versus the bombardment energy for Ho.

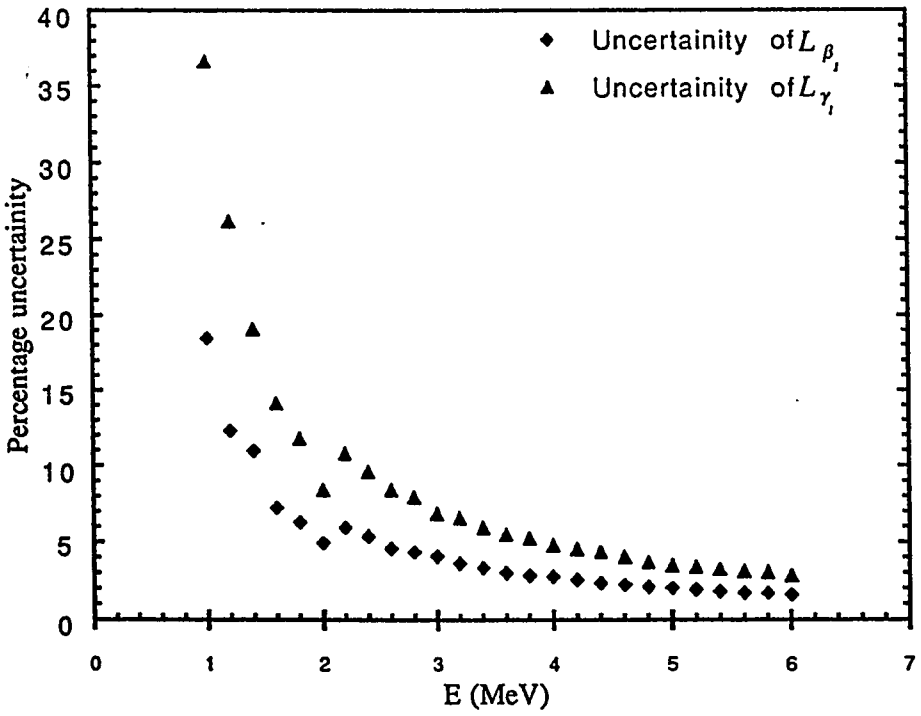

Figure 4-16: The uncertainties in L_{β_1} and L_{γ_1} yield measurements versus the bombardment energy for Er.

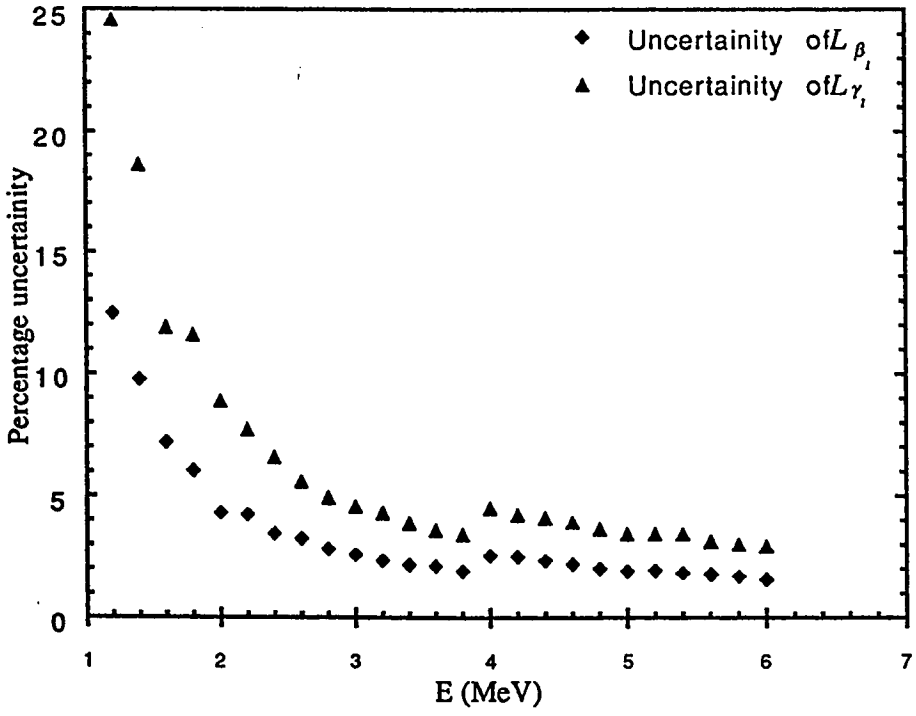

Figure 4-17: The uncertainties in L_{β_1} and L_{γ_1} yield measurements versus the bombardment energy for Tm.

Table 4.5: The normalized yields (count/particle) of L_α, L_{β_1}, and $L_{\gamma_{2,3}}$ for Ho.

Energy (MeV)	L_α/N^α	L_{β_1}/N^α	$L_{\gamma_{2,3}}/N^\alpha$
1.20	0.001399 ± 0.000095	0.001020 ± 0.000107	0.000167 ± 0.000056
1.40	0.004167 ± 0.000279	0.002461 ± 0.000262	0.000309 ± 0.000189
1.60	0.007802 ± 0.000345	0.005168 ± 0.000345	0.000507 ± 0.000184
1.80	0.013629 ± 0.000545	0.009623 ± 0.000544	0.000768 ± 0.000326
2.00	0.024782 ± 0.000771	0.014348 ± 0.000679	0.001126 ± 0.000344
2.20	0.038986 ± 0.001058	0.021741 ± 0.000944	0.001627 ± 0.000543
2.40	0.062620 ± 0.001487	0.034276 ± 0.001293	0.002494 ± 0.000727
2.60	0.082210 ± 0.001930	0.046849 ± 0.001673	0.003061 ± 0.000935
2.80	0.120736 ± 0.002546	0.067552 ± 0.002170	0.004069 ± 0.001284
3.00	0.166646 ± 0.003229	0.091554 ± 0.002684	0.005067 ± 0.001498
3.20	0.224067 ± 0.004200	0.135037 ± 0.003561	0.005923 ± 0.001922
3.40	0.296230 ± 0.005205	0.162617 ± 0.004177	0.006748 ± 0.002221
3.60	0.371910 ± 0.006320	0.214719 ± 0.005135	0.008654 ± 0.002688
3.80	0.493673 ± 0.008148	0.289366 ± 0.006504	0.011221 ± 0.003327
4.00	0.600731 ± 0.009662	0.348963 ± 0.007506	0.013527 ± 0.003815
4.20	0.755454 ± 0.011974	0.434362 ± 0.009072	0.016901 ± 0.004437
4.40	0.909800 ± 0.014232	0.545874 ± 0.010883	0.021365 ± 0.005177
4.60	1.131486 ± 0.017402	0.648195 ± 0.012685	0.027465 ± 0.005922
4.80	1.430465 ± 0.021733	0.855501 ± 0.015851	0.037079 ± 0.007499
5.00	1.734728 ± 0.026712	1.033938 ± 0.019117	0.045594 ± 0.008548
5.20	1.986987 ± 0.031380	1.199261 ± 0.022517	0.055914 ± 0.009697
5.40	2.293579 ± 0.035495	1.396319 ± 0.025290	0.068367 ± 0.011358
5.60	2.717386 ± 0.041697	1.703410 ± 0.029853	0.082067 ± 0.012080
5.80	3.204190 ± 0.050966	1.920975 ± 0.034936	0.104627 ± 0.014404
6.00	3.581718 ± 0.057251	2.230854 ± 0.040010	0.124974 ± 0.015816

Table 4.6: The normalized yields (count/particle) of L_α, L_{β_1}, and $L_{\gamma_{2,3}}$ for Er.

Energy (MeV)	L_α/N^α	L_{β_1}/N^α	$L_{\gamma_{2,3}}/N^\alpha$
1.00	0.000459 ± 0.000062	0.000372 ± 0.000069	0.000037 ± 0.000041
1.20	0.001793 ± 0.000134	0.001078 ± 0.000133	0.000144 ± 0.000076
1.40	0.004182 ± 0.000227	0.001972 ± 0.000217	0.000267 ± 0.000118
1.60	0.007953 ± 0.000366	0.004910 ± 0.000357	0.000443 ± 0.000176
1.80	0.014121 ± 0.000547	0.008500 ± 0.000538	0.000813 ± 0.000291
2.00	0.026048 ± 0.000810	0.015151 ± 0.000754	0.001156 ± 0.000411
2.20	0.043777 ± 0.001706	0.024907 ± 0.001494	0.001611 ± 0.000935
2.40	0.062065 ± 0.002253	0.036799 ± 0.002005	0.002167 ± 0.001115
2.60	0.092114 ± 0.002998	0.051898 ± 0.002445	0.003130 ± 0.001387
2.80	0.127685 ± 0.003878	0.071654 ± 0.003214	0.003988 ± 0.001940
3.00	0.183974 ± 0.005122	0.097765 ± 0.004160	0.004949 ± 0.002137
3.20	0.250012 ± 0.006558	0.136880 ± 0.005230	0.005999 ± 0.002983
3.40	0.327760 ± 0.008114	0.178040 ± 0.006381	0.008022 ± 0.003444
3.60	0.403706 ± 0.009897	0.240462 ± 0.007946	0.009167 ± 0.004152
3.80	0.516881 ± 0.012126	0.299385 ± 0.009503	0.010457 ± 0.004767
4.00	0.708901 ± 0.016318	0.390779 ± 0.012285	0.012816 ± 0.006089
4.20	0.845678 ± 0.019102	0.468464 ± 0.014004	0.016947 ± 0.006541
4.40	1.025900 ± 0.023287	0.600536 ± 0.017095	0.019496 ± 0.008027
4.60	1.243933 ± 0.027626	0.712594 ± 0.019894	0.025127 ± 0.009890
4.80	1.533745 ± 0.034295	0.881403 ± 0.024054	0.029096 ± 0.011139
5.00	1.736686 ± 0.038584	0.997743 ± 0.026982	0.038465 ± 0.011970
5.20	2.042513 ± 0.044892	1.184131 ± 0.031225	0.049060 ± 0.013385
5.40	2.315268 ± 0.051375	1.405438 ± 0.036385	0.060967 ± 0.015025
5.60	2.714257 ± 0.061958	1.675882 ± 0.043661	0.073722 ± 0.018036
5.80	3.144480 ± 0.073747	1.933521 ± 0.051417	0.091366 ± 0.020471
6.00	3.817353 ± 0.088185	2.274028 ± 0.059155	0.114990 ± 0.023285

Table 4.7: The normalized yields (count/particle) of L_α, L_{β_1}, and $L_{\gamma_{2,3}}$ for Tm.

Energy (MeV)	L_α/N^α	L_{β_1}/N^α	$L_{\gamma_{2,3}}/N^\alpha$
1.20	0.001395 ± 0.000107	0.000989 ± 0.000123	0.000171 ± 0.000053
1.40	0.003470 ± 0.000197	0.002179 ± 0.000213	0.000308 ± 0.000097
1.60	0.007484 ± 0.000336	0.004715 ± 0.000340	0.000525 ± 0.000209
1.80	0.014116 ± 0.000528	0.008436 ± 0.000511	0.000816 ± 0.000257
2.00	0.025471 ± 0.000726	0.015067 ± 0.000653	0.001235 ± 0.000344
2.20	0.041557 ± 0.001092	0.022889 ± 0.000976	0.001748 ± 0.000519
2.40	0.066283 ± 0.001489	0.037364 ± 0.001302	0.002376 ± 0.000743
2.60	0.096574 ± 0.002043	0.052700 ± 0.001747	0.003188 ± 0.000886
2.80	0.138105 ± 0.002620	0.076328 ± 0.002204	0.003961 ± 0.001255
3.00	0.193516 ± 0.003417	0.104276 ± 0.002807	0.005201 ± 0.001471
3.20	0.254836 ± 0.004302	0.142021 ± 0.003490	0.006112 ± 0.001822
3.40	0.333472 ± 0.005400	0.185889 ± 0.004304	0.007121 ± 0.002260
3.60	0.415116 ± 0.006605	0.231501 ± 0.005278	0.008124 ± 0.002719
3.80	0.566557 ± 0.008606	0.298447 ± 0.006319	0.010542 ± 0.003157
4.00	0.677855 ± 0.014251	0.363573 ± 0.010460	0.012870 ± 0.004927
4.20	0.826193 ± 0.017130	0.445804 ± 0.012812	0.015318 ± 0.005996
4.40	1.024381 ± 0.021422	0.570919 ± 0.015802	0.018221 ± 0.007477
4.60	1.260745 ± 0.026649	0.683510 ± 0.018534	0.022408 ± 0.008398
4.80	1.509172 ± 0.031404	0.839067 ± 0.021629	0.027874 ± 0.009237
5.00	1.846384 ± 0.039140	1.042151 ± 0.026692	0.034293 ± 0.011760
5.20	2.175920 ± 0.047627	1.236107 ± 0.032772	0.043065 ± 0.013336
5.40	2.441316 ± 0.052868	1.415394 ± 0.036603	0.051817 ± 0.014600
5.60	2.961849 ± 0.067119	1.675137 ± 0.044425	0.066765 ± 0.016831
5.80	3.464088 ± 0.079102	1.973148 ± 0.051752	0.082488 ± 0.018793
6.00	3.980565 ± 0.091804	2.414121 ± 0.062315	0.100089 ± 0.023640

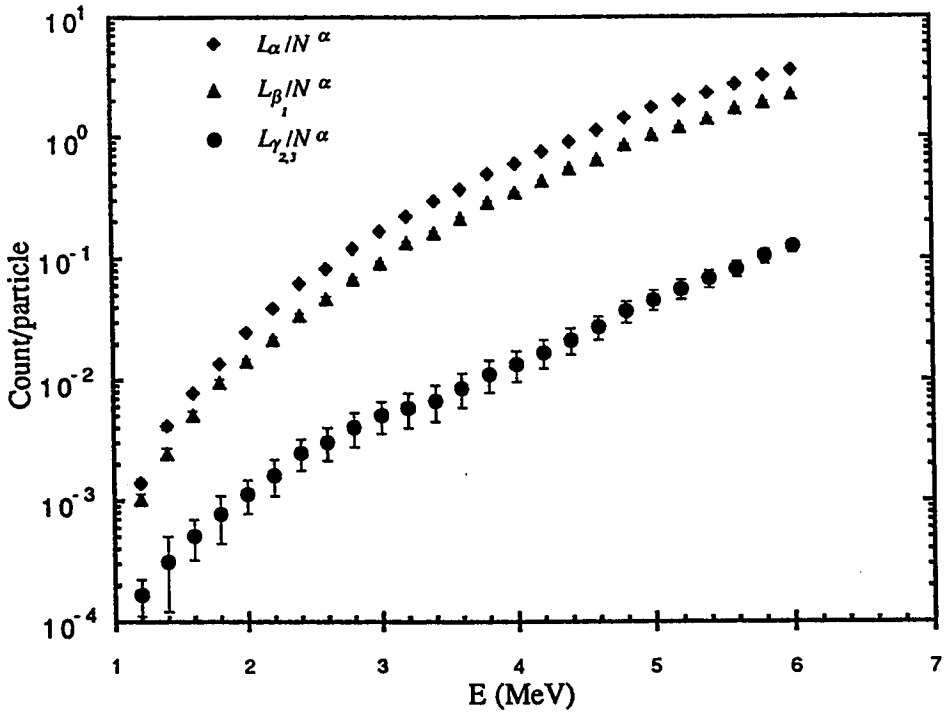

Figure 4-18: A plot of the L_α, L_{β_1}, and $L_{\gamma_{2,3}}$ (see the legend) normalized yields (count/particle) versus the α-particle energy for Ho. The uncertainty for each point is represented by an error bar. The efficiency is not incorporated.

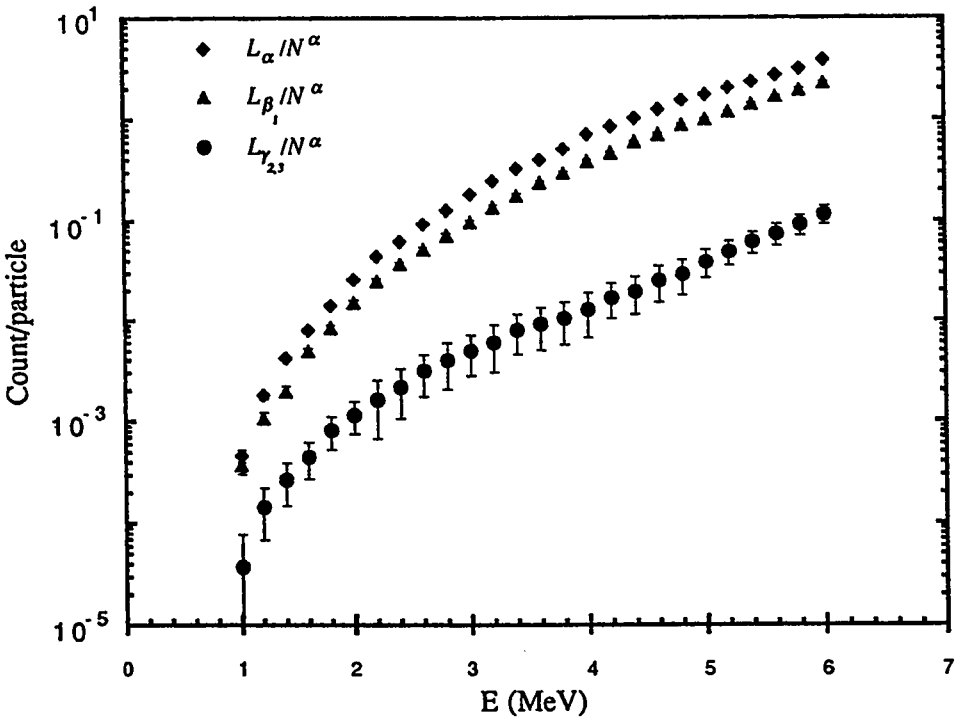

Figure 4-19: A plot of the L_α, L_{β_1}, and $L_{\gamma_{2,3}}$ (see the legend) normalized yields (count/particle) versus the α-particle energy for Er. The uncertainty for each point is represented by an error bar. The efficiency is not incorporated.

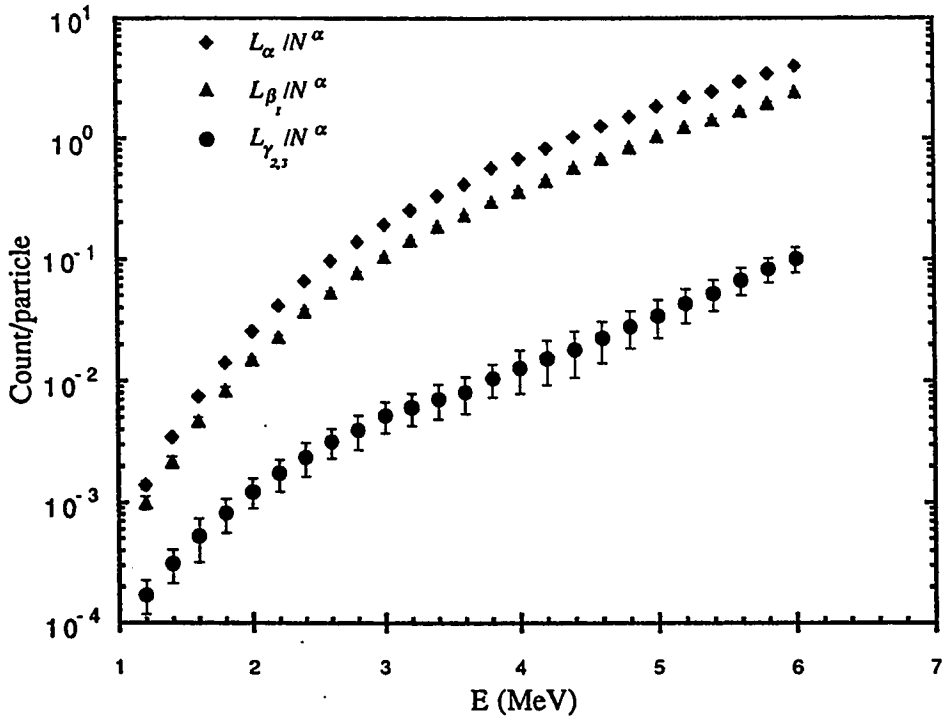

Figure 4-20: A plot of the L_α, L_{β_1}, and $L_{\gamma_{2,3}}$ (see the legend) normalized yields (count/particle) versus the α-particle energy for Tm. The uncertainty for each point is represented by an error bar. The efficiency is not incorporated.

Table 4.8: The 39.3 $\mu g/cm^2$ Nb L_α and K_α yields for 1 μC of 2.5 MeV protons at certain times during a long run.

L_α yield	K_α yield	Run duration (minutes)
4579 ± 96.16	2505 ± 67.64	000.0
4705 ± 98.81	2503 ± 67.58	044.0
4452 ± 93.49	2359 ± 63.69	172.0
4503 ± 94.56	2524 ± 68.15	291.0
4704 ± 98.78	2387 ± 64.45	410.0

4.2.2 Carbon Build-Up Effect

As a consequence of the heat produced by the energetic ion beam, the oxygen and the hydrogen are dissociated from the nuclepore backing and released as a water vapour, leaving a black spot of carbon. One must be cautious for the worst case when the thin film was etched, melted, or overlapped with the carbon spot. The carbon build on the target violates the effective thickness of the target. Accordingly, this effect would obscure the α-particle beam from the target and additionally this leads to an attenuation of the emitted X-ray.

This occasion appears in the *RBS* spectra as a shift of the peaks towards low energy side and in *PIXE* spectra as a degradation in the peak intensities. The existence of such effect was tested by subjecting a 39.3 $\mu g/cm^2$ niobium thin film standard (as 49.4 $\mu g/cm^2$ Nb_2O_3) to a long-time run by 3 nA proton beam at 2.5 MeV. The peak areas of Nb K_α and Nb L_α were measured for each $1\mu C$ charge accumulation during the run. Table (4.8) lists these peak areas for a certain time during the run. Figure (4-21) shows the plot of the K_α and L_α yields versus run duration. The average yield for each peak lies within the statistical fluctuation of the points, which are represented by the error bars, and there is no any obvious decreasing or increasing behaviour of the yields at different run times.

Another test was done when the X-ray spectrum for 5 μC of 4.4 MeV α particles on Tm were collected for fresh and exploited spots. The exploited spot was exposed to 165 μC of α particles. The normalized X-ray yields for L_α, L_{β_1}, and $L_{\gamma_{2,3}}$ are shown

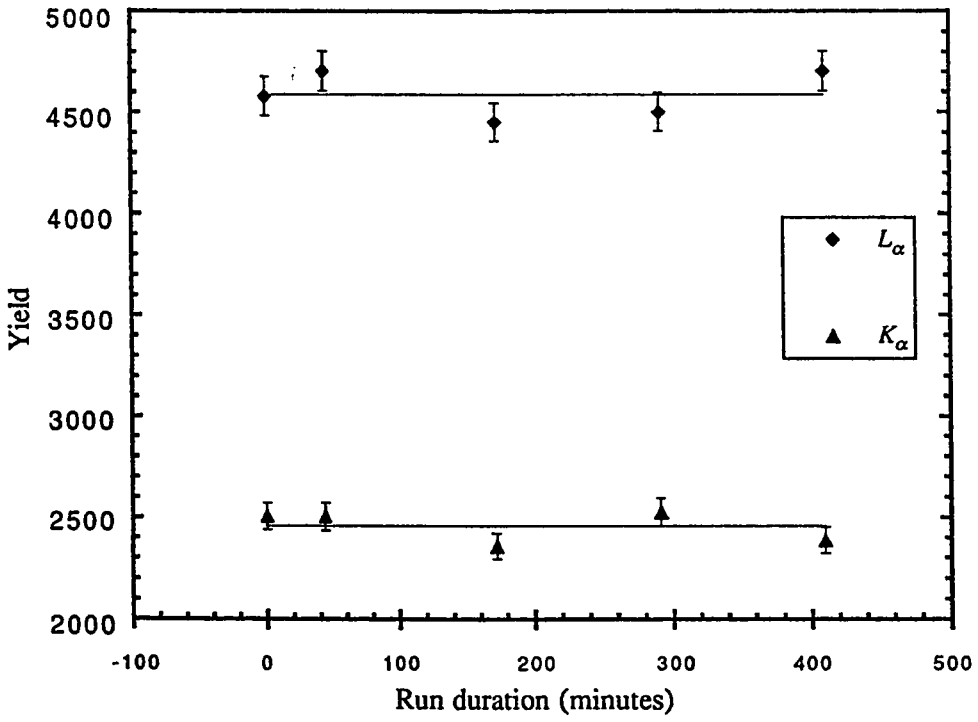

Figure 4-21: A plot of the 39.3 μg/cm^2 Nb K_α and L_α yields for 1 μC of 2.5 MeV protons versus run duration. The horizontal lines represent the average yield for each line.

Table 4.9: The normalized X-ray yields for L_α, L_{β_1}, and $L_{\gamma_{2,3}}$ lines by 5 μC of 4.4 MeV α particles for fresh and exploited spots. The exploited spot was exposed to 165 μC of α particles.

	L_α/N^α	L_{β_1}/N^α	$L_{\gamma_{2,3}}/N^\alpha$
Fresh spot	1.043057	0.613296	0.018002
exploited spot	1.023164	0.596841	0.017612
Difference %	1.907182	2.683044	2.166426

in table (4.9). The differences show that there are no any significant changes in the X-ray yields for the two spots.

Accordingly, the effect of carbon build up has no appreciable effect on the collected data and thus this effect was neglected in yield measurements.

4.2.3 Internal Conversion Effect

X rays emitted whenever internal conversion occurs in nuclear transitions. Coulomb excitation of heavy nuclei by incident charged particles will result, therefore, in the emission of characteristic X rays. For Ho, from equation (1.20), the maximum energy transfer to Ho nucleus by a single encounter equals to 0.093 E_o. When $E_o > 1$ MeV, the maximum energy transfer is sufficient to excite the abundant stable isotope, ^{165}Ho to the first excited state, that is 95 keV level and when E_o reaches 6 MeV the maximum energy transfer can excite ^{165}Ho to the ninth excited state[85]. For Er, the first excited state is approximately 80 keV and 1 MeV α particle can excite the nucleus to the first excited state since the maximum energy transfer to Er nucleus by α particles equals to 0.0913 E_o. Therefore, a higher excited sates can be reached when E_o reaches 6 MeV. The released γ rays subsequent to the de-excitation do not overlap the X-ray lines since the γ-ray energies lie beyond the detection range of the system at which the detector efficiency is very small. Nevertheless, the released γ rays give rise to internal conversion process, that enhances the X-ray lines.

The above argument does not fit Tm exactly. This is because the first excited state of the abundant stable nucleus, ^{169}Tm, is 8.41 keV. Therefore the emitted γ rays are

insufficient to ionize the K and L shells, however the γ rays here overlap the Tm $L_{\beta_{2,15}}$ line (8.46 keV). This is verified latter when the ratio $L_{\beta_{2,15}}/L_{\alpha}$ is compared to the values of SALEM *et al.*[15]. Additionally, the ^{169}Tm nucleus can be excited to higher energy levels by α particles, since the maximum energy transfer is 0.0904 E_o. Thus for $1 \leq E_o \leq 6$ MeV, the nucleus can be excited from the second level (118 keV) to the eighth level (437 keV), releasing γ rays[85].

The contribution of internal conversion to the total X-ray yields depends on the comparative cross sections for direct excitation and Coulomb excitation of the nucleus, as well as on the conversion coefficients for the nuclear excited states. Because of the large cross section for direct L-shell ionization, no correction for the effects of nuclear excitation is necessary for that shell, at least for incident protons[4]. This can hold for α particles according to the following justification. MERZBACHER and LEWIS[4] indicated that the produced γ rays in the transition from the 137 keV energy level in ^{181}Ta for 2 MeV protons is less than 10% of the K-shell yield by direct excitation and becoming less for higher bombarding energies as shown in figure (4-22). It is seen that the ratio of X rays to γ rays is less for α particles than for protons. It is found from the figure that the γ-ray yield by 3 MeV α particles on *thick* ^{181}Ta is less than 44% of K-shell yield by direct excitation[4]. Because Ta is heavier than elements of interest, one can conclude that

$$\sigma_K^x(E_\alpha) > \sigma_E^\gamma(E_\alpha) \tag{4.4}$$

Where $\sigma_K^x(E_\alpha)$ denotes the K-shell X-ray production cross section by direct excitation at certain α-particle energy, and $\sigma_E^\gamma(E_\alpha)$ denotes the γ-ray production cross section by Coulomb excitation at certain α-particle energy.

The K-shell internal conversion coefficients α_K of a transition is defined as the ratio of the number of electrons emitted from the K shell to the number of emitted γ-ray photons[1], i.e.

$$\alpha_K = \frac{n_e}{n_\gamma} \tag{4.5}$$

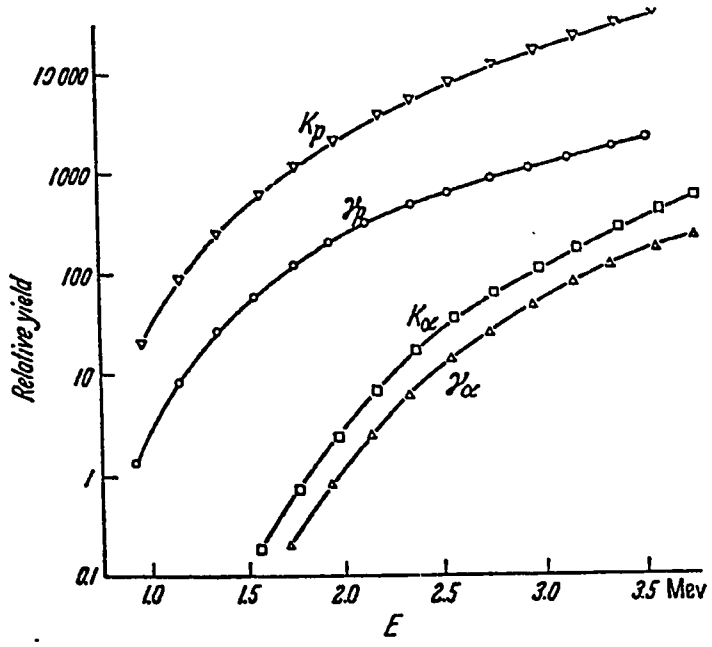

Figure 4-22: Yields of K shell X rays and 137 keV γ rays from ^{181}Ta under proton and α particle bombardment. (Taken from MERZBACHER and LEWIS, 1958.)

Definitions for the other shells follow similarly. Conversion of the K shell is more likely than in the other shells because of the greater probability of K electrons being found within the nuclear volume. The other main factor determining whether internal conversion is likely to occur is the multipolarity of the transition[1]. High multipolarities (corresponding to large changes in angular momentum of the nucleus) correspond to low probabilities of radiating electromagnetic energy, and hence in such cases the relative probability of internal conversion is high. Low transition energies also favour internal conversion[1]. The conversion coefficients as a function of γ-ray energies are rapidly decreasing function as γ-ray energy increases[85]. The K-shell conversion for γ rays produced by the most probable nuclear transitions, electric dipole transitions around 100 keV for elements of interest is close to unity[85]. Thus one can set as an upper limit that the conversion cross section for all shells, $\sigma_c^{\gamma}(E_\alpha) \sim \sigma_E^{\gamma}(E_\alpha)$. The L_2 and L_3-subshell ionization cross sections by α-particle bombardments follow the following inequality[51]

$$\sigma^{i}_{L_2,L_3} \gg \sigma^{i}_{K} > \sigma^{x}_{K}$$

Therefore one can directly deduce from inequality (4.4) that

$$\sigma^{i}_{L_2,L_3} \gg \sigma_c^{\gamma}(E_\alpha) \tag{4.6}$$

Which means that the internal conversion cross section is negligible with respect to L_2 and L_3-subshell ionization cross sections by α-particle bombardments.

For L_1 subshell, the conversion coefficient for electric dipole transition γ rays at 100 keV is $\sim$ 0.1 eV. Therefore the conversion cross section is just 10% of the γ-ray production cross section. Additionally the vacancy created in K shell does not affect the L_1 subshell appreciably due to the weakness of the magnetic dipole $K \rightarrow L_1$ vacancy migration. The Coster-Kronig transitions among L subshells also reduce the effect of

the conversion ionization for L_1 subshell. Accordingly, one can safely set

$$\sigma^i_{L_1} \gg \sigma^\gamma_c \tag{4.7}$$

Hence one can conclude from inequalities (4.6) and (4.7) that the internal conversion effect is negligible compared to direct excitation even by α-particle bombardments. For heavier ions, this effect requires careful estimations.

4.2.4 Impurity Effect

The samples were prepared at high purity conditions and they are kept and handled cautiously to maintain their purity. Since the detection system is very sensitive for small amount of materials (reaching part per million), an accident touch to the samples when they are fixed to the sample holder, or exposing the air that contains amount of dust and other suspended materials would affect the precision of the data due contamination.

The existence of some elements, such as Mn, Fe, Co, Ni, Cu, and Zn, those are widely suspended in the surrounding can violate the data since they can overlap the X-ray lines of Ho, Er, and Tm. For example Co K_α overlaps Ho and Er $L_{\alpha,\eta}$ line, and Co K_β line overlaps Ho and Er $L_{\beta_{1,2,3,4}}$ line. Similarly, Fe K_α overlaps Tm L_l and Fe K_β overlaps Tm $L_{\alpha,\eta}$.

Although the code TOS can identify the X-ray lines of the spectrum, however, it can not ensure whether the X-ray line is overlapped by other lines or not. This was tested during the fitting by using PIXANPC code. The criteria was the goodness of the χ^2_R of the fitting. The suspected elements were added to the shopping list and the fitting was carried out. It was found that adding impurity elements yields a small peak areas for these elements ranging between 7.5% to 12.5% of the L_α yield at low energies, when $E_\alpha < 2$ MeV. Nevertheless, the χ^2_R of the fitting increases by 139%, which means that adding such elements does not improve the fit. Additionally, when $E_\alpha > 2$ MeV, the peak areas of the impurities lie beneath the minimum detection limit.

This ensures that there are no impurities in the thin samples and one can carry out the calculations safely.

4.3 X-Ray Production Cross-Section Measurements

The yields of L_α, L_{β_1}, and $L_{\gamma_{2,3}}$ were employed to obtain the production cross sections for L_1, L_2, and L_3 subshell respectively. The yield of each X-ray line was converted into subshell yield, N_{L_i}, by dividing it by the branching ratio, i.e.

$$N_{L_1} = \frac{L_{\gamma_{2,3}}}{B_{L_{\gamma_{2,3}}}};\ N_{L_2} = \frac{L_{\beta_1}}{B_{L_{\beta_1}}};\ N_{L_3} = \frac{L_\alpha}{B_{L_\alpha}} \tag{4.8}$$

Where

$$B_{L_{\gamma_{2,3}}} = \frac{\Gamma_{L_{\gamma_{2,3}}}}{\Gamma_{L_1}};\ B_{L_{\beta_1}} = \frac{\Gamma_{L_{\beta_1}}}{\Gamma_{L_2}};\ B_{L_\alpha} = \frac{\Gamma_{L_\alpha}}{\Gamma_{L_3}} \tag{4.9}$$

And $\Gamma_{L_i} = \sum_{j=1}^{N} \Gamma_j$, the total L_i subshell emission rate. The values of the branching ratios were taken from the experimental values of SALEM *et al.*[15].

The total subshell yields were substituted in equation (2.125) to obtain the subshell production cross section. The geometric factor and efficiency in equation (2.125) were replaced by $\gamma(E)$ in equation (4.2). The values of $\gamma(E)$ were calculated for each line according to its energy.

The above procedures were adopted in the software *Mathematica*™ to calculate the values of X-ray production cross sections. This is shown in appendix C. The L_1, L_2, and L_3-subshell X-ray production cross sections are given in table (4.10) for Ho, table (4.11) for Er, and table (4.12) for Tm. Uncertainties in the X-ray production cross sections originate mainly from the determination of X-ray and *RBS* yield and efficiency-geometry factor $\gamma(E)$. The total error was calculated as the square root of the sum of squares of percentage partial errors.

A plots of X-ray production cross sections versus the bombardment energies are shown in figure (4-23) for Ho, figure (4-24) for Er, and figure (4-25) for Tm. The

Table 4.10: Ho L-subshell X-ray production cross sections by α particles.

Energy (MeV)	$\sigma^x_{L_1}$ (barn)	$\sigma^x_{L_2}$ (barn)	$\sigma^x_{L_3}$ (barn)
1.20	0.20936 ± 0.0723	00.5886 ± 00.0746	001.44530 ± 00.1419
1.40	0.28358 ± 0.1748	01.0440 ± 00.1335	003.16146 ± 00.3085
1.60	0.35639 ± 0.1317	01.6784 ± 00.1635	004.53223 ± 00.3792
1.80	0.42653 ± 0.1836	02.4691 ± 00.2241	006.25606 ± 00.5098
2.00	0.50693 ± 0.1591	02.9820 ± 00.2544	009.21407 ± 00.7142
2.20	0.60534 ± 0.2065	03.7344 ± 00.3108	011.97940 ± 00.9105
2.40	0.77936 ± 0.2338	04.9471 ± 00.3978	016.16800 ± 01.2104
2.60	0.81524 ± 0.2556	05.7616 ± 00.4579	018.08610 ± 01.3525
2.80	0.93436 ± 0.3022	07.1631 ± 00.5582	022.90290 ± 01.6963
3.00	1.01360 ± 0.3082	08.4571 ± 00.6496	027.53720 ± 02.0266
3.20	1.04130 ± 0.3459	10.9630 ± 00.8304	032.54210 ± 02.3897
3.40	1.05080 ± 0.3538	11.6950 ± 00.8830	038.11000 ± 02.7874
3.60	1.20210 ± 0.3830	13.7740 ± 01.0319	042.67760 ± 03.1157
3.80	1.39890 ± 0.4265	16.6600 ± 01.2407	050.84410 ± 03.7062
4.00	1.52200 ± 0.4427	18.1320 ± 01.3451	055.83770 ± 04.0649
4.20	1.72490 ± 0.4691	20.4710 ± 01.5150	063.69080 ± 04.6334
4.40	1.98670 ± 0.5017	23.4410 ± 01.7287	069.88900 ± 05.0811
4.60	2.33670 ± 0.5304	25.4670 ± 01.8756	079.52460 ± 05.7772
4.80	2.89720 ± 0.6210	30.8690 ± 02.2651	092.33420 ± 06.7041
5.00	3.28330 ± 0.6582	34.3830 ± 02.5226	103.19500 ± 07.4972
5.20	3.72270 ± 0.6976	36.8710 ± 02.7079	109.28400 ± 07.9488
5.40	4.22090 ± 0.7626	39.8090 ± 02.9170	116.97500 ± 08.5002
5.60	4.71120 ± 0.7700	45.1570 ± 03.3024	128.86700 ± 09.3608
5.80	5.59920 ± 0.8673	47.4730 ± 03.4794	141.65401 ± 10.3067
6.00	6.24960 ± 0.9069	51.5170 ± 03.7726	147.96400 ± 10.7684

Table 4.11: Er L-subshell X-ray production cross sections by α particles.

Energy (MeV)	$\sigma^x_{L_1}$ (barn)	$\sigma^x_{L_2}$ (barn)	$\sigma^x_{L_3}$ (barn)
1.20	0.17387 ± 0.0928	00.54928 ± 0.0780	001.60620 ± 00.1659
1.40	0.23652 ± 0.1059	00.73811 ± 0.0966	002.75139 ± 00.2460
1.60	0.30111 ± 0.1212	01.40685 ± 0.1429	004.00639 ± 00.3389
1.80	0.43629 ± 0.1591	01.92419 ± 0.1830	005.62054 ± 00.4547
2.00	0.50250 ± 0.1821	02.77833 ± 0.2409	008.39795 ± 00.6510
2.20	0.57876 ± 0.3385	03.77457 ± 0.3509	011.66430 ± 00.9447
2.40	0.65394 ± 0.3398	04.68603 ± 0.4193	013.89580 ± 01.1081
2.60	0.80479 ± 0.3611	05.63116 ± 0.4798	017.57270 ± 01.3725
2.80	0.88428 ± 0.4347	06.70375 ± 0.5630	021.00330 ± 01.6220
3.00	0.95589 ± 0.4184	07.96775 ± 0.6595	026.36180 ± 02.0104
3.20	1.01848 ± 0.5116	09.80476 ± 0.7905	031.48640 ± 02.3832
3.40	1.20637 ± 0.5249	11.29680 ± 0.8985	036.56450 ± 02.7494
3.60	1.22963 ± 0.5638	13.60940 ± 1.0658	040.17190 ± 03.0174
3.80	1.25892 ± 0.5808	15.20760 ± 1.1827	046.16210 ± 03.4518
4.00	1.39240 ± 0.6689	17.91460 ± 1.3911	057.13840 ± 04.2647
4.20	1.67004 ± 0.6554	19.47940 ± 1.5006	061.82560 ± 04.6064
4.40	1.75058 ± 0.7314	22.75260 ± 1.7404	068.33790 ± 05.0939
4.60	2.06430 ± 0.8256	24.70150 ± 1.8845	075.81290 ± 05.6399
4.80	2.19528 ± 0.8548	28.06010 ± 2.1344	085.84850 ± 06.3904
5.00	2.67469 ± 0.8537	29.27360 ± 2.2241	089.58660 ± 06.6648
5.20	3.15401 ± 0.8891	32.12110 ± 2.4328	097.41370 ± 07.2402
5.40	3.63452 ± 0.9321	35.35250 ± 2.6717	102.39400 ± 07.6167
5.60	4.08661 ± 1.041	39.19800 ± 2.9645	111.61900 ± 08.3245
5.80	4.72137 ± 1.1097	42.15890 ± 3.1963	120.54700 ± 09.0137
6.00	5.55261 ± 1.1915	46.33290 ± 3.5035	136.74800 ± 10.2101

Table 4.12: Tm L-subshell X-ray production cross sections by α particles.

Energy (MeV)	$\sigma^x_{L_1}$ (barn)	$\sigma^x_{L_2}$ (barn)	$\sigma^x_{L_3}$ (barn)
1.20	0.20010 ± 0.0636	00.45469 ± 0.0652	001.08740 ± 0.1135
1.40	0.26487 ± 0.0854	00.73624 ± 0.0889	001.98700 ± 0.1805
1.60	0.34589 ± 0.1397	01.21966 ± 0.1234	003.28076 ± 0.2755
1.80	0.42421 ± 0.1370	01.72404 ± 0.1609	004.88925 ± 0.3924
2.00	0.52025 ± 0.1498	02.49424 ± 0.2075	007.14582 ± 0.5467
2.20	0.60869 ± 0.1857	03.13146 ± 0.2594	009.63527 ± 0.7294
2.40	0.69533 ± 0.2230	04.29537 ± 0.3397	012.91370 ± 0.9617
2.60	0.79489 ± 0.2281	05.16217 ± 0.4045	016.03180 ± 1.1877
2.80	0.85144 ± 0.2765	06.44671 ± 0.4941	019.76800 ± 1.4528
3.00	0.97386 ± 0.2840	07.67202 ± 0.5826	024.12930 ± 1.7654
3.20	1.00596 ± 0.3083	09.18376 ± 0.6900	027.92730 ± 2.0381
3.40	1.03804 ± 0.3376	10.64790 ± 0.7952	032.37210 ± 2.3575
3.60	1.05645 ± 0.3615	11.82820 ± 0.8820	035.94460 ± 2.6154
3.80	1.23040 ± 0.3787	13.68580 ± 1.0140	044.02970 ± 3.1969
4.00	1.35558 ± 0.5278	15.04670 ± 1.1527	047.54300 ± 3.5204
4.20	1.46346 ± 0.5822	16.73460 ± 1.2818	052.55960 ± 3.8876
4.40	1.58615 ± 0.6606	19.52710 ± 1.4880	059.37800 ± 4.3949
4.60	1.78467 ± 0.6808	21.38940 ± 1.6256	066.86220 ± 4.9531
4.80	2.03890 ± 0.6910	24.11480 ± 1.8215	073.50650 ± 5.4385
5.00	2.31176 ± 0.8096	27.60320 ± 2.0835	082.88040 ± 6.1412
5.20	2.68409 ± 0.8528	30.27040 ± 2.2942	090.30370 ± 6.7093
5.40	2.99476 ± 0.8702	32.14100 ± 2.4287	093.95200 ± 6.9740
5.60	3.58799 ± 0.9397	35.37070 ± 2.6808	105.98800 ± 7.8992
5.80	4.13252 ± 0.9861	38.83940 ± 2.9397	115.55900 ± 8.6186
6.00	4.68555 ± 1.1556	44.40430 ± 3.3546	124.08300 ± 9.2630

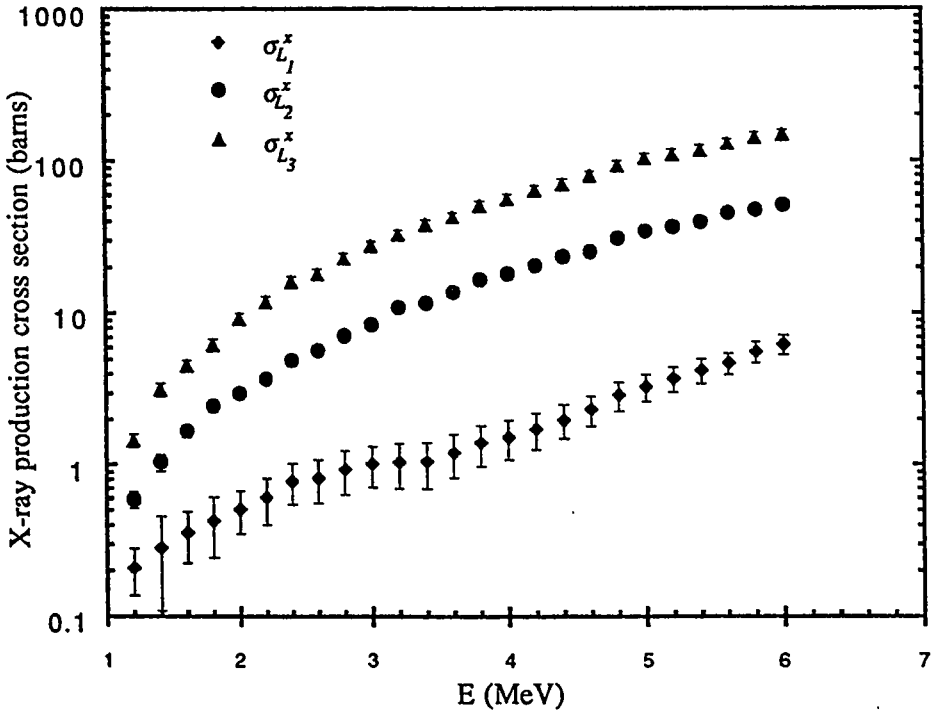

Figure 4-23: A plot of the L_1, L_2, and L_3-subshell X-ray production cross sections for Ho, versus α-particle bombardment energies.

uncertainties are represented by the error bars. The general tendency of the production cross section is similar to those of X-ray yield, due to the explicit dependence of the production cross section on the yield.

4.4 L-subshell Ionization Cross-Section Measurements

The production cross sections in section 4.3 were converted to ionization cross section by incorporating the Auger effect and Coster-Kronig transitions among L-subshells as indicated in section 2.3.3 and verified in equation (2.127), (2.129), and equation (2.131) for L_1, L_2, and L_3 subshells, respectively. The last term in those equations

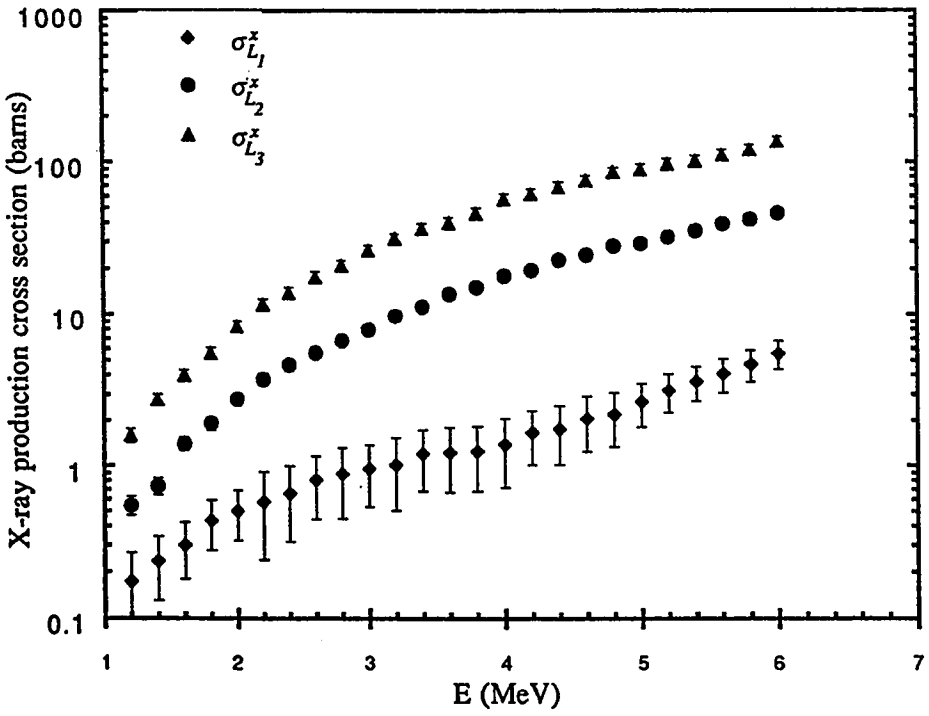

Figure 4-24: A plot of the L_1, L_2, and L_3-subshell X-ray production cross sections for Er, versus α-particle bombardment energies.

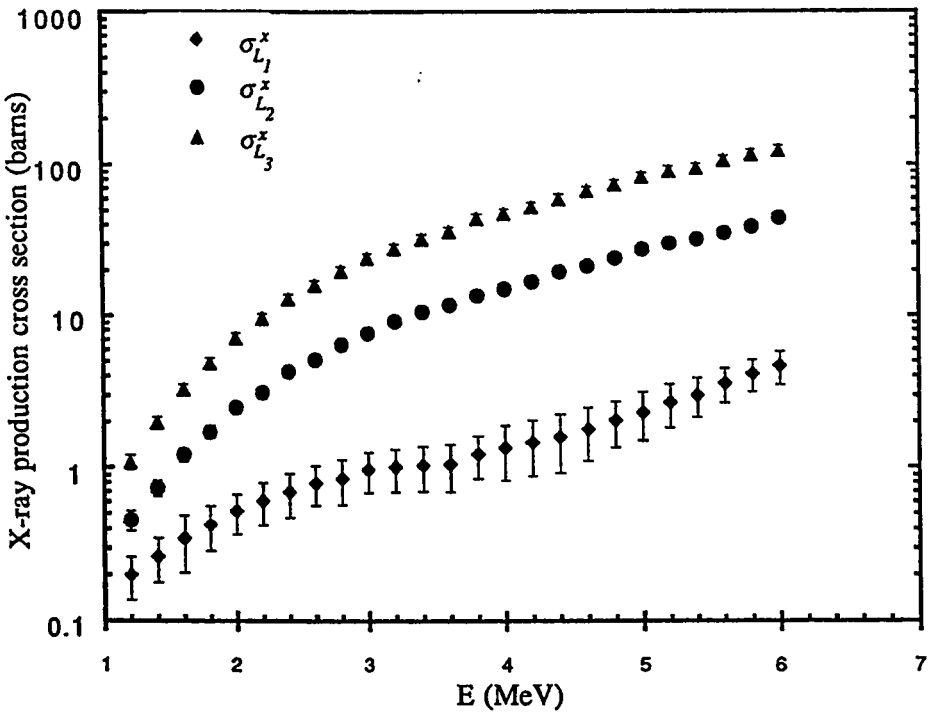

Figure 4-25: A plot of the L_1, L_2, and L_3-subshell X-ray production cross sections for Tm, versus α-particle bombardment energies.

Table 4.13: Fluorescence yields and Coster-Kronig factors.

KRAUSE, 1979						
Element	ω_1	ω_2	ω_3	f_{12}	f_{13}	f_{23}
Ho	0.0940	0.1890	0.1820	0.1900	0.3000	0.1420
Er	0.1000	0.2000	0.1920	0.1900	0.3000	0.1400
Tm	0.1060	0.2110	0.2010	0.1900	0.2900	0.1390
CHEN *et al.*, 1981						
Element	ω_1	ω_2	ω_3	f_{12}	f_{13}	f_{23}
Ho	0.0964	0.2100	0.1960	0.2180	0.3360	0.1520
Er	0.1020	0.2216	0.2051	0.1865	0.3415	0.1489
Tm	0.1090	0.2153	0.2153	0.1459	0.3466	0.1462

which accounts the vacancy migration induced by K-shell ionization was ignored. This is because the K-shell ionization cross section is very small compared to L_2 and L_3-subshell ionization cross sections as expected by all of the theoretical models. This may not hold precisely for L_1 subshell, but the vacancy migration probability from $K \rightarrow L_1$, $\eta_{K \rightarrow L_1}$, is very small since it represents the forbidden magnetic dipole transition. In fact the effect of vacancy migration induced by K-shell ionization was ignored even for proton impact as demonstrated by SOKHI and CRUMPTON[69] for Dy ($Z = 66$) and Yb ($Z = 70$), in which Ho, Er, and Tm lie between them.

Since the experimental data are sensitive to the atomic decay parameters adopted (fluorescence yields and Coster-Kronig transitions), it is interesting to use the two tribute data sets for the atomic decay parameters, those are the semi-empirical values of KRAUSE[10] and the theoretical values of CHEN *et al.*[11]. This is to compare the behaviour of the ionization cross section at two different data sets of decay parameters, and to find a reason for any possible discrepancy. The values of the atomic decay parameters for the two data sets are listed in table (4.13). The semi-empirical decay parameters of KRAUSE[10] are given directly in the reference for the desired elements, whereas the theoretical values of CHEN *et al.* were interpolated to obtain the decay parameters for the desired elements.

The calculation of ionization cross sections for Ho, Er, and Tm were carried out

using *Mathematica* as shown in appendix C. These values were then transferred to and listed in MS EXCELL data-base file. A plots of the L-subshell ionization cross sections by α-particle bombardments are shown in figure (4-26) for Ho, figure (4-27) for Er, and figure (4-28) for Tm. For the three elements, the general tendency of the ionization cross sections is similar. The solid points represent the ionization cross-section values that were calculated by adopting the atomic decay parameters of KRAUSE[10] whereas the hallow points represent that the ionization cross-section values that were calculated by adopting the atomic decay parameters of CHEN *et al.*[11]. The curves in the plots represents the *ECPSSR* theory predictions taken from COHEN and HARRIGAN[51]. The reason of choosing this version of *ECPSSR* is due to the accurate estimations of the integration limits of the form factor and correction factors and detailed tabulated cross section values at various bombardment energy of α particles. The error bars in the figures demonstrate the contribution of the X-ray production cross section uncertainties, neglecting the contributions of atomic decay parameters adopted in the calculations.

The general tendencies of the ionization cross section for the three elements are quite similar. Except L_1 subshell, the experimental values which were calculated by adopting the theoretical decay parameters of CHEN *et al.* are lower and closer to the theoretical predictions than those were calculated by adopting the semi-empirical decay parameters of KRAUSE. However, the theoretical prediction underestimates the experimental values for L_2 and L_3 subshells for the three elements when the bombardment energy is less than 4 MeV and discrepancies increase as the energy decreases. This agrees with the general results of most of the literatures[61, 2, 65, 67]. However for L_1 subshell, the theoretical prediction over estimate the experimental ionization cross sections when bombardment energy is less than 4 MeV whereas a satisfactory agreement between theory and experiment at energies higher than 4 MeV turns up. The trend of L_1 subshell experimental cross sections with respect to the theoretical predictions is similar to that given by CUZZOCREA *et al.*[86].

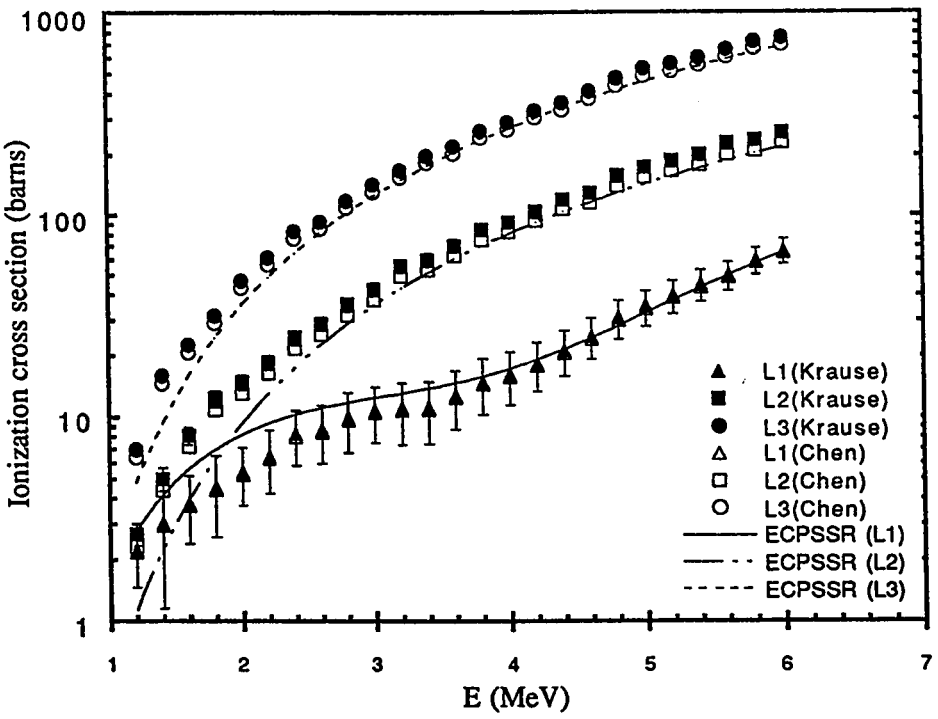

Figure 4-26: A plot of the L_1, L_2, and L_3-subshell ionization cross sections for Ho by α-particle bombardment, versus α-particle bombardment energies. The curves represent the predictions of the *ECPSSR* theory.

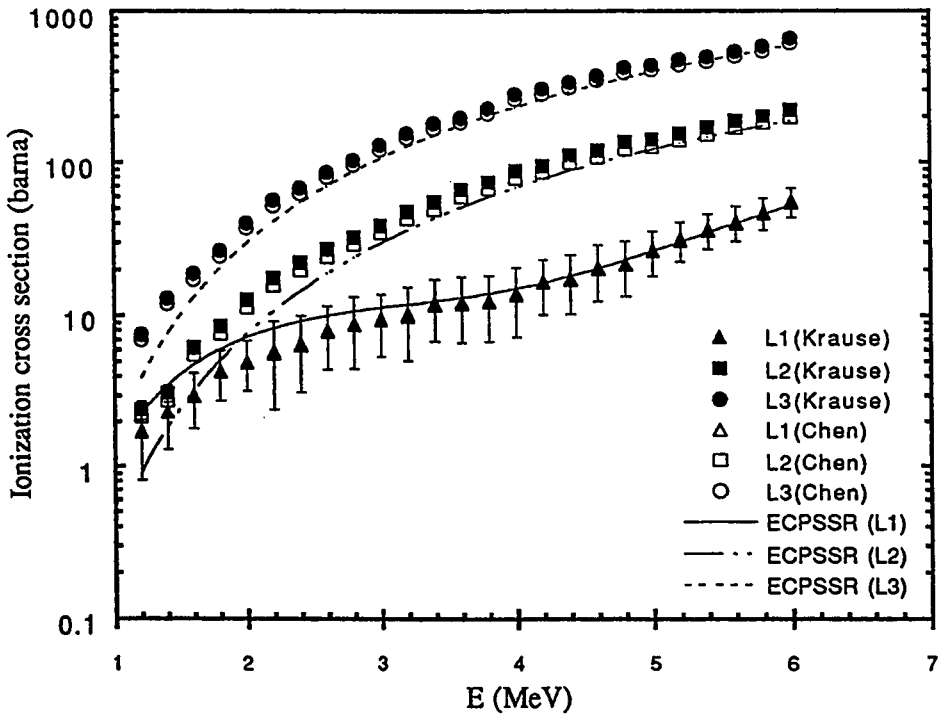

Figure 4-27: A plot of the L_1, L_2, and L_3-subshell ionization cross sections for Er by α-particle bombardment, versus α-particle bombardment energies. The curves represent the predictions of the *ECPSSR* theory.

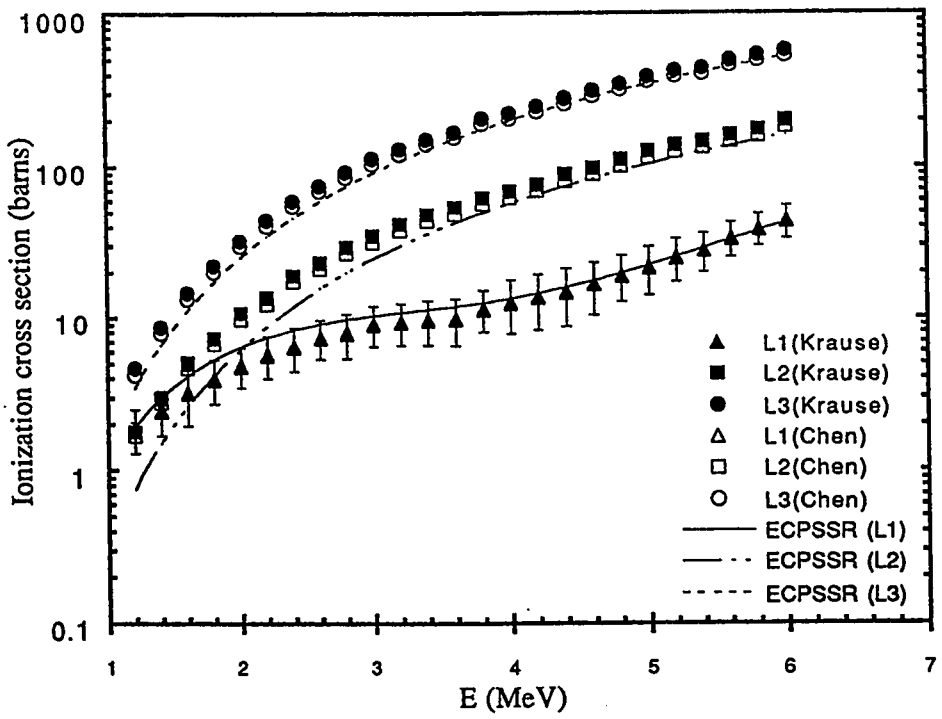

Figure 4-28: A plot of the L_1, L_2, and L_3-subshell ionization cross sections for Tm by α-particle bombardment, versus α-particle bombardment energies. The curves represent the predictions of the *ECPSSR* theory.

A possible conclusion from above discussion and from figures (4-26) to (4-28) is that the L_2 and L_3-subshell ionization cross sections increase on the expense of L_1-subshell ionization cross section. This can be explained in accordance to the collision-induced intra-shell transition effects explained in section 2.2.9. To support this conclusion, the experimental and theoretical total L-shell ionization cross sections are plotted versus the bombardment energies as shown in figure (4-29) for Ho, figure (4-30) for Er, and figure (4-31) for Tm. The total L-shell ionization cross section is given in term of the subshells ionization cross sections by the following equation

$$\sigma_L^i = \sigma_{L_1}^i + \sigma_{L_2}^i + \sigma_{L_3}^i$$

It turns out from the plots that the theoretical values agree with the experimental ones within the experimental errors, especially for values which are calculated using theoretical atomic parameters of CHEN *et al.*[11]. The agreement is excellent at energies greater than 2.6 MeV and fair at lower energies.

It should also be mentioned that in figures (4-26) to (4-28), the extrapolation of the experimental values at energies less than 1.2 MeV shows that $\sigma_{L_1}^i > \sigma_{L_2}^i$. This is predicted by the *ECPSSR* theory but at energies less than 2 MeV. This can be explained in view of binding effect. This effect at low energy α particles becomes much larger for L_2 subshell than L_1 subshell since the response time (inversely proportional to electronic binding energy as shown in section 2.2.6) of L_2 subshell electron is much longer than the collision time compared with L_1 subshell electron, that suppresses the ionization cross section of L_2 subshell significantly and raises this circumstance[52]. The binding effect no longer holds at high energies since the collision time is very short compared to the electronic response time in any particular subshell.

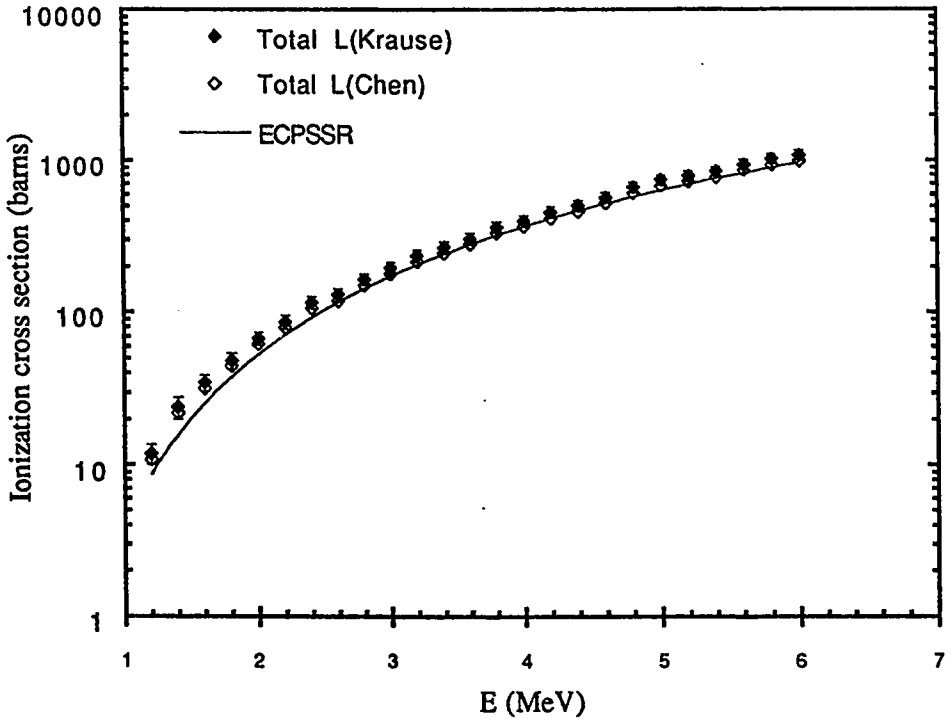

Figure 4-29: A plot of α-particle induced total L-shell ionization cross sections for Ho versus α-particle bombardment energies. The curves represent the predictions of the *ECPSSR* theory.

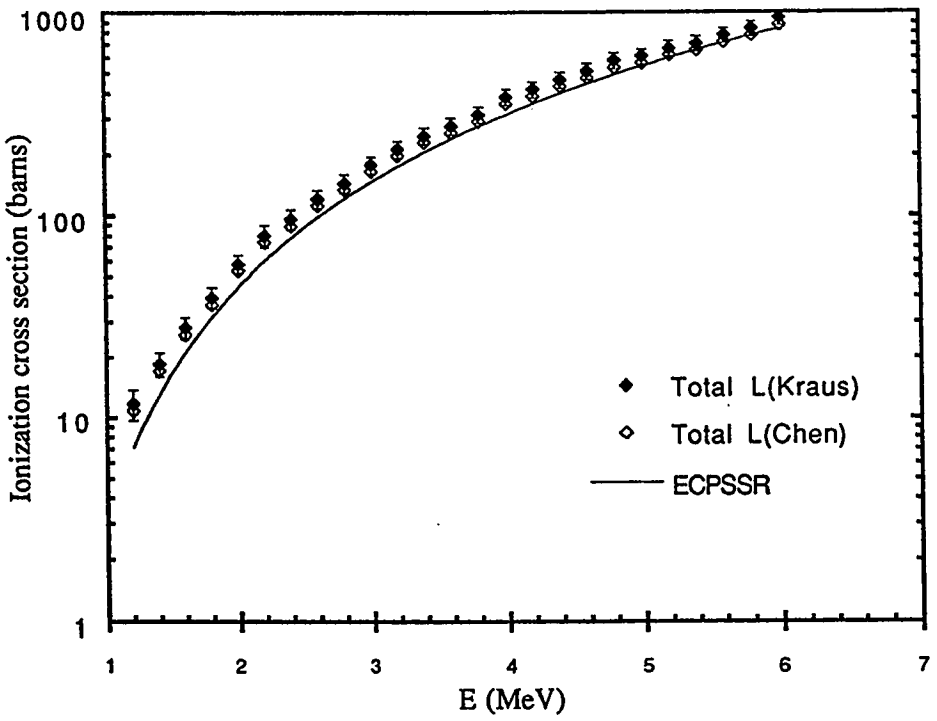

Figure 4-30: A plot of α-particle induced total L-shell ionization cross sections for Er versus α-particle bombardment energies. The curves represent the predictions of the *ECPSSR* theory.

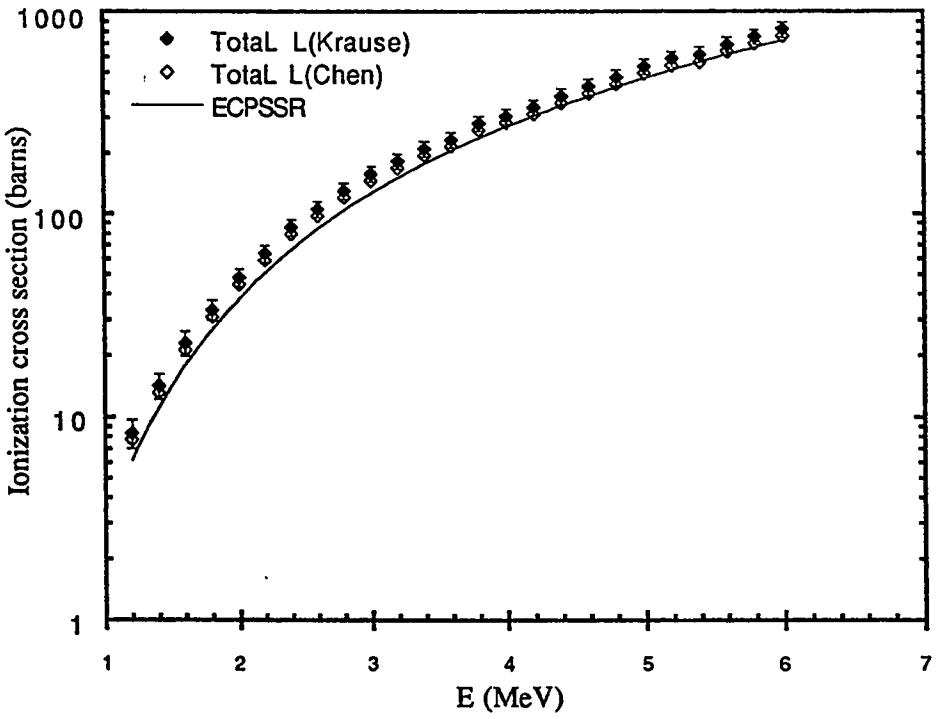

Figure 4-31: A plot of α-particle induced total L-shell ionization cross sections for Tm versus α-particle bombardment energies. The curves represent the predictions of the *ECPSSR* theory.

4.5 Discussion

With the purpose of analysing the experimental data properly, the experimental ionization cross sections must be normalized by the theoretical predictions and plotted versus relevant scaling parameter. In this case, the parameter is selected to be the reduced velocity parameter ξ_{L_i} which is given in equation (2.5) according to the definition of BASBAS *et al.*[36]. The parameter ξ_{L_i} was chosen because it gives the characteristic of a particular shell at certain bombardment energy. Moreover, one becomes able to distinct between the fast and slow collision according to the demarcation of BASBAS *et al.*[36]. In recent work, the parameter ξ_{L_i} is usually replaced by the relativistic reduced velocity parameter $\xi^R_{L_i}$ which is related to ξ_{L_i} as given in equation (2.63). However, one is not concerned in reducing the statistical fluctuations of the normalized data points, but in contrast to verify any possible discrepancies in order to come up with rigorous conclusions.

Figures (4-32), (4-33), and figure (4-34) shows the ratio $\sigma^{\exp}_{L_i}/\sigma^{ECPSSR}_{L_i}$ versus the reduced velocity parameter ξ_{L_i} of α-particle impact for L_1, L_2, and L_3 subshells, respectively. In figure (4-32), for L_1 subshell, the *ECPSSR* theory over estimates the experimental points when $\xi_{L_1} < 0.27$ and average deviation is estimated to be 27% within this range for all points either calculated by the decay parameters of KRAUSE or by CHEN *et al.* When $\xi_{L_1} > 0.27$, the points start improving and an average deviation around $\pm 3\%$ is estimated for the points which were calculated by the decay parameters of KRAUSE[10], and $\pm 2.6\%$ for the points which were calculated by the decay parameters of CHEN *et al.*[11].

In case of L_2 subshell the *ECPSSR* theory underestimates the experimental data up to factor 3 as shown in figure (4-33). The discrepancies decrease gradually with increasing reduced velocity. Improvement starts within the range $\xi_{L_2} > 0.28$, in which average deviation is estimated to be 7% for the points that were calculated by the decay parameters of CHEN *et al.* and 16% for the points those were calculated by the decay parameters of KRAUSE. Whereas a 29% and 36% average deviations are estimated for

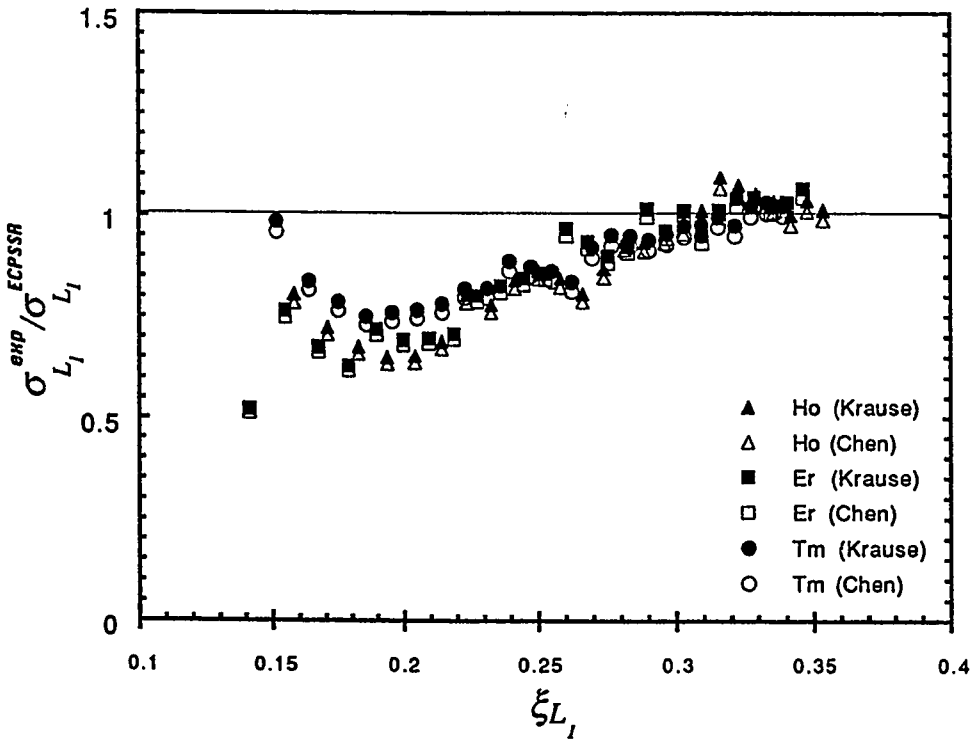

Figure 4-32: The ratio $\sigma^{exp}_{L_1}/\sigma^{ECPSSR}_{L_1}$ versus the reduced velocity parameter ξ_{L_1} for α-particle induced L_1-subshell ionization. Each element is marked by different symbol (see legend). Dark symbols indicate that the decay parameters of CHEN *et al.* are adopted and open symbols indicate that the decay parameters of KRAUSE are adopted.

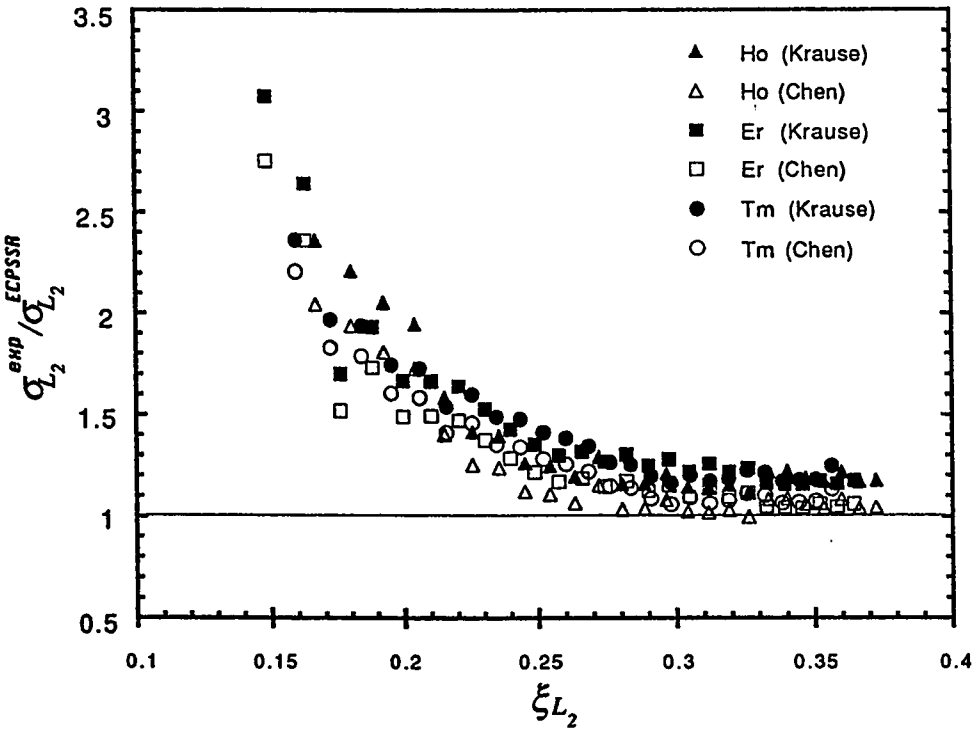

Figure 4-33: The ratio $\sigma^{exp}_{L_2}/\sigma^{ECPSSR}_{L_2}$ versus the reduced velocity parameter ξ_{L_2} for α-particle induced L_2-subshell ionization. Each element is marked by different symbol (see legend). Dark symbols indicate that the decay parameters of CHEN *et al.* are adopted and open symbols indicate that the decay parameters of KRAUSE are adopted.

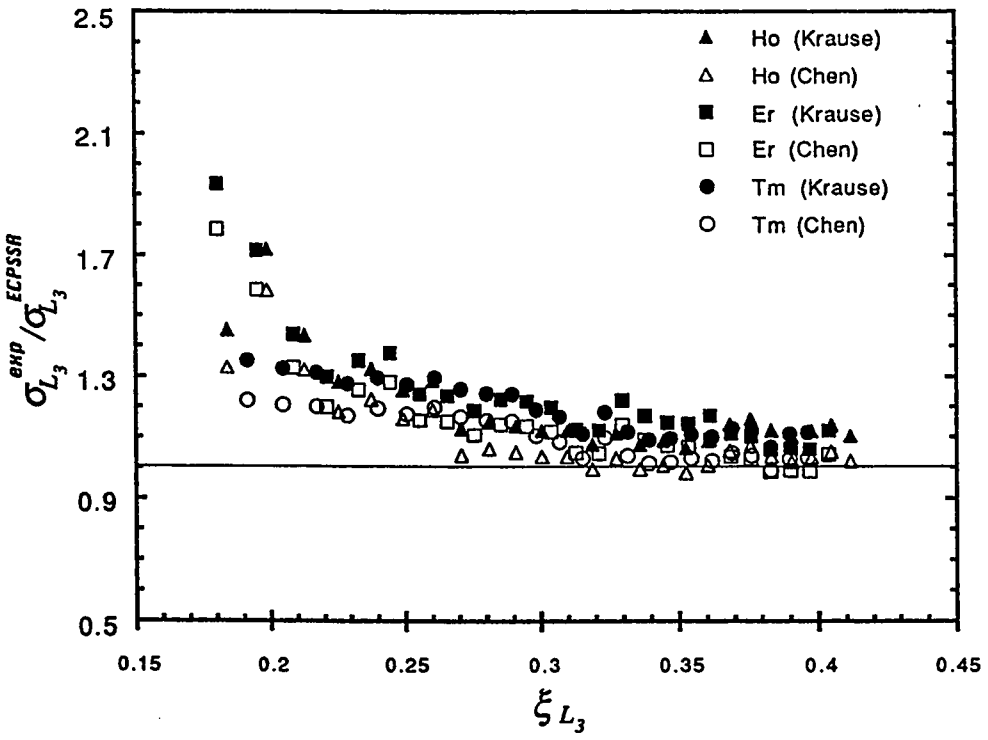

Figure 4-34: The ratio $\sigma^{exp}_{L_3}/\sigma^{ECPSSR}_{L_3}$ versus the reduced velocity parameter ξ_{L_3} for α-particle induced L_3-subshell ionization. Each element is marked by different symbol (see legend). Dark symbols indicate that the decay parameters of CHEN *et al.* are adopted and open symbols indicate that the decay parameters of KRAUSE are adopted.

the experimental values that were calculated by CHEN *et al.* and KRAUSE, respectively, when $\xi_{L_2} < 0.28$. A similar general tendency is observed for the L_3 subshell. However, here the experimental results agree much better with theory. The theory also underestimates the experimental values up to factor 1.8 as shown in figure (4-34). The average deviation is estimated to be 17% and 23% for the experimental values that were calculated by CHEN *et al.* and KRAUSE, respectively, at $\xi_{L_3} < 0.30$, while a 3.9% and 10.5% average deviations from the theory are estimated for the experimental values that were calculated by CHEN *et al.* and KRAUSE, respectively, when $\xi_{L_3} > 0.30$.

One can generally conclude that the there are fair agreements between the *ECPSSR* predictions and experimental values especially at low energies and the strongest discrepancies between the experimental data and theoretical predictions are found for the L_2 subshell. One claim, that is also mentioned in many literatures, is that the discrepancies are mainly due to the multi-vacancy configuration which alter the single-hole atomic decay parameters entirely. In multi-vacancy process, one expects that the detected X-ray lines to be broadened and comparable intensities of satellite lines are presented. These prospects were not detected in this experiment in such proclaims. However, another test can verify whether the multi-vacancy effect holds or not, that is to estimate the relative intensities of the X-ray lines, those originated from common subshell, and compare them with the corresponding single-vacancy relative intensity values of SALEM *et al.*[15]. This is because when a multi-vacancy creation takes place, the relative intensities of X-ray lines are altered drastically and large departure from the relative intensity values that are produced by single-vacancy creation. It was found that the $L_{\beta_{2,15}}/L_\alpha$, L_{γ_1}/L_{β_1}, and $L_{\gamma_{2,3}}/L_{\beta_3}$ values for the three elements are almost constant with respect to bombardment energies and agree well within the experimental errors with those values estimated by SALEM *et al.*[15], except for Tm $L_{\beta_{2,15}}/L_\alpha$, which is appreciably larger than the that of SALEM *et al.* due to the overlapping of $L_{\beta_{2,15}}$ line with the γ rays induced by the ^{169}Tm-8.41 keV level. Recalling that the relative intensities of SALEM *et al.*[15] are estimated by applying least-square fit for a numerous

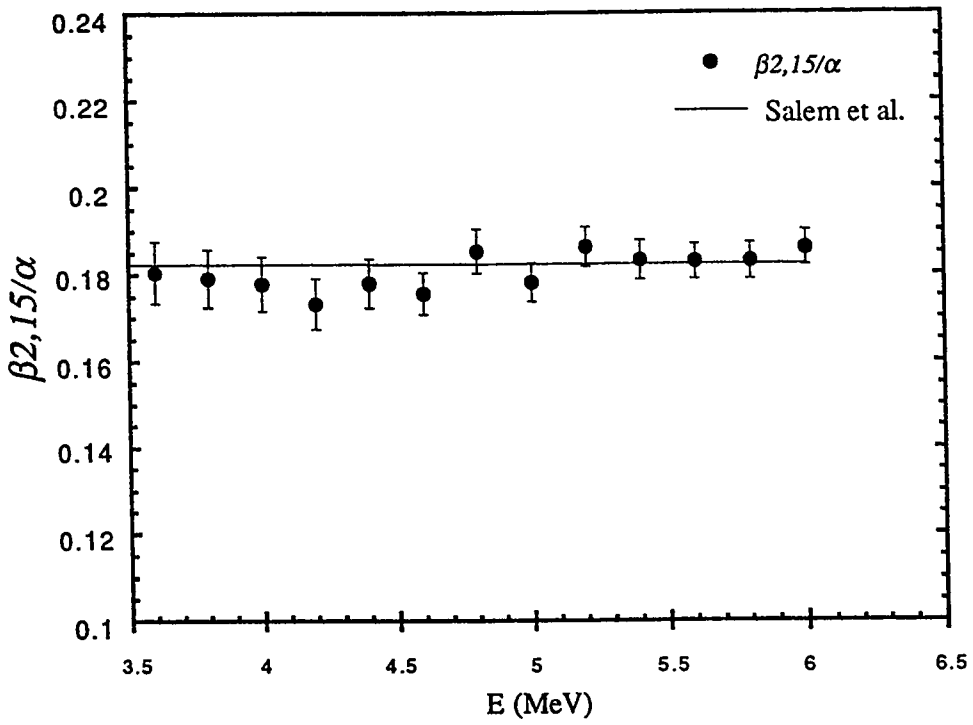

Figure 4-35: A plot of the values of $L_{\beta_{2,15}}/L_{\alpha}$ relative intensity for Ho versus α-particle bombardment energies. The error bars include the uncertainties in yield determination and efficiency of Si(Li) detector. The horizontal line represents the single-vacancy relative intensity estimation of SALEM *et al.*

experimental values that were measured using photon and electron bombardments to guarantee single-vacancy ionization. A selective plots display the values of $L_{\beta_{2,15}}/L_{\alpha}$, in figure (4-35), and the values of L_{γ_1}/L_{β_1} and $L_{\gamma_{2,3}}/L_{\beta_3}$, in figure (4-36), versus α-particle bombardment energies. The figures confirm the fact that the effect of multi-vacancy configuration is ineffective in our case.

The systematic discrepancies observed between experimental L_i-subshell ionization cross section and the predictions of *ECPSSR* theory found at low-velocity range can be reduced after taking into account the coupling between L subshells. As shown in section 2.2.9, the ionization process can not be treated independently for individual L subshells, because the projectile can induce secondary intrashell transitions among subshells. This

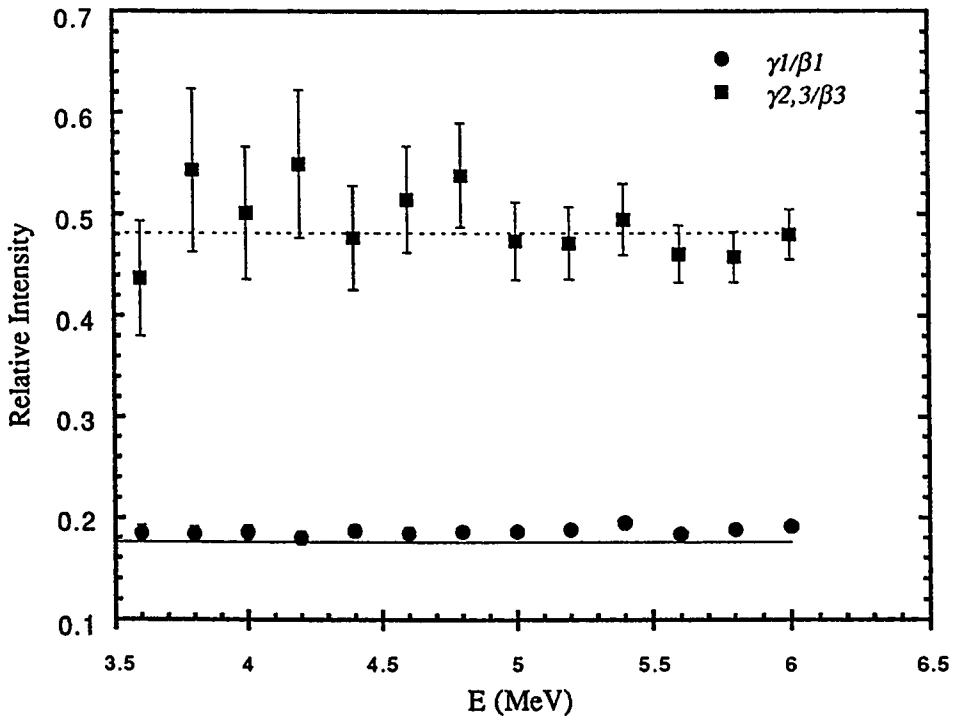

Figure 4-36: A plot of the values of L_{γ_1}/L_{β_1} and $L_{\gamma_{2,3}}/L_{\beta_3}$ relative intensities for Ho versus α-particle bombardment energies. The error bars include the uncertainties in yield determination and efficiency of Si(Li) detector. The horizontal line represents the single-vacancy relative intensity estimation of SALEM *et al.*

effect was introduced in the calculation for α particles using the coupled state model of SARKADI and MOKOYAMA[68, 87, 12, 67], as shown in section 2.2.9, which includes this effect within the *ECPSSR* frame-work via the multiplicative correction factor $C_{L_i}^{IS}(\xi_{L_i})$, given in equation (2.106). However, the values of the function $u_{L_i}(\xi_{L_i})$ in equation (2.107), (2.108), and equation (2.109) for L_1, L_2, and L_3 subshells, respectively, are redefined to be compatible with the selected definition of ξ_{L_i} instead of the definition of SARKADI and MOKOYAMA[67] in equation (2.105) (see the footnote in page 109).

The subsequent model, the *ECPSSR-IS*, is compared with the present data as shown in figure (4-37), (4-38), and figure (4-39) for L_1, L_2, and L_3 subshells, respectively. The main feature deduced from the figures that the systematic disagreements are appreciably reduced L_2, and L_3 subshells, but still velocity-independent discrepancies remain, being even increased, including the L_1 subshell. For L_1 subshell, the average deviation when $\xi_{L_1} < 0.27$ is reduced to 12.4% and 14.4% between the *ECPSSR-IS* predictions and the experimental values those were calculated by the decay parameters of CHEN *et al.* and KRAUSE, respectively. Whereas the average deviation when $\xi_{L_1} > 0.27$ is raised to 12% and 14% between the *ECPSSR-IS* predictions and the experimental values those were calculated by the decay parameters of CHEN *et al.* and KRAUSE, respectively.

For L_2 subshell, the *ECPSSR-IS* underestimates the experimental values up to factor of 1.86 instead of 3 in the *ECPSSR*. The average deviation is reduced to 26.6% and 34 % for the experimental values those were calculated by the decay parameters of CHEN *et al.* and KRAUSE, respectively, when $\xi_{L_2} < 0.28$. But when $\xi_{L_2} > 0.28$, the average deviation is raised to 17% (for the decay parameters of CHEN *et al.*) and 25% (for the decay parameters of KRAUSE). Similar tendency is observed for L_3 subshell. However, even at low velocities (when $\xi_{L_3} < 0.30$) the deviation increases to 27.7% (for the decay parameters of CHEN *et al.*) and 33% (for the decay parameters of KRAUSE), which corresponding to 10% increment with respect to *ECPSSR*. Additionally, when $\xi_{L_3} > 0.30$, the average deviation increases to 11.35% (for the decay parameters of

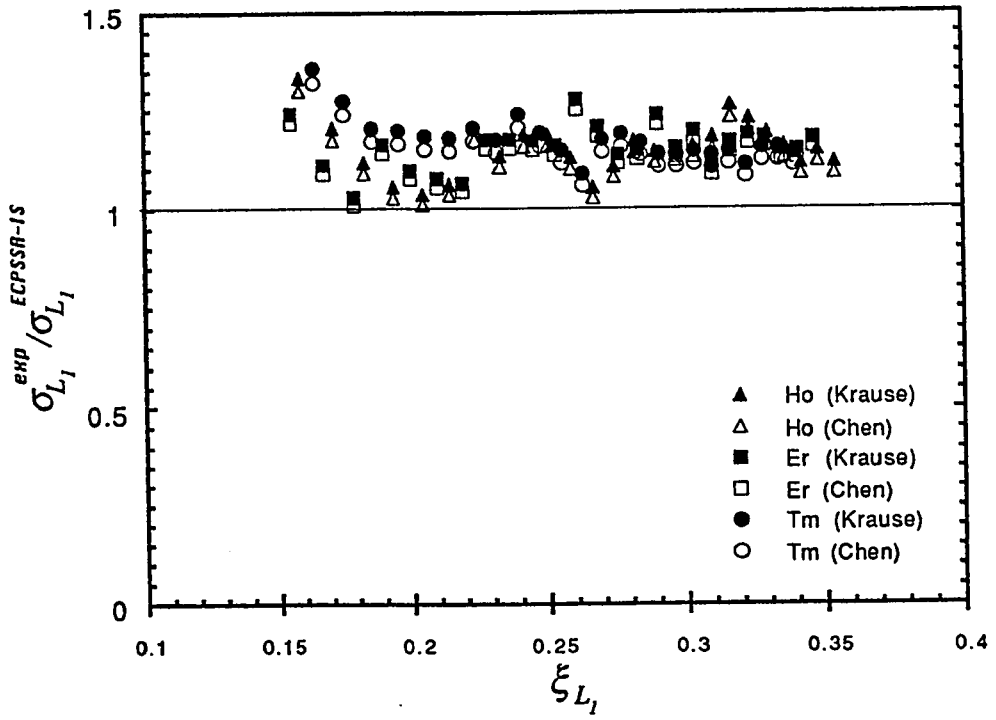

Figure 4-37: The ratio $\sigma_{L_1}^{exp}/\sigma_{L_1}^{ECPSSR-IS}$ versus the reduced velocity parameter ξ_{L_1} for α-particle induced L_1-subshell ionization. Each element is marked by different symbol (see legend). Dark symbols indicate that the decay parameters of CHEN *et al.* are adopted and open symbols indicate that the decay parameters of KRAUSE are adopted.

CHEN *et al.*) and 17.7% (for the decay parameters of KRAUSE).

Following the suggestion of VIGILANTE *et al.*[70], that the *ECPSSR* overestimates the binding effect, the "united atom" (*UA*) effect was incorporated in the *ECPSSR-IS* calculations by correcting the reduced velocity at united atom binding (in this case $I_{L_i}(Z_1 + Z_2)$ instead of $I_{L_i}(Z_2)$, where $Z_1 = 2$) using the multiplicative factor for the binding ϵ_{L_i}, as given in equation (2.110), and recalculate the *ECPSSR-IS* for the yielded reduced velocity parameter, following the recipe of SARKADI and MUKOYAMA[67], with considering the function $g_{L_i}(\xi_{L_i}) = 1$ through the ranges of the reduced velocity parameter. The binding energies were taken from BEARDEN and MURR[88]. This

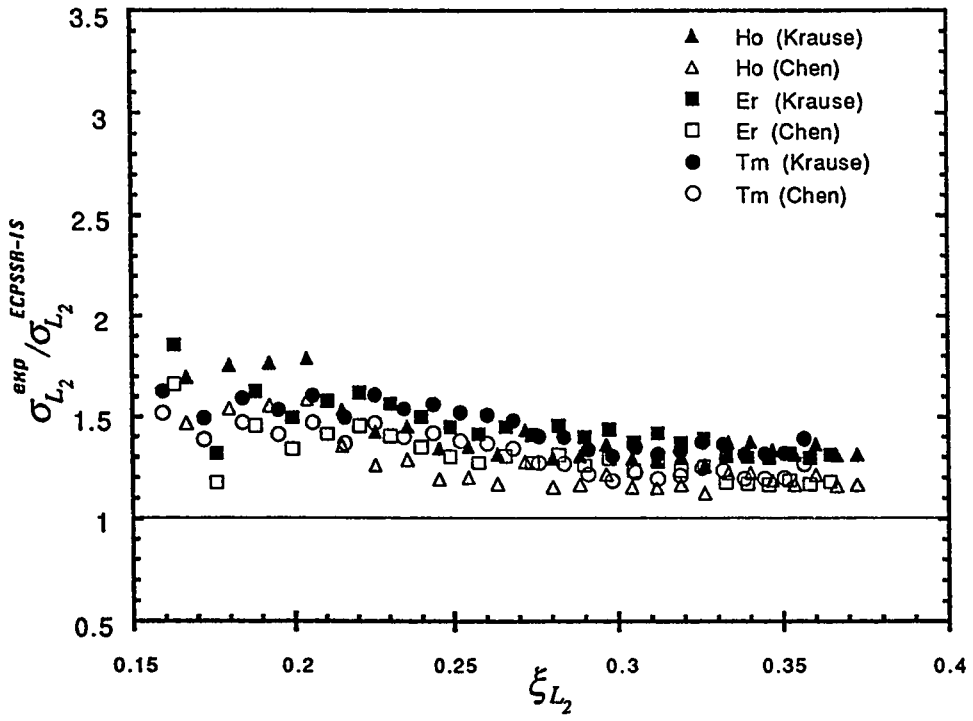

Figure 4-38: The ratio $\sigma_{L_2}^{exp}/\sigma_{L_2}^{ECPSSR-IS}$ versus the reduced velocity parameter ξ_{L_2} for α-particle induced L_2-subshell ionization. Each element is marked by different symbol (see legend). Dark symbols indicate that the decay parameters of CHEN *et al.* are adopted and open symbols indicate that the decay parameters of KRAUSE are adopted.

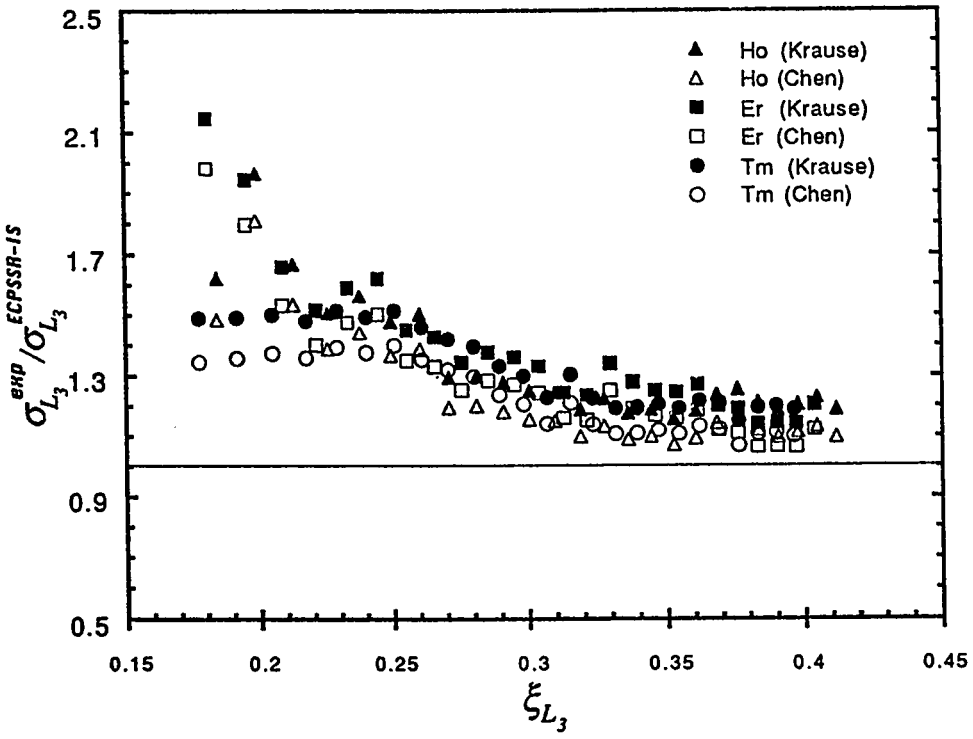

Figure 4-39: The ratio $\sigma_{L_3}^{exp}/\sigma_{L_3}^{ECPSSR-IS}$ versus the reduced velocity parameter ξ_{L_3} for α-particle induced L_3-subshell ionization. Each element is marked by different symbol (see legend). Dark symbols indicate that the decay parameters of CHEN *et al.* are adopted and open symbols indicate that the decay parameters of KRAUSE are adopted.

modification of the calculations, called *ECPSSR-IS-UA*, causes significant changes in the cross section for L_2 and L_3 subshells as shown in figure (4-40) and in figure (4-41) respectively. The agreement of the data is excellent for L_2 and L_3 subshells through the range of the reduced velocity parameter. The average deviation for L_2 subshell, through the range of the reduced velocity parameter, is reduced to 5.2% (for the decay parameters of CHEN *et al.*) and 7.3% (for the decay parameters of KRAUSE). Whereas the average deviation for L_3 subshell is reduced to 3.8% (for the decay parameters of CHEN *et al.*) and 4.3% (for the decay parameters of KRAUSE). The overall agreements for L_2 and L_3 subshells are better than those obtained by SARKADI and MUKOYAMA[67] and by SEMANIAK *et al.*[65]. In figure (4-42), (4-43), and figure (4-44), the L_2 and L_3 subshells experimental ionization cross sections, as well as the ionization cross sections of the *ECPSSR-IS-UA* model, are plotted versus the bombardment energy for the three elements, Ho, Er, and Tm, respectively. Obviously the model describes the experimental data points decently.

For L_1 subshell, the *ECPSSR-IS-UA* model describes the experimental values fairly when $E \leq 3.2$ MeV for the three elements, as shown in figure (4-45), (4-46), and figure (4-47) for the three elements, Ho, Er, and Tm, respectively. A large departure is observed at energies higher than 3.2 MeV and hence the discrepancies are not reduced. One possible reason is that the calculated binding energy should account the screening effect, which reduces the experienced effective charge of the projectile[89], especially at high energies in which the response time of the bound electron is much longer than the collision time. Therefore, the electron does not experience the charge of the projectile totally. In low energies, the electron becomes more sensitive for the Coulomb field of the projectile and capable to respond for this effect since the electronic response time is shorter or comparable to the collision time. Therefore, the *ECPSSR-IS-UA* model were recalculated at united atom binding energy $I_{L_i}(Z_2 + 1)$ which is shown in figure (4-45), (4-46), and figure (4-47) together with the *ECPSSR-IS-UA* for $I_{L_i}(Z_2 + 2)$. Good agreements can be achieved at high energies ($E > 4$ MeV) when the binding

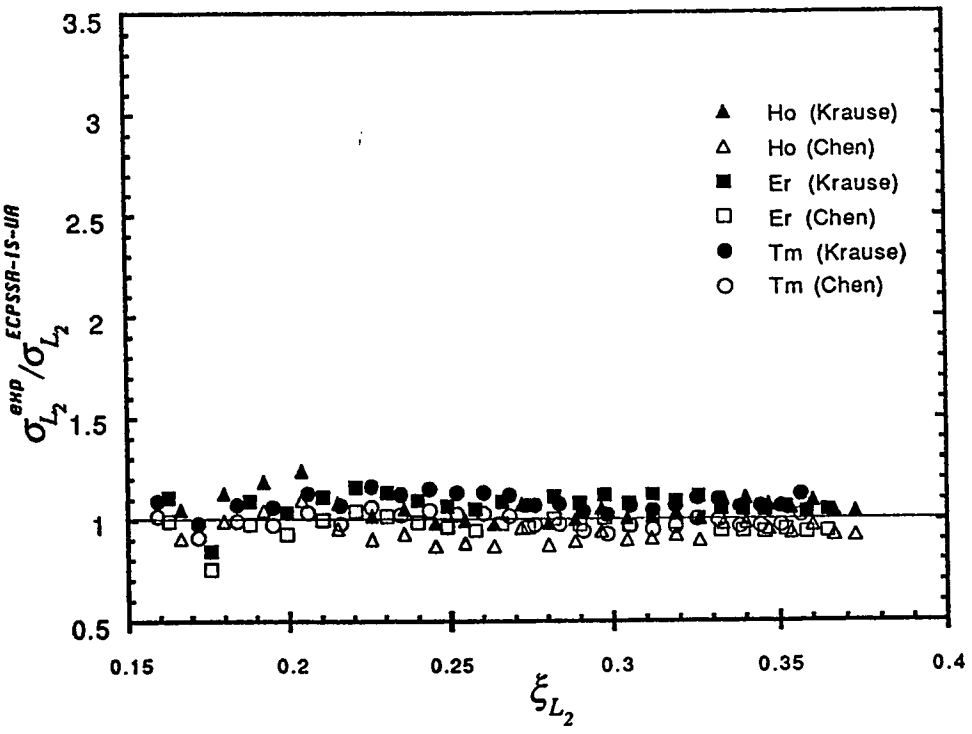

Figure 4-40: The ratio $\sigma_{L_2}^{exp}/\sigma_{L_2}^{ECPSSR-IS-UA}$ versus the reduced velocity parameter ξ_{L_2} for α-particle induced L_2-subshell ionization. Each element is marked by different symbol (see legend). Dark symbols indicate that the decay parameters of CHEN *et al.* are adopted and open symbols indicate that the decay parameters of KRAUSE are adopted.

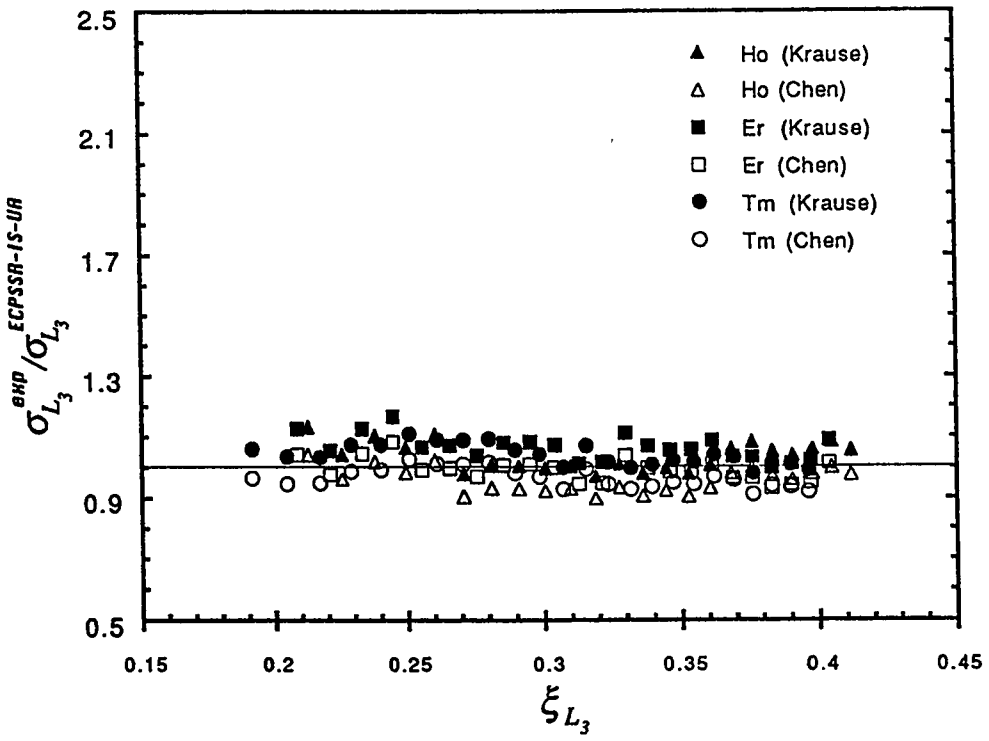

Figure 4-41: The ratio $\sigma^{exp}_{L_3}/\sigma^{ECPSSR-IS-UA}_{L_3}$ versus the reduced velocity parameter ξ_{L_3} for α-particle induced L_3-subshell ionization. Each element is marked by different symbol (see legend). Dark symbols indicate that the decay parameters of CHEN *et al.* are adopted and open symbols indicate that the decay parameters of KRAUSE are adopted.

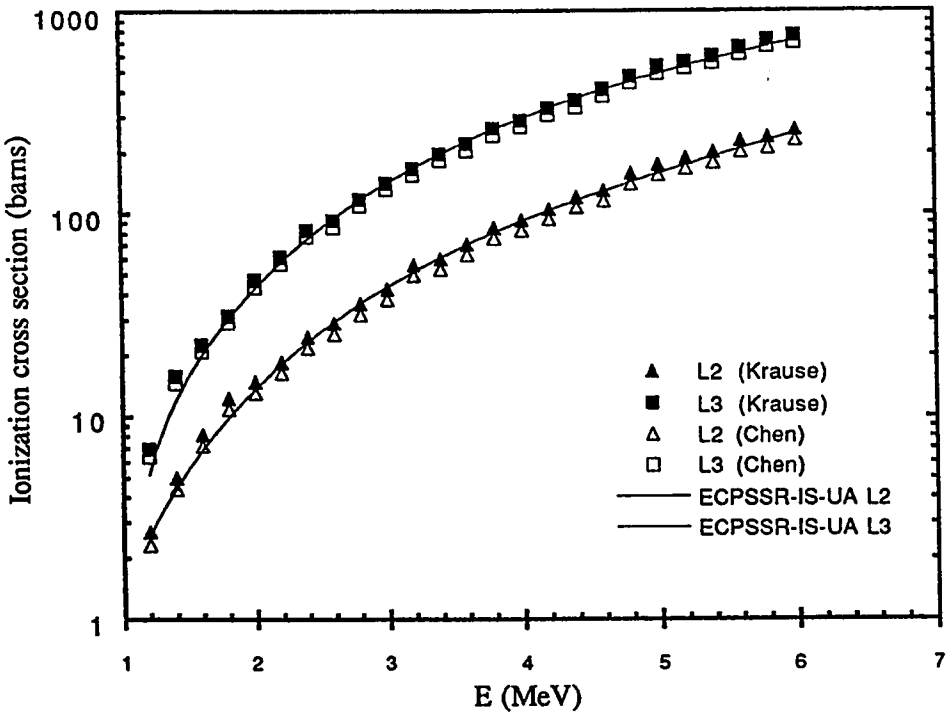

Figure 4-42: A plot of the L_2 and L_3-subshell ionization cross sections for Ho by α-particle bombardment, versus α-particle bombardment energies. The curves represent the predictions of the *ECPSSR-IS-UA* theory.

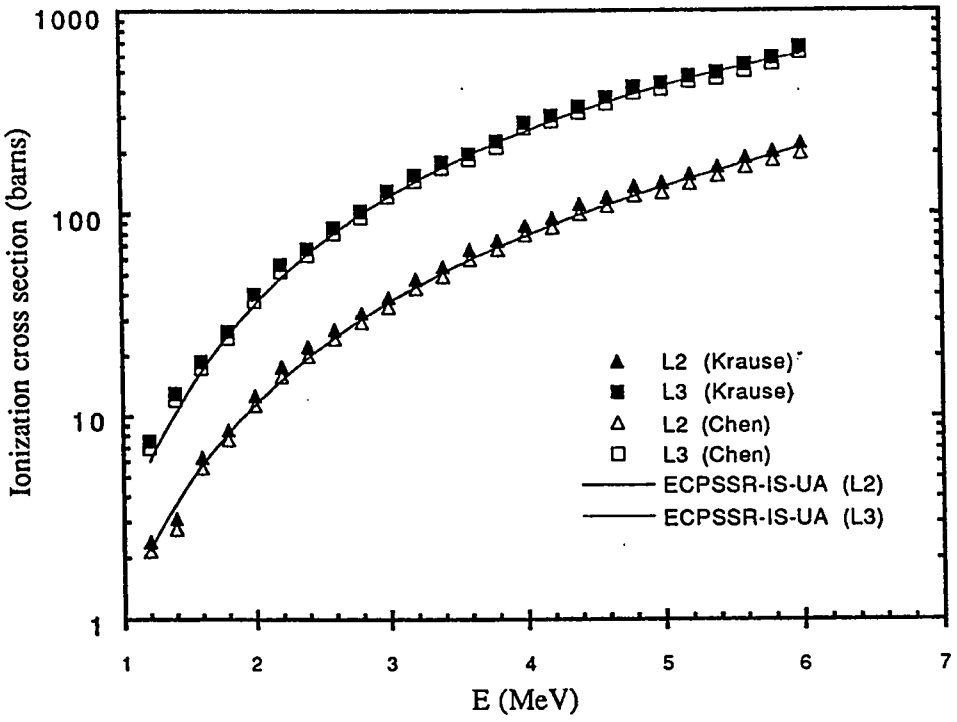

Figure 4-43: A plot of the L_2 and L_3-subshell ionization cross sections for Er by α-particle bombardment, versus α-particle bombardment energies. The curves represent the predictions of the *ECPSSR-IS-UA* theory.

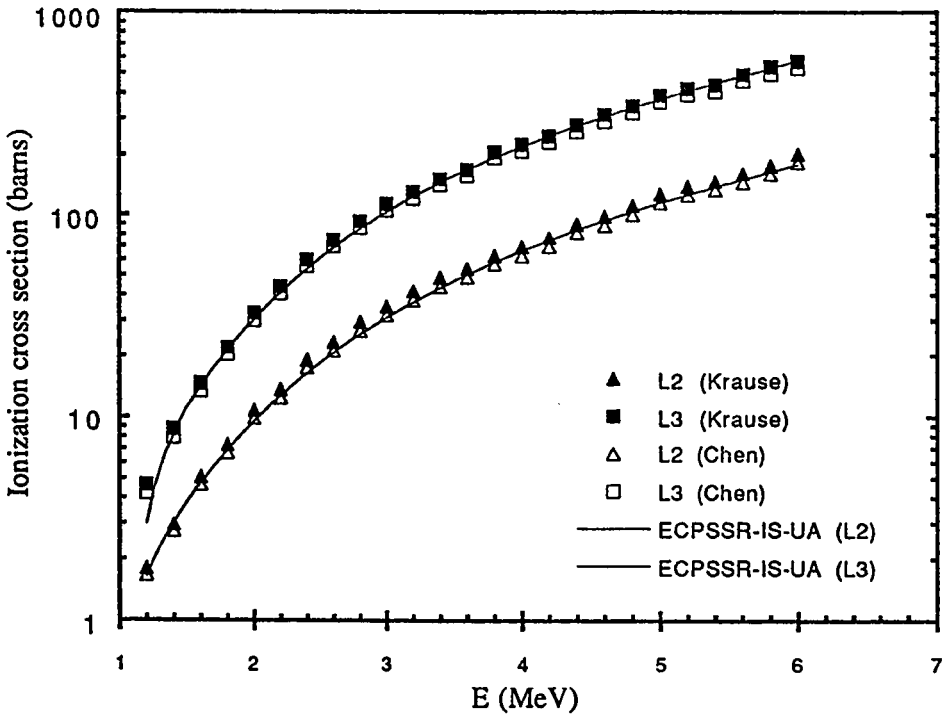

Figure 4-44: A plot of the L_2, and L_3-subshell ionization cross sections for Tm by α-particle bombardment, versus α-particle bombardment energies. The curves represent the predictions of the *ECPSSR-IS-UA* theory.

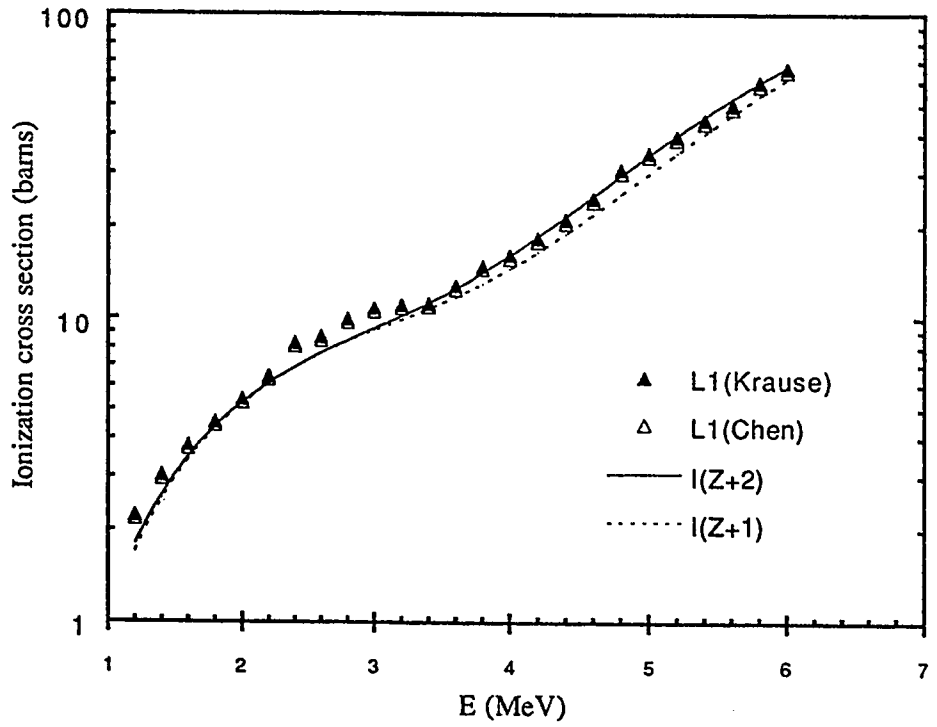

Figure 4-45: A plot of the L_1-subshell ionization cross sections for Ho by α-particle bombardment, versus bombardment energies. The curves represent the predictions of the *ECPSSR-IS-UA* theory.

energy correction in the united atom approach considers the effective charge of the projectile to be between 1 and 2 which is consistent with the previous presumption.

Additionally, the discrepancies between the *ECPSSR-IS-UA* model and the experimental L_1-subshell ionization cross sections is attributed to the use of unrealistic wave functions, which do not reflect the behaviour of the atomic electrons adequately[65]. Attempts to introduce such a description have been made by SARKADI and MUKOYAMA[12, 67]. They showed that the use of a Dirac-Hartree-Slater (DHS) wave functions instead of the screened hydrogen-like (SH) wave functions, which are adopted in the *ECPSSR* formalism, causes changes of the cross sections for L_1 subshell up to 60% for the lowest velocities measured, improving the agreement between the experiment and the theory[65, 67]. More recent attempts have been done by DECESARE *et al.*[90],

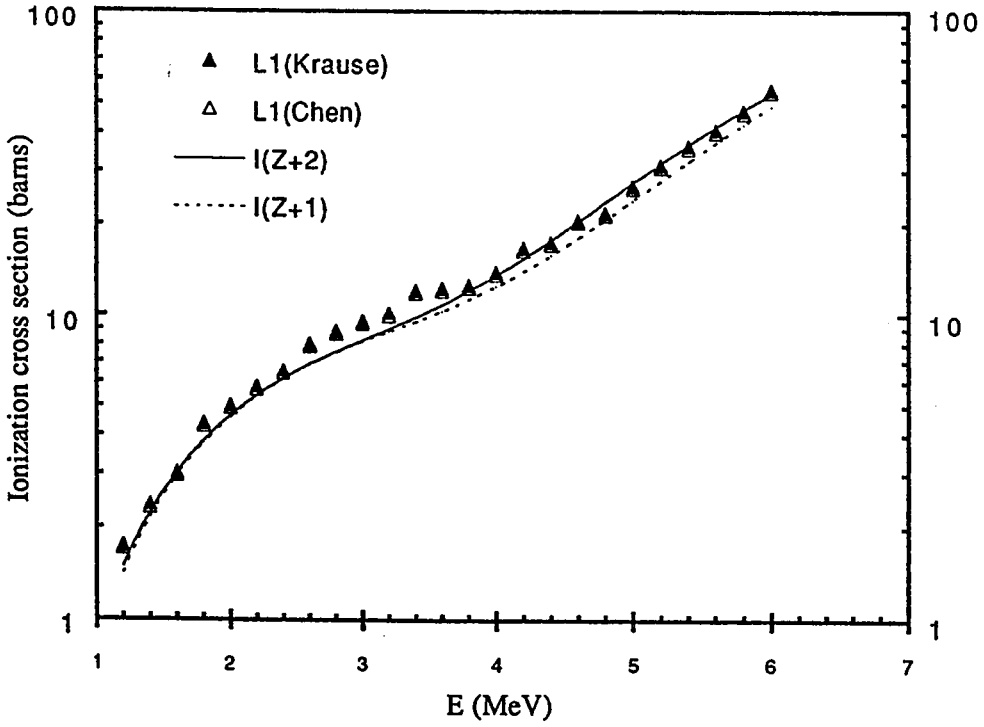

Figure 4-46: A plot of the L_1-subshell ionization cross sections for Er by α-particle bombardment, versus bombardment energies. The curves represent the predictions of the *ECPSSR-IS-UA* theory.

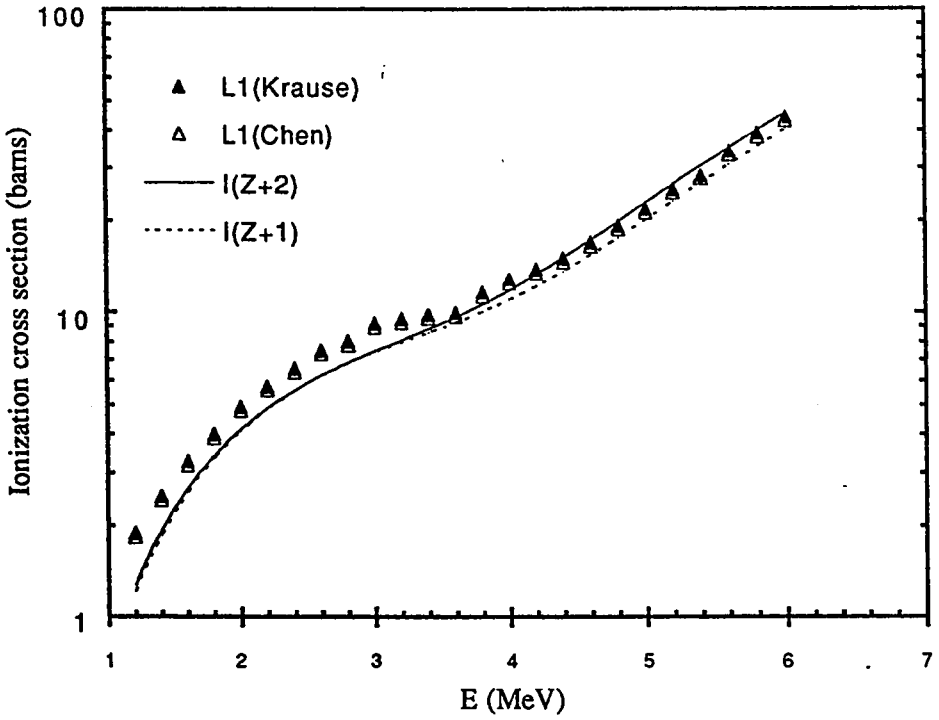

Figure 4-47: A plot of the L_1-subshell ionization cross sections for Tm by α-particle bombardment, versus bombardment energies. The curves represent the predictions of the *ECPSSR-IS-UA* theory.

through calculating the *ECPSSR-IS-UA-DHS* for α particles using the *RPWBA-BC* of CHEN and CRASEMAN[55] for protons taking advantage of the scaling law after re-calculating the *RPWBA-BC* at approximate integration limits of momentum transfer. This causes some improvements in the agreement with experimental data[90]. Moreover, they have attempted to incorporate more refined Coulomb deflection corrections within the *ECPSSR* formalism for further improvements[90].

4.6 Conclusion

The L-subshell ionization cross sections were measured for α-particle bombardments on Ho, Er, and Tm, through energy range 1-6 MeV. When the experimental values were compared to the *ECPSSR* theory for L_1, L_2, and L_3 subshells, a systematic disagreements are observed at low energies (1-3 MeV), while fair agreements are remarked at high energies. The strongest discrepancies between experimental data and theoretical predictions were found for L_2 subshell.

When the effect of induced intrashell transitions among the subshells are incorporated within the *ECPSSR* formalism by using the coupled state model, a modified formalism *ECPSSR-IS* is yielded. The comparison between this model and the experimental ionization cross sections shows that the systematic discrepancies significantly reduced, at least for L_2 and L_3 subshells. Nevertheless, the velocity-independent discrepancies remain due to the fact that the *ECPSSR-IS* model underestimate the experimental data for the three subshells over all energy range.

Therefore, the binding effect was reconsidered using the united atom approach, through calculating the reduced velocity parameter at the "saturated" united atom binding energy, and recalculate the *ECPSSR-IS* for the new parameter which yields further modified formalism, called the *ECPSSR-IS-UA*. This model is capable to describe the experimental ionization cross sections for L_2 and L_3 subshell very well over all energy range. Whereas the discrepancies remain for L_1 subshell. possible reason for

the discrepancies of L_1-subshell ionization cross sections with *ECPSSR-IS-UA* model may arise from the fact that the effective charge of α particles should be reduced by 2-3 units when employed in the united atom binding calculations for the reduced velocity parameter. Another reason is realised from using screened hydrogenic wave functions in the original *ECPSSR* formalism, that does not reflect the actual behaviour of the electrons within L_1 subshell.

Accordingly, further work can be recommended by evaluating the *ECPSSR-IS-UA* using DHS wave functions, which yielded the *ECPSSR-IS-UA-DHS* model, taking into account the precise effective charge of the projectile within the united atom approach. Furthermore, it seems that the experimental ionization cross sections which are calculated by adopting the atomic decay parameters of CHEN *et al.*[55] exhibit better agreements with all versions of the theories than those are calculated by adopting the atomic decay parameters of KRAUSE[10]. This implies that the theoretical atomic decay parameters of CHEN *et al.*[55] are more realistic.

Appendix A

Evaluation of Integrals

The mathematical techniques for performing the integrals are shown here. In order to calculate the scattering amplitude in Rutherford formula, the integral

$$I(q) = \int \frac{e^{i\mathbf{q}\cdot\mathbf{r}}}{|\mathbf{r}|} d\mathbf{r} \tag{A.1}$$

must be solved. Since there is no any preference in the space, one can choose $\mathbf{q}$ to be in the direction of the z-component of the vector $\mathbf{r}$. Thus, by means of spherical polar coordinates the integral becomes

$$I(q) = \int_0^{2\pi} d\phi \int_0^{\infty} r^2 dr \int_0^{\pi} \sin\theta \, d\theta \, \frac{e^{iqr\cos\theta}}{r}$$

Applying the integration over the angular part we are left with

$$I(q) = \frac{4\pi}{q} \int_0^{\infty} \sin qr \, dr$$

The radial part is given by[1]

$$\int_0^{\infty} \sin qr \, dr = \frac{1}{q} \tag{A.2}$$

[1]See for example J. MATHEWS and R. L. WALKER, "*Mathematical Methods of Physics.*" 2nd edition (1970), Addison-Wesley Publishing Co. Inc., Redwood City, California. Chapter 3.

Thus $I(q)$ is given as

$$I(q) = \int \frac{e^{i\mathbf{q}\cdot\mathbf{r}}}{|\mathbf{r}|} d\mathbf{r} \equiv \frac{4\pi}{q^2} \tag{A.3}$$

In the calculation of inner-shell ionization cross sections using *PWBA*, we encounter more complex integration than that given in integral (A.1), e.g.

$$y(\mathbf{r},\mathbf{q}) = \int \frac{e^{i\mathbf{q}\cdot\mathbf{R}}}{|\mathbf{R}-\mathbf{r}|} d\mathbf{R} \tag{A.4}$$

This does not look any easier. However, when multiply the integrand by $\exp(i\mathbf{q}\cdot\mathbf{r})$ and $\exp(-i\mathbf{q}\cdot\mathbf{r})$ we get

$$y(\mathbf{r},\mathbf{q}) = e^{i\mathbf{q}\cdot\mathbf{r}} \int \frac{e^{i\mathbf{q}\cdot(\mathbf{R}-\mathbf{r})}}{|\mathbf{R}-\mathbf{r}|} d\mathbf{R}$$

Assuming $\mathbf{x} = \mathbf{R} - \mathbf{r}$ and hence $d\mathbf{x} = d\mathbf{R}$, we get an easier form of the integral (A.4), given as

$$y(\mathbf{r},\mathbf{q}) = e^{i\mathbf{q}\cdot\mathbf{r}} \int \frac{e^{i\mathbf{q}\cdot\mathbf{x}}}{|\mathbf{x}|} d\mathbf{x} \tag{A.5}$$

Following the previous argument in evaluation integral (A.1) yields

$$y(\mathbf{r},\mathbf{q}) = \frac{4\pi}{q} e^{i\mathbf{q}\cdot\mathbf{r}} \int_0^\infty \sin qx \, dx$$

Make use of equation (A.2), we end up with

$$y(\mathbf{r},\mathbf{q}) = \int \frac{e^{i\mathbf{q}\cdot\mathbf{R}}}{|\mathbf{R}-\mathbf{r}|} d\mathbf{R} \equiv \frac{4\pi}{q^2} e^{i\mathbf{q}\cdot\mathbf{r}} \tag{A.6}$$

Appendix B

Energy Loss Calculations

In this appendix, the energy loss of proton beam after passing through 2 μm aluminium diffuser foil is calculated. This diffuser being used only for protons in order to obtain a homogeneous beam at the target. For the purpose of precise measurements of the beam energy, the energy loss effect must be taken into account. The process was modelled by means of the Monte Carlo simulation method in which the code RUMP-87 is used for a sufficient number of protons. The nuclear and electronic contributions to the total energy loss per unit path (dE/dx) were included in these calculations at different energies. As shown in figure (B-1) the relation between $(dE/dx)^{-1}$ and the energy of the protons, in energy range of interest, is linear. Therefore, one has

$$\left(\frac{dE}{dx}\right)^{-1} = a + b\,E \tag{B.1}$$

When the terms $(dE/dx)^{-1}$ and E are expressed in the units of Å/MeV and MeV, respectively, then the coefficients a and b are given by

$$a = 81819 \text{ and } b = 1.2768 \times 10^5 \tag{B.2}$$

Using equation (1.44) one can infer that the range R is related to the energy loss

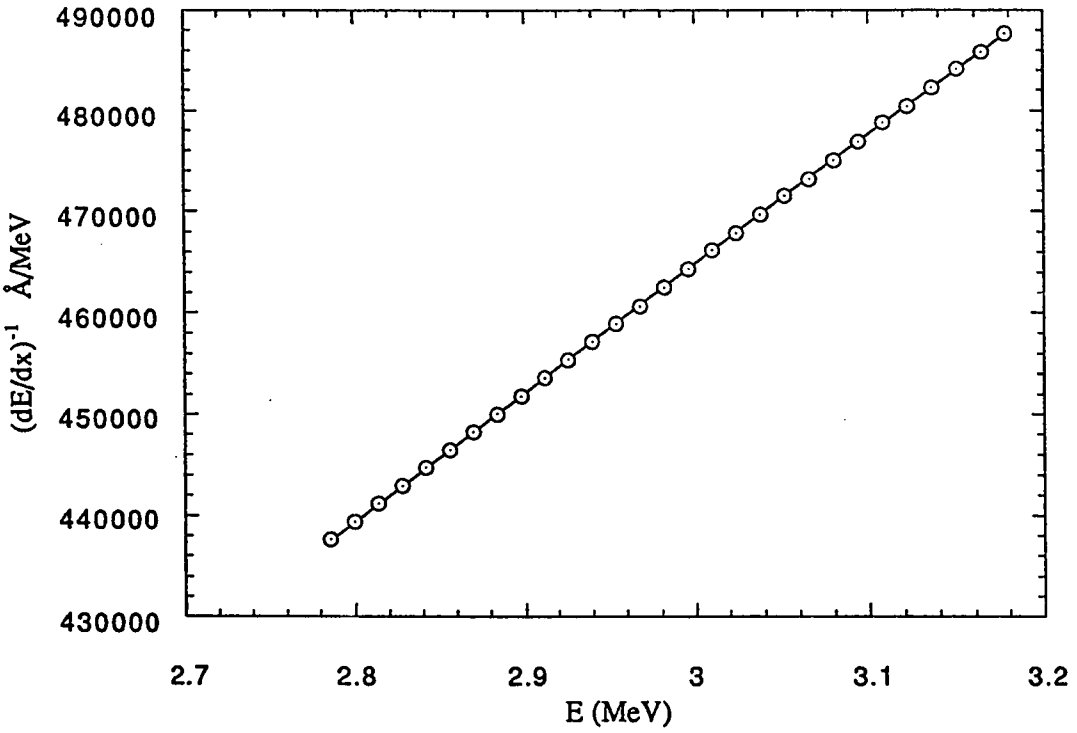

Figure B-1: Plot of $(dE/dx)^{-1}$ in Å/MeV versus energy in MeV for protons passes through 2 μm aluminium foil. The data are obtained from the Monte Carlo simulation of the code RUMP-87.

per unit path, (dE/dx), according to

$$R = \int_{E_o}^{E} -\left(\frac{dE'}{dx}\right)^{-1} dE' \tag{B.3}$$

where the integration limits E_o and E denote, respectively, the ion energy before and after passing through the aluminium diffuser foil. substituting equation (B.1) into equation (B.3), and after integrating, one obtains a quadratic equation for E and E_o. If the unphysical negative energy solution in this equation is excluded, an expression for the final energy E in terms of a, b, E_o, and R can be obtained as follows

$$E = \frac{-a + \sqrt{b^2 E_o^2 + 2\,a\,b\,E_o + a^2 - 2\,b\,R}}{b} \tag{B.4}$$

where E_o is in MeV and R is in Å. Similarly, one can obtain an expression for the initial energy E_o in terms of a, b, E, and R, as follows

$$E_o = \frac{-a + \sqrt{b^2 E^2 + 2\,a\,b\,E + a^2 + 2\,b\,R}}{b} \tag{B.5}$$

To obtain 2.5 MeV protons on the target after passing through the 20000 Å aluminium diffuser, the terminal voltage must be adjusted to yield protons of energies up to 2.55 MeV.

Appendix C

Calculation Procedures

This appendix displays the computer procedures that calculates the *L*-subshell ionization cross sections of Ho by α-particle bombardment. The program is written using *Mathematica*™ commands:

Calculations of $\alpha \rightarrow$Ho Ionization Cross Section

Part I, Peak Area Measurements

- This file evaluates the peak areas of L-alpha (`la`), L-beta1 (`lb1`), & L-gamma2,3 (`lg23`). Before proceeding quit *Mathematica* in order to erase any definitions for the symbols in the memory since they could be identified in other files.

- Go to file "eff_geo.ma" and run it.

Begin The File "eff_geo.ma"

- This file gives the geometry-efficiency as a function of X-ray line energies in (KeV) for Ho.

□ The X-ray lines and corresponding energies in KeV for L-alpha, Ll, L-eta, L-beta1, L-beta2&15, L-beta3, L-beta4, L-beta6, L-gamma1, L-gamma2, L-gamma3, L-gamma4, L-gamma5, and L-gamma2&3, respwctively, are:

```
{ea,ell,eeta,eb1,eb215,eb3,eb4,eb6,eg1,eg2,eg3,eg4,
eg5,eg23}=
{6.719, 5.942, 6.787, 7.524, 7.91, 7.65, 7.47, 7.634,
8.746, 9.049, 9.086, 9.373, 8.48,9.071};
```

□ The geometry-efficiency gamma as a function of X-ray energy in (KeV) is:

```
gamma[x_]=70.59247093178133351 + 63.2764325395290957*x-
50.260749042940294437*x^2 + 13.766842760578323304*x^3-
2.029659114961427046*x^4 + 0.181065759669687131*x^5-
0.010092760686441304481*x^6 + 0.000344525769622272245*x^7-
6.598598021943352108*10^-6*x^8 + 5.436880431*10^-8*x^9;
```

End The File "eff_geo.ma"

■ The energies of the projectile (e) in MeV are

```
e=Table[i,{i,1.2,6,0.2}];
```

■ The peak areas of L-alpha are obtained form PIXE spectrum fitting using the code PIXAN-PC

```
la;
```

■ The peak areas of L-gamma2,3 are obtained form PIXE spectrum fitting using the code PIXAN-PC

```
lg23;
```

■ The peak areas of L-beta1 are obtained form PIXE spectrum fitting using the code PIXAN-PC

```
lb1;
```

■ The peak areas for RBS-Ho peak are obtained using the code RUMP

```
nq;
```

- The normalized peak area (count/particle) is just the peak area divided by **nq**

```
nla=la/nq;
nlb1=lb1/nq;
nlg23=lg23/nq;
```

Part II, Evaluation of X-Ray Production Cross Sections

- This file is written to evaluate X-ray production cross sections from L1, L2, & L3 subshells for $\alpha \rightarrow$Ho.

- The branching ratios are taken from Salem *et al.* for L-alpha, L-beta1, Lbeta3, L-gamma1, and L-gamma2,3 respectively:

```
{ba,bb1,bb3,bg1,bg23}={0.8124718,0.830530,
                       0.453268062,0.176*0.830530,
                       0.4815*0.453268062};
```

- Rutherford backscattering cross section

  - The scattering angle ϕ

```
phi=(164/180) Pi;
```

  - The electric constant **k** (N m^2/C^2), the elementary charge **q** (Coulomb), and the energies of the projectile **ene** in MeV are repectively:

```
k=8.98755 10^9;
q=1.6021892 10^-19;
ene=e 10^6 q;
```

□ The atomic number and mass of the projectile are:

```
z1=2;

m1=4.002603;
```

□ The atomic number and mass of the target atoms Ho are:

```
z2=67;

m2=164.930421;
```

□ Rutherford formula (**ruthcross**) is:

```
ruthcross=N[(k^2*q^4*z1^2*z2^2*Csc[phi]^4*
(Cos[phi] + (1 - (m1^2*Sin[phi]^2)/m2^2)^(1/2))^2)/
(4*ene^2*(1 - (m1^2*Sin[phi]^2)/m2^2)^(1/2))];
```

□ The backscattering cross section in barn (**sigmar**) is given as:

```
sigmar=ruthcross 10^28;
```

■ X-ray production cross sections in barn "**psigmaLi**" for L1, L2, & L3 subshells are:

```
psigmaL1=N[(4 Pi nlg23 gamma[eg23] sigmar)/bg23];

psigmaL2=N[(4 Pi nlb1 gamma[eb1] sigmar)/bb1];

psigmaL3=N[(4 Pi nla  gamma[ea] sigmar)/ba];
```

■ Part III, Evaluation of inner shell ionization cross sections

■ The fluorescence yields **w1**, **w2**, and **w3** for L1, L2, &L3 subshells, respectively are taken from the semi-empirical calculations of Krause and the theoretical calculations of Chen *et al.* :

```
Krf={0.094,0.189,0.182};

Chf={0.0964,0.210,0.196};
```

□ Let us choose Krause's values

```
{w1,w2,w3}=Krf;
```

■ Coster-Kronig transition probabilities `f12,f13,` and `f23,` respectively are taken from the semi-empirical calculations of Krause and the theoretical calculations of Chen *et al.* :

```
Krck={0.19,0.3,0.142};

Chck={0.218,0.336,0.152};
```

□ Let us choose Krause's values

```
{f12,f13,f23}=Krck;
```

■ The ionization Cross sections for L1, L2, &L3 subshells, respectively, are:

```
isigmaL1=psigmaL1/w1;

isigmaL2=(psigmaL2/w2)-(f12 isigmaL1);

isigmaL3=(psigmaL3/w3)-(f23 isigmaL2)-
         ((f13-(f12 f23)) isigmaL1);
```

■ The ionization cross sections data or L1, L2, &L3 subshells, respectively, in table form are:

```
data={TableForm[isigmaL1],TableForm[isigmaL2],
      TableForm[isigmaL3]};
```

□ Send data to EXCEL

Bibliography

[1] DYSON, N. A., *"X-Rays in Atomic and Nuclear Physics."* second edition, Cambridge university press (1990), Cambridge, UK.

[2] CAI, X., Z. Y. LIU, X. M. CHEN, S. X. MA, Z. C. CHEN, Q. XU, H. P. LIU, and X. W. MA, *Nucl. Inst. Meth.*, **B72**(1992), 159.

[3] BRANSDEN, B. H., and C. J. JOACHAIN, *"Physics of Atomic and Moleculs."* Longman (1983), UK.

[4] MERZBACHER, E. and H. LEWIS, *Handbuch der Physik,* ed S. Flügge, Springer, Berlin, **34**(1958), 166.

[5] WHITE, H. W. *"Introduction to Atomic Spectra."* MacGraw Hill (1934), Tokyo, Japan.

[6] JOHANNSON, S. A. E., and J. L. CAMPBELL, *"PIXE: A Novel Technique for Elemental Analysis."* John Wiley & sons (1988), Chichester, UK.

[7] BAMBYNEK, W., B. CRASEMANN, R. W. FINK, H. U. FREUD, H. MARK, C. D. SWIFT, R. E. PRICE and P. VENUGOPALO RAO, *Rev. Mod. Phys.*, **44**(1972), 716.

[8] CHEN, M. H., B. CRASEMANN, and H. MARK, *Phys. Rev.*, **A21**(1980), 436.

[9] COHEN, D. D., *Nucl. Inst. Meth.*, **B22**(1987), 55.

[10] KRAUSE, M. O., *J. Phys. Chem. Ref. Data,* 8(1979), 307.

[11] CHEN, M. H., B. CRASEMANN, and H. MARK, *Phys. Rev.*, **A24**(1981), 177.

[12] SARKADI, L. and T. MUKOYAMA, *Phys. Rev.*, **A37**(1988), 4540.

[13] JITSCHIN, W., G. MATERLIK, U. WERNER, and P. FUNKE, *J. Phys. B: At. Mol. Phys.*, **18**(1985), 1139.

[14] KAUFMAN, S., *Phys. Rev.*, **40**(1932), 116.

[15] SALEM, S. I., S. L. PANOSSIAN and R. A. KRAUSE, *Atom. Data Nucl. Data Tables,* **14**(1974), 91.

[16] CHEN, J. R., J. D. REBER, D. J. ELLIS, and J. E. MILLER, *Phys. Rev.*, **A13**(1976), 941.

[17] SCOFIELD, J. H., *Phys. Rev.*, **A9**(1974), 1041.

[18] SCOFIELD, J. H., *Atom. Data Nucl. Data Tables,* **14**(1974), 121.

[19] SCOFIELD, J. H., *Phys. Rev.*, **A10**(1974), 1507.

[20] PERUJO, A., J. A. MAXWELL, W. J. TEESDALE, and J. L. CAMPBELL, *J. Phys. B: At. Mol. Phys.*, **20**(1987), 4973.

[21] COHEN, D. D., and M. HARRIGAN, *Atom. Data Nucl. Data Tables,* **34**(1986), 393.

[22] MARION, J. B. and F. C. YONG, *"Nuclear Reaction Analysis."* Norht-Holland Co. (1968), Amesterdam, Netherlands.

[23] RUTHERFORD, E., *Phil. Mag.*, **21**(1911), 669.

[24] KAPLAN, I., *"Nuclear Physics."* second edition, Addison-Wesley (1962), Massachusetts.

[25] CHU, W. K., J. W. MAYER and M. A. NICOLET, *"Backscattering Spectrometry."* Academic press (1978), New York.

[26] FELDMAN, L., J. MAYER and S. PICRAUX, *"Material Analysis by Ion Channelling."* Academic press (1982), New York.

[27] GASIOROWICZ, S., *"Quantum Physics."* Wiley (1974), New York.

[28] CHENG, H., H. SHEN, J. TANG, F. YANG, *Nucl. Inst. Meth.,* **B83**(1993), 449.

[29] BOZOIAN, M., *Nucl. Inst. Meth.,* **B82**(1993), 602.

[30] ZIEGLER, J. F., J. P. BIERASACK and U. LITTMARK, *"The Stopping Power and Range of Ions in Solids."* **Vol. I**, Pergamon press (1985), New York.

[31] ŠMIT, Ž., *Phys. Rev.,* **A48**(1993), 2070.

[32] CLAYTON, E., P. DUERDEN, and D. COHEN, *Nucl. Inst. Meth.,* **B22**(1987), 64.

[33] CLAYTON, E., *Nucl. Inst. Meth.,* **191**(1981), 567.

[34] FOLKMANN, F., C. GAARDE, T. HUUS, and K. KEMP, *Nucl. Inst. Meth.,* **116**(1972), 487.

[35] ISHII, K. and S. MORITA, *Int. J. PIXE,* **1**(1990), 1.

[36] BASBAS, G., W. BRANDT, and R. LAUBERT, *Phys. Rev.* **A7**(1973), 983.

[37] BANG, J. and J. HANSTEEN, *Kgl. Vid. Selsk. Mat. Fys. Medel.,* **31**(1959), 13.

[38] HENNEBERG, W., *Z. Physik,* **86**(1933), 592.

[39] GARCIA, J. D., *Phys. Rev.,* **A1**(1970), 280.

[40] KHANDELWAL, G. S., B. H. CHOI, and E. MERZBACHER, *Atom. Data. Nucl. Data Tables,* **1**(1963), 103.

[41] CHOI, B. H., E. MERZBACHER, and G. S. KHANDELWAL, *Atom. Data. Nucl. Data Tables,* **5**(1973), 291.

[42] BENKA, O. and A. KROPF, *Atom. Data. Nucl. Data Tables,* **22**(1978), 219.

[43] KOCBACH, I., J. M. HANSTEEN, and R. GUNDERSEN, *Nucl. Inst. Meth.,* **169**(1980), 281.

[44] KOOPMANS, T. H., *Physica,* **1**(1933), 104.

[45] KOSTROUND, V. O., M. CHEN, and B. CRASEMANN, *Phys. Rev.,* **A3**(1971), 533.

[46] GARCIA, J. D., R. J. FORTNER, and T. M. KAVANGH, *Rev. Mod. Phys.,* **45**(1973), 111.

[47] ZOUROS, T., D. LEE, J. SANDERS, and P. RICHARD, *Nucl. Inst. Meth.,* **B79**(1993), 166.

[48] BHALLA. C. P., R. SHINGAL, and S. GRABBE, *Nucl. Inst. Meth.,* **B79**(1993), 170.

[49] BRANDT, W. and G. LAPICKI, *Phys. Rev.,* **A20**(1979), 465.

[50] PAULI, M., *Phys. Lett.,* **A68**(1978), 223.

[51] COHEN, D. and M. HARRIGAN, *Atom. Data. Nucl. Data Tables,* **33**(1985), 255.

[52] HARRIGAN, M. and D. COHEN, *Nucl. Inst. Meth.,* **B15**(1986), 581.

[53] MOTT, N. F. and H. S. MASSEY, *"The Theory of Atomic Collisions."* second edition (1949), Oxford.

[54] BOTTRELL, G. J., *Nucl. Inst. Meth.,* **B79**(1993), 173.

[55] CHEN, M. and B. CRASEMANN, *Atom. Data. Nucl. Data Tables,* **33**(1985), 218.

[56] LAPICKI, G. and W. LOSONSKY, *Phys. Rev.*, **A20**(1979), 481.

[57] ANHOLT, R., *Phys. Rev.*, **A17**(1978), 983.

[58] BRANDT, W. and G. LAPICKI, *Phys. Rev.*, **A23**(1981), 1717.

[59] PAUL, H., *Nucl. Inst. Meth.*, **B4**(1984), 211.

[60] PAUL, H. and J. MUHR, *Phys. Rep.*, **135**(1986), 47.

[61] SARKADI, L., *Nucl. Inst. Meth.*, **214**(1983), 43.

[62] RODRÍGUEZ-FERNÁNDEZ, L., J. MIRANDA, A. OLIVER, F. CRUZ, and J. R. PEGUEROS, *Nucl. Inst. Meth.*, **B75**(1993), 49.

[63] MUKOYAMA, T. and L. SARKADI, *Nucl. Inst. Meth.*, **179**(1981), 573.

[64] YU, Y. C., *Nucl. Inst. Meth.*, **B79**(1993), 179.

[65] SEMANIAK, J., J. BRAZIEWICZ, M. PAJEK, A. KOBZEV, and T. TRAUTMANN, *Nucl. Inst. Meth.*, **B75**(1993), 63.

[66] METHA, R., J. L. DUGGAN, F. D. MCDANIEL, M. R. MCNEIR, Y. C. YU, D. K. MARBLE, and G. LAPICKI, *Nucl. Inst. Meth.*, **B79**(1993), 175.

[67] SARKADI, L. and T. MUKOYAMA, *Nucl. Inst. Meth.*, **B61**(1991), 167.

[68] SARKADI, L., *J. Phys. B: At. Mol. Phys.*, **19**(1986), 2519.

[69] SOKHI, R. S., and D. CRUMPTON, *J. Phys. B: At. Mol. Phys.*, **19**(1986), 4193.

[70] VIGILANTE, M., P. CUZZOCREA, N. DECESARE, F. MUROLO, E. PERILLO, and G. SPADACCINI, *Nucl. Inst. Meth.*, **B51**(1990), 232.

[71] ISOZUMI, Y., *Nucl. Inst. Meth.*, **A235**(1985), 164.

[72] HELENE, O., *Nucl. Inst. Meth.*, **228**(1984), 120.

[73] AL-NEAMI, A. K., A. AL-NEAMI, M. BORDAS, J. LARCHER, and C. HEITZ, *Int. J. PIXE,* **1**(1990), 63.

[74] PURI, S., D. MEHTA, B. CHAND, N. SINGH, J. H. HUBBELL, and P. N. TREHAN, *Nucl. Inst. Meth.,* **B83**(1993), 21.

[75] AL-JUWAIR, H., M. M. AL-KOFAHI, A. B. HALLAK, and M. RAJEH, *Nucl. Inst. Meth.,* **B50**(1990), 474.

[76] ALTON, G. D., *Nucl. Inst. Meth.,* **B73**(1993), 221.

[77] AL-JALAL, A., *"Measurement of Differential Cross Section of* $^{12}C(d,P)$ *Reaction at* $E_d = 160 - 300$ *keV."* Master Thesis (1991), KFUPM, Dhahran.

[78] HALLAK, A. B., and M. DAOUS, *"PIXE/RBS Development at The Tandetron Accelerator Laboratory."* Internal report RI-II-BAP-01-1992, Research Institute, KFUPM, Dhahran.

[79] EG & G ORTEC, *"Detectors & Instruments for Nuclear Spectroscopy."* 1991/92.

[80] KNOLL, G., *"Radiation Detection and Measurement."*, 2nd edition (1989), Wiley, New York.

[81] HALLAK, A. B., M. M. AL-KOFAHI, and H. A. AL-JUWAIR, *X-Ray Spectrometry,* **19**(1990), 113.

[82] DOOLITTLE, L. R., *Nucl. Inst. Meth.,* **B9**(1985), 334.

[83] DOOLITTLE, L. R., *Nucl. Inst. Meth.,* **B15**(1986), 227.

[84] COHEN, D. D., *Nucl. Inst. Meth.,* **178**(1980), 481.

[85] LEDERER, C. M. and V. SHIRLEY, *"Table of Isotopes."* Seventh edition (1978), John Wiley & sons, Inc., New York.

[86] CUZZOCREA, P., E. PERILLO, G. SPADACCINI, and M. VIGILANTE, *Nucl. Inst. Meth.*, **B15**(1986), 588.

[87] SARKADI, L., *J. Phys. B: At. Mol. Phys.*, **19**(1986), L755.

[88] BEARDEN, J. A. and A. F. BURR, *Rev. Mod. Phys.*, **39**(1967), 125.

[89] NASSER, I., private communication.

[90] DE SESARE, N., F. MUROLO, E. PERILLO, G. SPADACCINI, and M. VIGILANTE, *Nucl. Inst. Meth.*, **B84**(1994), 295.

[91] MOUS, D. J. W., R. KOUDIJS, P. DUBBELMAN, and H. A. P. VAN OOSTERHOUT, *Nucl. Inst. Meth.*, **B62**(1992), 421.

[92] CASTIGLIONI, M., G. GIANFORMA, M. MILAZZO, and M. SILIARI, *Nucl. Inst. Meth.*, **B71**(1992), 132.